Homogenized and analytical models for the diffusion MRI signal

Simona Schiavi

NNT : 2016SACLX083

Thèse de doctorat de l'Université Paris-Saclay préparée à l'École Polytechnique

Ecole doctorale n°574
Mathématiques Hadamard (EDMH)
Spécialité de doctorat : Mathématiques appliquées

par

Mme Simona Schiavi

Modélisation du signal de l'IRM de diffusion par des techniques analytiques et d'homogénéisation

Thèse présentée et soutenue à Palaiseau, le 1 Décembre 2016.

Composition du Jury :

M.	Rachid Deriche	Directeur de Recherche INRIA, Sophia Antipolis	(Président du Jury)
M.	Houssem Haddar	Directeur de Recherche INRIA, Saclay - École Polytechnique	(Directeur de thèse)
Mme	Jing-Rebecca Li	Chargée de recherche INRIA, Saclay - École Polytechnique	(Co-Directrice de thèse)
M.	Maher Moakher	Professeur École Nationale d'Ingénieurs de Tunis (ENIT)	(Examinateur)
M.	Evren Özarslan	Professeur Associé Linköping University	(Rapporteur)
M.	Bertrand Thirion	Directeur de Recherche INRIA-CEA Saclay	(Examinateur)
M.	Gary Hui Zhang	Professeur Associé University College of London (UCL)	(Rapporteur)

NNT : 2016SACLX083

THÈSE DE DOCTORAT

de

L'Université Paris-Saclay

École doctorale de mathématiques Hadamard (EDMH, ED 574)

Établissement d'inscription : École Polytechnique

Laboratoire d'accueil : Centre de Mathématiques Appliquées de Polytechnique, UMR 7641 CNRS

Spécialité de doctorat : Mathématiques appliquées

Simona SCHIAVI

Homogenized and analytical models for the diffusion MRI signal

Date de soutenance : 1 Décembre 2016

Après avis des rapporteurs : Evren Özarslan (Linköping University)
Gary Hui ZHANG (UCL)

Jury de soutenance :

Rachid DERICHE	(INRIA-Sophia Antipolis) Président du Jury
Houssem HADDAR	(INRIA-Saclay) Directeur de thèse
Jing-Rebecca LI	(INRIA-Saclay) Co-Directrice de thèse
Maher MOAKHER	(ENIT) Examinateur
Evren ÖZARSLAN	(Linköping University) Rapporteur
Bertrand THIRION	(INRIA-CEA Saclay) Examinateur
Gary Hui ZHANG	(UCL) Rapporteur

Modélisation du signal de l'IRM de diffusion par des techniques analytiques et d'homogénéisation

Résumé : L'imagerie par résonance magnétique de diffusion (IRMD) est une technique d'imagerie qui teste les propriétés diffusives d'un échantillon en le soumettant aux impulsions d'un gradient de champ magnétique. Plus précisément, elle détecte le mouvement de l'eau dû à la diffusion et s'avère donc être un outil puissant pour obtenir des informations sur la microstructure des tissus. Le signal acquis par le scanner IRM est une mesure moyennée sur un volume physique appelé voxel, dont la taille, pour des raisons techniques, est bien plus grande que l'échelle de variations microscopiques de la structure cellulaire. Ceci implique que les composants microscopiques des tissus ne sont pas visibles à la résolution spatiale de l'IRM et que les caractéristiques géométriques se trouvent agréger dans le signal macroscopique provenant du voxel. Une importante quantité mesurée par l'IRMD dans chaque voxel est le Coefficient de Diffusion Apparent (CDA) dont la dépendance au temps de diffusion est actée par de nombreuses expériences d'imagerie effectuées in vivo. Il existe dans la littérature un nombre important de modèles macroscopiques décrivant le CDA allant du plus simple au plus complexe (modèles phénoménologiques, stochastiques, géométriques, fondés sur des EDP, etc.), chacun étant valide sous certaines hypothèses techniques bien précises. Le but de cette thèse est de construire des modèles simples, disposant d'une bonne validité applicative, en se fondant sur une modélisation de la diffusion à l'échelle microscopique à l'aide d'EDP et de techniques d'homogénéisation.

Dans un article antérieur, le modèle homogénéisé FPK a été déduit de l'EDP de Bloch-Torrey sous l'hypothèse que la perméabilité de la membrane soit petite et le temps de diffusion long. Nous effectuons tout d'abord une analyse de ce modèle et établissons sa convergence vers le modèle classique de Kärger lorsque la durée des impulsions magnétiques tend vers 0. Notre analyse montre que le modèle FPK peut être vu comme une généralisation de celui de Kärger, permettant la prise en compte de durées d'impulsions magnétiques arbitraires. Nous donnons aussi une nouvelle définition, motivée par des raisons mathématiques, du temps de diffusion pour le modèle de Kärger (celle impliquant la plus grande vitesse de convergence).

Le CDA du modèle FPK est indépendant du temps ce qui entre en contradiction avec nombreuses observations expérimentales. Par conséquent, notre objectif suivant est de corriger ce modèle pour de petites valeurs de ce que l'on appelle des b-valeurs afin que le CDA homogénéisé qui en résulte soit sensible à la fois à la durée des impulsions et à la fois au temps de diffusion. Pour atteindre cet objectif, nous utilisons une technique d'homogénéisation similaire à celle utilisée pour le FPK, tout en proposant un redimensionnement adapté de l'échelle de temps et de l'intensité du gradient pour la gamme de b-valeurs considérées. Nous montrons, à l'aide de simulations numériques, l'excellente qualité de l'approximation du signal IRMD par ce nouveau modèle asymptotique pour de faibles b-valeurs. Nous établissons aussi (grâce à des développements en temps court des potentiels de surface associés à l'équation de la chaleur ou grâce à une décomposition de sa solution selon les fonctions propres) des résultats analytiques d'approximation du modèle asymptotique qui fournissent des formules explicites de la dépendance temporelle du CDA. Nos résultats sont en accord avec les résultats classiques présents dans la littérature et nous améliorons certains d'entre eux grâce à la prise en compte de la durée des impulsions.

Enfin nous étudions le problème inverse consistant en la détermination d'information qualitative se rapportant à la fraction volumique des cellules à partir de signaux IRMD mesurés. Si trouver la distribution de sphères semble possible à partir de la mesure du signal IRMD complet, il nous est apparu que la mesure du seul CDA ne serait pas suffisante.

Mots-clés : IRMD, CDA dependant du temps, modèle de Kärger, impulsions finies, modèles homogénéisés, problèmes inverses.

Homogenized and analytical models for the diffusion MRI signal

Abstract: Diffusion magnetic resonance imaging (dMRI) is an imaging modality that probes the diffusion characteristics of a sample via the application of magnetic field gradient pulses. More specifically, it encodes water displacement due to diffusion and is then a powerful tool to obtain information on the tissue microstructure. The signal measured by the MRI scanner is a mean-value measurement in a physical volume, called a voxel, whose size, due to technical reasons, is much larger than the scale of the microscopic variations of the cellular structure. It follows that the microscopic components of the tissues are not visible at the spatial resolution of dMRI. Rather, their geometric features are aggregated into the macroscopic signal coming from the voxels. An important quantity measured in dMRI in each voxel is the Apparent Diffusion Coefficient (ADC) and it is well-established from imaging experiments that, in the brain, in-vivo, the ADC is dependent on the diffusion time. There is a large variety (phenomenological, probabilistic, geometrical, PDE based model, etc.) of macroscopic models for ADC in the literature, ranging from simple to complicated. Indeed, each of these models is valid under a certain set of assumptions. The goal of this thesis is to derive simple (but sufficiently sound for applications) models starting from fine PDE modelling of diffusion at microscopic scale using homogenization techniques.

In a previous work, the homogenized FPK model was derived starting from the Bloch-Torrey PDE equation under the assumption that membrane's permeability is small and diffusion time is large. We first analyse this model and establish a convergence result to the well known Kärger model as the magnetic pulse duration goes to 0. In that sense, our analysis shows that the FPK model is a generalisation of the Kärger one for the case of arbitrary duration of the magnetic pulses. We also give a mathematically justified new definition of the diffusion time for the Kärger model (the one that provides the highest rate of convergence).

The ADC for the FPK model is time-independent which is not compatible with some experimental observations. Our goal next is to correct this model for small so called b-values so that the resulting homogenised ADC is sensitive to both the pulses duration and the diffusion time. To achieve this goal, we employed a similar homogenization technique as for FPK, but we include a suitable time and gradient intensity scalings for the range of considered b-values. Numerical simulations show that the derived asymptotic new model provides a very accurate approximation of the dMRI signal at low b-values. We also obtain some analytical approximations (using short time expansion of surface potentials for the heat equation and eigenvalue decompositions) of the asymptotic model that yield explicit formulas of the time dependency of ADC. Our results are in concordance with classical ones in the literature and we improved some of them by accounting for the pulses duration.

Finally we explored the inverse problem of determining qualitative information on the cells volume fractions from measured dMRI signals. While finding sphere distributions seems feasible from measurement of the whole dMRI signal, we show that ADC alone would not be sufficient to obtain this information.

Keywords: DMRI, time dependent ADC, Kärger model, finite-pulses, homogenized models, inverse problems.

Contents

Introduction (en français) **1**

Introduction **11**

1 Diffusion magnetic resonance imaging **19**
1.1 Diffusion . . . 19
1.2 Physics of diffusion magnetic resonance imaging (dMRI) . . . 21
1.3 Some biological applications and advanced acquisition . . . 23

2 Mathematical models **27**
2.1 The microscopic Bloch-Torrey model . . . 28
2.1.1 Probabilistic interpretation . . . 32
2.1.2 Important length scales . . . 33
2.1.3 Solutions of Bloch-Torrey equation . . . 33
2.1.4 Narrow pulse approximation . . . 36
2.1.5 The apparent diffusion coefficient (ADC) . . . 37
2.1.6 Gaussian phase approximation . . . 39
2.2 Approximate models . . . 40
2.2.1 Short-time approximation . . . 41
2.2.2 Long-time approximation . . . 41
2.2.3 Multi-compartments models . . . 42
2.2.4 Geometric models . . . 49

3 Finite pulse Kärger and Kärger Models **51**
3.1 Description of the models . . . 52
3.1.1 Finite Pulse Kärger model . . . 52
3.1.2 Kärger model . . . 54
3.2 Convergence of the Kärger model to the FPK model . . . 55
3.2.1 Asymptotic expansion in ζ . . . 56
3.2.2 Error estimates . . . 58
3.3 Kurtosis formula for FPK model . . . 63
3.4 Numerical results . . . 66
3.4.1 Trapezoidal PGSE . . . 67
3.5 Conclusions . . . 70

4 New homogenized model of time-dependent *ADC* (H-*ADC*) **71**
4.1 Problem setting . . . 74
4.1.1 Bloch-Torrey equation . . . 75
4.1.2 Periodicity length . . . 76
4.2 An asymptotic model . . . 77

4.2.1 Transformed Bloch-Torrey equation . . . 77
4.2.2 Choice of scaling . . . 78
4.2.3 Asymptotic model corresponding to $\alpha = \gamma = 2$ . . . 80
4.2.4 Asymptotic dMRI signal model and its *ADC* . . . 82
4.3 Numerical results . . . 84
4.3.1 Convergence . . . 85
4.3.2 Time-dependent *ADC* . . . 85
4.4 Comparison between the new asymptotic model and the linearized model . . . 88
4.4.1 Convergence . . . 91
4.5 Conclusions . . . 94

5 Other scalings for small b-values **95**
5.1 General equations . . . 96
5.2 Parameters limitations . . . 98
5.3 Diffusion time scale comparable with the cell size $\alpha = 1$ . . . 99
5.4 Diffusion time scale shorter than the cell size $\alpha = 2$ . . . 101
5.4.1 Moderate intensity: $\gamma = 0$ . . . 102
5.4.2 Relatively strong intensity: $\gamma = 1$ . . . 103
5.4.3 Very strong intensity: $\gamma = 3$ . . . 105
5.5 M_{ini} space dependent for $\alpha = 2$ . . . 106

6 Time-dependent ADC inside cells **111**
6.1 Effective diffusion coefficient in finite domains . . . 113
6.2 Solution of the model . . . 114
6.2.1 Eigenfunctions representation (finite pulse long-time formula, FPLT) . . . 114
6.2.2 Layer potential representation (short pulse short-time formula, SPST) . . . 116
6.2.3 Mixed approximation (short pulse long-time formula, SPLT) . . . 121
6.3 Averaging D^{eff} over multiple diffusion directions . . . 123
6.4 Numerical results . . . 124
6.5 Conclusions . . . 128

7 On the inverse problem **131**
7.1 Analysis based on the new formulas for *ADC* . . . 132
7.1.1 Finding the surface over volume ratio in the short-time limit using SPST . . . 132
7.1.2 Finding the surface over volume ratio and the eigenvalues . . . 136
7.2 On the determination of radii distributions . . . 140
7.3 On the detection of the fibers orientations . . . 146

Conclusions and Perspectives **149**

A Physical background **153**
A.1 Spatial and Contrast resolution . . . 154
A.1.1 Nuclear Magnetic Resonance . . . 154
A.1.2 Spin angular momentum . . . 156
A.1.3 Energy Levels . . . 157

A.2 Generating the signal . . . 158
A.2.1 Resonance . . . 158
A.2.2 Relaxation . . . 158
A.2.3 Contrast . . . 160
A.3 Gradient magnetic field . . . 161
A.3.1 Slice selection . . . 162
A.3.2 Frequency and Phase encoding . . . 163
A.4 Diffusion MRI . . . 164

Acknowledgements / Remerciements **167**

Bibliography **171**

Introduction (en français)

L'imagerie par résonance magnétique de diffusion (IRMD) est un outil puissant et non invasif qui donne une mesure du déplacement des molécules d'eau. Cette technique a été considérablement utilisée en science des matériaux pour étudier la structure et les propriétés de transport des milieux poreux tels que les roches sédimentaires, le béton et le ciment. En médecine et en biologie, elle a été employée pour l'analyse de la structure et des propriétés fonctionnelles des tissus biologiques de presque tous les organes du corps humain et, plus particulièrement, de ceux du cerveau (sur ces sujets on pourra consulter les articles de revue et de synthèse [30, 33, 40, 47, 80, 81, 90, 91, 169]).

Pour rendre l'IRM sensible à la diffusion, on applique un gradient encodant la diffusion afin de mesurer les effets d'atténuation sur le signal IRM provoqués par le mouvement incohérent des molécules d'eau, de par le déphasage de leur spin. Dans le cerveau, l'IRMD mesure le déplacement des spins (les protons présents dans l'eau) durant un temps de diffusion de l'ordre de quelques dizaines de microsecondes. Le signal IRMD représente la magnétisation transversale dans un volume tissulaire (appelé voxel) dont la taille est de l'ordre de 1 mm. Cependant, les dimensions caractéristiques des cellules du cerveau sont de l'ordre du micromètre, ce qui implique qu'elles ne peuvent être distinguées individuellement à la résolution de l'IRM.

Comme le déplacement de l'eau est condittionné (limité ou empêché) par la présence des membranes cellulaires, le signal IRMD mesuré pour des temps de diffusion différents, et pour des directions et des intensités du gradient différentes, dépend fortement de la microstructure des tissus. Le but de l'IRMD est de déterminer, à l'aide du signal IRM, la structure morphologique d'un échantillon et de caractériser la dynamique du système. Malgré les nombreuses applications concrètes de l'IRMD et malgré de nombreuses années d'étude théorique intensive, ce problème inverse n'a pas encore été complètement résolu et nécessite une analyse mathématique approfondie.

D'un point de vue mathématique, la description microscopique de la magnétisation complexe transversale est donnée par l'équation de Bloch-Torrey [180] :

$$\frac{\partial}{\partial t}M(\mathbf{x},t) - \operatorname{div}\left(\mathcal{D}_0 \nabla M(\mathbf{x},t)\right) + \imath\gamma B(\mathbf{x},t) M(\mathbf{x},t) = 0, \quad \mathbf{x} \in \Omega - \Gamma \tag{1}$$

où $B(\mathbf{x},t)$ représente le gradient magnétique appliqué, $\mathcal{D}_0$ est le coefficient de diffusion intrinsèque, γ le rapport gyromagnétique d'un proton de l'eau et $\imath$ l'unité imaginaire. On note Ω le volume considéré et Γ l'union de toutes les interfaces à l'intérieur de Ω qui sont susceptibles de gêner la diffusion. Cette équation aux dérivées partielles (EDP) doit être complétée par des conditions d'interface sur Γ. Dans cette thèse, nous considérons les conditions suivantes :

$$[\![\nabla M(\mathbf{z},t) \cdot \nu(\mathbf{z})]\!] = 0, \qquad \mathbf{z} \in \Gamma \tag{2}$$

$$\nabla M(\mathbf{z},t) \cdot \nu(\mathbf{z}) = \kappa [\![M(\mathbf{z},t)]\!], \quad \mathbf{z} \in \Gamma \tag{3}$$

où $\nu(\mathbf{z})$ est le vecteur normal unitaire extérieure à l'interface au point $\mathbf{z}$ et $[\![\ ]\!]$ est le saut au travers de l'interface. La première équation impose la continuité du flux traversant l'interface.

La seconde relie proportionnellement le flux au saut de la magnétisation sur l'interface, où la constante de proportionnalité κ est la perméabilité, qui modélise la facilité qu'a l'eau à traverser Γ. Si κ est nulle, l'interface est imperméable. Lorsque $\kappa \to +\infty$ (une interface complètement perméable), un flux fini n'est possible que si l'on impose la continuité de la magnétisation au travers de la frontière, c'est-à-dire $[\![M(\mathbf{z},t)]\!] = 0$.

L'équation de Bloch-Torrey est une équation de réaction-diffusion. Le fait que le rapport imaginaire $\iota\gamma B(\mathbf{x},t)$ apparaisse dans le terme réactif modifie de nombreuses propriétés de cette EDP. En conséquence, on ne peut obtenir des solutions analytiques que pour quelques cas très particuliers.

Le signal IRMD est la magnétisation transversale totale dans un voxel, c'est-à-dire

$$S(T_E) := \int_{\text{voxel}} M(\mathbf{x}, T_E) d\mathbf{x} \tag{4}$$

avec T_E un temps fixé appelé le temps d'écho. L'atténuation du signal est définie par $S(T_E)/S_0$, où S_0 est le signal associé à une expérience dans laquelle on n'applique pas de gradient de diffusion. Au vue de cette description, il est clair que le signal ne donne pas directement accès aux variations microscopiques de la magnétisation et que la moyenne faite sur le voxel masque les données structurelles du milieu. Ainsi le défi mathématique consiste-t-il à trouver une description macroscopique du signal, témoignant clairement de la dépendance à la microstructure.

Une quantité importante mesurée grâce à l'IRMD est le coefficient de diffusion apparent (CDA) aussi appelé coefficient de diffusion effectif (D^{eff}). Le premier terme est souvent utilisé par les chercheurs en médecine et certains physiciens travaillant sur la résonance magnétique. Le second terme est celui privilégié par les mathématiciens et quelques physiciens. Dans cette thèse, nous utiliserons les deux termes mais associons à chacun une signification différente. (Le choix que nous avons fait et que nous décrivons ci-dessous, est quelque peu arbitraire et nous espérons qu'il ne compromettra pas la clarté de cette thèse).

Dans cette thèse, le terme CDA désignera la quantité qui prend en compte les contributions de tous les compartiments géométriques présents dans le volume d'intérêt, alors que D_n^{eff} désignera la même quantité mais pour un unique compartiment n. (Par exemple, le compartiment 1 comprendrait toutes les cellules sphériques, le compartiment 2 toutes celles cylindriques et le compartiment 3 comprendrait tout l'espace extra-cellulaire. L'union de ces trois compartiments donne le volume total). Par conséquent, dans le cas où nous considérons un seul compartiment, on a $CDA = D^{\text{eff}}$, alors que si nous considérons $N > 1$ compartiments, et que les échanges entre ces compartiments sont négligeables, le CDA est alors :

$$CDA = \sum_{n=1}^{N} v_n D_n^{\text{eff}}, \tag{5}$$

où v_n est la fraction volumique occupée par les éléments du compartiment n, et D_n^{eff} est le coefficient effectif de diffusion associé au compartiment n. Les termes "apparent" et "effectif" indiquent que, dans les tissus, le processus de diffusion n'est pas indépendant de son milieu mais qu'il est, en fait, gêné et modulé par de nombreux mécanismes (la restriction à des espaces fermés, tortuosités autour d'obstacles, etc.) et que d'autres sources de déplacement incohérent de spin, comme dans le fluide cérébro-spinal présent dans les ventricules ou dans le sang de petits vaisseaux, peuvent contribuer au signal IRMD.

Nous donnons maintenant une définition mathématique précise du CDA dans la direction du gradient $\mathbf{u_g}$. Etant donné l'atténuation du signal $\frac{S(T_E)}{S_0}$ et la direction du gradient encodant la diffusion $\mathbf{u_g}$, on définit le coefficient de diffusion apparent dans cette direction comme :

$$CDA_{\mathbf{u_g}} := \lim_{g\to 0} -\frac{1}{\gamma^2 \int_0^{T_E} \left(\int_0^t f(s)ds\right)^2 dt} \frac{\partial}{\partial g^2} \log\left(\frac{S(T_E)}{S_0}\right), \tag{6}$$

avec g l'intensité du gradient encodant la diffusion et f son profil temporel. A partir de maintenant nous utiliserons le terme coefficient de diffusion apparent lorsque nous parlerons d'un volume contenant des géométries différentes et du coefficient de diffusion effectif dans le cas d'une seule géométrie (ou compartiment). De plus, dans toute la suite, afin de simplifier les notations, si $\mathbf{u_g}$ ne joue pas de rôle dans la discussion, nous écrirons CDA au lieu de $CDA_{\mathbf{u_g}}$ et D^{eff} au lieu de $D^{\text{eff}}_{\mathbf{u_g}}$.

On obtient le $CDA_{\mathbf{u_g}}$ à partir du signal expérimental, en faisant un fitting du signal avec une exponentielle décroissante :

$$\frac{S(T_E)}{S_0} = e^{-CDA_{\mathbf{u_g}}\, b}, \tag{7}$$

où b est une constante, appelée b-valeur, qui contient les caractéristiques du gradient de codage de diffusion appliqué,

$$b := \gamma^2 g^2 \int_0^{T_E} \left(\int_0^t f(s)ds\right)^2 dt. \tag{8}$$

Il est bien établi que le $CDA_{\mathbf{u_g}}$ est très sensible aux changements ayant lieu dans la microstructure des tissus. De plus, les expériences montrent que le $CDA_{\mathbf{u_g}}$, tiré de données d'imagerie du cerveau in-vivo, est souvent dépendant du temps. De nombreux travaux ont été réalisés afin de trouver une description appropriée du $CDA_{\mathbf{u_g}}$ dans certains cas particuliers, par exemple pour des temps de diffusion courts, pour des temps de diffusion longs, sous l'hypothèse de configurations géométriques simples, en supposant que les impulsions du gradient encodant la diffusion sont courtes comparées aux délais exitant entre elles, etc. Cependant, malgré les recherches intensives des physiciens pour trouver une caractérisation générale du $CDA_{\mathbf{u_g}}$, il existe encore un très grand nombre de régimes mettant en jeu des combinaisons variées de temps de diffusion, de perméabilité de la membrane, de configurations géométriques, qui ne dispose pas d'une description adéquate en terme de formules mathématiques (plus ou moins simples). Du point de vue mathématique, c'est cette question que cette thèse se propose d'aborder.

Dans cette thèse, l'équation de Bloch-Torrey dans un domaine hétérogène (Equations (1-3)) est approchée grâce à des techniques mathématiques d'homogénéisation. Nous cherchons notamment des développements asymptotiques de la solution de l'EDP, valides pour des b-valeurs petites. Le principe est de fixer un paramère sans dimension ε et d'écrire la solution des équations (1-3) sous la forme :

$$M(\mathbf{x}, t) = \sum_{i=0}^{\infty} \varepsilon^i M_i\left(\mathbf{x}, \frac{\mathbf{x}}{\varepsilon}, \frac{t}{\varepsilon^\alpha}\right) \tag{9}$$

où $M_i\left(\mathbf{x},\mathbf{y},\tau\right)$ dépend de la variable macroscopique $\mathbf{x}$, de la variable microscopique $\mathbf{y}=\mathbf{x}/\varepsilon$ et de la variable temporelle redimensionnée $\tau=t/\varepsilon^{\alpha}$. En remplaçant le développement (9) dans l'équation de Bloch-Torrey (1), en se servant des conditions d'interface (2, 3) et en égalant terme à terme en fonction de la puissance de ε, on obtient un ensemble d'équations qui détermine les M_i, $i\geqslant 0$ de façon récursive.

Un des principaux résultats de cette thèse est que pour le redimensionnement suivant portant sur le temps (t), la perméabilité biologique de la membrane cellulaire (κ), l'intensité du champ magnétique du gradient encodant la diffusion (g) et la période spatiale suivant la longueur de la géométrie cellulaire (L),

$$L=O(\varepsilon),\ \kappa=O(\varepsilon),\ g=O(\varepsilon^{-2}),\ t=O(\varepsilon^{2}), \tag{10}$$

nous avons obtenu un modèle mathématique particulièrement intéressant du signal d'IRMD après avoir égaler les termes du développement jusqu'à l'ordre deux en ε, i.e. $O(\varepsilon^3)$ (c'est-à-dire en effectuant la résolution jusqu'à M_2). Le modèle asymptotique qui en découle, contient des termes du signal IRMD allant jusquà l'ordre deux en g, i.e. $O(g^3)$. Autrement dit, ce modèle donne une description du CDA dépendant du temps. De manière plus précise, le signal IRMD associé à cette asymptotique s'écrit :

$$\frac{S(T_E)}{S_0}=1-\left(\sum_{n=1}^{N}v_n\left(D^{\text{eff}}_{\mathbf{u_g}}\right)_n\right)b, \tag{11}$$

où le coefficient de diffusion effectif $D^{\text{eff}}_{\mathbf{u_g}}$ (l'indice n a été supprimé) dans un compartiment fermé Ω soumis à un gradient de diffusion dirigé selon $\mathbf{u_g}$ a pour expression :

$$D^{\text{eff}}_{\mathbf{u_g}}=\mathcal{D}_0-\frac{\mathcal{D}_0}{\displaystyle\int_0^{T_E}F(t)^2dt}\int_0^{T_E}F(t)\,h(t)\,dt, \tag{12}$$

où

$$h(t)=\frac{1}{|\Omega|}\int_{\Omega}\mathbf{u_g}\cdot\nabla\omega(\mathbf{x},t)=\frac{1}{|\Omega|}\int_{\partial\Omega}\omega(\mathbf{y},t)\mathbf{u_g}\cdot\nu(\mathbf{y})ds_{\mathbf{y}} \tag{13}$$

est une quantité dépendant de ω, la solution d'une équation de diffusion homogène aux conditions aux limites de Neumann dépendant du temps et dont la condition initiale est nulle :

$$\begin{cases}\frac{\partial}{\partial t}\omega(\mathbf{x},t)-\nabla\left(\mathcal{D}_0\nabla\omega(\mathbf{x},t)\right)=0, & \mathbf{x}\in\Omega,\\ \mathcal{D}_0\nabla\omega(\mathbf{x},t)\cdot\nu(\mathbf{x})=\mathcal{D}_0F(t)\mathbf{u_g}\cdot\nu(\mathbf{x}), & \mathbf{x}\in\partial\Omega,\\ \omega(\mathbf{x},t)=0, & \mathbf{x}\in\Omega.\end{cases} \tag{14}$$

Dans les équations précédentes, $\nu(\mathbf{x})$ est le vecteur normal unitaire extérieur à l'interface au point $\mathbf{x}$ et $t\in[0,T_E]$. On peut remarquer que l'on est capable d'écrire $h(t)$ en fonction uniquement de quantités définies sur la frontière $\partial\Omega$ en appliquant le théorême de Green à l'EDP (14). Désormais, nous ferons référence au modèle ci-dessus en tant que "le nouveau modèle homogénéisé pour le CDA dépendant du temps" ou en tant que le "modèle H-CDA". On constate que le CDA du modèle H-CDA est la somme du coefficient de diffusion effectif de chaque compartiment

géométrique, pondéré par sa fraction volumique. Autrement dit, il n'y a aucun effet dû aux échanges entre les compartiments géométriques (i.e. M_0, M_1 et M_2 ne dépendent pas de la perméabilité κ).

Afin d'obtenir une relation plus concrète enre le $CDA_{\mathbf{u_g}}$ et les configurations géométriques, nous analysons le modèle H-CDA dans le cas de sous-domaines finis. En particulier, en utilisant la séquence PGSE (gradient pulsé écho de spin) [172] comme profil temporel, nous obtenons trois représentations du coefficient de diffusion effectif, correctes pour trois régimes temporels différents. En temps court (c'est-à-dire $t_D \ll \frac{L^2}{2\mathcal{D}_0}$ avec L la longueur caractéristique de la cellule, $\mathcal{D}_0$ le coefficient de diffusion intrinsèque et t_D le temps de diffusion), nous proposons une représentation fondée sur le potentiel de simple couche pour l'équation de diffusion, que nous dénommons "formule en pulsation courte et en temps court" (PCTC, ou SPST en anglais). En temps long (c'est-à-dire $NDD = \frac{\sqrt{2T_E\mathcal{D}_0}}{L/2} \gg 1$, où T_E est le temps d'écho et NDD signifie le déplacement diffusif normalisé) et lorsque les durées des pulsations ne sont pas petites, nous proposons une représentation fondée sur le développement selon les fonctions propres de l'opérateur de Neumann Laplace, que nous appelons "formule en pulsation finie et temps long" (PFTL ou FPLT en anglais). En temps long et quand la durée des pulsations est petite, nous proposons une représentation qui combine l'approche par simple couche durant les pulsations et l'approche par développement sur les fonctions propres entre les pulsations, que nous nommons "formule en pulsation courte et en temps long" (PCTL ou SPLT en anglais). Ce travail donne une explication quant à les façon dont les paramètres de la microstructure tissulaire tels que le rapport surface sur volume ou tels que les valeurs propres dominantes influencent le coefficient de diffusion effectif $D^{\text{eff}}_{\mathbf{u_g}}$. Nous soulignons, notamment, que la formule PCTC corrige la formule classique de Mitra valable en temps court ([130]), en tenant compte des durées de pulsations. Pour un domaine fini Ω, notre formule corrigée s'écrit :

$$D^{\text{eff}}_{\mathbf{u_g}} = \mathcal{D}_0 \left(1 - \frac{16}{35\sqrt{\pi}} \frac{\mathcal{D}_0^{1/2}}{\delta^2(3\Delta - \delta)} \left((\Delta+\delta)^{7/2} + (\Delta-\delta)^{7/2} - 2(\delta^{7/2} + \Delta^{7/2}) \right) \frac{\int_{\partial\Omega} (\mathbf{u_g} \cdot \nu)^2 ds_{\mathbf{x}}}{|\Omega|} \right)$$

où ν est le vecteur normal unitaire extérieur à $\partial\Omega$ et $s_{\mathbf{x}}$ est la mesure superficielle sur $\partial\Omega$. En plus du redimensionnement qui permet l'obtention du modèle H-CDA, nous avons aussi testé d'autres choix de redimensionnement. Nous en décrivons les étapes de calcul et examinons la pertinence des modèles qui en découlent.

Le second des résultats principaux de cette thèse est en rapport avec le modèle de Kärger [94] et le modèle de Kärger à pulsation fini (FPK) [42]. Le modèle de Kärger provient de la physique et est fondé sur des données empiriques concernant la diffusion dans un milieu comportant plusieurs compartiments, en faisant l'hypothèse des pulsations très courtes (c'est-à-dire la durée des pulsations est bien plus faible que le délai entre les deux pulsations). Le modèle FPK est un modèle mathématique récent qui étend le modèle de Kärger au cas des pulsations finies. A l'aide d'une analyse de ces deux modèles, nous montrons qu'en utilisant la séquence PGSE, lorsque l'hypothèse des pulsations très courtes n'est pas satisfaite, le choix le plus judicieux, du point de vue des mathématiques, quant au "temps d'évaluation" à utiliser dans le modèle de Kärger est $\Delta - \delta/3$. Nous montrons que ce choix donne une différence de l'ordre de b^3, $O(b^3)$, entre le modèle de Kärger et le modèle FPK, tandis que d'autres choix, comme par exemple Δ ou $\Delta + \delta$, donneraient une différence plus grande de l'ordre de b^2, $O(b^2)$. Nous montrons aussi

numériquement que, si l'on utilise le modèle de Kärger et qu'on choisit pour profil temporels $f(t)$ la séquence PGSE trapézoïdale, il est nécessaire de changer non seulement le temps d'évaluation, mais aussi le coefficient devant δ^2 présent dans les équations du modèle de Kärger. Puis nous indiquons comment le modèle de Kärger peut être adapté à des profils temporels plus généraux.

Dans le dernier chapitre de la thèse, nous présentons les tous premiers résultats que nous avons obtenus sur le problème inverse de l'IRMD pour des géométries élémentaires. Bien que ce travail est loin d'apporter une réponse complète au problème, il nous est déjà possible de présenter quelques résultats intéressants. Nous nous limitons au cas de géométries finies (ce qui est pertinent dans le cadre de la diffusion à l'intérieur des cellules) et au cas de la séquence PGSE. Nous montrons qu'en utilisant la formule (PCTC) nous sommes capables d'estimer correctement le rapport surface sur volume et, dans le cas de pulsations finies, nos résultats sont meilleurs que ceux obtenus grâce à la formule de Mitra ([130]). Puis, grâce à la formule PCTL, nous montrons que nous sommes en mesure d'estimer convenablement les valeurs propres dominantes et le moment d'ordre un des fonctions propres associées, mais que le rapport surface sur volume ne peut être estimé avec précision. Pour générer les données nous n'avons fait varier que le paramètre Δ dans le PGSE mais faire aussi varier le paramètre δ pourrait peut-être permettre d'aboutir à des résultats différents ; des études supplémentaires sont donc nécessaires. Nous traitons, en suite, le problème de retrouver la distribution des rayons pour une géométrie constituée seulement de cercles. Les données simulées utilisées sont soit 1) le signal IRMD obtenu pour différentes valeurs de Δ et de g ; soit 2) seulement le CDA pour différentes valeurs de Δ. Nous montrons qu'en appliquant la régularisation de Tikhonov à un algorithme d'Uzawa et qu'en utilisant comme données le signal IRMD pour différentes valeurs de Δ et g, nous parvenons à estimer, avec une précision suffisante, une distribution quelconque de rayons, même lorsque l'on ajoute aux données simulées un bruit (multiplicatif) de l'ordre de 5%. Par contre, si l'on utilise comme données le seul CDA pour différentes valeurs de Δ, notre algorithme ne converge pas ; une analyse complémentaire de ce cas est donc nécessaire. Finalement nous faisons une preuve mathématique démontrant que l'on ne peut étendre la méthode précédente pour trouver une distribution générale des orientations des fibres, même en utilisant le signal IRMD pour différentes valeurs Δ et g.

La thèse se clôt avec une discussion sur la pertinence de nos résultats dans le cadre des applications pratiques de l'IRMD et sur quelques perspectives de travail futur.

Aperçu de la thèse

La thèse est organisée comme suit.

Chapitre 1 : L'imagerie par résonance magnétique de diffusion Ce Chapitre présente brièvement la physique de l'IRMD et l'acquisition d'image ainsi que les applications médicales les plus connues.

Chapitre 2 : Des modèles mathématiques On donne la description mathématiques du signal modélisant le problème et une vue d'ensemble des techniques existantes utilisées pour traiter

ce problème. Nous passons en revue de nombreux modèles approximés fondés sur diverses hypothèses simplificatrices telles que des géométries élémentaires, l'hypothèse de pulsation étroite et l'approximation gaussienne de la phase.

Chapitre 3 : Le modèle FPK et le modèle de Kärger Un modèle mathématique récent, qui est une extension aux pulsations finies du model classique de Kärger ([94]), a été obtenu en utilisant des techniques mathématiques d'homogénéisation ([42]). La principale différence entre ces deux modèles est que le modèle FPK a été déduit mathématiquement en appliquant des techniques standards d'homogénéisation à l'équation de Bloch-Torrey, tandis que le second a été obtenu empiriquement. Nous prouvons que le modèle de Kärger est, en fait, d'un point de vue mathématique, un cas particulier du modèle FPK si l'on fait l'hypothèse des pulsations très courtes. Nous présentons toutes les preuves pour le cas de la séquence de gradient pulsé (PGSE) [172], et nous proposons une correction du temps d'évaluation du modèle de Kärger qui permet la prise en compte de pulsations finies. Nous montrons, notamment, que si on utilise le temps d'évaluation correct égal à $\Delta - \delta/3$, l'ordre de convergence entre ces deux modèles est de δ^6 (ou de b^3). Enfin, nous présentons des simulations numériques, en traitant aussi le cas de la séquence PGSE trapézoïdale afin de donner une idée de la façon dont on pourrait adapter les preuves dans le cas d'un profil temporels général.

Chapitre 4 : Un nouveau modèle pour le CDA dépendant du temps (le modèle H-CDA) Ce chapitre est le cœur de la thèse. L'idée principale est de relier le redimensionnement temporel et l'intensité du gradient au redimensionnnement spatial et à la perméabilité de la membrane en utilisant un petit paramètre sans dimension ε. Une fois les termes réunis et égalés en fonction de l'ordre de ε jusqu'à l'ordre deux en ε, $O(\varepsilon^2)$, nous obtenons un modèle asymptotique du signal IRMD. Ce modèle comprend des contributions au signal IRMD allant jusqu'à l'ordre g^2, et, de ce fait, nous le qualifions de modèle dépendant du temps pour le CDA (le modèle H-CDA). Ce modèle nous permet d'écrire le CDA en fonction de la solution d'une équation de diffusion homogène couplée à des conditions aux limites de Neumann dépendantes du temps et dont la condition initiale est nulle. Nous montrons plusieurs simulations numériques dans lesquelles nous comparons les résultats donnés par notre nouveau modèle au CDA calculé à partir de simulations numériques de l'équation de Bloch-Torrey et aux CDA donnés par deux formules préexistantes classiques, une en temps court ([130]) et l'autre en temps long ([179]). De plus, nous montrons que nous pouvons retrouver ce modèle en linéarisant l'équation de Bloch-Torrey par rapport à g et nous utilisons le théorême classique de l'énergie pour les équations de diffusions afin de prouver la convergence du signal à l'ordre trois en ε, $O(\varepsilon^3)$.

Chapitre 5 : A propos d'autres redimensionnements Dans ce Chapitre nous considérons la famille de modèle introduite au Chapitre 4 et nous analysons quelques choix particuliers de paramètres de redimensionnement temporel et d'intensité du gradient. Nous imposons notamment des restrictions mathématiques nécessaires à l'obtention d'un modèle pour des b-valeurs petites et expliquons quel type de modèle résulte d'un changement dans les paramètres de redimensionnement. Nous observons que, si nous posons $\alpha = 1$ (c'est-à-dire $t = O(\varepsilon)$), pour les différents choix possibles de redimensionnement de g respectant la contrainte d'induire de petites

b-valeurs, nous obtenons un modèle dont le CDA est indépendant du temps et coincide avec l'expression donnée par le modèle FPK. De la même façon, si nous posons $\alpha = 2$ (c'est-à-dire $t = O(\varepsilon^2)$), quelque soit le redimensionnement choisi sur g (respectant les mêmes restrictions mathématiques que précédemment), nous obtenons un modèle dont le CDA est dépendant du temps et coincide avec l'expression donnée par le modèle H-CDA présenté au chapitre 4. Cela nous permet d'expliquer d'une autre façon pourquoi le nouveau modèle introduit au chapitre 4 donne une bonne approximation pour une large gamme de déplacements de diffusion.

Chapitre 6 : CDA dépendant du temps à l'intérieur de domaines finis Dans ce Chapitre nous nous limitons au cas de domaines finis et au cas de la séquence PGSE, et nous analysons le nouveau modèle homogénéisé du CDA dépendant du temps. Nous considérons la solution de l'équation de diffusion homogène couplée à des conditions aux limites de Neumann dépendantes du temps et dont la condition initiale est nulle. En temps court, nous utilisons le potentiel de simple couche pour l'équation de diffusion afin d'écrire la solution sur la frontière. De cette façon, nous trouvons une nouvelle formule explicite pour le CDA qui dépend du rapport entre la portion de surface vue dans la direction du gradient et le volume. Cette formule généralise une formule en temps court existante pour le CDA ([130]) en prenant en compte la durée des pulsations. Nous l'appelons "approximation en pulsation courte et en temps court" (PCTC ou SPST en anglais). En temps long et pour des pulsations finies, nous utilisons le développement selon les fonctions propres de l'opérateur de Neumann Laplace pour écrire la solution de l'équation de diffusion. Nous appelons l'approximation qui en résulte "approximation en pulsation finie et en temps long (PFTL ou FPLT en anglais). En temps long et si la durée des pulsations est courte et que le décalage entre elles est long, nous utilisons le potentiel de simple couche durant les pulsations et le développement selon les fonctions propres entre elles. Nous appelons cette dernière approximation "approximation en pulsation courte et en temps long (PCTL ou SPLT en anglais).

Chapitre 7 : A propos du problème inverse Dans ce Chapitre nous proposons une étude preliminaire du problème inverse qui consiste à retrouver des informations liées à la microstructure en utilisant le CDA dépendant du temps ou le signal IRMD pour différentes valeurs de g et de temps diffusion, simulés grâce à l'équation de Bloch-Torrey. Ce travail est loin d'être complet et ouvre des voies d'exploration future. Le premier résultat que nous présentons est une application fructueuse de la formula PCTC pour retrouver le rapport surface sur volume. Nous montrons qu'avec cette nouvelle formule nous pouvons, même, ne pas nous limiter au cadre des pulsations très courtes et estimer de façon particulièrement stable le rapport surface sur volume de géométries fermées. Nous nous intéressons ensuite à l'utilisation de la formule PCTL dans le cadre de l'évalutation du rapport surface sur volume, des valeurs propres dominantes et du moment d'ordre un des fonctions propres associées pour des géométries élémentaires. Bien que nous ne puissions pas estimer correctement le rapport surface sur volume, nous sommes en mesure d'évaluer, avec une précision convenable, les premières valeurs propres et leurs contributions, qui peuvent être révélatrices de certaines caractéristiques géométriques. Puis nous étudions le problème consistant à déterminer la distribution des rayons d'une géométrie composée exclusivement de cercles. Négligeant le signal provenant du compartiment extracellulaire, nous exposons

une façon de résoudre le problème en appliquant l'algorithme d'Uzawa [183] et la régularisation de Tikhonov [178] aux différents signaux acquis lorsque l'on fait varier l'intensité du gradient et le décalage entre les pulsations. Nous montrons aussi la difficulté rencontrée dans le cas d'une application de cette méthode directement au CDA, sans utiliser la totalité du signal mesuré, mais un examen plus approfondi de ce cas particulier doit encore être mené. Enfin nous tentons d'aborder le problème qui consiste à trouver les orientations des fibres. Plus précisément, supposons que la géométrie est composée seulement par des ellipses de mêmes tailles, nous aimerions déterminer s'il est possible de trouver la distribution des ellipses en effectuant des mesures lorsque la direction du gradient varie. Nous donnons une preuve mathématique qui assure que la matrice reliée au problème 2D n'admet que trois valeurs singulières non nulles ce qui ne serait pas suffisant pour déterminer une distribution quelconques.

Conclusions et Perspectives Ce chapitre contient un bref résumé des résultats obtenus et donne quelques perspectives de recherche futures dans ce domaine.

Annexe A Dans ce Chapitre, nous décrivons de façon plus approfondie les phénomènes physique de base qui permettent de décrire l'IRMD. Cette annexe s'appuie sur les références suivantes [28, 79, 90, 118] et s'applique à mieux faire comprendre au lecteur les restrictions physiques auxquelles nous devons faire face ansi qu'à préciser le sens physique des quantités introduites.

Liste des publications

1. Houssem Haddar, Jing-Rebecca Li, and Simona Schiavi. *Adapting the Kärger model to account for finite diffusion-encoding pulses in diffusion MRI.* IMA Journal of Applied Mathematics, 2016.
2. Houssem Haddar, Jing-Rebecca Li, and Simona Schiavi. *A Macroscopic Model for the Diffusion MRI Signal Accounting for Time-Dependent Diffusivity.* SIAM Journal on Applied Mathematics, 76(3) :930–949, 2016.
3. Houssem Haddar, Jing-Rebecca Li, and Simona Schiavi. *Understanding the time-dependent diffusion coefficient measured by diffusion MRI : the intra-cellular case.* Preprint.

Introduction

Diffusion magnetic resonance imaging (dMRI) is a powerful non-invasive imaging modality that gives a measure of the displacement of water molecules. This technique has been extensively applied in materials science to investigate structural and transport properties of porous media such as sedimentary rocks, concrete, and cement. In medical and biological applications it has been used to study structural and functional properties of biological tissues in almost all organs, with the most common being the brain (for some review and survey papers, see [30, 33, 40, 47, 80, 81, 90, 91, 169]).

To make a MRI experiment sensitive to diffusion, a diffusion-encoding gradient is applied to capture the effects that the incoherent motion of water molecules has on the MRI signal through spin dephasing and signal attenuation. In the brain, dMRI measures the spin (water proton) displacement during a diffusion time on the order of tens of microseconds. The dMRI signal is the transverse magnetization in a tissue volume (called a voxel) whose size is on the order of 1 mm. However, the dimensions of cell features in the brain are of the order of micro-meters, meaning that they cannot be individually distinguished at the MRI resolution.

Because water displacement is affected (restricted or hindered) by the presence of cell membranes, the dMRI signal measured at different diffusion times, and gradient intensities and directions, is strongly dependent on the tissue microstructure. The aim of dMRI is inferring the morphological structure of a sample and characterizing the dynamics of the system from the MRI signal. In spite of numerous practical applications of dMRI and many years of intensive theoretical work, this inverse problem has not been fully solved. This constitute a strong motivation for mathematical investigations.

From a mathematical point of view, the microscopic description of the complex transverse magnetization is provided by the Bloch-Torrey equation [180]:

$$\frac{\partial}{\partial t}M(\mathbf{x},t) - \operatorname{div}\left(\mathcal{D}_0 \nabla M(\mathbf{x},t)\right) + \imath\gamma B(\mathbf{x},t) M(\mathbf{x},t) = 0, \quad \mathbf{x} \in \Omega - \Gamma \tag{15}$$

where $B(\mathbf{x},t)$ represent the applied magnetic gradient, $\mathcal{D}_0$ is the intrinsic diffusion coefficient, γ is the gyro-magnetic ratio of the water proton and $\imath$ is the imaginary unit. The volume under consideration is Ω and we will denote by Γ the union of all interfaces inside Ω that may hinder diffusion. This partial differential equation (PDE) needs to be completed with interface conditions on Γ. In particular for this work we consider the following interface conditions:

$$[\![\nabla M(\mathbf{z},t) \cdot \nu(\mathbf{z})]\!] = 0, \qquad \mathbf{z} \in \Gamma \tag{16}$$

$$\nabla M(\mathbf{z},t) \cdot \nu(\mathbf{z}) = \kappa [\![M(\mathbf{z},t)]\!], \quad \mathbf{z} \in \Gamma \tag{17}$$

where $\nu(\mathbf{z})$ is the unit outward-pointing normal vector to the interface at the point $\mathbf{z}$ and $[\![\ ]\!]$ denotes the jump across the interface. The first equation enforces the continuity of the flux across any interface. The second equation describes the flux as proportional to the jump in the magnetization across the interface, where the constant of proportionality κ is the permeability coefficient, which models the ease with which the water can cross Γ. If κ is zero the interface

is impermeable. As $\kappa \to +\infty$ (a fully permeable interface) a finite flux is only possible if one imposes the continuity of the magnetization across the boundary, i.e. $[\![M(\mathbf{z},t)]\!] = 0$.

The Bloch-Torrey equation is a diffusion-reaction equation. The fact that the reactive term contains the imaginary rate $\iota\gamma B(\mathbf{x},t)$ changes many properties of this PDE. As a consequence, analytical solutions have been obtained only for very few special cases.

The dMRI signal is the total transverse magnetization in a voxel, i.e.

$$S(T_E) := \int_{\text{voxel}} M(\mathbf{x}, T_E) d\mathbf{x} \tag{18}$$

where T_E is a fixed time called the echo time. The signal attenuation is defined as $S(T_E)/S_0$, where S_0 is the signal coming from an experiment where no diffusion gradient is applied. From this description it is clear that the signal does not give direct access to the microscopic variations of the magnetization and the averaging over the voxel obscures structural information about the medium. The mathematical challenge, thus, consists in finding a way to describe the macroscopic signal in a way that makes clearer the dependence on the microstructure.

An important quantity measured in dMRI is the apparent diffusion coefficient (ADC) or effective diffusion coefficient (D^{eff}), with the former term often used by medical researchers and some MR physicists. The latter is the preferred term among mathematicians and some physicists. In this thesis, we will use both ADC and D^{eff}, but we distinguish them in the following way. (The choice we made, described below, is somewhat arbitrary and we hope that it does not detract from the clarity of the thesis.)

In this thesis, the ADC will be used to designate the quantity that includes the contributions from all the geometrical compartments in a volume of interest, whereas D_n^{eff} will be used to designate the quantity that accounts for the contribution from a particular compartment n, within the volume of interest. (For example, all the spherical cells could comprise compartment 1, all the cylinder cells could comprise compartment 2, and the extra-cellular space compartment 3. The union of these three compartments make up the total volume.) As a consequence, if we are considering just one compartment, then $ADC = D^{\text{eff}}$, whereas if we are considering $N > 1$ compartments, and exchange between the compartments is negligible, the ADC is

$$ADC = \sum_{n=1}^{N} v_n D_n^{\text{eff}}, \tag{19}$$

where v_n is its volume fraction and D_n^{eff} is the effective diffusion coefficient of the nth compartment. The terms "apparent" or "effective" indicate that the diffusion process is not free in tissues but rather hindered and modulated by many mechanisms (restriction in closed spaces, tortuosity around obstacles, etc.) and that other sources of incoherent spin displacement, such as within the cerebrospinal fluid in ventricles or due to blood flow in small vessels, may contribute to the dMRI signal.

Now we give a mathematically precise definition of the ADC in the gradient direction $\mathbf{u_g}$. Given the signal attenuation $\frac{S(T_E)}{S_0}$, and diffusion-encoding gradient direction $\mathbf{u_g}$, the apparent diffusion coefficient in this direction is defined as

$$ADC_{\mathbf{u_g}} := \lim_{g\to 0} -\frac{1}{\gamma^2 \int_0^{T_E} \left(\int_0^t f(s)ds\right)^2 dt} \frac{\partial}{\partial g^2} \log\left(\frac{S(T_E)}{S_0}\right), \tag{20}$$

where g is the intensity of the diffusion-encoding gradient and f its time-profile. From now on we will use apparent diffusion coefficient when we talk about the diffusion coefficient coming from a volume containing different geometries and effective diffusion coefficient when we talk about a single geometry (or compartment). Additionally, in what follows, to simplify the notation, if $\mathbf{u_g}$ does not play a role in the discussion, we will write ADC instead of $ADC_{\mathbf{u_g}}$ and D^{eff} instead of $D^{\text{eff}}_{\mathbf{u_g}}$.

From the experimental signal, the $ADC_{\mathbf{u_g}}$ is obtained by fitting the signal as a decaying exponential:

$$\frac{S(T_E)}{S_0} = e^{-ADC_{\mathbf{u_g}}\, b}, \tag{21}$$

where b is a constant, called b-value, which contains the quantities from the applied diffusion-encoding gradient,

$$b := \gamma^2 g^2 \int_0^{T_E} \left(\int_0^t f(s)ds \right)^2 dt. \tag{22}$$

It has been well-established that the $ADC_{\mathbf{u_g}}$ is very sensitive to changes in tissue microstructure. Moreover, from experiments, it has been shown that the $ADC_{\mathbf{u_g}}$ from *in-vivo* brain imaging data is often time-dependent. Many works were done to find a proper description of the $ADC_{\mathbf{u_g}}$ under different assumptions, such as in the short diffusion time regime, in the long diffusion time regime, under the assumption of simple geometrical configurations, under the assumption that the pulses of the diffusion-encoding gradient are short comparing to the delay between them, etc. However, although physicists have worked intensively to find a general characterization of the $ADC_{\mathbf{u_g}}$, there are still many regimes involving various combinations of the diffusion time, membrane permeability, geometrical configuration, that still lack a valid description in terms of a (more or less simple) mathematical formula. This is the challenge this thesis takes up from a mathematical point of view.

In this thesis the Bloch-Torrey equation in a heterogeneous domain (Equations (15-17)) is approached using mathematical homogenization techniques. In particular, we search for asymptotic models of the solution of the PDE that hold for small b-values. The idea is to fix a non-dimensional parameter ε and write the solution of Equations (15-17) as

$$M(\mathbf{x}, t) = \sum_{i=0}^{\infty} \varepsilon^i M_i \left(\mathbf{x}, \frac{\mathbf{x}}{\varepsilon}, \frac{t}{\varepsilon^\alpha} \right) \tag{23}$$

where $M_i(\mathbf{x}, \mathbf{y}, \tau)$ depends on the macroscopic variable $\mathbf{x}$, the microscopic variable $\mathbf{y} = \mathbf{x}/\varepsilon$ and the scaled time variable $\tau = t/\varepsilon^\alpha$. Substituting the expansion (23) into the Bloch-Torrey equation (15), completed by the interface conditions (16,17), and equating the powers of ε lead to a set of equations that recursively determine M_i, $i \geqslant 0$.

A major result of this thesis is that for the following scaling relationship between the time (t), the biological cell membrane permeability (κ), the diffusion-encoding magnetic field gradient strength (g), and a periodicity length of the cellular geometry (L),

$$L = O(\varepsilon),\ \kappa = O(\varepsilon),\ g = O(\varepsilon^{-2}),\ t = O(\varepsilon^2), \tag{24}$$

we found a particularly interesting mathematical model of the dMRI signal after matching terms up to ε^2 (i.e. solving until M_2). The resulting asymptotic model contains terms of the dMRI

signal up to the g^2 term. In other words, this model gives a description of the time-dependent ADC. More precisely, the dMRI signal associated to this asymptotic model is:

$$\frac{S(T_E)}{S_0} = 1 - \left(\sum_{n=1}^{N} v_n \left(D^{\text{eff}}_{\mathbf{u_g}} \right)_n \right) b, \tag{25}$$

where the effective diffusion coefficient $D^{\text{eff}}_{\mathbf{u_g}}$ (we removed the compartment index n) in a closed compartment Ω subjected to a diffusion-encoding gradient in a direction $\mathbf{u_g}$ is obtained in the following way:

$$D^{\text{eff}}_{\mathbf{u_g}} = \mathcal{D}_0 - \frac{\mathcal{D}_0}{\int_0^{T_E} F(t)^2 dt} \int_0^{T_E} F(t)\, h(t)\, dt, \tag{26}$$

where

$$h(t) = \frac{1}{|\Omega|} \int_\Omega \mathbf{u_g} \cdot \nabla \omega(\mathbf{x}, t) = \frac{1}{|\Omega|} \int_{\partial\Omega} \omega(\mathbf{y}, t) \mathbf{u_g} \cdot \nu(\mathbf{y}) ds_{\mathbf{y}} \tag{27}$$

is a quantity related to a function ω that is the solution of the homogeneous diffusion equation with time-dependent Neumann boundary condition and zero initial condition:

$$\begin{cases} \frac{\partial}{\partial t}\omega(\mathbf{x}, t) - \nabla \left(\mathcal{D}_0 \nabla \omega(\mathbf{x}, t) \right) = 0, & \mathbf{x} \in \Omega, \\ \mathcal{D}_0 \nabla \omega(\mathbf{x}, t) \cdot \nu(\mathbf{x}) = \mathcal{D}_0 F(t) \mathbf{u_g} \cdot \nu(\mathbf{x}), & \mathbf{x} \in \partial\Omega, \\ \omega(\mathbf{x}, t) = 0, & \mathbf{x} \in \Omega. \end{cases} \tag{28}$$

In the above, $\nu(\mathbf{x})$ is the unit outward-pointing normal vector to the interface at the point $\mathbf{x}$ and $t \in [0, T_E]$. We observe that we are able to write $h(t)$ using just quantities on the boundary $\partial\Omega$ by applying the Green's theorem to the PDE (28). From now on we refer to the above model as "the new homogenized model for the time-dependent ADC" or the "H-ADC model". We note that the ADC of the H-ADC model is the sum of the effective diffusion coefficient in each geometrical compartment, weighed by its volume fraction. In other words, at least in the ADC term, there is no exchange effects between geometrical compartments (M_0, M_1, M_2 do not depend on the permeability κ).

To get a clearer connection between the $ADC_{\mathbf{u_g}}$ and the geometrical configurations, we analyse the H-ADC model in the case of finite sub-domains. In particular, using the PGSE (pulsed gradient spin echo) sequence [172] as the time profile, we obtain three representations of the effective diffusion coefficient that are appropriate in different time regimes. In the short-time regime (i.e. $t_D \ll \frac{L^2}{2\mathcal{D}_0}$ with L the characteristic length of the cell, $\mathcal{D}_0$ the intrinsic diffusion coefficient and t_D the diffusion time), we propose a representation based on the single layer potential for diffusion equation and we call it the short pulse short-time formula (SPST). In the long-time regime (i.e. $NDD = \frac{\sqrt{2T_E\mathcal{D}_0}}{L/2} \gg 1$, where T_E is the echo-time and NDD means normalized diffusion displacement) and when the pulses duration is not short, we propose a representation based on the eigenfunction expansion of the Neumann Laplace operator and we call it the finite pulse long-time formula (FPLT). In the long-time regime and when the pulses duration is short, we propose a representation that combines the single layer during the pulses with the eigenfunction expansion between the pulses and we call it the short pulse long-time formula (SPLT). This work helps to clarify how parameters of the tissue microstructure such as

the surface to volume ratio or the dominant eigenvalues affect the effective diffusion coefficient $D^{\text{eff}}_{\mathbf{ug}}$. We mention that, in particular, the SPST formula corrects the well known Mitra's short-time formula ([130]) by accounting for the pulses durations. For a finite domain Ω our correct formula is the following

$$D^{\text{eff}}_{\mathbf{ug}} = \mathcal{D}_0 \left(1 - \frac{16}{35\sqrt{\pi}} \frac{\mathcal{D}_0^{1/2}}{\delta^2(3\Delta - \delta)} \left((\Delta + \delta)^{7/2} + (\Delta - \delta)^{7/2} - 2(\delta^{7/2} + \Delta^{7/2}) \right) \frac{\int_{\partial\Omega} (\mathbf{ug} \cdot \nu)^2 ds_{\mathbf{x}}}{|\Omega|} \right)$$

where ν is the unit outward-pointing normal vector to the boundary $\partial\Omega$ and $s_{\mathbf{x}}$ is the surface variable of $\partial\Omega$. In addition to the scaling that gave the H-ADC model, we also tried other choices of scalings, we describe our calculations in these cases and we discuss the relevance of the obtained models.

A second main result of the thesis is related to the Kärger model [94] and the Finite-Pulse Kärger (FPK) model [42]. The Kärger model was proposed by physicists and is based on empirical evidence of diffusion in a multiple compartments medium, under the narrow pulse assumption (i.e. the duration of the pulses is much smaller than the delay between them). The FPK model is a recent mathematical model, which extended the Kärger model to the finite pulse case. By analysing these two models, we show that, using PGSE sequence, when the narrow pulse assumption is not satisfied, the most mathematically sensible choice of the "evaluation time" to insert into the Kärger model is $\Delta - \delta/3$. We show that this choice gives a difference of $O(b^3)$ between the Kärger model and the FPK model, whereas other choices, such as Δ or $\Delta + \delta$, would give a larger difference, of $O(b^2)$. We also numerically show that, if one uses the Kärger model with trapezoidal PGSE sequence, not only the evaluation time needs to be changed, but also a coefficient in the Kärger equations needs to change too. We then indicate how one can adapt the Kärger model to more general time profiles.

In the last chapter of the thesis we present some very preliminary results concerning the dMRI inverse problem in some simple geometries. Although this work is far from complete, some interesting results can be already presented. We restrict ourselves to the case of finite geometries (which is relevant to diffusion inside cells) and the PGSE sequence. We show that using the SPST formula we are able to estimate well the surface to volume ratio and, in the non-narrow pulse case, our results are better than the ones obtained using Mitra's Formula ([130]). Next, using the SPLT formula we show that we are able to estimate well the dominant eigenvalues and the first moment of the associated eigenfunctions, but not accurately the surface to volume ratio. More investigations need to be done because to generate the data we just varied the parameter Δ of PGSE but maybe varying also δ we can obtain different results. We then investigated the problem of finding the radii distributions for a geometry composed by only 2D circles, using as synthetic data either 1) the dMRI signal obtained at multiple values of Δ and g ; or 2) only the ADC at multiple values of Δ. We show that, applying Tikhonov regularization to the Uzawa algorithm and using as data the dMRI signal at multiple values of Δ and g, we are able to estimate sufficiently well a general radii distribution, even when the synthetic data contain up to 5% of (multiplicative) noise. On the contrary, if we use as data only the ADC at multiple values of Δ, our algorithm does not converge and thus this case requires more investigations. Finally, we show mathematically that we cannot extend the previous method to find general orientation distributions of fibers even when using the dMRI signal at multiple values of Δ and g.

The thesis ends with a discussion of the relevance of our results to practical dMRI applications and possible directions of future work.

Outline of the thesis

The thesis is organized as follows.

Chapter 1 Diffusion magnetic resonance imaging This Chapter contains a short description of the dMRI physics and image acquisition as well as some of the most popular medical applications.

Chapter 2: Mathematical models The mathematical description of the signal modeling problem and an overview of the existing techniques used to treat this problem are given. In particular, we review numerous approximate models based on various simplifying assumptions such as simplistic geometries, the narrow pulse assumption and the Gaussian phase approximation.

Chapter 3: FPK and Kärger models A recent mathematical model that extends the well known Kärger model ([94]) to finite pulses was obtained using mathematical homogenization techniques ([42]). The principal difference between these two is that the FPK was derived mathematically applying the standard homogenization techniques to the Bloch-Torrey equation, while the second was obtained empirically. We prove that, mathematically, the Kärger model is indeed a particular case of the FPK when we assume narrow pulses. We present all the proofs for the case of pulsed gradient sequence (PGSE) [172], and we suggest a correction for the evaluation time of the Kärger model to account for finite pulses. In particular, we show that if we use the correct evaluation time $\Delta - \delta/3$, the order of convergence between these two models is δ^6 (or b^3). Finally, we show numerical simulations also for trapezoidal PGSE to give an idea of what should be done to adapt the proofs to a general time profile.

Chapter 4: New homogenized model of the time-dependent ADC (H-ADC) This Chapter is the heart of the thesis. The main idea is to link the scaling of the time variable and the gradient intensity to the scaling of the space variable and the membrane permeability using a small non-dimensional parameter ε. After matching terms of ε up to $O(\varepsilon^2)$, we obtain an asymptotic model of the dMRI signal. This model contains contributions to the dMRI signal up to g^2, hence we call it a model for the time-dependent ADC (H-ADC). This model allows us to write the ADC in terms of the solution of a homogeneous diffusion equation with time-dependent Neumann boundary condition and zero initial condition. We show several numerical simulations in which we test the new model against the reference ADC coming from the numerical solution of the Bloch-Torrey equation and two already existing and well known ADC formulas, one in the short-time ([130]) and the other in the long-time regime ([179]). Moreover, we show that we can obtain this model also making a linearisation in g of the Bloch-Torrey equation and we use the classical energy theorem for diffusion equation to prove the convergence of order $O(\varepsilon^3)$ in the signal.

Chapter 5: On the other choices of scaling In this Chapter we consider the family of models introduced in Chapter 4 and we analyse some different possible choices of parameters for the scaling in time and gradient intensity. In particular we impose some mathematical limitations we need to get a model for small b-values and we explain which type of model we can achieve changing the scaling parameters. We observe that if we set $\alpha = 1$ (i.e. $t = O(\varepsilon)$) for possible choices of scaling on g which respects the constraint of giving small b-values, we obtain a model whose ADC results time-independent and coincides with the FPK expression. In the same way, if we set $\alpha = 2$ (i.e. $t = O(\varepsilon^2)$) no matter which scaling we choose for g (that respects the mathematical limitation imposed before), we obtain a model whose ADC results time-dependent and coincides with the H-ADC obtained in Chapter 4. This allows us to furnish another explanation on why the new model introduced in Chapter 4 gives a good approximation for a wide range of diffusion displacements.

Chapter 6: Time-dependent ADC inside finite domains In this Chapter we restrict ourselves to the case of finite domains and the PGSE sequence and analyse the new homogenized model of the time-dependent ADC. We consider the solution of the homogeneous diffusion equation with time-dependent Neumann boundary condition and zero initial condition. In the short-time regime, we use the single layer potential for the diffusion equation to write the solution on the boundary. In this way, we find a new explicit formula for ADC that depends on the portion of surface over volume ratio seen in the gradient direction. This formula generalises an existing short-time ADC formula ([130]) to account for the duration of the pulses and we call it short pulse short-time approximation (SPST). In the long-time regime and for finite pulses, we use the eigenfunctions expansion of the Neumann Laplace operator to write the solution of the diffusion equation and we call it finite pulse long-time approximation (FPLT). In the long-time regime and if the duration of the pulses is short while the time delay between them is long, we use the single layer potential during the pulses and the eigenfuctions expansion between them and we call it short pulse long-time approximation (SPLT).

Chapter 7: On the inverse problem In this Chapter we make a very preliminary study of the inverse problem of finding some information on the microstructure starting from the time-dependent ADC or the dMRI signal for multiple values of g and diffusion times simulated using the Bloch-Torrey equation. This work is far from being complete and opens many different future directions. The first result we present is the successful use of the SPST formula to recover the surface over volume ratio. We show that with this new formula we can go beyond the narrow pulse assumption and find, in a very stable way, the surface over volume ratio for closed geometries. We then investigate the use of the SPLT formula to find the surface over volume ratio and the most contributive eigenvalues and first moment of the related eigenfunctions for simple closed geometries. While we are not able to well estimate the surface over volume ratio, the first eigenvalues and their contributions are sufficiently well estimated and can be indicative on some features of the geometry. We then investigate the problem of finding the radii distribution of a geometry composed by 2D circles. Neglecting the signal coming from the extracellular compartment, we present a way to solve this problem using the Uzawa algorithm [183] and Tikhonov regularization [178] applied to signals acquired by varying the intensity of

the gradient and the delay between the pulses. We also show the difficulties encountered using the same method directly to *ADC* and not the whole signal but further investigations still need to be conducted for this case. Finally we try to approach the problem of finding the fiber orientations. In particular, supposing the geometry to be composed by 2D ellipses of the same sizes, our idea is to try to see if it is possible to find the ellipses distribution by taking measures for different gradient directions. We furnish a mathematical proof according which it should not be possible to answer to this question because the 2D matrix related to the problem has just three non zero singular values which are not sufficient.

Conclusions and Perspectives This Chapter contains a short summary of the obtained results and opens discussions about the future possible directions for this type of research.

Appendix A In this Chapter we describe the basic physical phenomena behind the dMRI image in more details. It is based on the references [28, 79, 90, 118] and is meant to give the reader a better understanding of the physical restrictions with which we have to deal, and clarify the physical meaning of all the quantities we have introduced.

List of Publications

1. Houssem Haddar, Jing-Rebecca Li, and Simona Schiavi. *Adapting the Kärger model to account for finite diffusion-encoding pulses in diffusion MRI.* IMA Journal of Applied Mathematics, 2016.
2. Houssem Haddar, Jing-Rebecca Li, and Simona Schiavi. *A Macroscopic Model for the Diffusion MRI Signal Accounting for Time-Dependent Diffusivity.* SIAM Journal on Applied Mathematics, 76(3):930–949, 2016.
3. Houssem Haddar, Jing-Rebecca Li, and Simona Schiavi. *Understanding the time-dependent diffusion coefficient measured by diffusion MRI: the intra-cellular case.* Preprint.

Chapter 1

Diffusion magnetic resonance imaging

Contents

1.1 Diffusion 19
1.2 Physics of diffusion magnetic resonance imaging (dMRI) 21
1.3 Some biological applications and advanced acquisition 23

Diffusion magnetic resonance imaging (dMRI) is a non-invasive technique which is extensively applied in material science to investigate structural and transport properties of porous media (such as sedimentary rocks or concrete), as well as in medical and neuroscience to study anatomical, physiological and functional properties of biological tissues (for some review and survey papers, see [30, 33, 40, 47, 80, 81, 90, 91, 169]). The original idea to make the classical MRI sensitive to diffusion, is to apply a diffusion-weighting (or diffusion-sensitizing) gradient to encode random trajectories of the water molecules (Brownian motion) in the direction specified by the applied diffusion gradient.

DMRI gives a measure of spins displacement during a diffusion time which can vary on the order of tens of microseconds. In particular, the dMRI signal is an average of the magnetization over a voxel, which, in clinical scanners, is a volume of the order of 1 mm^3. Since the dimensions of cells are of the order of micro-meters, they cannot be individually distinguished with the dMRI resolution. Measuring the signal at different diffusion times, and gradient intensities and directions, one aims at inferring the morphological structure of a sample and characterizing the dynamics of a system.

In this Chapter we present the self-diffusion phenomena and how spins incoherent motion is measured using diffusion MRI. In particular, after having described the meaning of self-diffusion we quickly introduce the principal physical phenomena involved to create the MRI signal and we explain how we can make this experiment sensitive to diffusion. To a more detailed description we refer to the Appendix A, which contains a summary of the references [28, 79, 90, 118, 158]. In the last Section we present few biological applications of dMRI.

1.1 Diffusion

On a molecular level self-diffusion results from collisions between atoms or molecules in liquid or gas state and it occurs even in thermodynamic equilibrium. This translational and random motion is called Brownian motion and it occurs when temperatures are above the zero degree Kelvin. It was observed for the first time by Robert Brown, who saw the random motions of pollen grains while studying them under his microscope [27]. A few years later [52, 53], Einstein used a probabilistic framework to describe the motion of an ensemble of particles undergoing diffusion. In particular, for his description he used the displacement probability and he defined

the probability as $P(\mathbf{x}_0, \mathbf{x}, t)$ where $\mathbf{x} - \mathbf{x}_0$ is the relative dynamic displacement at time t. This probability is solution of the diffusion equation

$$\frac{\partial}{\partial t} P = \mathcal{D}_0 \nabla^2 P, \tag{1.1}$$

where $\mathcal{D}_0$ is the diffusion coefficient that depends on molecular weight of the diffusing particles, intermolecular interactions (viscosity) and temperature. At $t = 0$ the probability density is a delta function on $\mathbf{x} - \mathbf{x}_0$.

In absence of obstacles, geometrical constraints or restrictions (*free diffusion*), the solution of (1.1) is a Gaussian function whose width is determined by the diffusion coefficient. Using the displacement distribution concept, Einstein was able to derive an explicit relationship between the mean-squared displacement of the ensemble in any direction, characterizing its Brownian motion, and the diffusion coefficient, $\mathcal{D}_0$

$$\langle \mathbf{x}^2 \rangle = 2\mathcal{D}_0 t \tag{1.2}$$

where $\langle \mathbf{x}^2 \rangle$ is the mean-squared displacement of particles during a diffusion time t. The diffusion coefficient $\mathcal{D}_0$ depends on the temperature, on the nature of the diffusing particles and on the environment in which the particles are diffusing. In particular, it satisfies the Stokes-Einstein equation

$$\mathcal{D}_0 = \frac{kT}{f} \tag{1.3}$$

where k is the Boltzmann constant, T is the temperature, and f is the friction coefficient which is related to the shape of the particles and the viscosity of the fluid (for more details see, for example, [158]). For free water at $T = 20°\text{C}$, the diffusion coefficient is about $2.13 \cdot 10^{-3}\text{mm}^2/\text{s}$.

In a more complex media, the self-diffusion is hindered by geometrical obstacles such as cell membranes and diffusion results hindered. In particular, P is still solution of the diffusion equation (1.1) but boundary conditions should be added to account for the cell membranes. In this case, a priori the solution will not be a Gaussian distribution and can be different along every direction.

For these reasons, we can define a macroscopic diffusion tensor $\overline{D}$ and we can distinguish between two cases.

— **Isotropic diffusion:** the tensor $\overline{D}$ is isotropic, this means that the molecules are equally likely to move in any direction (see Figure 1.1a and 1.1b). From the mathematical point of view, $\overline{D}$ is represented by a matrix which is a product between the identity and a constant.

— **Anisotropic diffusion:** the tensor $\overline{D}$ is anisotropic, this means particles diffuse more easily in some directions than others, possibly due to obstacles and hindrances (see Figure 1.1c and 1.1d). From the mathematical point of view, $\overline{D}$ is represented by a general positive definite symmetric matrix.

The goal of the diffusion MRI is to measure a signal due to the self-diffusion of particles and recover some information on the microstructure which has generated these values. We now briefly see how the experiment works and which are some of the physical phenomena involved (for more details we refer to the Appendix and the references cited there).

(a) Isotropic diffusion

(b) Diffusion tensor for isotropic diffusion

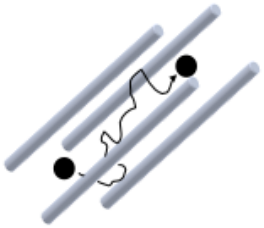

(c) Anisotropic diffusion

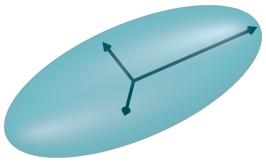

(d) Diffusion tensor for anisotropic diffusion

Figure 1.1 – Difference between free and restricted diffusion and their associated tensors.

1.2 Physics of diffusion magnetic resonance imaging (dMRI)

Magnetic resonance imaging (MRI) is a non-invasive technique based on the principle that, in presence of a constant external magnetic field $\mathbf{B}_0$, a set of particles that have non-zero spin, will see their magnetization align along the direction parallel to $\mathbf{B}_0$. For example, if we consider water protons, they have spin 1/2. Under a constant magnetic field $\mathbf{B}_0$, these nuclei have two state of energies, $\mu\mathbf{B}_0$ and $-\mu\mathbf{B}_0$, with μ being the nuclear magnetic moment. The energy difference corresponds to a resonant or Larmor frequency

$$w = \gamma \mathbf{B}_0, \tag{1.4}$$

where γ is called gyro-magnetic ratio, and for water protons is equal to $2.675 \cdot 10^8 \text{rad T}^{-1}\text{s}^{-1}$ (see [63]). At thermal equilibrium, the difference of state populations creates a net magnetization which is oriented along the direction of the magnetic field and is "precessing" around this direction at frequency w. Nevertheless, this net magnetization has very low intensity compared to the intensity of $\mathbf{B}_0$. In order to be able to measure it, the idea is to "flip" this magnetization on a transverse plane (or simply on a plane which forms an angle α with the direction of the applied magnetic field, where the amplitude depends on the application). To do so, a periodic magnetic field $\mathbf{B}_1$, rotating in the transverse plane at the Larmor frequency w, is applied for short time. This magnetic field $\mathbf{B}_1$ is called "RF pulse" because it consists in an electromagnetic radiation with a precise radiofrequency applied for a short time. Once $\mathbf{B}_1$ is turned off, the spins tend to come back to their initial condition via a phenomena called "relaxation" and we are then able to measure a signal which represents the loss in net magnetization. Since the magnetization can be represented as a vector, we decompose it into two components, parallel and perpendicular to the

direction parallel to $\mathbf{B}_0$, and we distinguish between two relaxation phenomena characterized by two times: T_1 which gives information on how fast the longitudinal magnetization comes back to the initial value and T_2 which gives information on how fast the transversal magnetization goes to 0. In general, signals would suffer additional suppression due to dephasing from external field inhomogeneities. A rephasing can be achieved by an additional RF pulse application, where the basic idea is to flip the phase of the spins by 180° in the transverse plane (for more details see for example [28, 90]). Following the 180° flip the dephasing is reversed, and the phases refocus at what is called echo time T_E. The signal is then acquired at time T_E.

To be able to localize the signal and create an image, also gradient fields are applied. A gradient field is a magnetic field which varies in space. In particular, three linear gradients are used: the "slice-selection" gradient ($\mathbf{G}_{sl}$) to select a region in which we want to excitate the spins, the "frequency" and "phase-encoding" gradients ($\mathbf{G}_x$ and $\mathbf{G}_y$) to generate the signal in the Fourier domain. These three gradients are also called "imaging gradients". The slice-selection gradient $\mathbf{G}_{sl}$ is applied at the same time as the RF pulse and thanks to it we select a volume of spins that precess at the Larmor frequency determined by $\mathbf{B}_0$, while the surrounding spins are precessing with different frequency. Lets suppose for simplicity that $\mathbf{B}_0$ is directed along the z-direction and that $\mathbf{B}_1$ flips the spins in the transversal plane xy. After spins are excited (i.e. after the application of $\mathbf{G}_{sl}$), new linear gradients are applied along the two in-plane directions (x and y) defining the excited slice. The resulting linear changes in magnetic field create corresponding linear changes in precessional frequency (i.e. the frequency w is determined by the sum of $\mathbf{B}_0$ and the linear gradients). As these frequencies vary over time with gradient duration, the excited spins accumulate also phases ϕ based on their location (x, y) and the integral in time of the applied gradients ($\mathbf{G}_x$ and $\mathbf{G}_y$)

$$\phi = 2\pi(k_x x + k_y y) \tag{1.5}$$

where

$$k_x = \gamma \int \mathbf{G}_x(t)dt \quad \text{and} \quad k_y = \gamma \int \mathbf{G}_y(t)dt. \tag{1.6}$$

The net magnetization across an excited slice can be represented as a function $S(T_E, x, y)$. The signal $\hat{S}(T_E, k_x, k_y)$ measured is the integrated signal from all spins expressed as

$$\hat{S}(T_E, k_x, k_y) = \int S(T_E, x, y) e^{\iota 2\pi(k_x x + k_y y)} dxdy. \tag{1.7}$$

Thus, the signal is the Fourier transform of the net magnetization across the slice $S(T_E, x, y)$. If one can measure $\hat{S}(T_E, k_x, k_y)$ for several values of k_x and k_y, it is possible to mathematically recover the function $S(T_E, x, y)$ by taking the inverse Fourier transform of $\hat{S}$ and then $S(T_E, x, y)$ is displayed as the MR image. Values of $\hat{S}$ at low values of k represent the low spatial frequencies which reflect values of the image S, while values of $\hat{S}$ at higher values of k reflect higher spatial frequencies which reflect the edges and details in S.

To make MRI sensitive to diffusion and generate dMRI signal we use additional magnetic gradients. The basics for diffusion weighting were introduced by Stejskal and Tanner in [172]. After excitation, and before signal sampling, a bipolar diffusion-weighting gradient is applied, as shown in Figure 1.2. This gradient adds to each spin's precession a positive phase proportional to its average position (along the direction of the gradient) during the first gradient pulse, and

a negative phase proportional to its average position during the second pulse. The sum of these phases is related to the difference between these two positions (i.e. the displacement). In particular, the bipolar gradient has no net effect on spins which do not move (because the initial and final positions are the same) and the signal becomes sensitive to movement in the direction of the magnetic gradient. The change of signal intensity that occurs as a result of diffusion is dependent on the diffusion coefficient, the diffusion time (how long we let this occurs) and on the strength of the applied diffusion-encoding magnetic gradient. We thus obtain that the signal from moving particles will be attenuated based on their displacements.

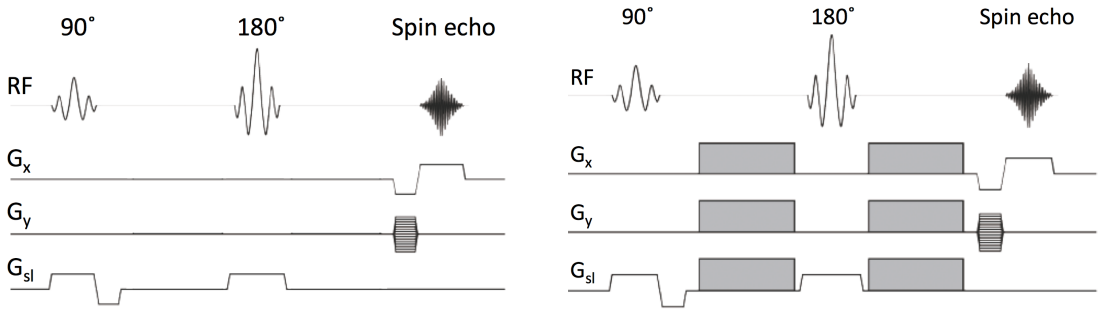

(a) MRI **(b)** Diffusion MRI

Figure 1.2 – Imaging and diffusion gradients.

1.3 Some biological applications and advanced acquisition

We have seen that the dMRI signal is the transverse magnetization in a volume of tissue called a voxel. The application of diffusion-encoding gradients causes an attenuation of the magnetization due to the dephasing of spins (water protons) from the incoherent motion of water. Since in biological tissues water diffusion is not free, and is instead strongly affected by the local environment that can contain hinderance to water displacement such as cell membranes and macromolecules, dMRI can reveal information about the tissue microstructure even though the signal is collected on a macroscopic level (voxel).

In biological tissues, the image contrast in water proton diffusion magnetic resonance imaging is given by the difference in the average water displacement due to the difference in diffusion between imaged tissues at different spatial positions [106]. Since the first diffusion MRI images of normal and diseased brain in [107], an early major application has been the study of acute cerebral ischemia in stroke [131, 187]. In the brain, dMRI has been also used to detect a wide range of physiological and pathological conditions, including tumors [125, 166, 174, 181], myelination abnormalities [80, 108], connectivity [105], as well as in functional imaging [110, 111].

There are multiple ways to display contrast using dMRI. Although this is not the focus of the thesis, for completeness, and in order to give the reader some basic references on the applications of this technique, here I report a short list of some of the most popular and used ways to display contrast using dMRI.

An early contrast is the simplest one, where the intensity of each pixel of the image represents

the magnitude of the transverse magnetization for a certain choice of diffusion-encoding gradient strength and direction. This contrast is the basis of diffusion-weighted imaging (DWI), which was shown to be more sensitive to early cellular changes after a stroke than more traditional MRI measurements (see for example [81, 82, 96, 131, 188] and Figure 1.3). DWI is most applicable when the tissue of interest results in isotropic water diffusion displacement, for example in the brain grey matter.

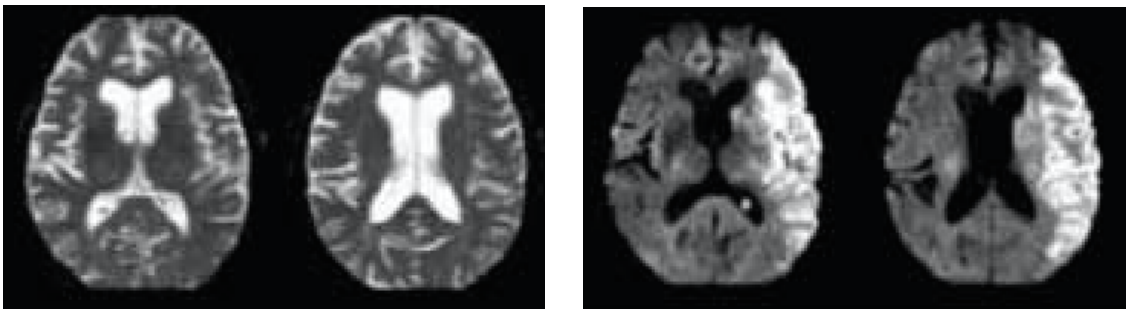

(a) MRI **(b)** Diffusion MRI

Figure 1.3 – Difference between MRI and dMRI in a brains affected by stoke. The zone affected by the stroke is clearly shown by dMRI. This image was taken at *http://www.eastportlandneurology.com/images/*.

In tissues where water diffusion is not isotropic, a contrast that takes into account the anisotropy is more appropriate. Diffusion tensor imaging (DTI) uses multiple diffusion-encoding gradient directions and fit a diffusion tensor at each voxel. Typical images assign contrast or colors to pixels based on the diffusion tensor eigenvalues (see for example [10, 16, 18, 109, 92, 154]).

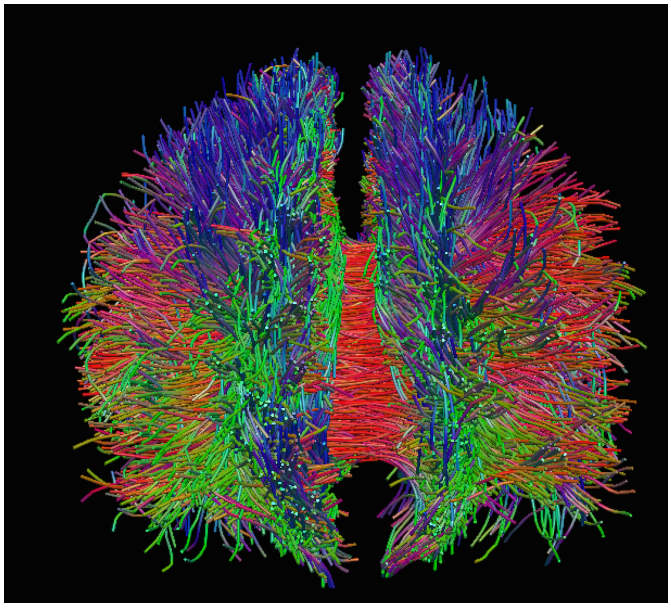

Figure 1.4 – Example of tractography of the white matter using DTI data. Image source: Alessandro Daducci, LTS5 diffusion group, Ecole Polytechnique federale de Lausanne.

DTI is then very useful to image tissues that have an internal fibrous structure such as the axons of brain white matter or muscle fibers in the heart. The fitted diffusion tensor in DTI has been used to produce tract or fiber images in the brain white matter (for a review see cite for example [10]), in the heart [35, 36, 97, 163], as well as other tissues, such as the prostate [71, 74, 157]. In the brain, the principal direction of the diffusion tensor have been used to infer the white-matter connectivity of the brain.

Recently, more advanced models of the diffusion process, that go beyond the description by a diffusion tensor, have been proposed. These include, among others, diffusion spectrum imaging (DSI) [189], q-space imaging [7, 30], high angular resolution diffusion imaging (HARDI) ([58, 59]), persistent angular structure MRI (PAS-MRI) [85], generalized diffusion tensor imaging (GDTI) [119, 145, 148], q-ball MRI [182], composite hindered and restricted model of diffusion MRI (CHARMED) [9], diffusion orientation transform (DOT) [147], diffusion kurtosis imaging (DKI) [88, 121] and multi-tensor MRI [39, 60, 84].

DTI and the derived advanced models are often used in tractography (Figure 1.4), an imagining techniques with which one tries to see which parts of the brain are connected (see for example [17, 48, 61, 105, 108, 151, 165] and references therein).

Chapter 2

Mathematical models

Contents

2.1 The microscopic Bloch-Torrey model 28
2.1.1 Probabilistic interpretation 32
2.1.2 Important length scales 33
2.1.3 Solutions of Bloch-Torrey equation 33
2.1.4 Narrow pulse approximation 36
2.1.5 The apparent diffusion coefficient (ADC) 37
2.1.6 Gaussian phase approximation 39
2.2 Approximate models 40
2.2.1 Short-time approximation 41
2.2.2 Long-time approximation 41
2.2.3 Multi-compartments models 42
2.2.4 Geometric models 49

After having made a brief overview of the physical principles behind dMRI we now introduce in detail the mathematical background which has the key role in this thesis. We start by introducing the Bloch-Torrey equation that describes the evolution of the complex transverse magnetization. We then describe various theoretical and phenomenological approaches to relate the microstructure to the macroscopic signal in order to specify the context for our work. To write these sections I found particularly useful the following surveys [63, 67, 99, 192].

This Chapter is organized as follows. In Section 2.1 we introduce the Bloch-Torrey equation and we explain how we can simplify it to add the dependence on the magnetic field $\mathbf{B}_0$ and the relaxation time T_2 after having found the solution. We also introduce all the interface conditions that we need to add to the Bloch-Torrey equation to consider the hindrance due to the membranes. Finally we describe few different time profiles for the diffusion-weighted gradient that we will consider in the following chapters. In Section 2.1.1 we describe how we can interpret the same phenomena using a probabilistic interpretation. In Section 2.1.2 we underline how many spatial scales are involved in the problem and that we should always take into account. We also define the short and long time regimes. In Section 2.1.3 we show the example of free space for which the analytical solution of the Bloch-Torrey equation is known. We also briefly describe how researchers are able to solve this equation using numerical techniques. We then introduce the most popular assumptions, the narrow pulse approximation (Section 2.1.4) and the Gaussian phase approximation (Section 2.1.6) that help in finding simplified models. Using the narrow pulse approximation, we give a mathematical definition for the apparent diffusion coefficient, and using the Gaussian phase approximation and the probabilistic interpretation we give an equivalent definition. In Section 2.2 we make a description of all the known models to

approximate the solution of the Bloch-Torrey equation under particular assumptions. We start introducing the most discussed in this thesis, which are the short and long time models and then we describe other models specifying under which assumptions they were derived. In Section 2.2.3 we explain how we can describe the problem in complex geometries using multi-compartments models. Finally in Section 2.2.4 we introduce the most principal models defined for very specific geometries that are particularly used in neuroscience applications.

2.1 The microscopic Bloch-Torrey model

During the dMRI experiment a magnetic field $\mathbf{B}_0 = (0, 0, B_z)$ is applied along a direction, conventionally denoted the z axis, and the resulting magnetization is oriented along the same direction. Then a 90° radio-frequency (RF) magnetic field pulse flips the magnetization into the transverse plane (xy) (where it starts to precess with the Larmor frequency $w_0 = \gamma B_z$). The magnetization $\mathbf{M} = (M_x, M_y, M_z)$ obeys the Bloch-Torrey equation [180]

$$\begin{cases} \dfrac{\partial}{\partial t} M_x = \operatorname{div}\left(\boldsymbol{\mathcal{D}}_0 \nabla M_x\right) + \gamma(\mathbf{M} \times \mathbf{B})_x - \dfrac{M_x}{T_2}, & \text{in } \Omega - \Gamma \times [0, T_E] \\ \dfrac{\partial}{\partial t} M_y = \operatorname{div}\left(\boldsymbol{\mathcal{D}}_0 \nabla M_y\right) + \gamma(\mathbf{M} \times \mathbf{B})_y - \dfrac{M_y}{T_2}, & \text{in } \Omega - \Gamma \times [0, T_E] \\ \dfrac{\partial}{\partial t} M_z = \operatorname{div}\left(\boldsymbol{\mathcal{D}}_0 \nabla M_z\right) + \gamma(\mathbf{M} \times \mathbf{B})_z - \dfrac{M_z - M_0}{T_1}, & \text{in } \Omega - \Gamma \times [0, T_E] \end{cases} \tag{2.1}$$

where div indicates the divergence operator, ∇ is the gradient operator, $\times$ indicates the vector product, Ω is the domain under consideration and Γ denotes the union of all the interfaces inside Ω that may hinder the diffusion. On the right hand side of this partial differential equation (PDE) there are three different mechanisms which affect the magnetization [67]:

(i) the diffusion of the nuclei with the diffusion tensor $\boldsymbol{\mathcal{D}}_0$ (in units mm^2/s);

(ii) the precession around the magnetic field $\boldsymbol{B}$;

(iii) the relaxation to the equilibrium magnetization $\mathbf{M}_{eq} = (0, 0, M_0)$ through the relaxation times T_1 and T_2.

Combining M_x and M_y into the complex-valued transverse magnetization $M = M_x + \imath M_y$ (where $\imath$ denotes the imaginary unit) and writing explicitly the components of the vector product $\mathbf{M} \times \mathbf{B}$, yield the compact form of the Bloch-Torrey PDE:

$$\frac{\partial}{\partial t} M(\mathbf{x}, t) = \operatorname{div}\left(\boldsymbol{\mathcal{D}}_0 \nabla M\right) - \imath\gamma B_z(\mathbf{x}, t) M(\mathbf{x}, t) - \frac{1}{T_2} M(\mathbf{x}, t) \tag{2.2}$$

From the mathematical point of view, this is a standard diffusion-reaction equation, where the reactive term contains the imaginary rate $\imath\gamma B_z(\mathbf{x}, t)$ which changes many properties of this partial differential equation.

Inside a voxel there are multiple hindrances to diffusion. Thus, it is usual to complement the Bloch-Torrey PDE (2.2) by conditions that slow down or stop diffusion at geometrical interfaces such as cell membranes. This partial differential equation needs, thus, to be completed with

boundary conditions on Γ. In particular, for this work we consider the following boundary conditions:

$$[\![\nabla M(\mathbf{y},t)\cdot\nu(\mathbf{y})]\!] = 0, \qquad \mathbf{y}\in\Gamma \tag{2.3}$$

$$\nabla M(\mathbf{y},t)\cdot\nu(\mathbf{y}) = \kappa[\![M(\mathbf{y},t)]\!], \quad \mathbf{y}\in\Gamma \tag{2.4}$$

where $\nu(\mathbf{y})$ is the unit outward-pointing normal vector to the interface at the point $\mathbf{y}$ and $[\![\ ]\!]$ denotes the jump across the interface. The first equation enforces the continuity of the flux across any interface. The second equation describes the flux as proportional to the jump in the magnetization across the interface, where the constant of proportionality κ represents the permeability coefficient which models the ease with which the water can cross the interface. If κ is zero the interface is impermeable. As $\kappa \to +\infty$ (a fully permeable interface) a finite flux is only possible if one imposes the continuity of the magnetization across the boundary, i.e. $[\![M(\mathbf{y},t)]\!] = 0$.

Finally we also set constant initial condition

$$M(\mathbf{x},0) = M_0 \tag{2.5}$$

where the values M_0 is often given by the density of the spin in the selected volume.

In this thesis, for simplicity, the transverse relaxation time T_2 is assumed space independent within a voxel. This means that all the nuclei inside the voxel are affected by the transverse relaxation in the same way, and thus the resulting magnetization attenuation can be factored out as e^{-t/T_2} independently of diffusion and precession. Making this assumption, the related T_2 term in (2.2) can be omitted because one can add its contribution directly in the final formula for the signal.

For simplicity, in this thesis, we also assume the diffusion tensor $\boldsymbol{\mathcal{D}}_0$ to be space-independent within a voxel. Moreover, in order to simplify the calculations, we frequently treat only the case where $\boldsymbol{\mathcal{D}}_0$ is isotropic (i.e. the diffusion tensor becomes a diffusion coefficient $\mathcal{D}_0$), but all the presented results can be extended to the anisotropic case. We emphasize that this assumption does not prevent to observe anisotropic diffusion at the macroscopic scale because the anisotropy can come from the geometrical hindrances to diffusion.

We note that the magnetic field $B_z(\mathbf{x},t)$ we are considering in the Bloch-Torrey equation (2.2) consists only in the diffusion-weighting gradient and does not include the imaging gradients described in 1. In particular $B_z(\mathbf{x},t)$ includes two terms [67]:

— a constant magnetic field B_0 to induce sufficient magnetization (which is always on during the experiment);

— a small spatially inhomogeneous field to encode the diffusive motion (which does not contain the imaging gradients).

Since the first field affects all the nuclei in the same way its contribution to the magnetization can be factored out as $e^{\imath\gamma B_0 t}$, using the same arguments we used before for the contribution coming from the term containing the T_2 relaxation. The second field, the diffusion-encoding field, is usually a linear gradient field:

$$B_z(\mathbf{x},t) = B_0 + \mathbf{x}\cdot\mathbf{G}(t). \tag{2.6}$$

There are also other configurations, like parabolic gradients, which will not be discussed in this thesis (see for example [63] and references therein). The gradient $\mathbf{G}(t)$ has a fixed direction $\mathbf{u_g}$ and a gradient strength g and, for convenience, we factor out the dimensionless time profile $f(t)$, where $\max|f(t)| = 1$:

$$B_z(\mathbf{x}, t) = B_0 + gf(t)\mathbf{x} \cdot \mathbf{u_g}. \tag{2.7}$$

The choice of the amplitude g (in units T/m), the direction $\mathbf{u_g}$ and the time profile $f(t)$ of the linear diffusion gradient depends on the experiment. There are several common choices for the function $f(t)$ and we list the following that we have considered in this thesis (for other types we refer for example to [63, 100, 142] and references therein).

(i) The Pulsed Gradient Sequence (PGSE) introduced by Stejskal and Tanner in [172, 176] consists in two ideal rectangular gradient pulses of duration δ with a time delay Δ between the start of the two pulses. There is also a 180 degree spin reversal between the two pulses which mathematically can be translated into the negation of the phase. One then ends up with (see Figure 2.1a)

$$f(t) = \begin{cases} 1 & t_0 \leqslant t < t_0 + \delta, \\ -1 & t_0 + \Delta \leqslant t < t_0 + \Delta + \delta, \\ 0 & \text{otherwise.} \end{cases} \tag{2.8}$$

(ii) A more realistic profile is the trapezoidal pulsed-gradient sequence (tPGSE)

$$f(t) := \begin{cases} \frac{t-t_0}{\chi} & \text{if } t_0 \leqslant t < t_0 + \chi, \\ 1 & \text{if } t_0 + \chi \leqslant t < t_0 + \delta - \chi, \\ -\frac{t-t_0-\delta}{\chi} & \text{if } t_0 + \delta - \chi \leqslant t < t_0 + \delta, \\ -\frac{t-t_0-\Delta}{\chi} & \text{if } t_0 + \Delta \leqslant t < t_0 + \Delta + \chi, \\ -1 & \text{if } t_0 + \Delta + \chi \leqslant t < t_0 + \Delta + \delta - \chi, \\ \frac{t-t_0-(\Delta+\delta)}{\chi} & \text{if } t_0 + \Delta + \delta - \chi \leqslant t < t_0 + \Delta + \delta, \\ 0 & \text{otherwise,} \end{cases} \tag{2.9}$$

where $\chi = c\delta$ is the rise time with c being a constant in $]0, 0.5]$ (see Figure 2.1b). It is important to consider this time profile because, since it is physically impossible to instantaneously turn on a gradient with strength g, is more realistic than (2.8).

(iii) The oscillating gradient profiles (OGSE) are meant to access short-time scales of diffusive motion (see for example [50, 141, 191]). It can take the form of either cosine or sine function during the pulses, i.e. it consists in two oscillating pulses of duration T, each containing n periods (hence the frequency is $w = \frac{2\pi n}{T}$) and with a time τ between the intervals (see Figure 2.1c and 2.1d):

$$f(t) := \begin{cases} \cos(w(t - t_0)) & \text{if } t_0 < t < t_0 + T, \\ -\cos(w(t - t_0 - \tau)) & \text{if } t_0 + \tau < t < t_0 + \tau + T, \\ 0 & \text{otherwise,} \end{cases} \tag{2.10}$$

or

$$f(t) := \begin{cases} \sin(w(t-t_0)) & \text{if } t_0 < t < t_0 + T, \\ -\sin(w(t-t_0-\tau)) & \text{if } t_0+\tau < t < t_0+\tau+T, \\ 0 & \text{otherwise.} \end{cases} \tag{2.11}$$

We also remark that OGSE is often described using a frequency variable instead of the time one (i.e. considering as variable $1/t$ [141]).

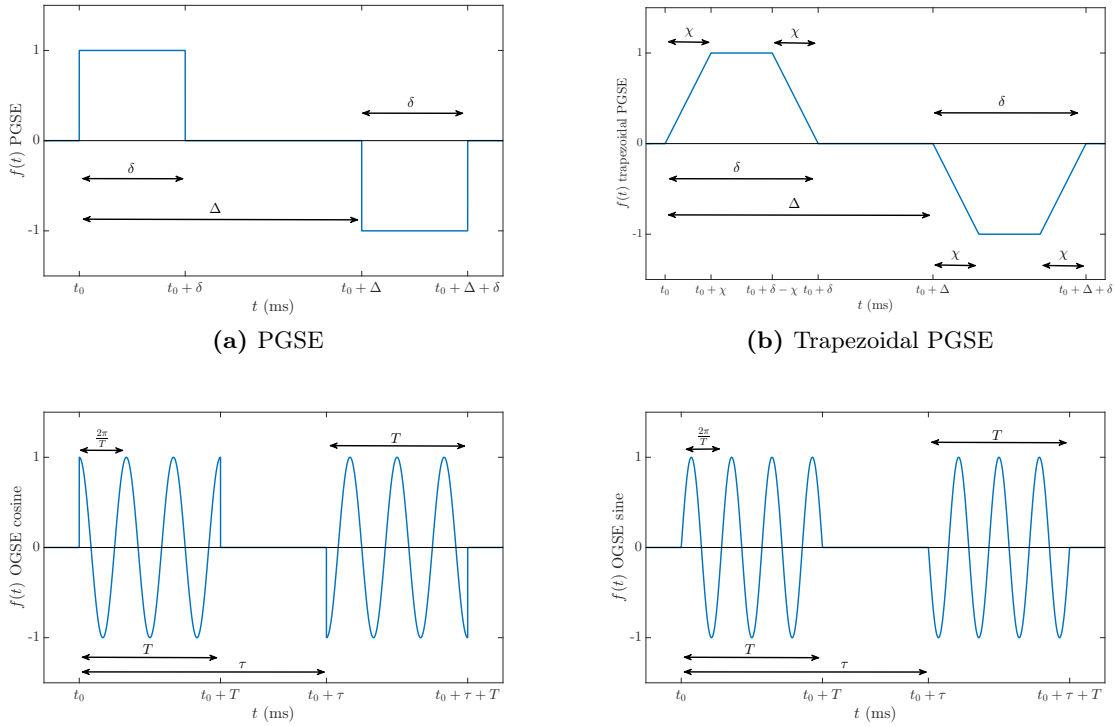

(a) PGSE **(b)** Trapezoidal PGSE

(c) OGSE cosine **(d)** OGSE sine

Figure 2.1 – Sequences time profiles

We emphasize that all these time profiles respect the so called "rephasing condition"

$$\int_0^{T_E} f(t) = 0, \tag{2.12}$$

where T_E is the echo-time. In particular, the above temporal profiles are also anti-symmetric, i.e. for every $t \in [0, T_E]$ they satisfy

$$f(t) = -f(T_E - t). \tag{2.13}$$

In practice, the macroscopic signal is the total magnetization over a volume of tissue called a voxel whose size depends on the spatial resolution of the image acquisition

$$S(T_E) = \int_{\text{voxel}} M(\mathbf{x}, T_E)\, d\mathbf{x}, \tag{2.14}$$

where T_E is the echo-time. Obviously this averaging eliminates a lot of structural information about the medium. The biggest challenge of the dMRI is then to recover some lost geometric features from studying the macroscopic signal. We also remark that, in the experiments, the macroscopic signal can only be measured at the echo time T_E and not at each instant.

This thesis will approach the Bloch-Torrey PDE (after the mentioned simplifications) subject to the constant initial condition M_0 (2.5) and the interface conditions (2.3) and (2.4) for which one will specify the values of κ, i.e. we are interested in studying

$$\begin{cases} \dfrac{\partial}{\partial t}M(\mathbf{x},t) = \operatorname{div}\left(\mathcal{D}_0\nabla M\right) - \imath\gamma g f(t)\mathbf{x}\cdot\mathbf{u_g}M(\mathbf{x},t), & \text{in } \Omega\times[0,T_E] \\ [\![\nabla M(\mathbf{x},t)\cdot\nu(\mathbf{x})]\!] = 0, & \text{on } \Gamma\times[0,T_E] \\ \nabla M(\mathbf{x},t)\cdot\nu(\mathbf{x}) = \kappa[\![M(\mathbf{x},t)]\!], & \text{on } \Gamma\times[0,T_E] \\ M(\mathbf{x},0) = M_0. & \text{in } \Omega \end{cases} \tag{2.15}$$

If we do not specify the time profile, then this means that the results are valid for all profiles that respect the rephasing condition (2.12) and not only the above presented four.

2.1.1 Probabilistic interpretation

As it is often done the case with diffusion (see for example [63, 67]), it would be useful to evoke the probabilistic interpretation of the macroscopic signal. Since the applied magnetic field $B_z(\mathbf{x},t)$ is not homogeneous, from the physics we know that some spins process faster then others, depending on their position in space. Consequently spins acquire a phase φ_t which is obtained by integrating the position-dependent Larmor frequency $\gamma B_z(\mathbf{x},t)$ along the random trajectory $\mathbf{x}(t)$ of the nucleus:

$$\varphi_t = \int_0^t \gamma B_z(\mathbf{x}(t'),t')\,dt'. \tag{2.16}$$

Looking at (2.16) we see that this random variable is a functional of the random trajectory $\mathbf{x}(t)$. Since in Section 2.1 we assumed that we can neglect the term containing the relaxation time, the amplitude of the local magnetization does not change, and thus the macroscopic signal can be obtained averaging the phase factor $e^{\imath\varphi_t}$ over all spins [63, 67]. Moreover, since the number of nuclei in a voxel is gigantic, the average can be replaced by the expectation over all the random trajectories $\mathbf{x}(t)$:

$$S = S_0\mathbb{E}\left\{e^{\imath\varphi_t}\right\}, \tag{2.17}$$

where the trajectories starting points are uniformly distributed over the voxel and S_0 is the reference signal obtained without employing the diffusion-weighting gradient. In other words the macroscopic signal can be interpreted as the characteristic function of the phase φ_t (2.17) as well as the integral of the magnetization $M(\mathbf{x},t)$ which obeys to the Bloch-Torrey equation (2.14).

The probabilistic interpretation of the signal is equivalent to the deterministic one obtained with the Bloch-Torrey equation but, according to the application, it can be more useful to use one or the other.

2.1.2 Important length scales

As we have already mentioned the signal measured by the dMRI scanner is a mean-value measurement in a physical volume, called voxel, whose size is much larger than the scale of the microscopic variation of the cellular structures. The resolution of dMRI is of the order of 1mm^3 for clinical scanners, meaning the dMRI signal combines the diffusion characteristics of a tissue volume of about 1mm^3. This is very large compared to cell features, which, for example in the brain, vary from sub-μm (diameter of neurites) to tens of μm (diameter of neuronal bodies, axons and glial cells). In other words, dMRI is used to show the averaged characteristics of the microscopic structure on a macroscopic scale.

There are four important different lengths that needs to be considered in the dMRI problem [63]:

— the size of geometrical compartment L;

— the diffusion length $L_d = \sqrt{\mathcal{D}_0 t}$, showing the average distance explored by spins during time t;

— the gradient length $L_g = (\gamma g t)^{-1}$, which characterize the overall phase shift during a time t;

— the permeation length $L_\kappa = \mathcal{D}_0/\kappa$ which characterize the effective distance travelled by the spins between the first arrival onto the surface and the full permeation.

As a result we have that different regimes of restricted diffusion depend on how short some of these lengths are with respect to the others. For example we say that we are in *short-time* regime if

$$t_D \ll \frac{L^2}{2\mathcal{D}_0}, \tag{2.18}$$

where t_D is the diffusion time, L is the characteristic length of the cell, $\mathcal{D}_0$ its intrinsic diffusion coefficient. In a similar way we say that we are in in *long-time* regime if

$$NDD := \frac{\sqrt{2T_E\mathcal{D}_0}}{L/2} \gg 1, \tag{2.19}$$

where NDD means normal diffusion displacement.

2.1.3 Solutions of Bloch-Torrey equation

In the case of unrestricted diffusion, the exact solution the Bloch-Torrey equation (2.15) is known [30, 95], and the macroscopic signal takes the exponential form

$$S(T_E) = S_0 e^{-\mathcal{D}_0 b} \tag{2.20}$$

where S_0 is the reference signal without diffusion-weighting gradient, and the b-value is defined as [107, 172]

$$b = \gamma^2 g^2 \int_0^{T_E} \left(\int_0^t f(s) ds \right)^2 dt, \tag{2.21}$$

where the rephasing condition (2.12) is assumed. We observe that for the previously introduced time profiles the b-value takes the form

$$b = \gamma^2 g^2 \left(\Delta - \frac{\delta}{3}\right) \quad \text{for PGSE} \tag{2.22}$$

$$b = \gamma^2 g^2 \delta^2 \left[(1-c)^2\Delta + \left(\frac{8}{15}c^3 - \frac{7}{6}c^2 + c - \frac{1}{3}\right)\delta\right] \quad \text{for tPGSE} \tag{2.23}$$

$$b = \gamma^2 g^2 \frac{T}{w^2} \quad \text{for OGSE cosine.} \tag{2.24}$$

$$b = \gamma^2 g^2 \frac{3T}{w^2} \quad \text{for OGSE sine.} \tag{2.25}$$

To obtain (2.20) one considers the Bloch-Torrey equation in $\mathbb{R}^d$ with a constant diffusion coefficient $\mathcal{D}_0$ and initial condition M_0 given by

$$\begin{cases} \dfrac{\partial}{\partial t} M(\mathbf{x},t) + \imath\gamma g \mathbf{u_g}\cdot\mathbf{x} f(t) M(\mathbf{x},t) - \operatorname{div}_{\mathbf{x}}\left(\mathcal{D}_0 \nabla_{\mathbf{x}} M(\mathbf{x},t)\right) = 0, & \text{in } \mathbb{R}^d \times]0, T_E[, \\ M(\mathbf{x},0) = M_0(\mathbf{x}), & \text{in } \mathbb{R}^d. \end{cases} \tag{2.26}$$

The Fourier transform $\hat{M}(\xi,t)$ of the solution $M(x,t)$, with respect to the spatial variable, solves

$$\begin{cases} \dfrac{\partial}{\partial t}\hat{M}(\xi,t) - \gamma g f(t)\mathbf{u_g}\cdot\nabla_\xi \hat{M}(\xi,t) - \xi^T \mathcal{D}_0 \xi \hat{M}(\xi,t) = 0, & \text{in } \mathbb{R}^d \times]0, T_E[, \\ \hat{M}(\xi,0) = \hat{M}_0(\xi), & \text{in } \mathbb{R}^d. \end{cases} \tag{2.27}$$

This problem can be solved using the method of characteristic, and we obtain

$$\hat{M}(\xi,t) = \hat{M}_0\left(\xi + \gamma g \mathbf{u_g}\int_0^t f(s)ds\right) e^{-\int_0^T \mathcal{D}_0\left(\xi+\gamma g\mathbf{u_g}\int_s^t f(\mu)d\mu\right)\cdot\left(\xi+\gamma g\mathbf{u_g}\int_s^t f(\mu)d\mu\right)}. \tag{2.28}$$

Then, since $S(T_E) = \int_{\mathbb{R}^d} M(\mathbf{x},T_E)d\mathbf{x} = \hat{M}(0,T_E)$ we can get an expression of the signal as

$$S(T_E, g, \mathbf{u_g}) := \int_{\mathbb{R}^d} M(\mathbf{x},T_E)d\mathbf{x} = \hat{M}(0,T_E) \tag{2.29}$$

that, using the rephase condition (2.12) and that $\mathcal{D}_0$ is a coefficient and $\|\mathbf{u_g}\| = 1$, simplifies to

$$S(T_E, g, \mathbf{u_g}) = \hat{M}_0(0) e^{-\gamma^2 g^2 \mathcal{D}_0 \mathbf{u_g}\cdot\mathbf{u_g}\int_0^{T_E}\left(\int_0^t f(s)ds\right)^2 dt} = S_0 e^{-\mathcal{D}_0 b}. \tag{2.30}$$

Even for very simple geometry configurations, it is difficult to obtain explicit solutions for general profile $f(t)$. Some known solutions for one-dimensional configurations can be found in [14, 95, 163]. The lack of known analytical solutions underlines the mathematical difficulties in interpreting the relation between the macroscopical signal and the microstructure.

For this reason, as we will see in the following sections, the majority of researchers tries to develop techniques to find a good approximation of the solution of the Bloch-Torrey equation or directly of the signal under some specific assumptions. Nevertheless, in order to test their approximations, they need to have a reference model and for this purpose several numerical models are used to numerically solve the Bloch-Torrey equation. Here we report three classes:

1. **Finite differences method (FDM), finite elements method (FEM), boundary elements method, etc.** A domain and/or its boundary are discretized with a regular or adaptive mesh. The original continuous problem is then replaced by a set of linear equations to be solved numerically. The solution is obtained at all mesh nodes at successive time steps. Since the accuracy and efficiency of these deterministic numerical schemes significantly rely in the discretization, mesh construction turns out to be the key issue and often a limiting factor, especially in three dimensions. These methods have been frequently applied for computing dMRI signals (for more details see [25, 38, 57, 68, 83, 134, 190]). In particular, to test the validity of our work in the simulations of the following chapters we will employ the FEM to solve the Bloch-Torrey equation.
2. **Monte Carlo simulations.** A probabilistic interpretation of diffusion equations is employed to represent the original continuous problem as the expectation of a functional of an appropriate stochastic process (like we have seen in Section 2.1.1). Many random trajectories of this process are then generated and used to approximate the expectation and thus the solution. Monte Carlo techniques are flexible and relatively easy to implement and thus have been often used in dMRI (see for example [12, 43, 62, 117, 126]).
3. **Matrix formalism**. If one considers the magnetic field $B_z(\mathbf{x}, t)$ as a perturbation of the Laplace operator, the magnetization $M(\mathbf{x}, t)$ can be decomposed on the complete basis of Laplacian eigenfunctions to deal with restricted diffusion in bounded domains ([15, 63, 64, 65]). The projection onto eigenfunctions reduces the Bloch-Torrey PDE to an infinite system of linear differential equations which can be truncated and then solved numerically. The solution is then obtained by matrix operations [63]. This technique is used especially when one is considering long time, whereas for strong gradients could be too slow.

On the imaginary part of the signal

By definition, $M(\mathbf{x}, t)$ solution of the Bloch-Torrey equation (2.15) is a complex-valued function and so is the signal $S(T_E) = \int_\Omega M(\mathbf{x}, T_E) d\mathbf{x}$ (this because the magnetization has a magnitude and a phase). The imaginary part of M represents the solution without diffusion, i.e. the difference in phase, while the real part represent the attenuation due to diffusion [128]. Often the phase of the measurement is discarded since inhomogeneities in $\mathbf{B}_0$ and movement of the sample make it unstable. In practice, it is also common to take the modulus of $S(T_E)$ as the real-valued dMRI signal [1]. However there are few cases in which mathematically we can be sure that the signal is just real. One of them is if we assume that the gradient time profile satisfies the rephase condition (2.12) and it is also anti-symmetric (2.13). A standard proof of this result uses the probabilistic interpretation of the signal (2.17) and can be found in [63]. Since the most used time profile introduced previously satisfies both these conditions, in this thesis we will concentrate our attention on the real part of the acquired signal. It is important to observe that for some years researchers believed that just the rephase condition (2.12) was sufficient to get that the imaginary part of the signal is zero for small values of the product $\gamma g \delta$, but the prove is still an open question. Recent works show that this is not true for high values of $\gamma g \delta$ or special tortuous and asymmetric domain, and some of them claim that acquiring separately the imaginary part could improve the signal to noise ratio in the image (see for example

[23, 100, 104, 120, 144, 156] and references therein).

2.1.4 Narrow pulse approximation [30, 43, 172, 176]

Since the Bloch-Torrey equation (2.15) does not admit simple solutions for generic temporal time profile $f(t)$, the idea of Stejskal and Tanner was that it could be possible to adapt the function $f(t)$ in order to simplify the mathematics using a change on the physical setup. They ended up suggesting the use of narrow pulse gradients [172, 176]. Thus, when the pulse duration is short, $\delta \ll \Delta$, we now say that we are under the narrow pulse assumption (NPA). Under NPA, after the first pulse, the complex phase due to spins that were at position $\mathbf{x}_0$ before the pulse is $e^{i\delta\gamma\mathbf{g}\cdot\mathbf{x}_0}$. Because the gradient magnetic field is turned off after the first pulse, the phase of the spins does not change until the application of the radio-frequency (RF) pulse, used to apply the 180 degree spin reversal. After the 180 degree RF pulse, the complex phase becomes $e^{-i\delta\gamma\mathbf{g}\cdot\mathbf{x}_0}$. The phase of the spins stays the same until the application of the second pulse, after which the complex phase due to spins ending up at position $\mathbf{x}_f$ becomes $e^{i\delta\gamma\mathbf{g}\cdot(\mathbf{x}_f-\mathbf{x}_0)}$. The dMRI signal S (total water proton magnetization in a physical voxel V) averaged over all the possible initial spins positions $\mathbf{x}_0$ is:

$$S = \iint_V P(\mathbf{x}, \mathbf{x}_0, \Delta)\rho(\mathbf{x}_0)e^{i\delta\gamma\mathbf{g}\cdot(\mathbf{x}-\mathbf{x}_0)}\, d\mathbf{x}_0 d\mathbf{x}, \tag{2.31}$$

where $P(\mathbf{x}, \mathbf{x}_0, \Delta)$ is the diffusion propagator describing the probability for a molecule to move from point $\mathbf{x}_0$ to point $\mathbf{x}$ in a time Δ and $\rho(\mathbf{x}_0)$ is an initial spin density at $\mathbf{x}_0$. The diffusion propagator $P(\mathbf{x}, \mathbf{x}_0, \Delta)$ is a solution of the diffusion equation,

$$\frac{\partial}{\partial t}P = \operatorname{div}(\mathcal{D}_0 \nabla P) \tag{2.32}$$

with specific boundary conditions like (2.3) and (2.4), and with the initial condition $P(\mathbf{x}, \mathbf{x}_0, 0) = \delta(\mathbf{x} - \mathbf{x}_0)$, where $\delta(\mathbf{x} - \mathbf{x}_0)$ is the Dirac delta function.

Through the equation (2.31) we can see the signal as a Fourier transform where the wavevector is given by $\gamma\delta\mathbf{g}$. In particular, if the water is freely diffusing with the isotropic diffusion coefficient $\mathcal{D}_0$, then

$$P(\mathbf{x}, \mathbf{x}_0, \Delta) = \frac{e^{-\frac{||\mathbf{x}-\mathbf{x}_0||^2}{4\mathcal{D}_0\Delta}}}{(4\pi\mathcal{D}_0\Delta)^{d/2}}, \tag{2.33}$$

where d is the dimension of the problem. In this case P is thus the diffusion (heat) Green's function in free space. Moreover, if we assume that the diffusion displacement is small compared to the side lengths of the voxel (which is true for dMRI), the signal is given by

$$S = S_0 e^{-\mathcal{D}_0||\gamma\delta\mathbf{g}||^2}. \tag{2.34}$$

Thus, by measuring the macroscopic signal for various values of the wavevector and then inverting the Fourier transform, one can access to the averaged propagator that incorporates the geometric features of the microstructure.

For simple isolated domains (e.g. sphere, cylinder, slab) some analytical formulas for the signal were derived especially in the long time limit (Δ very large) [30, 43]. These formulae were extensively experimentally validated (see for example [31]).

In spite of the simplicity of the theoretical analysis of the NPA, there are limitations to its validity and implementation [67]:

(i) the assumption of immobile nuclei during the gradient pulses may not be valid;

(ii) an experimental implementation of very short and at the same time strong gradient pulses has instrumental limitations.

Thus, even if this assumption is widely used to derive theoretical models to better understand the relationship between the microstructure and the macroscopic signal, it is not usually realizable in the experiments. For these reasons, finding a model which goes beyond this assumption would be desirable.

2.1.5 The apparent diffusion coefficient (ADC)

An important quantity measured in dMRI is the apparent diffusion coefficient (ADC) or effective diffusion coefficient (D^{eff}), with the former term often used by medical researchers and some MR physicists. The latter is the preferred term among mathematicians and some physicists. In this thesis, we will use both ADC and D^{eff}, but we distinguish them in the following way. (The choice we made, described below, is somewhat arbitrary and we hope that it does not detract from the clarity of the thesis.)

In this thesis, the ADC will be used to designate the quantity that includes the contributions from all the geometrical compartments in a volume of interest, whereas D_n^{eff} will be used to designate the quantity that accounts for the contribution from a particular compartment n, within the volume of interest. (For example, all the spherical cells could comprise compartment 1, all the cylinder cells could comprise compartment 2, and the extra-cellular space compartment 3. The union of these three compartments make up the total volume.) As a consequence, if we are considering just one compartment, then $ADC = D^{\text{eff}}$, whereas if we are considering $N > 1$ compartments, and exchange between the compartments is negligible, the ADC is

$$ADC = \sum_{n=1}^{N} v_n D_n^{\text{eff}}, \tag{2.35}$$

where v_n is its volume fraction and D_n^{eff} is the effective diffusion coefficient of the nth geometry.

This quantity is based on a measure of the mean diffusion displacement inside an imaging voxel. The mean squared displacement of spins during a diffusion time t_D is defined as:

$$MSD(t_D) \equiv \frac{1}{\int_{\mathbf{x}_0} \rho(\mathbf{x}_0) d\mathbf{x}_0} \int_{\mathbf{x}_0} \int_{\mathbf{x}} \rho(\mathbf{x}_0) \left((\mathbf{x} - \mathbf{x}_0) \cdot \mathbf{u_g}\right)^2 P(\mathbf{x}_0, \mathbf{x}, t_D) d\mathbf{x}\, d\mathbf{x}_0. \tag{2.36}$$

where $P(\mathbf{x}_0, \mathbf{x}, t_D)$ is the proportion of spins starting at $\mathbf{x}_0$ when $t = 0$, ending up at position $\mathbf{x}$ after a time t_D, $\rho(\mathbf{x}_0)$ is the density of spins at $\mathbf{x}_0$. Using the formulas for free diffusion introduced in Section 1.1, we can define an apparent diffusion coefficient in the direction $\mathbf{u_g}$ by the following expression:

$$\frac{1}{2\, t_D} MSD(t_D). \tag{2.37}$$

Since the mean squared displacement in a heterogeneous medium is not necessarily linear in t_D (as we have pointed out in Section 1.1), the apparent diffusion coefficient typically depends on t_D in a different way and we need to adapt this definition for the general case.

The MSD can be measured by dMRI using the previously introduced PGSE sequence. In the ideal case, where the pulse duration is very short compared to the delay between them, $\delta \ll \Delta$, called the narrow pulse case (Section 2.1.4 above), it is easy to relate the magnetization of spins to the diffusion propagator $P(\mathbf{x}, \mathbf{x}_0, t_D)$. In particular, the magnetization at position $\mathbf{x}$ and the echo time T_E, results

$$M(\mathbf{x}, T_E) \approx \int_{\mathbf{x}_0} \rho(\mathbf{x}_0)\ P(\mathbf{x}, \mathbf{x}_0, \Delta)\ e^{i\delta\gamma g \mathbf{u_g}\cdot(\mathbf{x}-\mathbf{x}_0)} d\mathbf{x}_0, \tag{2.38}$$

where we used the assumption that $\delta \ll \Delta$. We have seen that the dMRI signal S is the total water proton magnetization in an imaging voxel V, i.e.

$$S = \int_{\mathbf{x}\in V} M(\mathbf{x}, T_E)\ d\mathbf{x}. \tag{2.39}$$

Because the diffusion displacement is usually much shorter than the size of the imaging voxel, we can ignore spins that enter and leave the voxel during the signal acquisition and thus take domain of integration in Equation (2.39) to be $\mathbb{R}^3$. Using properties of the Fourier transform, we obtain

$$\left.\frac{\partial \frac{S}{S_0}}{\partial\,(\delta\gamma g)^2}\right|_{\delta\gamma g=0} \approx MSD(\Delta), \tag{2.40}$$

in the case of the narrow pulse PGSE sequence, where S_0 is the signal at $g = 0$ (a derivation of this statement can be found in [115] and uses the same techniques employed in Section 2.1.4).

Without the narrow pulse assumption, Equation (2.38) does not hold exactly. Rather, $M(\mathbf{x}, t)$ is governed by the Bloch-Torrey PDE, (2.15).

We have seen that, in case of unrestricted diffusion in a homogeneous medium with a diffusion coefficient $\mathcal{D}_0$, the MRI signal takes the exponential form [30, 95]

$$S = S_0 e^{-\mathcal{D}_0 b}, \tag{2.41}$$

where the b-value is defined in (2.21).

To adapt the definition of the apparent diffusion coefficient to the non-narrow pulse case, we make the following mathematical definition of the apparent diffusion coefficient in the gradient direction $\mathbf{u_g}$:

$$ADC_{\mathbf{u_g}} := -\frac{1}{\gamma^2 \int_0^{T_E} F(t)^2 dt} \frac{\partial}{\partial g^2} \ln\left(\frac{S(T_E)}{S_0}\right)\Bigg|_{g=0}. \tag{2.42}$$

We emphasize that $ADC_{\mathbf{u_g}}$ defined in the above formula depends on the gradient direction $\mathbf{u_g}$ and the temporal profile $f(t)$, but not on the gradient amplitude. We also emphasize that the apparent diffusion coefficient results in general to be "time-dependent" (i.e. depends on the diffusion time). Thus, one often accesses to its behaviour as a function of characteristic time for the chosen gradient profile (Δ for PGSE and tPGSE and τ for $OGSE$). We highlight that with the phrase "diffusion time-dependent" we actually mean dependent on the intra-pulse time and the pulses duration. Additionally, in what follows, to simplify the notation, if $\mathbf{u_g}$ does not play a role in the discussion, we will write ADC instead of $ADC_{\mathbf{u_g}}$ and D^{eff} instead of $D^{\text{eff}}_{\mathbf{u_g}}$.

For the relation between the intensity of the gradient g and the b-value, in practice, the value of ADC can be also extrapolated from the measured signal by fitting $\ln\left(\frac{S(T_E)}{S_0}\right)$ as an appropriate polynomial of b over the experimentally available range of b-values and taking the coefficient in front of the linear term in b. Measuring the macroscopic signal at several b-values allows one to estimate ADC which is related to the microstructure. Indeed, small ADC means that there are a lot of membranes which confine the movement. The ADC is widely used in the applications especially in medical imaging. For instance ADC maps of brain are used to identify tumours (see [108, 182]).

2.1.6 Gaussian phase approximation [63, 67, 99, 107, 133, 162]

Another standard approximation for dMRI signal modelling goes under the name of Gaussian phase approximation (GPA). The intuition behind the employment of this approximation consists in assuming that diffusion in the medium would remain Gaussian but is slowed down due to bumping and rebounding of the nuclei on obstacles or walls. The first use of this assumption goes back to the sixties when Robertson used it to recover the signal for diffusion between two parallel planes along with the Laplacian eigenfunctions [162]. Neumann a bit later extended this result to cylinders and spheres [133]. Later on the GPA has been extensively used for the analysis of dMRI signals in a variety of structures (see [63, 67]).

Under this hypothesis one can still apply the exponential form (2.20) in which the intrinsic diffusion coefficient $\mathcal{D}_0$ is replaced by the effective or apparent diffusion coefficient defined in Section 2.1.5 [107]:

$$S(T_E) \approx e^{-ADCb} \tag{2.43}$$

with the b-value defined in equation (2.21).

We can define the ADC also using the probabilistic interpretation of the signal (2.17). In particular a Taylor expansion of the exponential function at $t = T_E$ is done in order to make an accurate analysis in the case of weak gradients

$$\frac{S}{S_0} = 1 + \imath\mathbb{E}\{\varphi_{T_E}\} - \frac{1}{2}\mathbb{E}\{\varphi_{T_E}^2\} - \frac{\imath}{6}\mathbb{E}\{\varphi_{T_E}^3\} + \frac{1}{24}\mathbb{E}\{\varphi_{T_E}^4\} + O(\varphi_{T_E}^5) \tag{2.44}$$

which, using the properties of the exponential function, can also be written as the cumulant expansion [99]

$$\ln(S/S_0) = \imath\langle\varphi_{T_E}\rangle_c - \frac{1}{2}\langle\varphi_{T_E}^2\rangle_c - \frac{\imath}{6}\langle\varphi_{T_E}^3\rangle_c + \frac{1}{24}\langle\varphi_{T_E}^4\rangle_c + O(\langle\varphi_{T_E}^5\rangle_c) \tag{2.45}$$

where the cumulant moments $\langle\varphi_{T_E}^n\rangle_c$ can be expressed in terms of ordinary moments $\mathbb{E}\{\varphi_{T_E}^n\}$. Under the rephasing condition (2.12), and if the temporal profiles are anti-symmetric (2.13), all odd-order moments vanish and the leading (lowest-order) term is the second moment $\langle\varphi_{T_E}^2\rangle_c = \mathbb{E}\{\varphi_{T_E}^2\}$ [63, 67]. The Gaussian phase approximation consists in neglecting higher order terms which are expected to be small for weak gradients, from which

$$S \approx S_0 e^{-\mathbb{E}\{\varphi_{T_E}^2/2\}}. \tag{2.46}$$

According to the definition of the random phase φ_{T_E} in (2.16) the second moment can be written in terms of the position autocorrelation function

$$\mathbb{E}\{\varphi_{T_E}^2/2\} = \gamma^2 g^2 \int_0^{T_E} dt_1 f(t_1) \int_{t_1}^{T_E} dt_2 f(t_2) \mathbb{E}\{(\mathbf{x}(t_1)\cdot\mathbf{u_g})(\mathbf{x}(t_2)\cdot\mathbf{u_g})\}, \tag{2.47}$$

where we have used the symmetry of this function to order the variables t_1 and t_2 [63, 67].

Since the *ADC* contains all the available information on the microstructure it is really important to find a correct interpretation of this quantity in terms of the geometry. Moreover the final goal is to be able to invert its expression in order to find significant parameters which characterize the features of the geometry.

When the gradient increases the lowest order $\mathbb{E}\{\varphi_{T_E}^2/2\}$ grows slower than the higher-order terms and it is necessary to consider more contributions. This happens when the function $\ln(S(T_E)/S_0)$, as a function of b, starts to deviate from a straight line. At this point one can include the next term of the expansion

$$S(T_E) \approx S_0 e^{-\frac{1}{2}\langle\varphi_{T_E}^2\rangle_c + \frac{1}{24}\langle\varphi_{T_E}^4\rangle_c}, \tag{2.48}$$

where $\langle\varphi_{T_E}^2\rangle_c = \mathbb{E}\{\varphi_{T_E}^2\}$ and $\langle\varphi_{T_E}^4\rangle_c = \mathbb{E}\{\varphi_{T_E}^4\} - 3\left(\mathbb{E}\{\varphi_{T_E}^2\}\right)^2$, under the rephase condition (2.12). The above relation is known as Kurtosis model and it's equivalent to

$$S \approx S_0 e^{-ADCb + \frac{1}{6}KUR(ADCb)^2}, \tag{2.49}$$

where

$$KUR := \frac{\langle\varphi_{T_E}^4\rangle_c}{\left(\langle\varphi_{T_E}^2\rangle_c\right)^2} = \frac{\mathbb{E}\{\varphi_{T_E}^4\}}{\left(\mathbb{E}\{\varphi_{T_E}^2\}\right)^2} - 3 \tag{2.50}$$

is the apparent diffusion kurtosis [88]. This quantity characterize how far the phase distribution is from the Gaussian one for which one can prove that all the higher order terms $\langle\varphi_{T_E}^n\rangle_c$ with $n > 2$ vanish [63, 67, 99]. Since diffusion is influenced by obstacles and walls, the Kurtosis term was suggested as an indicator of tissue heterogeneity (see [86, 88]). As for the *ADC* in the experiment the *KUR* can be obtained by fitting the $\ln(S(T_E)/S_0)$ with a polynomial in b and then taking the coefficient in front of the quadratic term in b.

The inclusion of more terms would not improve the accuracy of the cumulant expansion for many different reasons among which the fact that at higher b-values the signal could be already too much attenuated and then strongly affected by noise (for more details see [99]).

2.2 Approximate models

The aim of this Section is to introduce some theoretical models used in literature to approximate and analyse the solution of the Bloch-Torrey equation or directly the expression of the signal. We will present them specifying under which approximations (narrow pulse and/or Gaussian) where derived. Some of the models we are going to introduce will be used in the following Chapters to validate our work.

2.2.1 Short-time approximation [103, 129, 130, 138]

Considering a very short time of observation t (short-time defined in Section 2.1.2), one can estimate the time dependence of the diffusion coefficient in a medium with impermeable restrictions. Indeed the presence of the impermeable wall affects only the molecules in the adjacent layer [99]. The thickness of this layer is of the order of the diffusion length $\sqrt{\mathcal{D}_0 t}$, where $\mathcal{D}_0$ is the bulk intrinsic diffusion coefficient. The diffusion coefficient of molecules in this layer is thus significantly reduced, that is it can be estimated by dimensional arguments as $const \cdot \mathcal{D}_0$, where $const < 1$. Denoting by S/V the ratio of the total restriction surface area to the total water volume, molecules with this effectively restricted diffusion coefficient occupy the volume fraction $\sqrt{\mathcal{D}_0 t} S/V$, which is much smaller than unity for short times. Bulk water has the diffusion coefficient $\mathcal{D}_0$ with a volume fraction $1 - \sqrt{\mathcal{D}_0 t} S/V$. Averaging this two contributions we get the apparent diffusion coefficient

$$ADC_{short}(t) = \mathcal{D}_0 \left(1 - const' \frac{S}{V} \sqrt{\mathcal{D}_0 t}\right), \tag{2.51}$$

where $const'$ is another constant. The exact calculation in [129, 130], using Laplace transformation of the solution of the diffusion equation and asymptotic series, gives $const' = \frac{4}{3d\sqrt{\pi}}$, where d is the spatial dimension. This result was lately extended to the case of permeable membranes of permeability coefficient κ ([103, 138]) as

$$ADC_{short}(t) := \mathcal{D}_0 \left[1 - \frac{S}{dV} \left(\frac{4\sqrt{\mathcal{D}_0 t}}{3\sqrt{\pi}} - \kappa t\right)\right]. \tag{2.52}$$

It was also shown that, in the case of anisotropic media subjected to a linear gradient with direction $\mathbf{u_g}$, one should consider the coefficient $\frac{\int_{\partial\Omega} (\mathbf{u_g} \cdot \nu)^2 d\mathbf{x}}{|\Omega|}$ instead of $\frac{S}{dV}$ [11, 63].

The use of short-time asymptotics is limited to relatively large obstacles. For instance, water molecules diffuse on average few microns during one millisecond, and then the obstacles should be much larger to estimate the surface-to-volume ratio. One possibility would be to consider smaller time but for now this is impossible due to hardware limitations. Another possibility is to use another time profile, i.e. instead of using PGSE one can use oscillating techniques to obtain an Oscillating Pulse Gradient Sequence (OGSE). In this case a formula for the apparent diffusion coefficient was found by Novikov and Kiselev in [138]

$$ADC_{short}(w) \approx \mathcal{D}_0 \left(1 - \frac{S}{dV} \sqrt{\frac{\mathcal{D}_0}{2w}}\right). \tag{2.53}$$

2.2.2 Long-time approximation [44, 46, 63, 67, 78, 103, 133, 162, 167]

In the long time limit (see definition in Section 2.1.2) the behaviour is very different for isolate pore and connected pore but, in both cases, it was observed that the diffusion becomes effectively Gaussian.

Using PGSE, the first case was investigated in details by Robertson and Neumann in [162] and [133] respectively. From their results one gets that the nuclei explore the whole available space then their mean square displacement saturates while the ADC decrease as the time between the

pulses (Δ) increases. For an isolate cell of a typical size R, in the case of PGSE and assuming narrow pulse hypothesis, using eigenfunction expansion one gets

$$ADC_{long}(\Delta) \approx C\frac{R^2}{\Delta} \tag{2.54}$$

where C is a geometrical constant (for example $C = 1/4$ for reflecting cylinder and $C = 1/12$ for a 1D configuration [30, 63, 67]. Using this approximation one can estimate the size of the pore.

In the case of interconnected pore or tissue formed by cell with permeable membranes the asymptotic is different. In fact, although the motion is hindered by the membranes, the nuclei can slowly explore new region without limitation. In particular for open geometries one gets [46, 78, 103]

$$ADC_{long}(t) \approx ADC_\infty + \frac{k_1\mathcal{D}_0}{t} + \frac{k_{3/2}\mathcal{D}_0}{t^{3/2}} + O\left(\frac{1}{t^{5/2}}\right) \quad (t \to +\infty) \tag{2.55}$$

where the coefficient $k_1, k_{3/2}$ depend on the confining geometry and ADC_∞ is the limit reached by ADC if the observation time t tends to infinity. Moreover, if one considers permeable membranes a new leading term $t^{-1/2}$ should be added [167]. In this regime, the free diffusion coefficient $\mathcal{D}_0$ is reduced to ADC_∞ by a geometrical factor $\mathcal{T}$ called tortuosity (i.e. $\frac{ADC_\infty}{\mathcal{D}_0} = \frac{1}{\mathcal{T}}$ [63, 67]). This is an important macroscopic characteristic of porous materials and biological tissues. Indeed, the tortuosity reflects how the microstructure and the surface exchange affect diffusion at long times. In the same light, some years before Crick proposed a simple relation between ADC_∞ and the permeability κ of equidistant barriers separate by a distance a [44]

$$\frac{1}{ADC_\infty} = \frac{1}{\mathcal{D}_0} + \frac{1}{a\kappa}. \tag{2.56}$$

This approximation can be useful to estimate intracellular diffusion coefficient and membrane permeability but has the limitation of being retrieved only for one-dimensional medium (or d-dimensional geometry which can be reduced to 1-dimensional).

Recently, Novikov et al. proposed an effective medium theory in which spatial variation of the diffusion coefficient where related to correlation functions of heterogeneities of a medium [140]. They also studied the effect of spatial configurations of permeable membranes onto the time-dependent diffusion coefficient [138] and they ended up with a more general formula

$$ADC_{long}(t) = ADC_\infty + \frac{c}{t^\theta} \quad (t \to +\infty) \tag{2.57}$$

where θ is related to a structural exponent p of the disorder as $\theta = (p + d)/2$ (see [29, 55, 139] for further details).

In the following sections we will see that the long-time limit ADC_∞ can be obtained using mathematical homogenization techniques [42] or a long-time periodic approximation [179].

2.2.3 Multi-compartments models [34, 39, 88, 123, 124, 132, 136, 192]

The dMRI is often realized on biological tissues (such as brain, lungs and heart) and from the practical experiment one can observe a significant deviation from the mono-exponential

behaviour in (2.43). It was realized that when one varies the diffusion gradient direction $\mathbf{u_g}$ or magnitude g the ADC may vary significantly. As we have already observed, ones get different values of ADC by varying the time delay between the pulses. In practice, by fixing the latter parameter along with the direction $\mathbf{u_g}$ and varying the amplitude g, one can see clearly that the diffusion-induced MRI signal attenuation has not an exponential decay in b [34, 39, 88, 123, 124, 132, 136]. The reason for this is that in biological tissue the diffusion environment seen by water molecules during the diffusion time (tens of milliseconds) is not homogeneous due to the presence of cells, membranes and other heterogeneities. Indeed, a biological tissue consists in cells which are separated from each other and from the extracellular space by semi-permeable membranes. If the exchange between different compartments can be neglected, the total signal is a linear combination of signals from compartments (weighted by their volume fraction) which, under the GPA (i.e. at weak gradient), results

$$\frac{S(T_E)}{S_0} = \sum_j v_j e^{-D_j b} \tag{2.58}$$

where v_j are the volume fractions of compartments (representing the relative amount of the nuclei), and D_j are their ADCs. In particular we observe that $\sum_j v_j = 1$.

An application of multi-compartments hypothesis can be found in [192], where the signal model is an integral of a continuum of Gaussian diffusion groups, each with a different effective diffusion coefficient.

Bi-exponential model [39, 66, 132, 136, 170]

In general, if all cells or pores composing the microstructure have similar shapes and sizes, their signals can be combined into an effective intracellular signal, yielding the "popular" bi-exponential form ([67])

$$\frac{S(T_E)}{S_0} = ve^{-D_c b} + (1-v)e^{-D_e b}, \tag{2.59}$$

where v is the volume fraction of the (joint) intracellular compartment, and D_c and D_e are the apparent diffusion coefficients for both intra- and extra-cellular compartments. The bi-exponential form (2.59) has been employed in many biomedical applications, in particular, for brain dMRI [39, 132, 136, 170]. Conventionally, the larger diffusion coefficient D_e is associated with faster hindered diffusion in the extracellular space, while the smaller diffusion coefficient D_c represents slower restricted diffusion in the intracellular compartments [66]. It is mandatory to observe that, even if the the bi-exponential form (2.59) accurately fits the macroscopic signal in brain tissue, it could fail in capturing the microstructure. Indeed it is sufficient to observe that D_e and D_c are apparent diffusion coefficients and are strongly affected by the microstructure and the chosen gradient time profile [66]. For instance both vary in with time (according to the definition of "time-dependent diffusivity" given in Section 2.1.5) in different a way. For example for closed geometry in the long time limit D_c vanish while D_e reaches a positive limit. Then measuring D_c and D_e on the same microstructure at different diffusion time can yield different values of the fraction v from the bi-exponential fit. This dependence on time is mainly caused by the exchange between the compartments and it happens mainly at large b-values [66]. However,

taking in account this dependence on time for small exchange between the compartments, one can employ this formulation.

We now introduce two models which take in accounts the exchange between the compartments of the tissue. This exchange is characterized by the permeability κ of the cellular membrane which varies significantly among the different tissues, from sub 10^{-6}m/s to more than 10^{-3}m/s (see for example [49] for more details). To give an indication we can claim that the values of κ below 10^{-6}m/s mean that the membrane can be considered as impermeable while values between 10^{-6}m/s and 10^{-4}m/s correspond to semi-permeable membranes and bigger values to very permeable membrane [49].

Kärger model [93, 94]

Kärger et al. proposed a simple model to account for the exchange between colloids that they recovered through the experiments [93, 94]. The essence of the Kärger model as it was presented is the following: there exists two molecular spin-carrying pools, labelled 1 and 2, both occupying the same volume of a voxel [56]. The exchange between the pools was assumed to be uncorrelated from diffusion and to follow standard linear kinetics. The concentrations $c_1(\mathbf{x},t)$ and $c_2(\mathbf{x},t)$ of molecules in the two pools obey the standard diffusion-reaction equations

$$\begin{cases} \dfrac{\partial}{\partial t}c_1(\mathbf{x},t) &= D_1\nabla^2 c_1(\mathbf{x},t) - \eta_{21}c_1(\mathbf{x},t) + \eta_{12}c_2(\mathbf{x},t), \\ \dfrac{\partial}{\partial t}c_2(\mathbf{x},t) &= D_2\nabla^2 c_2(\mathbf{x},t) - \eta_{12}c_2(\mathbf{x},t) + \eta_{21}c_1(\mathbf{x},t), \end{cases} \tag{2.60}$$

where $\mathbf{x} \in \mathbb{R}^d$ (with d the dimension of the problem) and the second and third terms in the right-hand side describe the exchange between the two pools, η_{12} and η_{21} being the exchange rates of moving from the first pool to the second pool and vice-versa. These exchange rates can be related to the permeability κ and the surface to volume ration S/V of the medium:

$$\eta_{21} = \frac{\kappa}{v_1}\frac{S}{V} \quad \text{and} \quad \eta_{12} = \frac{\kappa}{v_2}\frac{S}{V} \tag{2.61}$$

with v_1 and v_2 being the volume fractions of the two pools ($v_1 + v_2 = 1$). Since the pools were introduced to substitute the microstructure, these equations have no boundary conditions but they are subjected to the initial condition $c_j(\mathbf{x},0) = v^j\tilde{\delta}(\mathbf{x})$, $j = 1,2$, with $\tilde{\delta}(\mathbf{x})$ being the Dirac delta distribution at $\mathbf{x} = 0$. Under the narrow pulse approximation for PGSE sequence, $\delta << \Delta$ the compartment magnetization takes the form

$$M_j(t) = \int_{\mathbb{R}^d} e^{\imath\gamma g\delta\mathbf{u_g}\cdot\mathbf{x}}c_j(\mathbf{x},t)d\mathbf{x}, \tag{2.62}$$

i.e. is a Fourier transformation of the concentrations c_j, $j = 1,2$ with respect to the wave vector $\gamma g\mathbf{u_g}\delta$ ([30]). Taking the time derivative of M_j and using the Green's identity, the Karger model can be obtained as system of two ordinary differential equations (ODE)

$$\begin{cases} \dfrac{\partial}{\partial t}M_1(t) &= -\left(D_1\|\gamma g\mathbf{u_g}\|^2\delta^2 + \eta_{21}\right)M_1(t) + \eta_{12}M_2(t), \\ \dfrac{\partial}{\partial t}M_2(t) &= -\left(D_2\|\gamma g\mathbf{u_g}\|^2\delta^2 + \eta_{12}\right)M_2(t) + \eta_{21}M_1(t), \end{cases} \tag{2.63}$$

supplemented by the initial conditions

$$M_j(0) = v_j, \quad j = 1, 2. \tag{2.64}$$

These equations can then be solved analytically to get the explicit formula for the macroscopic signal $S = M_1(t_{\text{eval}}) + M_2(t_{\text{eval}})$, where t_{eval} is the evaluation time and sometimes is chosen as the diffusion time ([56]). We remark that originally Karger proposed Δ as t_{eval}, but in [115] was observed that (if the pulses are not narrow) is better to consider $t_{\text{eval}} = \Delta - \delta/3$ in the simulations. In Chapter 3 we clarify this aspect showing why $t_{\text{eval}} = \Delta - \delta/3$ is the correct choice of evaluation.

Fitting the macroscopic signal one can then estimate the coefficients D_1 and D_2, the volume fractions v_1 and v_2, and the exchange rates η_{12} and η_{21} from which the product $\kappa S/V$ can be deducted ([67]). We observe that the diffusion coefficients D_1 and D_2 must be different otherwise there is no difference between the pools and one ends up with the same signal as unrestricted diffusion. Furthermore they correspond to the apparent diffusion coefficients of the two pools. Then, for a closed geometry and in a long-time regime, one can simplify one of the two equations using the fact that its diffusion coefficient will be 0. An extension to multiple compartments (and nor only two) is straightforward and is reported in the Chapter 3. It is also easy to recover the model for anisotropic diffusion, i.e. containing an apparent diffusion tensor rather then a coefficient. In Chapter 3 is also reported the resulting analytical formula for the Kärger signal.

Finite pulse Kärger model [42, 115, 135]

An extension of the Kärger model beyond the NPA was proposed by Coatléven et all [42, 115]. Using periodic homogenization techniques, in which the voxel is assumed to be formed by numerous periodic copies of a smaller but representative volume of a tissue [22]. The approximation of the solution of multi-compartments Bloch-Torrey equation was reduced to a system of coupled differential equations for the relative signals S_j from the compartment Ω_j constituting the medium. For instance, when there are only two compartments one obtains

$$\begin{cases} \dfrac{\partial}{\partial t} M_1(t) &= -\left(D_1 \|\gamma g \mathbf{u_g}\|^2 F^2(t) + \eta_{21}\right) M_1(t) + \eta_{12} M_2(t), \\ \dfrac{\partial}{\partial t} M_2(t) &= -\left(D_2 \|\gamma g \mathbf{u_g}\|^2 F^2(t) + \eta_{12}\right) M_2(t) + \eta_{21} M_1(t), \end{cases} \tag{2.65}$$

where $F(t) = \displaystyle\int_0^t f(s)ds$. Roughly speaking, under the narrow pulse approximation one can say that $F(t) \approx \delta^2$ and retrieves the equations (2.63). For a more precise analysis of convergence between the two models, we refer to Chapter 3. The presence of $F(t)$, which is time dependent, prevents one to find an analytical solution of (2.65). On the contrary, a numerical solution of these simple ODEs is simpler and much faster then that of Bloch-Torrey PDE which is space and time dependent. In [135], it was also shown that when the gradient pulses are not narrow, this model is more convenient for estimating the parameters than the original Kärger one. Furthermore in [42, 115] also an analytic formula to compute the effective diffusion coefficient D_1 and D_2 was given. Indeed starting from the Bloch-Torrey multi-compartments equation with the boundary conditions (2.3) and (2.4), and assuming that one can relate the length of

the periodicity box and the permeability to be linearly dependent to the same non-dimensional small parameter ε, one can use a multiscale expansion for the magnetization (see [22]) and the effective diffusion tensors $\overline{\mathbf{D}}^j_{il}$, for each compartment Ω_j of the voxel, can be written as

$$\overline{\mathbf{D}}^j_{il} = \frac{1}{v_j}\int_{\Omega_j} \mathcal{D}^j_0 \left(\nabla\omega^j_l(\mathbf{x})\cdot\mathbf{e}_i + \mathbf{e}_l\cdot\mathbf{e}_i\right) d\mathbf{x} \tag{2.66}$$

where v_j is the volume fraction of Ω_j, $\mathbf{e}_i$ is the i-th vector of the standard basis of $\mathbb{R}^d$ (d space dimension) and the auxiliary functions $\omega^j_i(\mathbf{x})$, for $l = 1,\dots,d$, are computed by solving the following Laplace equation with Neumann boundary condition

$$\begin{cases} -\mathrm{div}\left(\mathcal{D}^j_0\nabla\omega^j_i + \mathcal{D}^j_0\mathbf{e}_i\right) = 0 & \text{in } \Omega_j \\ \mathcal{D}^j_0\nabla\omega^j_i\cdot\nu + \mathcal{D}^j_0\mathbf{e}_i\cdot\nu = 0 & \text{on } \partial\Omega_j. \end{cases} \tag{2.67}$$

In addition, the periodic boundary conditions are imposed at the outer boundary of the representative volume. We emphasize that the tensor $\overline{\mathbf{D}}^j$ is defined for any microstructure and is independent of the gradient encoding. Once one has computed this tensor solving numerically the equations (2.67) for a prescribed configuration, the diffusion coefficient in (2.65) can be obtained as

$$D_j = \mathbf{u_g}^T\overline{\mathbf{D}}^j\mathbf{u_g}.$$

If the compartment Ω_j is bounded (e.g. the intracellular space enclosed by a weakly permeable membrane), each solution ω^j_i of equation (2.67) is constant, and equation (2.66) implies $\overline{\mathbf{D}}^j = 0$. In turn, when the compartment Ω_m is connected to its periodic copies (e.g. extracellular space), the effective diffusion tensor $\overline{\mathbf{D}}^j$ characterizes diffusion in the long time limit (i.e. D_∞). Diagonalizing this tensor one can probe the macroscopic anisotropy of the voxel. This homogenization approach yields the first order approximation of the long-time ADC under the assumption of low permeability κ and moderate gradients.

In the next Chapter we will better investigate the relationship between the Kärger and the Finite Pulse Kärger models and we will furnish the precise convergence result.

We remark that the derivation of the FPK model was deliberately not detailed in this Section because our work is based on the derivation of new models using the same homogenization techniques but with different scalings. Since in Chapter 4 we will go into the details of more general calculations using homogenization, we preferred to not make the reading repetitive and just give an idea for now.

An alternative derivation of this long-time limit tensor for the case of highly permeable boundaries was shown in [37] in the case of periodic media. Considering $Y = \prod_{i=1\cdots d}[0, L_i]$ as periodicity box of the medium, then

$$\left(\overline{D}^j_\infty\right)_{il} := \frac{1}{v_j}\int_{Y_j} \mathcal{D}^j_0\nabla u^j_i(\mathbf{x})\cdot\mathbf{e}_l\, d\mathbf{x}, \tag{2.68}$$

where the functions $u^j_i(\mathbf{x})$, $i = 1,\dots,d$, are defined piecewise on Y_j and satisfy the time inde-

pendent PDE:

$$\begin{aligned} \operatorname{div}\left(\mathcal{D}_0^j \nabla u_i^j(\mathbf{x})\right) &= 0 && \text{in } Y_j, \\ \mathcal{D}_0^j \nabla u_i^j(\mathbf{x}) \cdot \nu - \mathcal{D}_0^k \nabla u_i^k(\mathbf{x}) \cdot \nu &= 0 && \text{on } \Gamma_{jk}, \\ \mathcal{D}_0^j \nabla u_i^j(\mathbf{x}) \cdot \nu &= \kappa(u_i^j(\mathbf{x}) - u_i^k(\mathbf{x})) && \text{on } \Gamma_{jk}, \\ u_i^j(\mathbf{x} + L_i \mathbf{e}_i) &= u_i^j(\mathbf{x}) + L_i && \text{on } \partial Y, \\ u_i^j(\mathbf{x} + L_l \mathbf{e}_l) &= u_i^j(\mathbf{x}), \quad l \neq i, && \text{on } \partial Y. \end{aligned} \tag{2.69}$$

In this case then one has

$$ADC_\infty = \sum_j v_j \overline{D}_\infty^j. \tag{2.70}$$

If Y only contains simple geometries such as cubes and spheres, analytic formulae for $\overline{D}_\infty^j$ have been formulated [77, 102, 175, 179].

Anomalous diffusion [21, 20, 24, 26, 75, 122, 123, 127, 149, 152, 196]

In order to extend the concept of apparent diffusion coefficient for a multi-compartments tissue Bennet and co-workers [21, 20] presented a new method for describing the dMRI signal using the so called "stretched exponential" function, i.e.

$$S = S_0 e^{-(bD)^\alpha}, \tag{2.71}$$

where α is the stretching parameter which characterizes the deviation of the signal from the Gaussian (mono-exponential) behaviour. In particular, α is an arbitrary real number between 0 and 1 and an higher heterogeneity of a confining medium typically corresponds to smaller values [66, 123].

Following this idea the Bloch-Torrey equation where extended to the case of continuous time random walks (CTRW) using fractional time and space derivatives which incorporate non-local variations of the transverse magnetization in space and time [26, 127]. As a consequence, the macroscopic signal may inherit some anomalous features, e.g. the stretched exponential dependence on the inter-pulse time Δ and/or the wavevector $\delta\gamma\mathbf{g}$:

$$S \approx S_0 e^{-D_{\alpha,\beta}|\delta\gamma\mathbf{g}|^{2\beta}\Delta^\alpha}, \tag{2.72}$$

where α and β are two scaling exponents, and $D_{\alpha,\beta}$ is the generalized diffusion coefficient (in units $\mathrm{m}^{2\beta}/\mathrm{s}^\alpha$) [24, 75, 122, 123, 149, 152]. The Gaussian behaviour is obtained for $\alpha = \beta = 1$. The stretched exponential form (2.72) offers more degree of freedom to fit the signal and the fitted parameters (α and β) are suggested as potential biomarkers for the biological tissue [196]. Nevertheless this phenomenological approach needs to be more investigated because the relation between the parameters and the microscopic geometries remains still not very clear.

There exist also models for which the anomalous diffusion is modelled by just fractional time dependence. For example, in [143], the authors introduced a method to characterize the diffusion-time dependence of the dMRI signal in biological tissues using the theory of diffusion in disordered media and systems exhibiting fractal behaviour. For this type of domains, diffusion

results to be anomalous in the sense that the mean-square displacement has a diffusion time dependence characterized by the power law

$$\langle \mathbf{x}^2 \rangle \propto t^{2/d_w}, \tag{2.73}$$

where d_w is the fractional dimension of the diffusion process. Moreover, the return to the origin probability (RTOP), which represents the likelihood of molecules to undergo zero net displacement during the diffusion time considered, satisfies this relation

$$RTOP \propto t^{-d_s/2} \tag{2.74}$$

where d_s is the spectral dimension. Using the above two relations, the authors were able to express the evolution of the average propagator coming from the MR experiments as function of the fractal dimension d_w and the spectral dimension d_s. Fitting these two parameters they were able to show that water diffusion in human tissues is anomalous and in particular the mean square displacements vary slower than linearly with diffusion time.

Using this approach, in [146] Özarslan and co-authors where able to introduce a new type of contrast based on the temporal scaling (TS) characteristics of diffusion. To do that they extended the model in [143] to the even $m-$th order moments of the diffusion displacement ($\langle \mathbf{x}^m \rangle$) allowing the possibility that their temporal scalings can be described by a different exponents (not necessarily equal to d_w which is the one of the mean square displacement). By studying the relationship between the TS characteristics and diffusion anisotropy using the anisotropy of TS, they showed the robustness and reproducibility of this method to marker tissues microstructure properties.

Effective medium theory [140, 138, 139]

Recently Novikov et Kiselev [140] developed a new model using the effective medium theory (ETM). This theory is usually employed in physics to model the effective (macroscopic) properties of composite materials starting from local (microscopic) properties of the components which are not detectable with the experiments. In general ETM consists in averaging the multiple characteristics of the microscopic components that directly make up the composite material. It is thus a way to represent a microscopically heterogeneous medium as an apparently homogeneous medium whose observable macroscopic properties are modified by the microstructure. This idea is then similar to the one behind the mathematical homogenization but using a stochastic interpretation.

In this light Novikov et Kiselev employed the ETM concept in dMRI. In particular, they treated the microstructural details of a biologic tissue as random "disorder" and, making the natural statistical average, they found that the geometric complexity of a biological tissue can be captured through an effective space-dependent parameter such as a diffusion coefficient $D(\mathbf{x})$ [140]. In this way they somehow removed the boundary conditions of the Bloch-Torrey equation which implicitly determined the microstructure and presented the main challenge in its analysis. In the narrow pulse regime they ended up with three diffusion characteristic metrics: dispersive diffusivity $\mathcal{D}(w)$, the retarded velocity correlation function $\mathrm{D}(t)$ and the standard time-dependent diffusion coefficient $D(t)$. These three contain the same amount of information

about the structure and can thus be expressed one as a function of the others and so one can decide which one is better according to the application. Using them and the cumulant expansion they where able to approximate the signal coming from any diffusion gradient wave-form $\mathbf{g}f(t)$.

As we have already discussed in Section 2.1.4 using this techniques they were able to investigate the asymptotic behaviour of the time-dependent diffusion coefficient [138, 139].

2.2.4 Geometric models

Since the relation between the microstructure and the macroscopic signal is not yet fully clear geometric models, based on specific applications, were developed to fit the signal. Without any pretence to be exhaustive, here we describe some of them which are suitable for brain applications (for a more complete review we refer, for example, to [150, 54]).

In [19] Behrens et al. proposed a voxel-level model, called "ball and stick", which assumes that diffusion within axons is along a single direction and that outside axons is isotropic.

In [2] Alexander investigated the feasibility of using diffusion MRI to measure axon dimensions in white matter *in-vivo*. To relate axon radius to the diffusion MRI signal he used a two-compartments model that incorporates a pore radius. To model of the extra-axonal space, he used a cylindrically symmetric tensor with the principal eigenvector indicating the fibre direction. The model for the intra-axonal space was a cylinder with non-zero pore size, unlike Behrens' stick model, which is a cylinder with radius zero. Moreover, for the signal model used the Gaussian phase approximation ([51]) for cylinders of radius R described in [173, 184].

The model in [2] is a simplification of Assaf's CHARMED (Composite Hindered and Restricted Model of Diffusion) model in [7], which also assumes cylindrical restriction in the intra-axonal space. There, the authors used Neuman's expression in [133] for diffusion in cylindrical confinement for a pulse-gradient spin-echo (PGSE) experiment, which satisfies the narrow pulse approximation ([158]). Unlike Alexander's model, which assumes a single cylinder radius, CHARMED model assumes cylinders with gamma-distributed radii. This introduces one extra parameter to estimate, although in [7] both gamma parameters were fixed rather than estimated.

In [8] Assaf et al. used an extension of CHARMED model to estimate distributions of axon diameters of bovine optic and sciatic nerve samples. They extended the CHARMED framework by considering the diameter distribution of cylindrical axons as an unknown to be estimated from their data. They named this method AxCaliber. To gain sensitivity for estimating the axons diameters they use a fixed gradient direction perpendicular to the axons with a combination of different diffusion times and gradient strengths.

There exists also other methods which describe diffusion with three or more compartments and allow exchange between them. For example, in [13] the authors studied the diameters distribution of axons in the rat corpus callosum in-vivo using a three-compartments model. The model resulted an extension of the AxCaliber model in [8] with the addition of an isotropic-diffusion compartment to account for partial volume contributions from areas of cerebrospinal fluid (CSF).

Stanisz et al. in [171] constructed a three-pools model with prolate ellipsoidal axons and spherical glial cells each with partially permeable membranes. Fitting such a complex model requires very high quality measurements, but experiments suggest that the full complexity of the model is required to explain the data.

Recently, Alexander et al. in [3] demonstrate orientationally invariant estimation of axon diameters and density in both fixed monkey brains and in-vivo human brains with their ActiveAx technique. They use a four-compartments tissue model: a combination of the two-compartments model used in [2] with a CSF compartment similar to [13], and a fourth compartment which accounts for water coming from stationary water molecules trapped in glial cells and other subcellular structures similar to [171]. Besides the restricted and hindered compartments previously considered by [7], this model accounts also for stationary water trapped within small structures such as glial cells, in a similar way to [171], as well as free water characterized by isotropic diffusion. Later, it was extended to improve the estimation in brain regions with orientation dispersion ([194]) and crossing fibers ([193]). To enable the estimation of useful microstructural information also within clinical scan times it was further improved in [195]. In the resulting technique, named Neurite Orientation Dispersion and Density Imaging (NODDI), the axon diameter parameter was dropped from the model and the formulation was rather optimized to describe the observed dMRI signal as a function of the volume fraction and orientation dispersion of the axons, as well as the partial volume with cerebrospinal fluid.

Chapter 3

Finite pulse Kärger and Kärger Models

Contents

3.1 Description of the models 52
3.1.1 Finite Pulse Kärger model 52
3.1.2 Kärger model 54
3.2 Convergence of the Kärger model to the FPK model 55
3.2.1 Asymptotic expansion in ζ 56
3.2.2 Error estimates 58
3.3 Kurtosis formula for FPK model 63
3.4 Numerical results 66
3.4.1 Trapezoidal PGSE 67
3.5 Conclusions 70

As it was previously introduced a standard way to encode diffusion using MRI is by applying the PGSE ([172]) sequence which ideally means that the gradient magnetic field $\mathbf{G}$ is applied during two very short pulses of duration δ with a time delay Δ between the start of the two pulses and an 180 degree spin reversal between the two pulses. Under the so called narrow pulse assumption ($\delta \ll \Delta$), and if additionally, the imaging voxel can be spatially divided into different Gaussian diffusion compartments with inter-compartment exchange governed by linear kinetics, we have seen that the dMRI signal can be described by the Kärger model [94], which is a well-known model in NMR that has been also used for biological tissue dMRI [6, 113, 126, 137, 153, 161, 164, 171, 186]. We recall that the Kärger model describes the evolution of the transverse magnetization using coupled, constant coefficient, ordinary differential equations (see Section 2.2.3). The analytical solution of the ODEs system can be obtained by a matrix eigen-decomposition. Under the assumption that $\delta \ll \Delta$ (narrow pulse), the suggested time at which to evaluate the Kärger model to obtain the dMRI signal is unambiguously the delay between the pulses [94].

Since in physically realistic MRI experiments, the condition $\delta \ll \Delta$ is rarely satisfied, in Section 2.2.3 we have seen that recently, a new model of the dMRI signal, the Finite-Pulse Kärger (FPK) model [42], was derived for arbitrary gradient profiles. The FPK model takes the form of a coupled ODE system with time-dependent coefficients and the term "finite-pulse" was used to mean not requiring $\delta \ll \Delta$. In this Chapter, relying on the FPK model, we show that for finite pulses, the time at which to evaluate the Kärger model should be shortened by one third of the pulse duration. For this choice, we prove that the convergence of the Kärger model to the FPK model is of order six in the pulse duration, while for all the other reasonable choices the order is three. This clarifies an important issue that is often overlooked by those using the Kärger model to analyse MRI diffusion data, i.e. at which time one should evaluate

this model when the narrow pulse assumption is not satisfied. We can state that the FPK model is a more general model (which was derived with rigorous mathematical procedures) and it helps us to better explain the meaning of the Kärger model (which was derived empirically from the experiments). We present all the results for the standard rectangular PGSE as it was done in our published paper [72], but we also add two sections to complement the results. We first derive the Kurtosis term of the FPK model and show that the convergence to the Kärger one is also of order three in the b-value. We then give a numerical proof of what one should consider as evaluation time for the case of trapezoidal PGSE, which is a more realistic time profile. In particular, for this case we show that it is not sufficient to just change the evaluation time, but we also need to modify the coefficient in front of δ^2 in the two ODEs describing the Kärger model.

The Chapter is organized as follows. In Section 3.1 we describe the Kärger and the FPK models. In Section 3.2 we prove that the signal of the Kärger model, when evaluated at $t = \Delta - \frac{\delta}{3}$, converges to the FPK signal with order six in the pulse duration. We also show that two other possible choices of the evaluation point, $t = \Delta$ and $t = \Delta + \delta$, result only in third order convergence. In Section 3.3 we derive the Kurtosis formula for the FPK model and show its convergence to the Kärger Kurtosis formula. In Section 3.4 we validate our convergence results by numerical simulations. We also give an intuition of what happens if we consider a trapezoidal PGSE and we show some numerical results of convergence. Section 3.5 contains our conclusions regarding the physical interpretation of the FPK model.

3.1 Description of the models

In order to provide a clear presentation of the Kärger and the FPK models, we begin here by describing them for the simple case where there are two Gaussian diffusion compartments in the tissue. For us, the two compartments will be

1. the intra-cellular compartment, comprising the ensemble of all the biological cells in a voxel;
2. the extra-cellular compartment, comprising the space in the exterior of all the cells in a voxel.

In the more general case, different types of cells and cell components can be separated into several different diffusion compartments. Our later results will be valid for the general case of multiple diffusion compartments.

3.1.1 Finite Pulse Kärger model

The FPK model for two Gaussian diffusion compartments of total volume $|Y|$ has been proposed in [42] and takes the form of two coupled ODEs with time-dependent coefficients:

$$\begin{cases} \dfrac{d}{dt} m_e^{\mathrm{FPK}}(t) + q^2 F_\delta^2(t) D_e^{\mathrm{eff}} m_e^{\mathrm{FPK}}(t) + \eta_e m_e^{\mathrm{FPK}}(t) - \eta_c m_c^{\mathrm{FPK}}(t) = 0 \\ \dfrac{d}{dt} m_c^{\mathrm{FPK}}(t) + q^2 F_\delta^2(t) D_c^{\mathrm{eff}} m_c^{\mathrm{FPK}}(t) + \eta_c m_c^{\mathrm{FPK}}(t) - \eta_e m_e^{\mathrm{FPK}}(t) = 0 \\ m_e^{\mathrm{FPK}}(0) = v_e\,; \quad m_c^{\mathrm{FPK}}(0) = v_c \end{cases} \tag{3.1}$$

where

— m_e^{FPK} and m_c^{FPK} are the transverse water proton magnetization of the extra-cellular compartment and of the intra-cellular compartment respectively;

— q is the intensity of the diffusion-encoding magnetic gradient multiplied by the gyromagnetic ratio of the water proton (i.e. $q = \gamma g$) [1];

— D_e^{eff} and D_c^{eff} are, with an abuse of notation, the effective diffusion coefficients for the two compartments in the direction of the diffusion-encoding gradient. The definition and meaning of these coefficients are quite subtle. For a periodic medium these coefficients can be unambiguously defined as infinite time limits and can be obtained after solving Laplace equations in the compartments. In particular, when the compartment is closed (restricted), then the effective diffusion coefficient would be 0. For details, see [116];

— $\eta_e = \frac{\kappa|\Gamma_m|}{|Y_e|}$ and $\eta_c = \frac{\kappa|\Gamma_m|}{|Y_c|}$, with $|Y_e|$ and $|Y_c|$ being the volume of the extra-cellular and intra-cellular compartment, respectively, $|\Gamma_m|$ the total surface area of the biological cell membranes, and κ the permeability of the membrane;

— $v_e = \frac{|Y_e|}{|Y|}$ and $v_c = \frac{|Y_c|}{|Y|}$ are the volume fractions of the two compartments;

— δ is the pulse duration and Δ is the time delay between the start of the two pulses of the classical Pulsed Gradient Spin Echo (PSGE) sequence, for which the time profile is given by

$$f(t) = \begin{cases} 1 & \text{if } 0 < t \leqslant \delta \\ -1 & \text{if } \Delta < t \leqslant \Delta + \delta \\ 0 & \text{elsewhere} \end{cases} ; \tag{3.2}$$

and we define

$$F_\delta(t) := \int_0^t f(s)ds = \begin{cases} t & \text{if } 0 < t \leqslant \delta \\ \delta & \text{if } \delta < t \leqslant \Delta \\ \Delta + \delta - t & \text{if } \Delta < t \leqslant \Delta + \delta \\ 0 & \text{elsewhere} \end{cases} ; \tag{3.3}$$

The dMRI signal is the sum of all the compartment magnetizations at the end of the second pulse:

$$S^{\text{FPK}} := m_e^{\text{FPK}}(\Delta + \delta) + m_c^{\text{FPK}}(\Delta + \delta). \tag{3.4}$$

When there is only one compartment, with the effective diffusion coefficient D^{eff}, it is easy to show that the analytical signal is:

$$S^{\text{FPK}} = e^{-b\, D^{\text{eff}}}, \tag{3.5}$$

where the b is a commonly used quantity in dMRI called the b-value that in the case of PGSE is defined as:

$$b(q, \delta, \Delta) := q^2\delta^2\left(\Delta - \frac{\delta}{3}\right). \tag{3.6}$$

When $\delta \ll \Delta$ it is easy to interpret Δ as the measured diffusion time.

1. It is important to note that in this case, and for the rest of the thesis, q does not denote a wave vector, as it often does in physics

3.1.2 Kärger model

The Kärger model [94] was formulated heuristically, originally for microporous crystallites and later applied to biological tissue dMRI, on the basis of phenomenological modeling of the experimentally obtained signal curves. Using the same notation as for the FPK model above, the Kärger model for two diffusion compartments of total volume $|Y|$ takes the form of two coupled ODEs with *constant* coefficients:

$$\begin{cases} \dfrac{d}{dt} m_e^{\mathrm{KAR}}(t) + q^2\delta^2 D_e^{\mathrm{eff}} m_e^{\mathrm{KAR}}(t) + \eta_e m_e^{\mathrm{KAR}}(t) - \eta_c m_c^{\mathrm{KAR}}(t) = 0, \\ \dfrac{d}{dt} m_c^{\mathrm{KAR}}(t) + q^2\delta^2 D_c^{\mathrm{eff}} m_c^{\mathrm{KAR}}(t) + \eta_c m_c^{\mathrm{KAR}}(t) - \eta_e m_e^{\mathrm{KAR}}(t) = 0, \\ m_e^{\mathrm{KAR}}(0) = v_e\,; \quad m_c^{\mathrm{KAR}}(0) = v_c. \end{cases} \tag{3.7}$$

Being a system of constant coefficient ODEs, the Kärger model (3.7) can be solved by matrix eigen-decomposition and we give the explicit solution for two compartments:

$$m^{\mathrm{KAR}}(t) = m_e^{\mathrm{KAR}}(t) + m_c^{\mathrm{KAR}}(t) = v^f(q)\, e^{-D^f(q) q^2\delta^2 t} + v^s(q)\, e^{-D^s(q) q^2\delta^2 t}, \tag{3.8}$$

where

$$\begin{aligned} D^{f,s}(q) &= \frac{1}{2}\left(D_e^{\mathrm{eff}} + D_c^{\mathrm{eff}} + \frac{1}{q^2\delta^2}(\eta_e + \eta_c) \pm \sqrt{\left(D_e^{\mathrm{eff}} - D_c^{\mathrm{eff}} + \frac{1}{q^2\delta^2}(\eta_e - \eta_c) \right)^2 + \frac{4\eta_e\eta_c}{q^4\delta^4}} \right), \\ v^f(q) &= \frac{1}{D^f(q) - D^s(q)} \left(v_e D_e^{\mathrm{eff}} + v_c D_c^{\mathrm{eff}} - D^s(q) \right), \\ v^s(q) &= 1 - v^f(q)\,. \end{aligned}$$

The Kärger model appears as a special case of FPK model when the time profile of the diffusion-encoding magnetic field gradient sequence is the PGSE (3.2) and the pulse duration δ is very small compared to the time delay between the start of the two pulses, in other words, $\delta \ll \Delta$. One of the purposes of this chapter is to specify in which sense the Kärger model can be seen as an approximation of the FPK model.

We first observe that

$$\lim_{\delta\to 0} \frac{1}{\delta} F_\delta(t) = F(t) = \begin{cases} 1 & \text{if } 0 \leqslant t \leqslant \Delta \\ 0 & \text{if } t > \Delta \end{cases}.$$

The Kärger model can then be interpreted as a pointwise limit of the FPK model as $\delta \to 0$. However, the convergence is not uniform since,

$$\sup_{t\in[0,\Delta+\delta]} \left| \frac{1}{\delta} F_\delta(t) - F(t) \right| \xrightarrow[\delta\to 0]{} 1.$$

This is why it is not guaranteed that the Kärger model provides an accurate approximation of FPK as $\delta \to 0$.

The main purpose of this chapter is to clarify what has been already observed by the numerical simulations [116]: if we compute the total magnetization using the Kärger model

$$m^{\mathrm{KAR}}(t) := m_e^{\mathrm{KAR}}(t) + m_c^{\mathrm{KAR}}(t),$$

it is better to evaluate m^{KAR} at time $t = \Delta - \frac{\delta}{3}$ instead of $t = \Delta$ (the time delay between the pulses, as suggested in the original Kärger paper [94]) or at $t = \Delta + \delta$ (at the end of the second pulse). In other words, $m^{\mathrm{KAR}}(\Delta - \delta/3)$ is closer to S^{FPK} than either $m^{\mathrm{KAR}}(\Delta)$ or $m^{\mathrm{KAR}}(\Delta + \delta)$. Certainly in the homogeneous case where there is only one compartment, it is easy to see that $m^{\mathrm{KAR}}(\Delta - \frac{\delta}{3})$ is exactly S^{FPK} (3.5). In the following we shall prove rigorously that evaluating m^{KAR} at $t = \Delta - \frac{\delta}{3}$ gives a much better approximation to S^{FPK} than evaluating it at the two natural alternatives: $t = \Delta$ or $t = \Delta + \delta$.

3.2 Convergence of the Kärger model to the FPK model

In this section we analyze the convergence of $m^{\mathrm{KAR}}(\Delta - \delta/3)$, $m^{\mathrm{KAR}}(\Delta)$ and $m^{\mathrm{KAR}}(\Delta + \delta)$, respectively, to S^{FPK}. For this purpose we introduce a dimensionless parameter

$$\zeta = \frac{\delta}{\Delta}$$

that goes to zero under the narrow pulse assumption ($\delta \ll \Delta$). Moreover, we shall consider the general case of N different compartments, with $N \geqslant 2$. In order to do the analysis for time-dimensioneless coefficients we also make the change of variables

$$t \to \frac{t}{\Delta}, \qquad q \to q\Delta, \qquad D_\ell^{\mathrm{eff}} \to D_\ell^{\mathrm{eff}}\Delta \qquad \text{and} \qquad \eta_\ell \to \eta_\ell\Delta, \quad \ell = 1, \cdots N. \tag{3.9}$$

We rewrite the models for N compartments in matrix notation as

$$\begin{cases} \dfrac{d}{dt}M^{\mathrm{KAR}}(t) + q^2\zeta^2\boldsymbol{\mathcal{D}}M^{\mathrm{KAR}}(t) + \boldsymbol{\eta}M^{\mathrm{KAR}}(t) = 0 \quad t \geqslant 0, \\ M^{\mathrm{KAR}}(0) = M_0 \in \mathbb{R}^N \end{cases} \tag{3.10}$$

for the Kärger model and

$$\begin{cases} \dfrac{d}{dt}M^{\mathrm{FPK}}(t) + q^2F_\zeta^2(t)\boldsymbol{\mathcal{D}}M^{\mathrm{FPK}}(t) + \boldsymbol{\eta}M^{\mathrm{FPK}}(t) = 0 \quad t \geqslant 0, \\ M^{\mathrm{FPK}}(0) = M_0 \in \mathbb{R}^N, \end{cases} \tag{3.11}$$

for FPK model, where

$$F_\zeta(t) \quad := \quad \begin{cases} t & \text{if } 0 < t \leqslant \zeta \\ \zeta & \text{if } \zeta < t \leqslant 1 \\ 1 + \zeta - t & \text{if } 1 < t \leqslant 1 + \zeta \\ 0 & \text{elsewhere} \end{cases} \quad \left(= \quad \frac{1}{\Delta}F_\delta(\Delta t) \right),$$

$$M^{\mathrm{KAR}}(t) := \begin{pmatrix} m_1^{\mathrm{KAR}}(t) \\ \vdots \\ m_N^{\mathrm{KAR}}(t) \end{pmatrix}, \quad M^{\mathrm{FPK}}(t) := \begin{pmatrix} m_1^{\mathrm{FPK}}(t) \\ \vdots \\ m_N^{\mathrm{FPK}}(t) \end{pmatrix}, \quad M_0 := \begin{pmatrix} m_0^1 \\ \vdots \\ m_0^N \end{pmatrix},$$

and $\boldsymbol{\mathcal{D}}$ and $\boldsymbol{\eta}$ are matrices with dimension $N \times N$. We define the total magnetization at time t by

$$m^{\mathrm{KAR}}(t) := \sum_{n=1}^{N} m_n^{\mathrm{KAR}}(t) \quad \text{and} \quad m^{\mathrm{FPK}}(t) := \sum_{n=1}^{N} m_n^{\mathrm{FPK}}(t). \tag{3.12}$$

To enforce mass conservation, we impose the condition that the sum of the entries of $\boldsymbol{\eta}$ is zero for each column, i.e.,

$$\sum_{n=1}^{N} \boldsymbol{\eta}_{nj} = 0 \qquad \forall j = 1, \dots, N. \tag{3.13}$$

For the two compartments models (3.1) and (3.7), $N = 2$, and

$$\boldsymbol{\mathcal{D}} = \frac{1}{\Delta} \begin{pmatrix} D_e^{\mathrm{eff}} & 0 \\ 0 & D_c^{\mathrm{eff}} \end{pmatrix} \qquad \text{and} \qquad \boldsymbol{\eta} = \frac{1}{\Delta} \begin{pmatrix} \eta_e & -\eta_c \\ -\eta_e & \eta_c \end{pmatrix}.$$

We observe in particular that assumption (3.13) is satisfied in this case.

3.2.1 Asymptotic expansion in ζ

In order to compare the total magnetizations coming from the solutions of (3.10) and (3.11) we expand $M^{\mathrm{KAR}}(t)$ and $M^{\mathrm{FPK}}(t)$ using asymptotic expansions with respect to ζ. More precisely we shall prove that

$$M^{\mathrm{KAR}}(t) = \sum_{i=1}^{\infty} \zeta^i M_i^{\mathrm{KAR}}(t) \quad t \geqslant 0 \tag{3.14}$$

and

$$\begin{cases} M^{\mathrm{FPK}}(t) = \displaystyle\sum_{i=1}^{\infty} \zeta^i M_i^{\mathrm{F}-}\big(t/\zeta\big) & 0 \leqslant t \leqslant \zeta \\ M^{\mathrm{FPK}}(t) = \displaystyle\sum_{i=1}^{\infty} \zeta^i M_i^{\mathrm{F}}\big(t\big) & \zeta \leqslant t \leqslant 1 \\ M^{\mathrm{FPK}}(t) = \displaystyle\sum_{i=1}^{\infty} \zeta^i M_i^{\mathrm{F}+}\big((t-1)/\zeta\big) & 1 \leqslant t \leqslant 1+\zeta \end{cases} \tag{3.15}$$

where M_i^{KAR}, $M_i^{\mathrm{F}-}$, M_i^{F} and $M_i^{\mathrm{F}+}$ are functions independent of ζ and the series converge with respect to the C^0 norm on any bounded interval.

The aim of such expansions is to facilitate the comparison between the magnetizations in terms of ζ. To simplify the analysis we make the change of variables

$$\tilde{M}^{\mathrm{KAR}}(t) = e^{\boldsymbol{\eta} t} M^{\mathrm{KAR}}(t) \quad \text{and} \quad \tilde{M}^{\mathrm{FPK}}(t) = e^{\boldsymbol{\eta} t} M^{\mathrm{FPK}}(t)$$

in problems (3.10) and (3.11) to obtain

$$\begin{cases} \dfrac{d}{dt}\tilde{M}^{\mathrm{KAR}}(t) + q^2\zeta^2 e^{\boldsymbol{\eta} t}\boldsymbol{\mathcal{D}} e^{-\boldsymbol{\eta} t}\tilde{M}^{\mathrm{KAR}}(t) = 0 \quad t \geqslant 0, \\ \tilde{M}^{\mathrm{KAR}}(0) = M_0, \end{cases} \tag{3.16}$$

and

$$\begin{cases} \dfrac{d}{dt}\tilde{M}^{\mathrm{FPK}}(t) + q^2 F_\zeta^2(t) e^{\boldsymbol{\eta} t}\boldsymbol{\mathcal{D}} e^{-\boldsymbol{\eta} t}\tilde{M}^{\mathrm{FPK}}(t) = 0 \quad t \geqslant 0, \\ \tilde{M}^{\mathrm{FPK}}(0) = M_0. \end{cases} \tag{3.17}$$

For the Kärger model (3.16) we observe that we can write the solution as

$$\tilde{M}^{\mathrm{KAR}}(t) = e^{t\boldsymbol{\eta}} \exp\left(-t\left(q^2\zeta^2\boldsymbol{\mathcal{D}} + \boldsymbol{\eta}\right)\right) M_0.$$

One can expand the exponential term using the Taylor series as

$$\exp\left(-t\left(q^2\zeta^2\boldsymbol{\mathcal{D}} + \boldsymbol{\eta}\right)\right) = 1 + \sum_{h=1}^{\infty} \frac{\left(-t\left(q^2\zeta^2\boldsymbol{\mathcal{D}} + \boldsymbol{\eta}\right)\right)^h}{h!}$$

It is then clear that $\tilde{M}^{\mathrm{KAR}}$, and therefore M^{KAR}, can be expanded as in (3.14). For the FPK model, we define

$$\begin{cases} \tilde{M}^{\mathrm{F}-}(\tau) := \tilde{M}^{\mathrm{FPK}}(t) & \tau = \frac{t}{\zeta} \text{ for } t \in [0, \zeta], \\ \tilde{M}^{\mathrm{F}}(t) := \tilde{M}^{\mathrm{FPK}}(t) & \text{for } t \in [\zeta, 1], \\ \tilde{M}^{\mathrm{F}-}(\tilde{\tau}) := \tilde{M}^{\mathrm{FPK}}(t) & \text{and } \tilde{\tau} = \frac{t-1}{\zeta} \text{ for } t \in [1, 1+\zeta]. \end{cases}$$

We then can rewrite (3.17) as

$$\begin{cases} \dfrac{d}{d\tau}\zeta^{-1}\tilde{M}^{\mathrm{F}-}(\tau) + q^2\zeta^2\tau^2 e^{\boldsymbol{\eta}\zeta\tau}\boldsymbol{\mathcal{D}} e^{-\boldsymbol{\eta}\zeta\tau}\tilde{M}^{\mathrm{F}-}(\tau) = 0 & \tau \in [0,1] \\ \tilde{M}^{\mathrm{F}-}(0) = M_0 & \\ \dfrac{d}{dt}\tilde{M}^{\mathrm{F}}(t) + q^2\zeta^2 e^{\boldsymbol{\eta} t}\boldsymbol{\mathcal{D}} e^{-\boldsymbol{\eta} t}\tilde{M}^{\mathrm{F}}(t) = 0 & t \in [\zeta, 1] \\ \tilde{M}^{\mathrm{F}}(\zeta) = \tilde{M}^{\mathrm{F}-}(1) & \\ \dfrac{d}{d\tilde{\tau}}\zeta^{-1}\tilde{M}^{\mathrm{F}+}(\tau) + q^2\zeta^2(1-\tilde{\tau})^2 e^{\boldsymbol{\eta}\zeta(1-\tilde{\tau})}\boldsymbol{\mathcal{D}} e^{-\boldsymbol{\eta}\zeta(1-\tilde{\tau})}\tilde{M}^{\mathrm{F}+}(\tilde{\tau}) = 0 & \tilde{\tau} \in [0,1] \\ \tilde{M}^{\mathrm{F}+}(0) = \tilde{M}^{\mathrm{F}}(1) & \end{cases}.$$

For $\tau \in [0,1]$, we observe that

$$\tilde{M}^{\mathrm{F}-}(\tau) = M_0 + \zeta^3 \int_0^\tau q^2 z^2 e^{\boldsymbol{\eta}\zeta z}\boldsymbol{\mathcal{D}} e^{-\boldsymbol{\eta}\zeta z}\tilde{M}^{\mathrm{F}-}(z)dz$$

which first proves that, for ζ sufficiently small, $\tilde{M}^{\mathrm{F}-}(\tau) = M_0 + O(\zeta^3)$ uniformly for $\tau \in [0,1]$. This allows us to prove by induction the first asymptotic expansion in (3.15) by adding and substracting (at step k of the induction) the truncated asymptotic expansion (at step $k-1$ of the induction) inside the integral and expanding the exponential function in power series with respect to $\boldsymbol{\eta}\zeta z$.

For $t \in [\zeta, 1]$ it is convenient to extend $\tilde{M}^{\mathrm{F}}$ to a function defined on $[0,1]$ such that it verifies

$$\frac{d}{dt}\tilde{M}^{\mathrm{F}}(t) + q^2\zeta^2 e^{\boldsymbol{\eta} t}\boldsymbol{\mathcal{D}} e^{-\boldsymbol{\eta} t}\tilde{M}^{\mathrm{F}}(t) = 0 \quad t \in [0,1]$$

and using the Taylor expansion, replace the initial condition $\tilde{M}^{\mathrm{F}}(\zeta) = \tilde{M}^{\mathrm{F}-}(1)$ with

$$\tilde{M}^{\mathrm{F}}(0) = \tilde{M}^{\mathrm{F}-}(1) - \sum_{i=1}^{\infty} \frac{\zeta^i}{i!} \frac{d^i}{dt^i} \tilde{M}^{\mathrm{F}}(0).$$

Similarly as for the Kärger model, we have that the analytic solution is given by

$$\tilde{M}^{\mathrm{F}}(t) = e^{t\boldsymbol{\eta}} \exp\left(-t\left(q^2\zeta^2\boldsymbol{\mathcal{D}} + \boldsymbol{\eta}\right)\right)\tilde{M}^{\mathrm{F}}(0).$$

The second part of (3.15) then follows from the fact that $\tilde{M}^{\mathrm{F}-}(1)$ (and therefore $\tilde{M}^{\mathrm{F}}(0)$) can be expanded as a convergent power series in terms of ζ. Finally for $\tilde{\tau} \in [0,1]$ we make similar arguments as for $\tilde{M}^{\mathrm{F}-}(\tau)$, by writing

$$\tilde{M}^{\mathrm{F}+}(\tilde{\tau}) = \tilde{M}^{\mathrm{F}}(1) + \zeta^3 \int_0^{\tau} q^2(1-z)^2 e^{\boldsymbol{\eta}\zeta(1-z)}\boldsymbol{\mathcal{D}}e^{-\boldsymbol{\eta}\zeta(1-z)}\tilde{M}^{\mathrm{F}+}(z)dz$$

and using the expansion in terms of ζ of $\tilde{M}^{\mathrm{F}}(1)$ to initiate an induction argument (following the same lines as for $\tilde{M}^{\mathrm{F}-}$).

3.2.2 Error estimates

The goal of this section is to prove that

$$m^{\mathrm{KAR}}\left(1 - \tfrac{\zeta}{3}\right) - m^{\mathrm{FPK}}(1+\zeta) = O(\zeta^6).$$

We remark that this convergence holds only for the sum of the magnetizations m and not for each of the compartment magnetizations. In fact one only has $M^{\mathrm{KAR}}\left(1 - \frac{\zeta}{3}\right) - M^{\mathrm{FPK}}(1+\zeta) = O(\zeta)$. For arbitrary $\boldsymbol{\mathcal{D}}$, the convergence result does not hold for a general choice of the initial data M_0 but only for those such that

$$\boldsymbol{\eta}M_0 = 0. \tag{3.18}$$

This condition is indeed verified for dMRI applications where the components of M_0 are the volume fractions of the compartments. We observe that as a direct consequence of (3.13) and (3.18) we have the following identities.

Lemma 3.2.1. *Let $\boldsymbol{\eta}$ satisfy (3.13) and $M_0 \in \mathbb{R}^N$ such that $\boldsymbol{\eta}M_0 = \mathbf{0}$. Then for all $\boldsymbol{\alpha} \in \mathbb{R}^{N\times N}$, the following properties are satisfied*

$$\sum_{n=1}^{N} (\boldsymbol{\eta}^h\boldsymbol{\alpha}M_0)_n = \sum_{n=1}^{N} (\boldsymbol{\alpha}\boldsymbol{\eta}^h M_0)_n = 0 \quad \text{for all } h \in \mathbb{N}, h \geqslant 1; \tag{3.19}$$

$$\sum_{n=1}^{N} (\boldsymbol{\alpha}e^{-\boldsymbol{\eta}}M_0)_n = \sum_{n=1}^{N} (\boldsymbol{\alpha}M_0)_n \quad \text{and} \quad \sum_{n=1}^{N} (\boldsymbol{\alpha}\boldsymbol{\eta}e^{-\boldsymbol{\eta}}M_0)_n = 0. \tag{3.20}$$

The proof is staightforward.
We now state and prove the main theorem of this section.

Theorem 3.2.2. Under the hypothesis of Lemma 3.2.1 there exists two constant $C_{\boldsymbol{\mathcal{D}},\boldsymbol{\eta},M_0} > 0$ and ζ_0 that only depends on $\boldsymbol{\mathcal{D}}$, $\boldsymbol{\eta}$ and M_0 such that, for all $0 \leqslant \zeta \leqslant \zeta_0$,

$$\left| m^{\mathrm{KAR}}\left(1-\tfrac{\zeta}{3}\right) - m^{\mathrm{FPK}}(1+\zeta) \right| \leqslant C_{\boldsymbol{\mathcal{D}},\boldsymbol{\eta},M_0}\, q^4\zeta^6,$$

where

$$C_{\boldsymbol{\mathcal{D}},\boldsymbol{\eta},M_0} := \sum_{n=1}^{N} \frac{2}{9}\left(\boldsymbol{\mathcal{D}}^2 M_0\right)_n - \frac{5}{36}\int_0^1 \left(\boldsymbol{\mathcal{D}}\boldsymbol{\eta} e^{\boldsymbol{\eta}(s-1)\boldsymbol{\mathcal{D}}M_0}\right)_n ds + \left(\frac{2}{9}\boldsymbol{\mathcal{D}}e^{-\boldsymbol{\eta}}\boldsymbol{\mathcal{D}}M_0\right)_n + \left(\frac{1}{4}\boldsymbol{\mathcal{D}}\boldsymbol{\eta}\boldsymbol{\mathcal{D}}M_0\right)_n.$$

Proof. The proof relies on the expansions (3.14) and(3.15) and the explicit expressions of the terms of these expansions. In order to compute these terms, we found it easier to follow another route than the one used for proving the existence of these expansions. More precisely we shall first identify the set of differential equations satisfied by these terms by inserting the asymptotic expansions into the differential equations then match the terms in front of the same power of ζ. We then solve (inductively) these equations to obtain the desired explicit expressions of the expansions in terms of the data. In the case of the Kärger model, inserting expansion (3.14) in (3.10) we obtain the following problems for $i \geqslant 0$

$$\begin{cases} \dfrac{d}{dt}M_i^{\mathrm{KAR}}(t) + q^2\boldsymbol{\mathcal{D}}M_{i-2}^{\mathrm{KAR}}(t) + \boldsymbol{\eta}M_i^{\mathrm{KAR}}(t) = 0 \\ M_0^{\mathrm{KAR}}(0) = M_0 \text{ and } M_i^{\mathrm{KAR}}(0) = 0 \text{ for } i \geqslant 1 \end{cases} \tag{3.21}$$

where we used the convention that the terms with a negative index are 0. Then one easily verifies that $M_{2i+1}^{\mathrm{KAR}}(t) = 0$ for all $i \geqslant 0$ and

$$M_0^{\mathrm{KAR}}(t) = e^{-\boldsymbol{\eta}t}M_0, \quad M_2^{\mathrm{KAR}}(t) = -q^2\int_0^t \left(e^{\boldsymbol{\eta}(s-t)}\boldsymbol{\mathcal{D}}M_0^{\mathrm{KAR}}(s)\right)ds\,,$$
$$M_4^{\mathrm{KAR}}(t) = -q^2\int_0^t \left(e^{\boldsymbol{\eta}(s-t)}\boldsymbol{\mathcal{D}}M_2^{\mathrm{KAR}}(s)\right)ds \quad \text{and} \quad M_6^{\mathrm{KAR}}(t) = -q^2\int_0^t \left(e^{\boldsymbol{\eta}(s-t)}\boldsymbol{\mathcal{D}}M_4^{\mathrm{KAR}}(s)\right)ds.$$

For a vector $V \in \mathbb{R}^N$ we denote $\overline{V} := \sum_{n=1}^{N} V_n$. Using Taylor's expansion we obtain

$$m^{\mathrm{KAR}}\Big(1-\frac{\zeta}{3}\Big) = \sum_{i=0}^{\infty}\zeta^i\overline{M_i^{\mathrm{KAR}}}\Big(1-\frac{\zeta}{3}\Big) = \sum_{i=1}^{\infty}\zeta^i\left(\overline{M_i^{\mathrm{KAR}}}(1) + \sum_{h=1}^{i}\frac{1}{(-3)^h(h!)}\frac{d^h}{dt^h}\overline{M_{i-h}^{\mathrm{KAR}}}(t)|_{t=1}\right).$$

Therefore,

$$m^{\mathrm{KAR}}\Big(1-\frac{\zeta}{3}\Big) = \overline{M_0^{\mathrm{KAR}}}(1) + \zeta^2\overline{M_2^{\mathrm{KAR}}}(1) - \frac{\zeta^3}{3}\Big(\frac{d}{dt}\overline{M_2^{\mathrm{KAR}}}(1)\Big) + \zeta^4\overline{M_4^{\mathrm{KAR}}}(1)$$
$$- \frac{\zeta^5}{3}\Big(\frac{d}{dt}\overline{M_4^{\mathrm{KAR}}}(1)\Big) + \zeta^5\left(\overline{M_6^{\mathrm{KAR}}}(1) + \frac{1}{18}\frac{d^2}{dt^2}\overline{M_4^{\mathrm{KAR}}}(1)\right) + O(\zeta^7).$$

Using the analytic expression of the solutions and properties (3.13), (3.18) and (3.20) we finally obtain

$$
\begin{aligned}
m^{\mathrm{KAR}}\Big(1-\frac{\zeta}{3}\Big) &= \overline{M_0} - \zeta^2 q^2 \overline{\boldsymbol{\mathcal{D}} M_0} + \zeta^3 \frac{q^2}{3} \overline{\boldsymbol{\mathcal{D}} M_0} \\
&\quad - \zeta^4 q^4 \int_0^1 \int_0^s \left(\overline{e^{\boldsymbol{\eta}(s-1)} \boldsymbol{\mathcal{D}} e^{\boldsymbol{\eta}(t-s)} \boldsymbol{\mathcal{D}} M_0} \right) dt\, ds - \zeta^5 \frac{q^4}{3} \int_0^1 \left(\overline{\boldsymbol{\mathcal{D}} e^{\boldsymbol{\eta}(s-1)} \boldsymbol{\mathcal{D}} M_0} \right) ds \\
&\quad + \zeta^6 \Bigg[q^6 \int_0^1 \left(\overline{e^{\boldsymbol{\eta}(s-1)} \boldsymbol{\mathcal{D}} \int_0^s \left(e^{\boldsymbol{\eta}(z-s)} \boldsymbol{\mathcal{D}} \int_0^t \left(e^{\boldsymbol{\eta}(z-t)} \boldsymbol{\mathcal{D}} M_0 \right) dt \right) dz} \right) ds \\
&\qquad + \frac{q^4}{18} \left(\overline{\boldsymbol{\mathcal{D}}^2 M_0} - \int_0^1 \left(\overline{\boldsymbol{\mathcal{D}} \boldsymbol{\eta} e^{-\boldsymbol{\eta}(s-1)} \boldsymbol{\mathcal{D}} M_0} \right) ds \right) \Bigg] + O(\zeta^7).
\end{aligned}
$$

To get the analytic expansion of the signal given by the FPK model in terms of ζ we have already observed that it is convenient to split the time interval in three different parts in which the F_ζ has different expressions and to extend the one in the middle as a function in the time interval $[0,1]$. We then rewrite the problem (3.11) as

$$
\begin{cases}
\dfrac{d}{d\tau} \zeta^{-1} M^{\mathrm{F}-}(\tau) + q^2 \zeta^2 \tau^2 \boldsymbol{\mathcal{D}} M^{\mathrm{F}-}(\tau) + \boldsymbol{\eta} M^{\mathrm{F}-}(\tau) = 0 & \tau \in [0,1], \\
M^{\mathrm{F}-}(0) = M_0, & \\
\dfrac{d}{dt} M^{\mathrm{F}}(t) + q^2 \zeta^2 \boldsymbol{\mathcal{D}} M^{\mathrm{F}}(t) + \boldsymbol{\eta} M^{\mathrm{F}}(t) = 0 & t \in [0,1], \\
M^{\mathrm{F}}(0) = M^{\mathrm{F}-}(1) - \displaystyle\sum_{i=1}^{\infty} \frac{\zeta^i}{i!} \frac{d^i}{dt^i} M^{\mathrm{F}}(0), & \\
\dfrac{d}{d\tilde{\tau}} \zeta^{-1} M^{\mathrm{F}+}(\tilde{\tau}) + q^2 \zeta^2 (1-\tilde{\tau})^2 \boldsymbol{\mathcal{D}} M^{\mathrm{F}+}(\tilde{\tau}) + \boldsymbol{\eta} M^{\mathrm{F}+}(\tilde{\tau}) = 0 & \tilde{\tau} \in [0,1], \\
M^{\mathrm{F}+}(0) = M^{\mathrm{F}}(1). &
\end{cases}
\tag{3.22}
$$

Inserting the expansion (3.15) in (3.22) and equating the same powers of ζ yields for $i \geqslant 0$

$$
\begin{cases}
\dfrac{d}{d\tau} M_i^{\mathrm{F}-}(\tau) + q^2 \tau^2 \boldsymbol{\mathcal{D}} M_{i-3}^{\mathrm{F}-}(\tau) + \boldsymbol{\eta} M_{i-1}^{\mathrm{F}-}(\tau) = 0, \\
M_0^{\mathrm{F}-}(0) = M_0 \text{ and } M_i^{\mathrm{F}-}(0) = 0 \text{ for } i \geqslant 1,
\end{cases}
\tag{3.23}
$$

$$
\begin{cases}
\dfrac{d}{dt} M_i^{\mathrm{F}}(t) + q^2 \boldsymbol{\mathcal{D}} M_{i-2}^{\mathrm{F}}(t) + \boldsymbol{\eta} M_i^{\mathrm{F}}(t) = 0, \\
M_i^{\mathrm{F}}(0) = M_i^{\mathrm{F}-}(1) - \displaystyle\sum_{h=1}^{i} \frac{1}{h!} \frac{d^h}{dt^h} M_{i-h}^{\mathrm{F}}(t)|_{t=0},
\end{cases}
\tag{3.24}
$$

$$
\begin{cases}
\dfrac{d}{d\tilde{\tau}} M_i^{\mathrm{F}+}(\tilde{\tau}) + q^2 (1-\tilde{\tau})^2 \boldsymbol{\mathcal{D}} M_{i-3}^{\mathrm{F}+}(\tilde{\tau}) + \boldsymbol{\eta} M_{i-1}^{\mathrm{F}+}(\tilde{\tau}) = 0, \\
M_i^{\mathrm{F}-}(0) = M_i^{\mathrm{F}}(1),
\end{cases}
\tag{3.25}
$$

where we again use the convention that the terms with a negative index are 0. We hereafter shall not detail all the calculations (which are lengthy but not difficult) and restrict ourselves to

the main steps and results. Since we are interested in the signal

$$m^{\mathrm{FPK}}(1+\zeta) = \overline{M^{\mathrm{F}+}}(1) = \sum_{i=0}^{\infty} \zeta^i \overline{M_i^{\mathrm{F}+}} \tag{3.26}$$

we focus on evaluating $\overline{M_i^{\mathrm{F}+}}$. For $i = 0$, one straightforwardly gets

$$M_0^{\mathrm{F}-}(\tau) = M_0, \quad M_0^{\mathrm{F}}(t) = e^{-\boldsymbol{\eta} t} M_0 \text{ and } M_0^{\mathrm{F}+}(\tilde{\tau}) = e^{-\boldsymbol{\eta}} M_0,$$

which implies, using (3.20)

$$\overline{M_0^{\mathrm{F}+}}(1) = \overline{M_0}.$$

The solutions of (3.23)-(3.25) for $i = 1$ are

$$M_1^{\mathrm{F}-}(\tau) = -\tau \boldsymbol{\eta} M_0, \quad M_1^{\mathrm{F}}(t) = 0 \quad \text{and} \quad M_1^{\mathrm{F}+}(\tilde{\tau}) = -\tilde{\tau} \boldsymbol{\eta}\, e^{-\boldsymbol{\eta}} M_0.$$

Using (3.20) one then gets

$$\overline{M_1^{\mathrm{F}+}}(1) = 0.$$

For $i = 2$ the solutions are

$$M_2^{\mathrm{F}-}(\tau) = \frac{\tau^2}{2} \boldsymbol{\eta}^2 M_0, \quad M_2^{\mathrm{F}}(t) = -q^2 \int_0^t \left(e^{\boldsymbol{\eta}(s-t)} \boldsymbol{\mathcal{D}} e^{-\boldsymbol{\eta} s} M_0 \right) ds,$$
$$M_2^{\mathrm{F}+}(\tilde{\tau}) = \frac{\tilde{\tau}^2}{2} (\boldsymbol{\eta}^2 e^{-\boldsymbol{\eta}} M_0) + M_2^{\mathrm{F}}(1).$$

Then, using (3.19) and (3.20), one gets

$$\overline{M_2^{\mathrm{F}+}}(1) = -q^2 \overline{\boldsymbol{\mathcal{D}} M_0}.$$

For $i = 3$ one obtains

$$M_3^{\mathrm{F}-}(\tau) = -\frac{q^2}{3} \tau^3 \boldsymbol{\mathcal{D}} M_0 - \frac{\tau^3}{6} \boldsymbol{\eta}^3 M_0, \quad M_3^{\mathrm{F}}(t) = \frac{2}{3} q^2 e^{-\boldsymbol{\eta} t} \boldsymbol{\mathcal{D}} M_0,$$
$$M_3^{\mathrm{F}+}(\tilde{\tau}) = \frac{q^2}{3} ((1-\tilde{\tau})^3 - 1) \boldsymbol{\mathcal{D}} e^{-\boldsymbol{\eta}} M_0 - \frac{\tilde{\tau}^3}{6} \boldsymbol{\eta}^3 e^{-\boldsymbol{\eta}} M_0 + \tilde{\tau} \boldsymbol{\eta} M_2^{\mathrm{F}}(1) + \frac{2}{3} q^2 e^{-\boldsymbol{\eta}} \boldsymbol{\mathcal{D}} M_0$$

Then, using (3.19) and (3.20) one gets

$$\overline{M_3^{\mathrm{F}+}}(1) = \frac{q^2}{3} \overline{\boldsymbol{\mathcal{D}} M_0}.$$

For $i = 4$ one has

$$M_4^{\mathrm{F}-}(\tau) = \frac{q^2}{4} \tau^4 \boldsymbol{\mathcal{D}} \boldsymbol{\eta} M_0 + \frac{q^2}{12} \tau^4 \boldsymbol{\eta} \boldsymbol{\mathcal{D}} M_0 + \frac{\tau^4}{24} \boldsymbol{\eta}^4 M_0,$$
$$M_4^{\mathrm{F}}(t) = -q^2 \int_0^t \left(e^{\boldsymbol{\eta}(s-t)} \boldsymbol{\mathcal{D}} M_2^{\mathrm{F}}(s) \right) ds - \frac{q^2}{4} (\boldsymbol{\mathcal{D}} \boldsymbol{\eta} M_0 - \boldsymbol{\eta} \boldsymbol{\mathcal{D}} M_0),$$
$$M_4^{\mathrm{F}+}(\tilde{\tau}) = q^2 \frac{\tilde{\tau}^2}{12} \left(3\tilde{\tau}^2 - 8\tilde{\tau} + 6 \right) \boldsymbol{\mathcal{D}} \boldsymbol{\eta} e^{-\eta} M_0 - \int_0^{\tilde{\tau}} \boldsymbol{\eta} M_3^{\mathrm{F}+}(s) ds + M_4^{\mathrm{F}}(1)$$

and using again (3.19) and (3.20),

$$\overline{M_4^{\mathrm{F}+}}(1) = -q^4 \int_0^1 \int_0^s \left(\overline{e^{\boldsymbol{\eta}(s-1)} \boldsymbol{\mathcal{D}} e^{\boldsymbol{\eta}(t-s)} \boldsymbol{\mathcal{D}} M_0} \right) dt\, ds.$$

For $i = 5$ to find the solutions in the last two time intervals it is better to first take the sum of the equations in order to directly cancel the terms that are right-multiplied by $\boldsymbol{\eta}$. One then gets

$$\begin{aligned} M_5^{\mathrm{F}-}(\tau) &= -\frac{q^2}{10}\tau^5 \boldsymbol{\mathcal{D}}\boldsymbol{\eta}^2 M_0 - \frac{q^2}{20}\tau^5 \boldsymbol{\eta}\boldsymbol{\mathcal{D}}\boldsymbol{\eta} M_0 - \frac{q^2}{60}\tau^5 \boldsymbol{\eta}^2 \boldsymbol{\mathcal{D}} M_0 - \frac{\tau^5}{120}\boldsymbol{\eta}^5 M_0, \\ \overline{M_5^{\mathrm{F}}}(t) &= -\frac{2}{3} q^4 \int_0^t (\overline{\boldsymbol{\mathcal{D}} e^{-\eta s} \boldsymbol{\mathcal{D}} M_0})\, ds, \\ \overline{M_5^{\mathrm{F}+}}(\tilde{\tau}) &= \frac{q^4}{3}((1-\tilde{\tau})^3 - 1) \int_0^1 \overline{\boldsymbol{\mathcal{D}} e^{\boldsymbol{\eta}(s-1)} \boldsymbol{\mathcal{D}} e^{-\eta s} M_0}\, ds + \overline{M_5^{\mathrm{F}}(1)}. \end{aligned}$$

Consequently, using a change of variable and the property (3.20) in order to simplify the first integral, one ends up with

$$\overline{M_5^{\mathrm{F}+}}(1) = \frac{q^4}{3} \int_0^1 \overline{\boldsymbol{\mathcal{D}} e^{\boldsymbol{\eta}(s-1)} \boldsymbol{\mathcal{D}} e^{-\eta s} M_0}\, ds - \frac{2}{3} q^4 \int_0^1 \overline{\boldsymbol{\mathcal{D}} e^{-\eta s} \boldsymbol{\mathcal{D}} M_0} ds = -\frac{1}{3} q^4 \int_0^1 \overline{\boldsymbol{\mathcal{D}} e^{-\eta s} \boldsymbol{\mathcal{D}} M_0} ds.$$

Finally for $i = 6$ it is again better to first take the sum of the equations in order to directly cancel the terms that are right-multiplied by $\boldsymbol{\eta}$ in the last two intervals. One then gets

$$\begin{aligned} M_6^{\mathrm{F}-}(\tau) = \;& \frac{q^4}{18}\tau^6 \boldsymbol{\mathcal{D}}^2 M_0 + \frac{q^2}{36}\tau^6 \boldsymbol{\mathcal{D}}\eta^3 M_0 + \frac{q^2}{60}\tau^6 \boldsymbol{\eta}\boldsymbol{\mathcal{D}}\boldsymbol{\eta}^2 M_0 + \frac{q^2}{120}\tau^6 \boldsymbol{\eta}^2 \boldsymbol{\mathcal{D}}\boldsymbol{\eta} M_0 \\ & + \frac{q^2}{360}\tau^6 \boldsymbol{\eta}^3 \boldsymbol{\mathcal{D}} M_0 + \frac{\tau^6}{720}\boldsymbol{\eta}^6 M_0 \\ \overline{M_6^{\mathrm{F}}}(t) = \;& -q^2 \int_0^{\tilde{t}} \overline{e^{\boldsymbol{\eta}(s-\tilde{t})} \boldsymbol{\mathcal{D}} M_5^{\mathrm{F}}(s)} ds + \frac{2}{9} \overline{\boldsymbol{\mathcal{D}}^2 M_0} \\ \overline{M_6^{\mathrm{F}+}}(\tilde{\tau}) = \;& \frac{q^4}{18}\tilde{\tau}^2(\tilde{\tau}^2 - 3\tilde{\tau} + 3)^2 \overline{\boldsymbol{\mathcal{D}}^2 M_0} + \frac{q^4}{12}\tilde{\tau}^2(3\tilde{\tau}^2 - 8\tilde{\tau} + 6) \int_0^1 \overline{\boldsymbol{\mathcal{D}} e^{\boldsymbol{\eta}(s-1)} \boldsymbol{\mathcal{D}} M_0} \\ & - \frac{2}{9} q^4 \tilde{\tau}(\tilde{\tau}^2 - 3\tilde{\tau} + 3) \overline{\boldsymbol{\mathcal{D}} e^{-\boldsymbol{\eta}} \boldsymbol{\mathcal{D}} M_0} + \overline{M_6^{\mathrm{F}}}(1) \end{aligned}$$

and using again (3.19) and (3.20):

$$\overline{M_6^{\mathrm{F}+}}(1) = \frac{5q^4}{18} \overline{\boldsymbol{\mathcal{D}}^2 M_0} + \frac{q^4}{12} \int_0^1 \overline{\boldsymbol{\mathcal{D}} e^{\boldsymbol{\eta}(s-1)} \boldsymbol{\mathcal{D}} M_0} ds - \frac{2}{9} q^4 \overline{\boldsymbol{\mathcal{D}} e^{-\boldsymbol{\eta}} \boldsymbol{\mathcal{D}} M_0} - q^2 \int_0^1 \overline{e^{\boldsymbol{\eta}(s-1)} \boldsymbol{\mathcal{D}} M_4^{\mathrm{F}}(s)} ds.$$

We thus have proved that $m^{\mathrm{FPK}}(1+\zeta)$ has the same asymptotic expansion as $m^{\mathrm{KAR}}(1-\frac{\zeta}{3})$ up to, but not including $O(\zeta^6)$ terms, which yields the claim of our theorem. □

Remark 3.2.3. *We remark that, for $i = 1, \ldots, 5$, the magnetizations M_i^{FPK} are different from M_i^{KAR}.*

Theorem 3.2.4. Under the hypothesis of Theorem 3.2.2 we have that

$$m^{\mathrm{KAR}}(1) - m^{\mathrm{FPK}}(1+\zeta) = O(\zeta^3)$$

and

$$m^{\mathrm{KAR}}(1+\zeta) - m^{\mathrm{FPK}}(1+\zeta) = O(\zeta^3).$$

Proof. With the previous Theorem we have proved that

$$m^{\mathrm{KAR}}(1-\zeta/3) - m^{\mathrm{FPK}}(1+\zeta) = O(\zeta^6).$$

Following a similar approach it can be also easily shown that if we evaluate the Kärger model at $t = 1$ or $t = 1+\zeta$ the order of convergence drops to $O(\zeta^3)$ because the constants of the expansions in front of ζ^3 become different. □

3.3 Kurtosis formula for FPK model

The dMRI signal can be measured for several values of q, δ, Δ and directions $\mathbf{u_q}$. We have already remarked that it is common in the dMRI community not to display the signal as a function of q, but as a function of the so called b-value that for PGSE is defined in (3.6). In [87] and [88] Jensen, Helpern and their collaborators have shown how to quantify the Non-Gaussian water diffusion by using Kurtosis analysis. The term of Kurtosis (KUR) for a dMRI signal is defined as the normalized second order term of the Taylor expansion in b-value of the logarithm of the signal attenuation, i.e.

$$S(b) = \exp\Big(- ADC\, b + \frac{1}{6} ADC^2 KUR^2 b^2 + O(b^3)\Big)\,. \tag{3.27}$$

In [116] was shown that for Kärger and FPK models the ADC term is equal, but the analysis of the Kurtosis term was not done. The goal of this section is to derive an analytic formula for the FPK's Kurtosis term in the case of $N = 2$ compartments and show that it converges to the Kärger one which is well known in literature. To recover this formula we proceed in a similar way to the previous section by making an asymptotic expansion of the magnetization of the FPK model but this time in term of q^2 as was done in [42]. We have already proved that there exists a constant $C_{\boldsymbol{\mathcal{D}},\boldsymbol{\eta},M_0} > 0$ for which $|S^{\mathrm{KAR}}(q,\mathbf{u_q}) - S^{\mathrm{FPK}}(q,\mathbf{u_q})| \leqslant C_{\boldsymbol{\mathcal{D}},\boldsymbol{\eta},M_0}\zeta^6$, (where $\zeta = \frac{\delta}{\Delta}$). Showing that the FPK kurtosis formula converges the well known Kärger one means that there exists another constant $C > 0$ for which $|S^{\mathrm{KAR}}(b) - S^{\mathrm{FPK}}(b)| \leqslant Cb^2$.

Theorem 3.3.1. We can write the signal attenuation in terms of the b-value as

$$\frac{S(b)}{S(0)} = \exp\Big(- ADC\, b + \frac{1}{6} ADC^2 KUR\, b^2 + O(b^3)\Big) \tag{3.28}$$

where for the two compartments FPK model in $\mathbf{u_q}$ direction we have that

$$ADC = v_e D_e^{\mathrm{eff}} + v_c D_c^{\mathrm{eff}} \tag{3.29}$$

and

$$\begin{aligned} KUR = \frac{2(D_e^{\mathrm{eff}} - D_c^{\mathrm{eff}})^2 \eta_e \eta_c}{5\delta^4\left(\Delta - \frac{\delta}{3}\right)^2 (v_e D_e^{\mathrm{eff}} + v_c D_c^{\mathrm{eff}})^2 (\eta_e+\eta_c)^8} \Bigg(& -120 + 60 e^{-(\eta_e+\eta_c)T_e} \\ & + 120\big(\delta(\eta_e+\eta_c)+1\big)e^{-(\eta_e+\eta_c)\delta} + 120\big(\delta(\eta_e+\eta_c)-1\big)e^{-(\eta_e+\eta_c)\Delta} \\ & + 60\big(\delta(\eta_e+\eta_c)-1\big)^2 e^{-(\eta_e+\eta_c)(\Delta-\delta)} + 60\delta^2(\eta_e+\eta_c)^2 \\ & - 40\delta^3(\eta_e+\eta_c)^3 + 15\delta^4\Delta(\eta_e+\eta_c)^5 - 9\delta^5(\eta_e+\eta_c)^5 \Bigg). \end{aligned} \tag{3.30}$$

Proof. As it was done in [42] we extend the definition of the FPK model for any complex number z as

$$\begin{cases} \dfrac{d}{dt}m_e(z,\cdot)(t) + zD_e^{\text{eff}}\left(\displaystyle\int_0^t f(s)ds\right)^2 m_e(z,t) + \eta_e m_e(z,t) - \eta_c m_c(z,t) = 0 \\ \dfrac{d}{dt}m_c(z,\cdot)(t) + zD_c^{\text{eff}}\left(\displaystyle\int_0^t f(s)ds\right)^2 m_c(z,t) + \eta_c m_c(z,t) - \eta_e m_e(z,t) = 0 \\ m_e(z,0) = m_e^0 \text{ and } m_c(z,0) = m_c^0 \end{cases} \tag{3.31}$$

where we remind that $\eta_e = \frac{\kappa|\Gamma_m|}{|Y_e|}$, $\eta_c = \frac{\kappa|\Gamma_m|}{|Y_c|}$ with $|Y_e|$ and $|Y_c|$ being the volume of the extra-cellular and intra-cellular compartment, respectively, $|\Gamma_m|$ the total surface area of the biological cell membranes, κ the permeability of the membrane and, D_e^{eff} and D_c^{eff} are, with an abuse of notation, the effective diffusion coefficient in the $\mathbf{u_q}$ direction. The solutions $(m_e(z), m_c(z))$ belong to $\mathcal{C}^1(0,T_E)$ and thus to $L^\infty(0,T_E)$. It is quite easy to see that $(m_e(\cdot,t), m_c(\cdot,t))$ can be differentiated with respect to z for any $z \in \mathbb{C}$. Then $m_e(\cdot,t)$ and $m_c(\cdot,t)$ are holomorphic on all $\mathbb{C}$ and admit an expansion of the form

$$m_e(z,t) = \sum_{n=0}^{+\infty} z^n m_{e,n}(t) \text{ and } m_c(z,t) = \sum_{n=0}^{+\infty} z^n m_{c,n}(t).$$

Inserting these expansions in (3.31) we find

$$\begin{cases} m_{e,0}(t) = \dfrac{\eta_c(m_e^0 + m_c^0)}{\eta_e + \eta_c} + \dfrac{\eta_e m_e^0 - \eta_c m_c^0}{\eta_e + \eta_c} e^{-(\eta_e+\eta_c)t} \\ m_{c,0}(t) = \dfrac{\eta_e(m_e^0 + m_c^0)}{\eta_e + \eta_c} - \dfrac{\eta_e m_e^0 - \eta_c m_c^0}{\eta_e + \eta_c} e^{-(\eta_e+\eta_c)t} \\ m_{e,n}(t) = \displaystyle\int_0^t \left(\frac{-\eta_c - \eta_e e^{(\eta_e+\eta_c)(s-t)}}{\eta_e + \eta_c} D_e^{\text{eff}} m_{e,n-1}(s) \right. \\ \qquad\qquad \left. - \dfrac{\eta_c - \eta_c e^{(\eta_e+\eta_c)(s-t)}}{\eta_e + \eta_c} D_c^{\text{eff}} m_{c,n-1}(s) \right) \left(\displaystyle\int_0^s f(\xi)d\xi \right)^2 ds \\ m_{c,n}(t) = \displaystyle\int_0^t \left(\frac{-\eta_e + \eta_e e^{(\eta_e+\eta_c)(s-t)}}{\eta_e + \eta_c} D_e^{\text{eff}} m_{e,n-1}(s) \right. \\ \qquad\qquad \left. - \dfrac{\eta_e + \eta_c e^{(\eta_e+\eta_c)(s-t)}}{\eta_e + \eta_c} D_c^{\text{eff}} m_{c,n-1}(s) \right) \left(\displaystyle\int_0^s f(\xi)d\xi \right)^2 ds \end{cases}$$

This allows us to obtain an expansion of the measured signal with respect to z as

$$\begin{aligned} S\left(\sqrt{z}, \mathbf{u_q}\right) &= m^0 - \sum_{n=1}^{+\infty} z^n \int_0^{T_E} \left(D_e^{\text{eff}} m_{e,n-1}(s) + D_c^{\text{eff}} m_{c,n-1}(s) \right) \left(\int_0^s f(\xi)d\xi \right)^2 ds \\ &\approx m^0 - z \int_0^{T_E} \left(D_e^{\text{eff}} m_{e,0}(s) + D_c^{\text{eff}} m_{c,0}(s) \right) \left(\int_0^s f(\xi)d\xi \right)^2 ds \\ &\quad - z^2 \int_0^{T_E} \left(D_e^{\text{eff}} m_{e,1}(s) + D_c^{\text{eff}} m_{c,1}(s) \right) \left(\int_0^s f(\xi)d\xi \right)^2 ds + O(z^3) \end{aligned}$$

where $T_E = \delta + \Delta$ is the echo time.

Then, considering the logarithm of the normalized signal given by $\log\left(\frac{S(q,\mathbf{u_q})}{S(0,\mathbf{u_q})}\right)$, where $S(0,\mathbf{u_q}) = m^0$, and using the Taylor's expansion $\log(1+x) \approx x - \frac{x^2}{2} + O(x^3)$ we obtain

$$\begin{aligned}
\log\left(\frac{S(q,\mathbf{u_q})}{S(0,\mathbf{u_q})}\right) \approx & -b(v_e D_e^{\text{eff}} + v_c D_c^{\text{eff}}) \\
& + \frac{b^2}{2}\left[\frac{(\eta_e D_e^{\text{eff}} + \eta_c D_c^{\text{eff}})^2}{(\eta_e+\eta_c)^2} - \left(v_e D_e^{\text{eff}} + v_c D_c^{\text{eff}}\right)^2\right] \\
& + \frac{q^4 (D_e^{\text{eff}} - D_c^{\text{eff}})^2 \eta_e \eta_c}{15\,(\eta_e+\eta_c)^8}\Bigg(-120 + 60e^{-(\eta_e+\eta_c)T_E} + 60\delta^2(\eta_e+\eta_c)^2 \\
& \quad + 120\big(\delta(\eta_e+\eta_c)+1\big)e^{-(\eta_e+\eta_c)\delta} + 120\big(\delta(\eta_e+\eta_c)-1\big)e^{-(\eta_e+\eta_c)\Delta} \\
& \quad + 60\big(\delta^2(\eta_e+\eta_c)^2 - 2\delta(\eta_e+\eta_c)+1\big)e^{-(\eta_e+\eta_c)(\Delta-\delta)} \\
& \quad - 40\delta^3(\eta_e+\eta_c)^3 + 15\delta^4\Delta(\eta_e+\eta_c)^5 - 9\delta^5(\eta_e+\eta_c)^5\Bigg) + O(q^6).
\end{aligned}$$

We observe, that from our domain's assumptions,

$$\frac{(\eta_e D_e^{\text{eff}} + \eta_c D_c^{\text{eff}})^2}{(\eta_e+\eta_c)^2} - \left(v_e D_e^{\text{eff}} + v_c D_c^{\text{eff}}\right)^2 = 0$$

and, remembering that $b = q^2\delta^2(\Delta - \frac{\delta}{3})$, we can rewrite the logarithm of the normalized signal as

$$\begin{aligned}
\log\left(\frac{S(q,\mathbf{u_q})}{S(0,\mathbf{u_q})}\right) \approx & -b(v_e D_e^{\text{eff}} + v_c D_c^{\text{eff}}) \\
& + \frac{b^2 (D_e^{\text{eff}} - D_c^{\text{eff}})^2 \eta_e \eta_c}{15\delta^4\left(\Delta - \frac{\delta}{3}\right)^2(\eta_e+\eta_c)^8}\Bigg(-120 + 60e^{-(\eta_e+\eta_c)T_E} + 60\delta^2(\eta_e+\eta_c)^2 \\
& \quad + 120\big(\delta(\eta_e+\eta_c)+1\big)e^{-(\eta_e+\eta_c)\delta} + 120\big(\delta(\eta_e+\eta_c)-1\big)e^{-(\eta_e+\eta_c)\Delta} \\
& \quad + 60\big(\delta^2(\eta_e+\eta_c)^2 - 2\delta(\eta_e+\eta_c)+1\big)e^{-(\eta_e+\eta_c)(\Delta-\delta)} \\
& \quad - 40\delta^3(\eta_e+\eta_c)^3 + 15\delta^4\Delta(\eta_e+\eta_c)^5 - 9\delta^5(\eta_e+\eta_c)^5\Bigg) + O(b^3).
\end{aligned}$$

Then using the equations (3.28) and (3.29) we recover that the Kurtosis term is exactly the one in (3.30). □

Remark 3.3.2. *If we make the substitution*

$$\eta_e = \frac{k v_c}{T_e} \quad \textit{and} \quad \eta_c = \frac{k v_e}{T_e},$$

where $k = \frac{T_e}{\tau_{ex}}$, *and* $\tau_{ex} = \tau_c v_e$ *is the intra-cellular resident time multiplied by the external volume fraction (see [116]), and we take the limit for* $\delta \to 0$ *(narrow pulse hypothesis) we obtain the*

well known kurtosis term for the Kärger model which is

$$\frac{6v_e v_c \left(D_e^{eff} - D_c^{eff}\right)^2}{(v_e D_e^{eff} + v_c D_c^{eff})^2} \frac{\left(k - 1 + e^{-k}\right)}{k^2}.$$

We have thus shown that under the narrow pulse hypothesis the Kurtosis term that we computed analytically for FPK method reduces to the well known Kärger one. Hence we have proved that there exist a constant C such that

$$|S^{\mathrm{FPK}}(b) - S^{\mathrm{KAR}}(b)| \leqslant Cb^2\,.$$

3.4 Numerical results

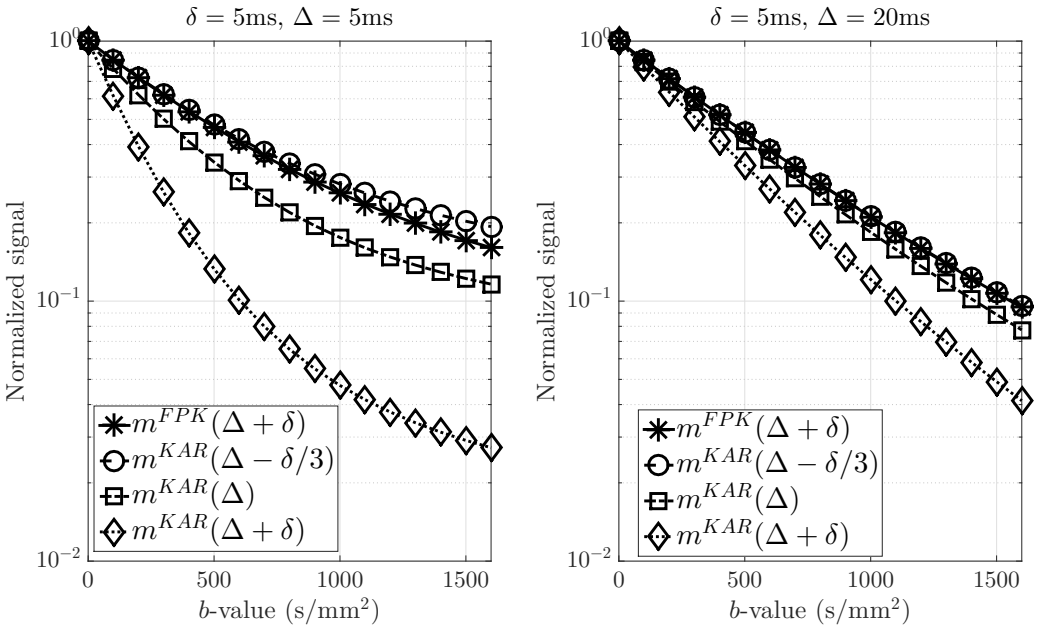

Figure 3.1 – DMRI signals given by FPK model and by the Kärger model at three different evaluation times, $\delta = 5$ms, left: $\Delta = 5$ms, right: $\Delta = 20$ms, for various b-values.

We provide numerical validation of our results of the previous section using a two compartments example. The parameters of the FPK and Kärger models come from a simple tissue geometry consisting of cylindrical biological cells, with the diffusion-encoding direction being transverse to the cylinder axes. The first compartment is the cylindrical cells compartment and the second compartment is the extra-cellular space. For details on how to obtain FPK and Kärger model parameters using homogenization, we refer to reader to [42]. Here, we only give the values of these parameters:

$$D_e^{\mathrm{eff}} = 1.7 \times 10^{-3}\mathrm{mm}^2/\mathrm{s},\ D_c^{\mathrm{eff}} = 0\mathrm{mm}^2/\mathrm{s},\ \kappa = 5 \times 10^{-5}\mathrm{m/s},\ q = 5 \times 10^{-5}\mu\mathrm{m}^{-1}\mathrm{ms}^{-1}$$
$$v_e = 0.72,\ |\Gamma| = 1.8842\mu\mathrm{m}^2,\ \eta_e = 1.3 \times 10^{-1}\mathrm{ms}^{-1},\ \eta_c = 3.34 \times 10^{-1}\mathrm{ms}^{-1}.$$

We compute the dMRI signal given by the FPK model and the total magnetization of the Kärger model evaluated at three different times: $t = \Delta$, $t = \Delta + \delta$, and $t = \Delta - \delta/3$, for several b-values (defined in (3.6)). In Figure 3.1 we see that for both $\Delta = 5$ms and $\Delta = 20$ms the Kärger signal evaluated at $t = \Delta - \frac{\delta}{3}$ is much closer to S^{FPK} over the entire range of the b-values considered than the other two choices.

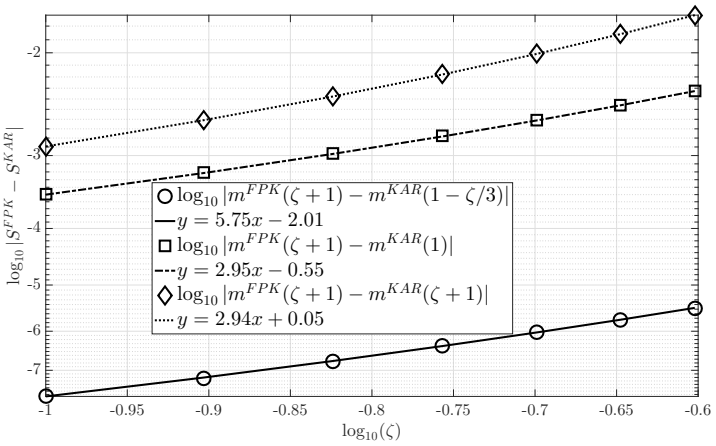

Figure 3.2 – The convergence of $m^{\mathrm{KAR}}(\Delta - \delta/3)$, $m^{\mathrm{KAR}}(\Delta + \delta)$ and $m^{\mathrm{KAR}}(\Delta)$ to S^{FPK} as $\zeta = \delta/\Delta$ goes to 0. $q = 1 \times 10^{-5}\mu\mathrm{m}^{-1}\mathrm{ms}^{-1}$, $\Delta = 20$ms, for various $\delta \in [1.5, 5]$ms.

Next we verify numerically the order of convergence with respect to the dimensionless parameter $\zeta = \delta/\Delta$. We fix $\Delta = 20$ms and vary δ in the interval $[2, 5]$ms. In Figure 3.2 we see that $m^{\mathrm{KAR}}(\Delta - \delta/3)$ converges to S^{FPK} with order 6, whereas $m^{\mathrm{KAR}}(\Delta + \delta)$ and $m^{\mathrm{KAR}}(\Delta)$ converge to S^{FPK} with order 3.

3.4.1 Trapezoidal PGSE

In this section we want to give an intuition of what happens if we consider as time profile a trapezoidal PGSE instead of the standard rectangular PGSE, i.e. if we have that the rise time of the pulse is not instantaneous (which is the case in the experimental situations). To support this argument we will provide some numerical results. We remind that the profile of the trapezoidal PGSE is

$$f(t) := \begin{cases} \dfrac{t - t_0}{T} & \text{if } t_0 \leqslant t < t_0 + T \\ 1 & \text{if } t_0 + T \leqslant t < t_0 + \delta - T \\ -\dfrac{t - t_0 - \delta}{T} & \text{if } t_0 + \delta - T \leqslant t < t_0 + \delta \\ -\dfrac{t - t_0 - \Delta}{T} & \text{if } t_0 + \Delta \leqslant t < t_0 + \Delta + T \\ -1 & \text{if } t_0 + \Delta + T \leqslant t < t_0 + \Delta + \delta - T \\ \dfrac{t - t_0 - (\Delta + \delta)}{T} & \text{if } t_0 + \Delta + \delta - T \leqslant t < t_0 + \Delta + \delta \\ 0 & \text{otherwise} \end{cases},$$

where $T = c\,\delta$ (with $c \in]0, 0.5]$) is the rise time. See Figure 3.3.

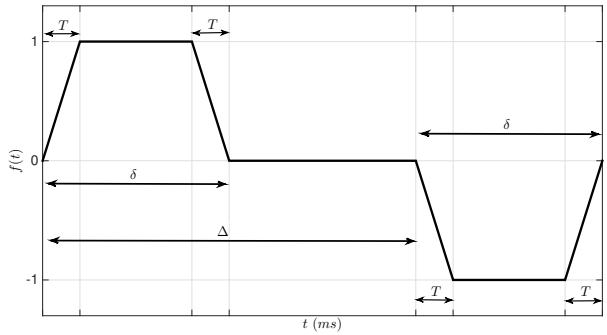

Figure 3.3 – Trapezoidal time profile

First of all we observe that, using this time profile, the b-value becomes

$$b(q,c,\delta,\Delta) = q^2\delta^2\left[(1-c)^2\Delta + \left(\frac{8}{15}c^3 - \frac{7}{6}c^2 + c - \frac{1}{3}\right)\delta\right]. \tag{3.32}$$

Furthermore as the rectangular PGSE is a particular case of trapezoidal profile when $c \to 0$, we observe that if we take this limit we obtain the b-value defined in (3.6).

As for the previous case, the first idea was to evaluate the solution of the Kärger model in

$$t_1^{\mathrm{KAR}} = (1-c)^2\Delta + \left(\frac{8}{15}c^3 - \frac{7}{6}c^2 + c - \frac{1}{3}\right)\delta \tag{3.33}$$

which is the term that we need to get the b-value in the exponent of (3.8). As we can see in Figure 3.4 if we use this time for the evaluation we obtain an order of convergence equal to 4 in the dimensionless parameter $\zeta = \frac{\delta}{\Delta}$ instead of the expected order 6 that we have obtained before.

Furthermore, analysing the new time-profile we notice that

$$\lim_{\delta\to 0}\frac{1}{\delta}\int_0^t f(s)\,ds = F_c(t) = \begin{cases} 1-c & 0 \leqslant t \leqslant \Delta \\ 0 & t > \Delta \end{cases}$$

which is different than the limit that we have found for the rectangular PGSE. Indeed for $t \in [0,\Delta]$, instead of 1 the limit is equal to $1-c$. Besides, if we look carefully at the expression (3.32), we find that the square of this term is a constant in front of Δ which was not the case in (3.6). Indeed, in (3.6) Δ has 1 as factor. The idea is then to incorporate this quantity with δ and consider $\delta^2(1-c)^2$ as an unique term and thus change also the expression of the Kärger model using $\delta^2(1-c)^2$ instead of δ^2 in the equations. With this choice the Kärger model for two compartments becomes

$$\begin{cases} \dfrac{d}{dt}m_e^{\mathrm{KAR}}(t) + q^2\delta^2(1-c)^2 D_e^{\mathrm{eff}} m_e^{\mathrm{KAR}}(t) + \eta_e m_e^{\mathrm{KAR}}(t) - \eta_c m_c^{\mathrm{KAR}}(t) = 0 \\ \dfrac{d}{dt}m_c^{\mathrm{KAR}}(t) + q^2\delta^2(1-c)^2 D_c^{\mathrm{eff}} m_c^{\mathrm{KAR}}(t) + \eta_c m_c^{\mathrm{KAR}}(t) - \eta_e m_e^{\mathrm{KAR}}(t) = 0 \\ m_e^{\mathrm{KAR}}(0) = v_e\,; \quad m_c^{\mathrm{KAR}}(0) = v_c \end{cases} . \tag{3.34}$$

As an obvious consequence we also have that the analytic expression of the solution is different. In particular in the exponent of (3.8) we already have $\delta^2(1-c)^2$ no matter which point of evaluation we consider. So, following the same idea of the previous sections, the time of evaluation to obtain the maximum order of convergence between the two models, should be

$$t^{\mathrm{KAR}} = \Delta + \Big(\frac{8}{15}c^3 - \frac{7}{6}c^2 + c - \frac{1}{3}\Big)\frac{\delta}{(1-c)^2}. \tag{3.35}$$

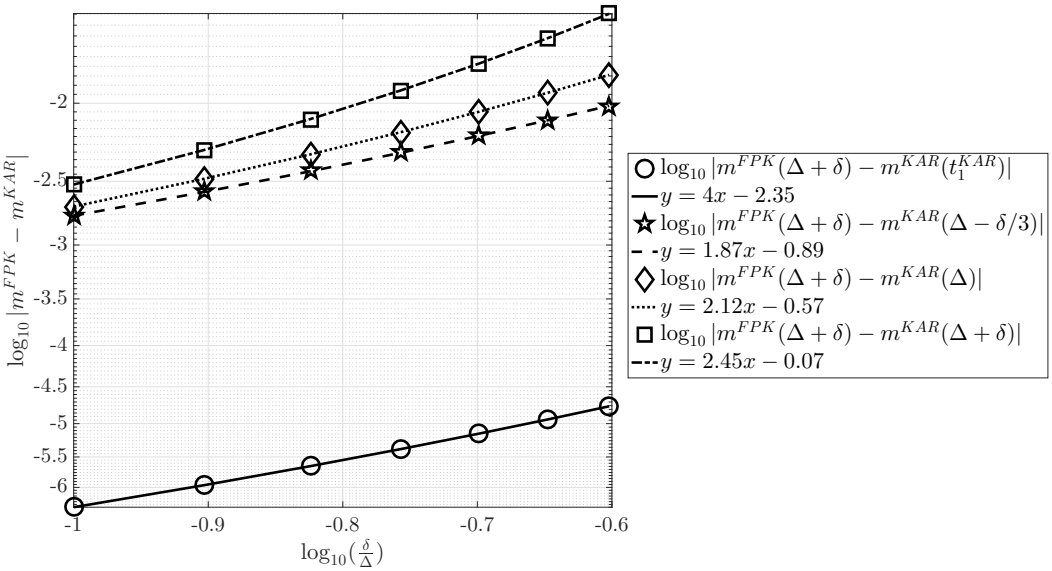

(a) Usual Kärger Model (3.7)

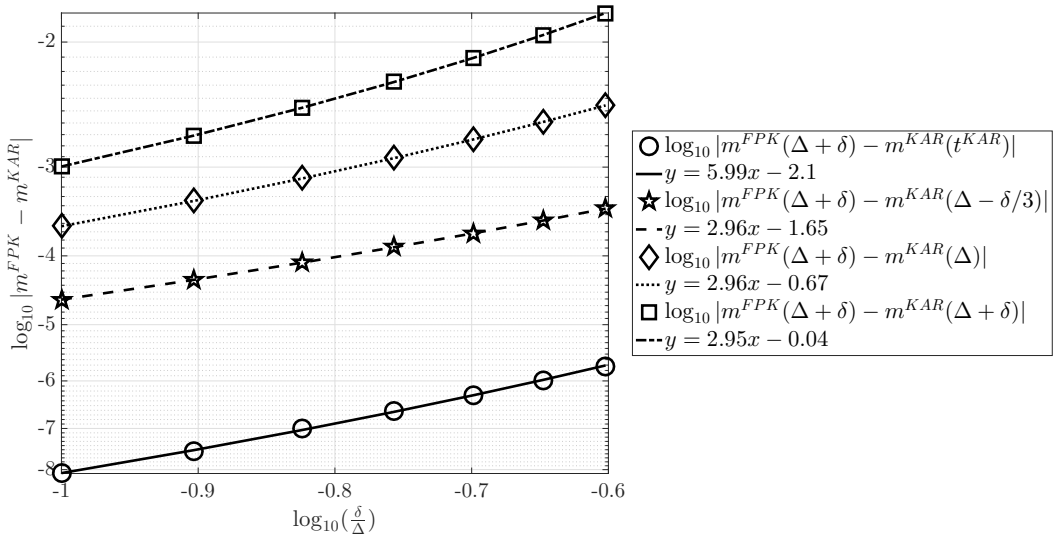

(b) Modified Kärger Model (3.34)

Figure 3.4 – Different orders of convergence of FPK signal to Kärger signal depending on the choice of echo-time for Kärger model in the case of trapezoidal time profile

In Figure 3.4 are shown the results of our simulations for the same geometry and physical parameters as before but with the new time profile. As we can see in Figure 3.4a, if we consider the standard Kärger model and FPK, we obtain an order of convergence 2 in ζ, if we evaluate the Kärger model in Δ, $\Delta + \delta$ or $\Delta - \delta/3$, and an order 4 if we evaluate in t_1^{KAR}. In contrast, Figure 3.4b shows that if we modify the Kärger model using the form (3.34), we obtain an order 3 if we evaluate in Δ, $\Delta + \delta$ or $\Delta - \delta/3$, and the expected order 6 if we evaluate at the suggested time t^{KAR}. These results are the analogous, in the case of trapezoidal time profile, of the ones in Theorem 3.3.1. The analytical proof of these results should be done in the same way as Theorem 3.2.2 with the only difference that one should expand the magnetizations in six time intervals and not three as before, because the trapezoidal time profile changes its expression six time in the interval $[0, \Delta + \delta]$.

3.5 Conclusions

By expanding the solutions of the Kärger and the FPK models we showed that in the case of finite pulses (when the duration of the gradient pulses is not short compared to the delay between the start of the pulses) the time at which to evaluate the Kärger model should be the time delay between the start of the pulses, shortened by one third of the pulse duration. We showed that with this choice, the convergence of the Kärger model to the FPK model is of order six in the pulse duration. This result helps to clarify the long standing question of how to adapt the Kärger model to account for finite diffusion-encoding pulse sequences.

To strengthen this result we also derived an analytic Kurtoris formula for the FPK model and we showed its convergence to the Kärger one which was already known in literature. Moreover we gave an idea of what should be done in the case of trapezoidal PGSE which is a more realistic time profile for the experiments and we provided a numerical proof for this result.

Chapter 4

New homogenized model of time-dependent ADC (H-ADC)

Contents

4.1 Problem setting . . . 74
4.1.1 Bloch-Torrey equation . . . 75
4.1.2 Periodicity length . . . 76
4.2 An asymptotic model . . . 77
4.2.1 Transformed Bloch-Torrey equation . . . 77
4.2.2 Choice of scaling . . . 78
4.2.3 Asymptotic model corresponding to $\alpha = \gamma = 2$ . . . 80
4.2.4 Asymptotic dMRI signal model and its ADC . . . 82
4.3 Numerical results . . . 84
4.3.1 Convergence . . . 85
4.3.2 Time-dependent ADC . . . 85
4.4 Comparison between the new asymptotic model and the linearized model 88
4.4.1 Convergence . . . 91
4.5 Conclusions . . . 94

In Section 2.1.5 we have seen that an important quantity in dMRI is the apparent diffusion coefficient (ADC) or effective diffusion coefficient (D^{eff}) and it is usually obtained by measuring S for a given gradient direction $\mathbf{u_g}$ at several b-values and fitting the following formula:

$$\log S(T_E) = \log S_0 - (ADC)b, \tag{4.1}$$

where S_0 is the dMRI signal when $b = 0$. We remark again that, $ADC = \mathcal{D}_0$ in the case of free diffusion (i.e. the effective diffusion coefficient is equal to the intrinsic diffusion coefficient).

In the context of dMRI brain tissue diffusion is not free, and this is evidenced by the fact that the fitted ADC depends on the applied gradient strength g, its direction $\mathbf{u_g}$, the diffusion time and the duration of the pulses. Thus, it is hoped that a signal model more accurate and complicated than (4.1) would provide additional information on the tissue microstructure. As a consequence, there have been many proposed extensions to (4.1), formulated heuristically, by dMRI researchers. For example, the dMRI signal as a sum of multiple exponentials was proposed in [39, 124, 132, 136], a term that is $O(\gamma^4 g^4 \delta^4 (\Delta - \delta/3)^2)$ was added to (4.1) in [34, 88], and fractional order diffusion was used in [24, 122, 123]. In [192], the signal model is an integral of a continuum of Gaussian diffusion groups, each with a different effective diffusion coefficient. In [140] the signal model is an expansion in a perturbation of the mean diffusivity. The models of [8, 89, 168] separate the cylindrical-shaped axons and dendrites from the space outside them to

make two diffusion compartments and assume there is no water exchange between them. The Kärger model [94] supposes multiple Gaussian diffusion compartments, where the water exchange between the compartments is described by simple constant rate terms that can be added to the diffusion terms, and these assumptions enable the formulation of a system of coupled ordinary differential equations (ODEs) that describes the time evolution of the total magnetization in the different compartments.

The previously mentioned models can be characterized as phenomenological models that incorporate certain physical assumptions and insights about the spatial and time scales of water diffusion in a complex geometrical environment. On the other hand, one can also proceed mathematically starting from a detailed and accurate description using partial differential equations (PDEs). The Bloch-Torrey PDE [180], introduced in Chapter 2, can be used to describe the water proton magnetization at all spatial positions in a voxel once the positions and shapes of the biological cells and the permeability of the cell membranes are prescribed. Obviously, this very accurate microscopic description cannot be used as a practical model of the dMRI signal because its inputs - the complete geometrical description of the biological cells in a voxel and its immediate neighbours - are too complicated compared to the physically obtainable data. This is the motivation for formulating asymptotic models from the Bloch-Torrey PDE.

In Chapter 2 we have seen that two simple asymptotic models for PGSE and narrow pulse approximation are the following. In the short-time limit (defined in Section 2.1.2), where only a small fraction of random walkers have encountered the membrane, the signal model given in [138], which is a general case of the formula in [130], is

$$\log S_{short}(T_E) := \log S_0 + ADC_{short}(\Delta) q^2 \delta^2(\Delta), \tag{4.2}$$

where $q = ||\gamma \mathbf{g}||$ [1] and the diffusion time dependent effective diffusion coefficient $ADC_{short}(\Delta)$ in the presence of multiple geometrical sub-domains Y_j, each with boundary Γ_{jk} and intrinsic diffusion coefficient $\mathcal{D}_0^j$, is

$$ADC_{short}(\Delta) := \sum_j v_j D^j_{short}(\Delta), \tag{4.3}$$

where v_j is the volume fraction of sub-domain Y_j and

$$D^j_{short}(\Delta) := \mathcal{D}_0^j \left[1 - \frac{|\Gamma_j|}{d|Y_j|} \left(\frac{4\sqrt{\mathcal{D}_0^j \Delta}}{3\sqrt{\pi}} - \kappa \Delta \right) \right], \tag{4.4}$$

d being the space dimension, and κ is the membrane permeability.

In the long time limit (defined in Section 2.1.2), when the diffusion becomes effectively Gaussian, the signal model is exponential:

$$\log S_{long} := \log S_0 - (\mathbf{u_g}^T \overline{ADC}_\infty \mathbf{u_g}) q^2 \delta^2 (\Delta - \delta/3), \tag{4.5}$$

where $\overline{ADC}_\infty \in \mathbb{R}^d \times \mathbb{R}^d$ is the long time apparent diffusion tensor. It was shown in [37] that in the case of periodic media, where $Y = \prod_{i=1\cdots d}[0, L_i]$ is a periodicity box of the medium, then

$$\left(\overline{ADC}_\infty\right)_{il} := \frac{1}{|Y|} \sum_j \int_{Y_j} \mathcal{D}_0^j(\mathbf{x}) \nabla u_i^j(\mathbf{x}) \cdot \mathbf{e}_l \, d\mathbf{x}, \tag{4.6}$$

1. It is important to note again that for us q does not denote a wave vector, as it often does in physics.

where the functions $u_i^j(\mathbf{x})$, $i = 1, \ldots, d$, are defined piecewise on Y_j and satisfy the time independent PDE:

$$\begin{aligned}
\operatorname{div}\left(\mathcal{D}_0^j(\mathbf{x})\nabla u_i^j(\mathbf{x})\right) &= 0 && \text{in } Y_j,\\
\mathcal{D}_0^j(\mathbf{x})\nabla u_i^j(\mathbf{x})\cdot\nu - \mathcal{D}_0^k(\mathbf{x})\nabla u_i^k(\mathbf{x})\cdot\nu &= 0 && \text{on } \Gamma_{jk},\\
\mathcal{D}_0^j(\mathbf{x})\nabla u_i^j(\mathbf{x})\cdot\nu &= \kappa(u_i^j(\mathbf{x}) - u_i^k(\mathbf{x})) && \text{on } \Gamma_{jk},\\
u_i^j(\mathbf{x} + L_i\mathbf{e}_i) &= u_i^j(\mathbf{x}) + L_i && \text{on } \partial Y,\\
u_i^j(\mathbf{x} + L_l\mathbf{e}_l) &= u_i^j(\mathbf{x}), \quad l \neq i, && \text{on } \partial Y,
\end{aligned} \tag{4.7}$$

If Y only contains simple geometries such as cubes and spheres, analytic formulae for $\overline{ADC}_\infty$ have been formulated in [77, 102, 175, 179].

As we have already mentioned in the previous chapters in [42] Coatléven *et al.* derived an asymptotic model from the Bloch-Torrey equation using periodic homogenization techniques by choosing a particular scaling of time, the membrane permeability, the diffusion-encoding gradient amplitude, and a periodicity length of the medium. The resulting model is valid for long diffusion times when the signal may nevertheless exhibit a non-Gaussian behavior due to water exchange between the sub-domains. The assumption of low membrane permeability means the exchange is governed by linear kinetics and gives the signal model a particularly simple form as the solution of a system of coupled ordinary differential equations. Indeed, in Chapter 3 we showed that this model generalizes the Kärger model, which was a dMRI signal model formulated heuristically by physicists for long diffusion times, but which is subject to the restriction that the duration of the pulses of a diffusion-encoding sequence is much shorter than the delay between the pulses. In contrast to the Kärger model, the model in [42] is not restricted to the case where the pulse duration is small. For this reason it was named Finite-Pulse Kärger (FPK) model.

A deficiency of the Kärger and the FPK signal models is that they do not reproduce the experimentally observed (see for example [160] and the references contained therein) dependence of the *ADC* on Δ (and δ in the non-narrow pulse case).

For this reason, in this Chapter, we chose a different scaling than that used to derive the FPK model and we derived a new asymptotic dMRI signal model whose *ADC* depends on the duration of the pulses and the time delay between them, again using periodic homogenization. We numerically validate, in some two-dimensional geometries and using PGSE sequence, that the *ADC* of the new asymptotic model is a good approximation of the *ADC* of the Bloch-Torrey PDE description over a wide range of Δ and δ. We note that even though our new asymptotic model is derived using periodic homogenization, the use of the model is not limited to periodic domains. We cite the non-periodic homogenization approach in porous media [4, 5], where the difference between the periodic and the non-periodic cases is in the definition and interpretation of the macroscopic model coefficients.

Our new asymptotic model requires the solution of several homogeneous diffusion equations with source terms defined on the biological cell membranes. Unlike in [42], we could not put this model in the form of a system of coupled ODEs. However, as we will see in Chapter 6 this model can be further simplified since homogeneous diffusion equations with boundary sources terms has some different expansions. We believe that a mathematical homogenization approach is a useful complement to the phenomenological approach used by physicists, as seen

by the FPK model of [42], formulated by homogenization, that elucidates and generalizes the phenomenological Kärger model. The novel result of this work is a time-dependent *ADC* model that can lend itself to systematic mathematical analysis. In Chapter 6 we will see that it is possible to obtain a characterization of the time-dependent *ADC* in terms of tissue-related quantities such as the average surface to volume ratio and the dominant Neumann Laplace eigenfunctions of the biological cells that are contained in an imaging voxel. The ultimate goal is of course the estimation of these tissue-related quantities from the measured dMRI signal.

This Chapter contains the results showed in our published paper [73] but we also add a derivation of the same model through linearization and a mathematical proof of convergence between the signal of new model and the signal obtained solving the Bloch-Torrey equation. The Chapter is organized as follows. In Section 4.1 we introduce the Bloch-Torrey PDE that describes the complex transverse water proton magnetization due to diffusion-encoding magnetic field gradient pulses and pose the problem on the microscopic scale in a heterogeneous domain. For simplicity, we make the hypothesis that the domain to be modelled is periodic, which allows us to apply periodic homogenization theory. In Section 4.2 we make the formal homogenization of our model problem in the periodic context, using a particular choice of scaling in the non-dimensional parameter ε for the time, the biological cell membrane permeability, the diffusion-encoding magnetic field gradient strength, and the periodicity length of the cellular geometry. We give the description of our asymptotic dMRI signal model and its *ADC*. In Section 4.3 we numerically validate the asymptotic model for some two dimensional geometrical configurations. We show the convergence for both the signal and the *ADC*. We then show that the *ADC* of our new model is a good approximation of the *ADC* of the reference model (the microscopic description using the Bloch-Torrey PDE) over a wide range of times. In Section 4.4 we show how to derive the new model using a different technique (linearization using the product between the gradient strength and the integral of the time profile small, along with a small permeability) and we prove that the convergence between the solution of the Bloch-Torrey PDE and this new approximation is of order $O(\varepsilon^3)$. Section 4.5 contains our conclusions.

4.1 Problem setting

For a volume $\Omega \subset \mathbb{R}^d$ of biological tissue, we denote by $\Gamma_I \subset \mathbb{R}^{d-1}$ the union of the boundaries of biological cells, in other words, the cell membranes, in Ω. In this paper, we assume the cell membranes are represented as $(d-1)$-dimensional objects. The cell membranes Γ_I thus delimits two subdomains: the extra-cellular domain Ω_e (e for extra-cellular) and the intra-cellular domain Ω_c (c for cellular). The domain Ω_{ext} then represents the union of the extra-cellular and intra-cellular open domains:

$$\Omega_{ext} \equiv \Omega \backslash \Gamma_I \equiv \Omega_e \cup \Omega_c \,.$$

4.1.1 Bloch-Torrey equation

The complex transverse water proton magnetization M can be described by the following Bloch-Torrey PDE[180] with jump on Γ_I:

$$\begin{cases} \dfrac{\partial}{\partial t}M(\mathbf{x},t) + \imath q \mathbf{u_g}\cdot\mathbf{x} f(t) M(\mathbf{x},t) - \operatorname{div}(\mathcal{D}_0(\mathbf{x})\nabla M(\mathbf{x},t)) = 0 & \text{in } \Omega_{ext}\times]0,T[, \\ \mathcal{D}_0\nabla M\cdot\nu|_{\Gamma_I} = \kappa[\![M]\!]_{\Gamma_I} & \text{on } \Gamma_I\times]0,T[, \\ [\![\mathcal{D}_0\nabla M\cdot\nu]\!]_{\Gamma_I} = 0 & \text{on } \Gamma_I\times]0,T[, \\ M(\cdot,0) = M_{\text{ini}} & \text{in } \Omega_{ext}, \\ \text{and appropriate boundary conditions on } \partial\Omega_{ext}, \end{cases} \tag{4.8}$$

where ν is the exterior normal to Ω_c, $[\![\cdot]\!]_{\Gamma_I}$ is the jump (extra-cellular minus intra-cellular) on Γ_I, κ is the membrane permeability coefficient, $\imath$ is the imaginary unit, M_{init} is the initial magnetization. The physical meaning of the parameter q is $q = \|\gamma\mathbf{g}\|$, where γ is the gyromagnetic ratio of the water proton, $\mathbf{g}$ gives the amplitude and direction of the diffusion-encoding gradient, and $\mathbf{u_g} = \mathbf{g}/\|\mathbf{g}\| \in \mathbb{R}^d$ is the unit vector in the direction of $\mathbf{g}$.

For simplicity of notation, the microscopic scale diffusion is assumed to be isotropic, and hence it is described by an intrinsic diffusion coefficient $\mathcal{D}_0(\mathbf{x}) \in \mathbb{R}$, rather than a tensor. The case of the tensor can be treated in a similar way but with more cumbersome notation. The function $f(t)$ gives the time profile of the diffusion-encoding magnetic field gradient pulses. For the classic Pulsed Gradient Spin Echo (PGSE) sequence [172], simplified to include only the parameters relevant to diffusion (the imaging gradients are ignored),

$$f(t) = \begin{cases} 1 & t_s < t \leqslant t_s + \delta, \\ -1 & t_s + \Delta < t \leqslant t_s + \Delta + \delta, \\ 0 & \text{elsewhere,} \end{cases}$$

where t_s is the start of the first pulse and we made $f(t)$ negative in the second pulse to include the effect of the 180 degree spin reversal between the pulses. The time at which the signal is measured is called the echo time $T_E \geqslant \delta + \Delta$. For simplicity, since t_s does not play a role in the results of this paper, we set $t_s = 0$. For the same reason, we set $T_E = \delta + \Delta$ in this Chapter. The dMRI signal is then the total magnetization at $t = \delta + \Delta$:

$$S(T_E) = \int_V M(\mathbf{x}, \delta + \Delta) d\mathbf{x}, \tag{4.9}$$

where M is the solution of Eq. (4.8), and V is the voxel. We observe that, because the diffusion displacement in dMRI ($O(10\mu m)$) is usually very small compared to the size of the voxel ($O(1mm)$), the boundary conditions on $\partial\Omega_{ext}$ in 4.8 can be any appropriate artificial boundary conditions because the support of the solution will be away from $\partial\Omega_{ext}$ during the simulation time. The logarithm of the signal is usually plotted against a quantity called the b-value

$$b := q^2 \int_0^{\Delta+\delta} \left(\int_0^t f(s)\, ds \right)^2 dt = q^2\delta^2 \left(\Delta - \frac{\delta}{3} \right), \tag{4.10}$$

because in a homogeneous medium:

$$\log S(T_E) = \log S_0 - \mathcal{D}_0\, b. \tag{4.11}$$

The b-value is a very important quantity in dMRI because the b-values are usually kept constant across different experiments. For different choices of the duration of the pulses and the time delay between them, the values of q are adjusted according to 4.10 so that the same set of b-values is used to compute the dMRI signal. The range of b-values are usually chosen so that the signal attenuation, $S(T_E)/S_0$, varies in a physically detectable range. This range will depend on the application and tissue type (brain, heart, etc.).

In the case of PGSE to obtain the ADC from a dMRI experiment, one fixes the choice of Δ and δ, computes the necessary q's to obtain several b-values that give an attenuation $S(T_E)/S_0$ that is not too small (closer to 1 than to 0), and computes the slope of $\log S$ versus the b-values. To make the concept of the ADC mathematically rigorous, in Chapter 1 we choose the following definition:

$$ADC := -\frac{1}{\delta^2(\Delta - \delta/3)} \frac{\partial(\log S(T_E))}{\partial(q^2)}\bigg|_{q^2=0}, \tag{4.12}$$

where the analytical derivative of $\log S$ is taken at $q^2 = 0$ (while Δ and δ are fixed). We can write the derivative with respect to q^2 because, due to the symmetry of diffusion, only even powers of q appear in S. With this definition, we note that ADC may depend on $\mathbf{u_g}$ and time (Δ and δ). In the narrow pulse limit, in a heterogeneous medium, the physical meaning of ADC is that it is the mean squared distance travelled by water molecules (averaged over all starting positions) divided by 2Δ.

4.1.2 Periodicity length

We will use the techniques of periodic homogenization. This means we will assume that the volume to be modelled, Ω, can be described as a periodic domain: there exists a period εL_0, which represents the average size of a representative volume of Ω, and which is small compared to the size of Ω. For simplicity, we will assume the periodicity box is a cube. We define the normalized periodicity box to be $Y = [0, L_0]^d$ and let $Y = Y_e \cup Y_c$, where Y_e is the extra-cellular domain, Y_c is the intra-cellular domain. Y_c is an open set that may be made of several disconnected parts. We denote the boundary of Y_c by $\partial Y_c \equiv \Gamma_m$. We thus have

$$\Omega_e^\varepsilon = \bigcup_{\mathbf{z}\in\mathbb{Z}^d} \varepsilon(Y_e + \mathbf{z}L_0), \quad \Omega_c^\varepsilon = \bigcup_{\mathbf{z}\in\mathbb{Z}^d} \varepsilon(Y_c + \mathbf{z}L_0), \quad \Omega_{ext}^\varepsilon = \Omega_e^\varepsilon \cup \Omega_c^\varepsilon$$
$$\text{and} \quad \Gamma_m^\varepsilon = \partial\Omega_e^\varepsilon \backslash \overline{\partial\Omega} = \bigcup_{\mathbf{z}\in\mathbb{Z}^d} \varepsilon(\Gamma_m + \mathbf{z}L_0).$$

Of course, the diffusion coefficient will be assumed to be periodic as well, i.e., there exists $\hat{\mathcal{D}_0} \in L^\infty(Y)$ such that $\mathcal{D}_0(\mathbf{x}) = \hat{\mathcal{D}_0}(\frac{\mathbf{x}}{\epsilon})$, with

$$\hat{\mathcal{D}_0} = \begin{cases} \mathcal{D}_0^e & \text{in } Y_e \\ \mathcal{D}_0^c & \text{in } Y_c \end{cases}.$$

The most common and practical choice for $\mathcal{D}_0^e$ and $\mathcal{D}_0^c$ is to consider them both as constant so that $\hat{\mathcal{D}_0}$ is piecewise constant. With this more precise description of the domain, our reference

model can be rewritten as

$$\begin{cases} \frac{\partial}{\partial t} M_\varepsilon(\mathbf{x},t) + \imath q\, \mathbf{u_g}\cdot\mathbf{x} f(t) M_\varepsilon(\mathbf{x},t) - \operatorname{div}(\hat{\mathcal{D}}_{0\varepsilon}\nabla M_\varepsilon(\mathbf{x},t)) = 0 & \text{in } \Omega^\varepsilon_{ext}\times]0,T[, \\ \hat{\mathcal{D}}_{0\varepsilon}\nabla M_\varepsilon\cdot\nu|_{\Gamma^\varepsilon_m} = \kappa^\varepsilon [\![M_\varepsilon]\!]_{\Gamma^\varepsilon_m}, & \text{on } \Gamma_m\times]0,T[, \\ [\![\hat{\mathcal{D}}_{0\varepsilon}\nabla M_\varepsilon\cdot\nu]\!]_{\Gamma^\varepsilon_m} = 0, & \text{on } \Gamma_m\times]0,T[\\ M_\varepsilon(\cdot,0) = M_{\text{ini}} & \text{in } \Omega^\varepsilon_{ext}, \end{cases} \tag{4.13}$$

where $\hat{\mathcal{D}}_{0\varepsilon} = \hat{\mathcal{D}}_0(\frac{\mathbf{x}}{\varepsilon})$. Finally, we will assume that the time profile f belongs to $L^\infty(]0,T[)$ and that the initial data M_{ini} is defined on Ω independently of ε and it is constant in each compartment.

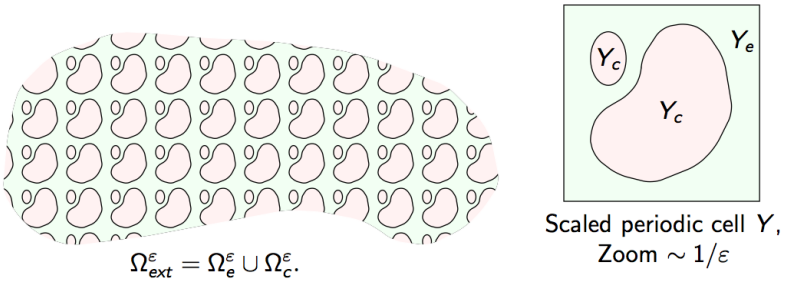

Figure 4.1 – Illustration of a periodic domain and the periodicity box Y.

4.2 An asymptotic model

In this section, we derive the new asymptotic model.

4.2.1 Transformed Bloch-Torrey equation

As was already observed in [42], M_ε does not satisfy the Bloch-Torrey equation in all Ω^ε_{ext}, but only in Ω^ε_e and Ω^ε_c separately with jump conditions on the interfaces. We transform the Bloch-Torrey equation by defining a new unknown $\widetilde{M}_\varepsilon$ almost everywhere on $\mathbb{R}^d\times]0,T[$ by

$$\widetilde{M}_\varepsilon(\mathbf{x},t) = M_\varepsilon(\mathbf{x},t) e^{\imath q\, \mathbf{u_g}\cdot\mathbf{x}\, F(t)},$$

where

$$F(t) := \int_0^t f(s)ds.$$

Multiplying the equations of the system (4.13) by $e^{\imath q \mathbf{u_g}\cdot\mathbf{x} F(t)}$ and using the definition of $\widetilde{M}_\varepsilon$, we obtain the following transformed PDE:

$$\begin{cases} \dfrac{\partial}{\partial t}\widetilde{M}_\varepsilon(\mathbf{x},t) - \operatorname{div}\big(\hat{\mathcal{D}}_{0\varepsilon}\nabla\widetilde{M}_\varepsilon(\mathbf{x},t) - \imath q\mathbf{u_g} F(t)\hat{\mathcal{D}}_{0\varepsilon}\widetilde{M}_\varepsilon(\mathbf{x},t)\big) \\ \qquad + \imath q\mathbf{u_g} F(t)\hat{\mathcal{D}}_{0\varepsilon}\nabla\widetilde{M}_\varepsilon(\mathbf{x},t) + q^2F(t)^2\hat{\mathcal{D}}_{0\varepsilon}\widetilde{M}_\varepsilon(\mathbf{x},t) = 0 & \text{in } \Omega^\varepsilon_{ext}\times]0,T[, \\ \hat{\mathcal{D}}_{0\varepsilon}\nabla\widetilde{M}_\varepsilon\cdot\nu - \imath q\mathbf{u_g}F(t)\hat{\mathcal{D}}_{0\varepsilon}\widetilde{M}_\varepsilon\cdot\nu = \kappa^\varepsilon[\![\widetilde{M}_\varepsilon]\!]_{\Gamma^\varepsilon_m} & \text{on } \Gamma^\varepsilon_m\times]0,T[, \\ [\![\hat{\mathcal{D}}_{0\varepsilon}\nabla\widetilde{M}_\varepsilon\cdot\nu - \imath q\mathbf{u_g}F(t)\hat{\mathcal{D}}_{0\varepsilon}\widetilde{M}_\varepsilon\cdot\nu]\!]_{\Gamma^\varepsilon_m} = 0 & \text{on } \Gamma^\varepsilon_m\times]0,T[, \\ \widetilde{M}_\varepsilon(\cdot,0) = M_{\text{ini}} & \text{in } \Omega^\varepsilon_{ext}. \end{cases} \tag{4.14}$$

4.2.2 Choice of scaling

As explained previously, we have chosen the scaling of the periodicity length to be:

$$L = \varepsilon L_0, \tag{4.15}$$

where L_0 has the unit of *length*. We note that ε is without dimension.

We keep the same scaling of the membrane permeability as was used in [42]:

$$\kappa = \varepsilon \kappa_0, \tag{4.16}$$

where κ_0 has the unit of *length/time*. Other scalings of permeability may be chosen (and lead to other asymptotic models), but because biological cell membranes impede the movement of water, the permeability should be "small". For a mathematical description of other possible choices for the permeability's scaling we refer to [41].

Now we come to the choice of the scaling of b, which depends on both q and time (through the values of the duration of the pulses and the delay between them). We set the scaling of time to be:

$$t = \varepsilon^\alpha \tau, \tag{4.17}$$

which in the case of PGSE implies

$$\delta = \varepsilon^\alpha \delta_0 \qquad \text{and} \qquad \Delta = \varepsilon^\alpha \Delta_0,$$

and F becomes

$$F_\varepsilon(t) = \varepsilon^\alpha F_0\left(\frac{t}{\varepsilon^\alpha}\right) = \varepsilon^\alpha F_0(\tau)\,.$$

We note that τ has the unit of *time*. We set the scaling of the gradient strength to be

$$q = \frac{q_0}{\varepsilon^\gamma}, \tag{4.18}$$

and q_0 has the unit of $\frac{1}{length \times time}$ [2]. In consequence, the scaling on b is

$$b = q^2 \int_0^{\Delta+\delta} F^2(t)dt = \frac{q_0^2}{\varepsilon^{2\gamma}} \varepsilon^{2\alpha} \delta_0^2 \left(\varepsilon^\alpha \Delta_0 - \frac{\varepsilon^\alpha \delta_0}{3}\right) = \varepsilon^{3\alpha - 2\gamma} b_0\,. \tag{4.19}$$

Before we choose the values of α and γ definitively, we use the periodic homogenization techniques [22], to develop $\widetilde{M}_\varepsilon$ using two-scale asymptotic expansions for Ω_e^ε and Ω_c^ε, along with the new time scaling, for general α and γ. We write

$$\widetilde{M}_\varepsilon(\mathbf{x}, t) = \begin{cases} \widetilde{M}_\varepsilon^e(\mathbf{x}, t) = \sum_{i=0}^{\infty} \varepsilon^i \widetilde{M}_{ie}(\mathbf{x}, \mathbf{y}, \tau) & \text{in } Y_e \\ \widetilde{M}_\varepsilon^c(\mathbf{x}, t) = \sum_{i=0}^{\infty} \varepsilon^i \widetilde{M}_{ic}(\mathbf{x}, \mathbf{y}, \tau) & \text{in } Y_c \end{cases} \tag{4.20}$$

2. Here γ is a positive exponent used to introduce a scaling on q and it should not be confused with the gyro-magnetic ratio introduced before.

where

$$\mathbf{y} = \frac{\mathbf{x}}{\varepsilon} \qquad \text{and} \qquad \tau = \frac{t}{\varepsilon^{\alpha}}$$

and the functions $\widetilde{M}_{ie}(\mathbf{x},\mathbf{y},\tau)$ and $\widetilde{M}_{ic}(\mathbf{x},\mathbf{y},\tau)$ are defined on $\Omega\times Y_e\times]0,T/\varepsilon^{\alpha}[$ and $\Omega\times Y_c\times]0,T/\varepsilon^{\alpha}[$ respectively, and the $\widetilde{M}_{ij}$ are assumed Y-periodic in $\mathbf{y}$. The aim of this ansatz is to obtain a new problem in which the different scales are linked.

To get the PDEs for each of the $\widetilde{M}_{ie}$ and the $\widetilde{M}_{ic}$, we start by noticing that for $j \in \{\, c, e \,\}$,

$$\frac{\partial}{\partial t}\widetilde{M}_{ij}(\mathbf{x},\mathbf{y},\tau) = \varepsilon^{-\alpha}\frac{\partial}{\partial \tau}\widetilde{M}_{ij}(\mathbf{x},\mathbf{y},\tau)\,,$$

$$\nabla\widetilde{M}_{ij}(\mathbf{x},\mathbf{y},\tau) = \nabla_{\mathbf{x}}\widetilde{M}_{ij}(\mathbf{x},\mathbf{y},\tau) + \varepsilon^{-1}\nabla_{\mathbf{y}}\widetilde{M}_{ij}(\mathbf{x},\mathbf{y},\tau),$$

and therefore

$$\begin{aligned}
\operatorname{div}\big(\mathcal{D}_0^j(\mathbf{y})\nabla\widetilde{M}_{ij}(\mathbf{x},\mathbf{y},\tau) - \imath q\mathbf{u_g}F(t)\mathcal{D}_0^j(\mathbf{y})\widetilde{M}_{ij}(\mathbf{x},\mathbf{y},\tau)\big) = \\
&+ \operatorname{div}_{\mathbf{x}}\big(\mathcal{D}_0^j(\mathbf{y})\nabla_{\mathbf{x}}\widetilde{M}_{ij}(\mathbf{x},\mathbf{y},\tau)\big) + \varepsilon^{-2}\operatorname{div}_{\mathbf{y}}\big(\mathcal{D}_0^j(\mathbf{y})\nabla_{\mathbf{y}}\widetilde{M}_{ij}(\mathbf{x},\mathbf{y},\tau)\big) \\
&+ \varepsilon^{-1}\Big(\operatorname{div}_{\mathbf{y}}\big(\mathcal{D}_0^j(\mathbf{y})\nabla_{\mathbf{x}}\widetilde{M}_{ij}(\mathbf{x},\mathbf{y},\tau)\big) + \operatorname{div}_{\mathbf{x}}\big(\mathcal{D}_0^j(\mathbf{y})\nabla_{\mathbf{y}}\widetilde{M}_{ij}(\mathbf{x},\mathbf{y},\tau)\big)\Big) \\
&- \varepsilon^{\alpha-\gamma}\operatorname{div}_{\mathbf{x}}\big(\imath q_0\mathbf{u_g}F_0(\tau)\mathcal{D}_0^j(\mathbf{y})\widetilde{M}_{ij}(\mathbf{x},\mathbf{y},\tau)\big) \\
&- \varepsilon^{\alpha-\gamma-1}\operatorname{div}_{\mathbf{y}}\big(\imath q_0\mathbf{u_g}F_0(\tau)\mathcal{D}_0^j(\mathbf{y})\widetilde{M}_{ij}(\mathbf{x},\mathbf{y},\tau)\big)\,.
\end{aligned}$$

Substituting these relations into the transformed Bloch-Torrey PDE 4.14 and using the ansatz in 4.20 we obtain the following PDE for $j \in \{\, c, e \,\}$:

$$\begin{aligned}
\sum_{i=0}^{\infty}\varepsilon^{i-\alpha}\frac{\partial}{\partial\tau}\widetilde{M}_{ij} + \varepsilon^{i+2\alpha-2\gamma}q_0^2\mathbf{u_g}\cdot\mathbf{u_g}F_0(\tau)^2\mathcal{D}_0^j\widetilde{M}_{ij} \\
&+ \varepsilon^{i+\alpha-\gamma}\imath q_0\mathbf{u_g}F_0(\tau)\mathcal{D}_0^j(\nabla_{\mathbf{x}}\widetilde{M}_{ij} + \varepsilon^{-1}\nabla_{\mathbf{y}}\widetilde{M}_{ij}) - \varepsilon^{i}\operatorname{div}_{\mathbf{x}}(\mathcal{D}_0^j\nabla_{\mathbf{x}}\widetilde{M}_{ij}) \\
&- \varepsilon^{i-1}\operatorname{div}_{\mathbf{x}}(\mathcal{D}_0^j\nabla_{\mathbf{y}}\widetilde{M}_{ij}) - \varepsilon^{i-1}\operatorname{div}_{\mathbf{y}}(\mathcal{D}_0^j\nabla_{\mathbf{x}}\widetilde{M}_{ij}) - \varepsilon^{i-2}\operatorname{div}_{\mathbf{y}}(\mathcal{D}_0^j\nabla_{\mathbf{y}}\widetilde{M}_{ij}) \\
&+ \varepsilon^{i+\alpha-\gamma}\operatorname{div}_{\mathbf{x}}(\imath q_0\mathbf{u_g}F_0(\tau)\mathcal{D}_0^j\widetilde{M}_{ij}) + \varepsilon^{i+\alpha-\gamma-1}\operatorname{div}_{\mathbf{y}}(\imath q_0\mathbf{u_g}F_0(\tau)\mathcal{D}_0^j\widetilde{M}_{ij}) = 0. \qquad (4.21)
\end{aligned}$$

To obtain the analogous conditions for the traces, for $\mathbf{x} \in \Gamma_m^{\varepsilon}$, we write the ansatz for the jumps of $\widetilde{M}_{\varepsilon}$ and its fluxes,

$$[\![\widetilde{M}_{\varepsilon}(\mathbf{x},t)]\!]_{\Gamma_m^{\varepsilon}} = \sum_{i=0}^{\infty}\varepsilon^{i}\Big(\widetilde{M}_{ie}(\mathbf{x},\mathbf{y},\tau) - \widetilde{M}_{ic}(\mathbf{x},\mathbf{y},\tau)\Big)\,, \qquad (4.22)$$

and

$$\begin{aligned}
[\![\hat{\mathcal{D}}_{0\varepsilon}\nabla\widetilde{M}_{\varepsilon}\cdot\nu - \imath q\mathbf{u_g}F\hat{\mathcal{D}}_{0\varepsilon}\widetilde{M}_{\varepsilon}\cdot\nu]\!]_{\Gamma_m^{\varepsilon}} = \\
&\sum_{i=0}^{\infty}\Big(\mathcal{D}_0^e\nabla\widetilde{M}_{ie}(\mathbf{x},\mathbf{y},\tau)\cdot\nu - \imath q_0\mathbf{u_g}F_0(\tau)\mathcal{D}_0^e\widetilde{M}_{ie}(\mathbf{x},\mathbf{y},\tau)\cdot\nu \\
&\qquad - \mathcal{D}_0^c\nabla\widetilde{M}_{ic}(\mathbf{x},\mathbf{y},\tau)\cdot\nu - \imath q_0\mathbf{u_g}F_0(\tau)\mathcal{D}_0^c\widetilde{M}_{ic}(\mathbf{x},\mathbf{y},\tau)\cdot\nu\Big)\,. \qquad (4.23)
\end{aligned}$$

The conditions for the traces, $j \in \{e, c\}$, are then

$$\sum_{i=0}^{\infty} \varepsilon^{i+1} \kappa_0 \left(\widetilde{M}_{ie} - \widetilde{M}_{ic} \right) = \varepsilon^{-1} \mathcal{D}_0^j \nabla_{\mathbf{y}} \widetilde{M}_{0j} \cdot \nu + \varepsilon^0 \left(\mathcal{D}_0^j \nabla_{\mathbf{y}} \widetilde{M}_{1j} + \mathcal{D}_0^j \nabla_{\mathbf{x}} \widetilde{M}_{0j} - \imath q_0 \mathbf{u_g} F_0 \mathcal{D}_0^j \widetilde{M}_{0j} \right) \cdot \nu + \sum_{i=1}^{\infty} \varepsilon^i \left(\mathcal{D}_0^j \nabla_{\mathbf{y}} \widetilde{M}_{i+1j} + \mathcal{D}_0^j \nabla_{\mathbf{x}} \widetilde{M}_{ij} - \imath q_0 \mathbf{u_g} F_0 \mathcal{D}_0^j \widetilde{M}_{ij} \right) \cdot \nu \,. \tag{4.24}$$

The initial conditions, for $j \in \{e, c\}$, are

$$\begin{aligned} \widetilde{M}_{0j}(\cdot, \cdot, 0) &= M_{\text{ini}} \\ \widetilde{M}_{ij}(\cdot, \cdot, 0) &= 0 \qquad \forall i \geqslant 1. \end{aligned}$$

As our purpose was to find an accurate approximation of the (time-dependent) *ADC* for low b-values, whose scaling is

$$b = \varepsilon^{\theta} b_0 \,, \tag{4.25}$$

where $\theta = 3\alpha - 2\gamma$, we require $\theta > 0$. We also need the time to be small since, if not, the effective diffusion would become Gaussian and therefore the *ADC* would not be time dependent. Hence we require that $\alpha > 0$.

Analyzing (4.21) we are led to choose α and γ so that the term $\varepsilon^{i+2\alpha-2\gamma} q_0^2 \mathbf{u_g} \cdot \mathbf{u_g} F_0^2 \mathcal{D}_0 \widetilde{M}_{ij}$ appears in the early values of i, since this is the term that contains quantities related to the b-value. The choice $\alpha = \gamma = 0$, which implies $b = O(1)$, was made in our previous work [42] which resulted in an *ADC* that is time independent. We then tried $\alpha = \gamma = 1$, which implies $b = O(\varepsilon)$, but this choice also led to an *ADC* that is time independent. This means that the scaling in b is not sufficiently small. We thus proceeded to the scaling $b = O(\varepsilon^2)$, which resulted from the choice:

$$\alpha = \gamma = 2 \,. \tag{4.26}$$

For this choice, the interesting term appears in the PDE for $\widetilde{M}_{2j}$, $j \in \{e, c\}$. In what follows, we thus fix the choice of α and γ to be that in Eq. (4.26) and derive the corresponding asymptotic model. Other scalings will be discussed in the next Chapter.

4.2.3 Asymptotic model corresponding to $\alpha = \gamma = 2$

We recall that the functions $\widetilde{M}_{ie}(\mathbf{x}, \mathbf{y}, \tau)$ and $\widetilde{M}_{ic}(\mathbf{x}, \mathbf{y}, \tau)$ are defined on $\Omega \times Y_e \times]0, T/\varepsilon^{\alpha}[$ and $\Omega \times Y_c \times]0, T/\varepsilon^{\alpha}[$ respectively, and the $\widetilde{M}_{ij}$ are assumed Y-periodic in $\mathbf{y}$. To produce our new asymptotic model up to $O(\varepsilon^2)$, we substitute $\alpha = \gamma = 2$ and match the terms in front of the same power of ε of 4.21. We then get the following periodicity box problems for the first three orders: $i = 0, 1, 2$.

The problem for $\widetilde{M}_{0j}$ is then given by

$$\begin{cases} -\operatorname{div}_{\mathbf{y}} \left(\mathcal{D}_0^j \nabla_{\mathbf{y}} \widetilde{M}_{0j} \right) + \dfrac{\partial}{\partial \tau} \widetilde{M}_{0j} = 0 & \text{in } Y_j \times]0, T/\varepsilon^{\alpha}[, \\ \mathcal{D}_0^j \nabla_{\mathbf{y}} \widetilde{M}_{0j} \cdot \nu = 0 & \text{on } \Gamma_m \times]0, T/\varepsilon^{\alpha}[, \\ \widetilde{M}_{0j}(\cdot, 0) = M_{\text{ini}} & \text{in } Y_j, \\ \widetilde{M}_{0j} \text{ is } Y\text{-periodic.} \end{cases} \tag{4.27}$$

Since the initial conditions is constant, we deduce that

$$\widetilde{M}_{0j} \equiv M_{\text{ini}}, \quad j \in \{e, c\}. \tag{4.28}$$

The periodic box problem for $\widetilde{M}_{1j}$ is

$$\begin{cases} -\mathrm{div}_{\mathbf{y}}\big(\mathcal{D}_0^j \nabla_{\mathbf{y}} \widetilde{M}_{1j} + \mathcal{D}_0^j \nabla_{\mathbf{x}} \widetilde{M}_{0j} - \imath q_0 \mathbf{u_g} F_0 \mathcal{D}_0^j \widetilde{M}_{0j}\big) = -\dfrac{\partial}{\partial \tau} \widetilde{M}_{1j} \\ \qquad\qquad - \imath q_0 \mathbf{u_g} F_0 \mathcal{D}_0^j \nabla_{\mathbf{y}} \widetilde{M}_{0j} + \mathrm{div}_{\mathbf{x}}\big(\mathcal{D}_0^j \nabla_{\mathbf{y}} \widetilde{M}_{0j}\big) & \text{in } Y_j \times]0, T/\varepsilon^\alpha[, \\ \mathcal{D}_0^j \nabla_{\mathbf{y}} \widetilde{M}_{1j} \cdot \nu + \mathcal{D}_0^j \nabla_{\mathbf{x}} \widetilde{M}_{0j} \cdot \nu - \imath q_0 \mathbf{u_g} F_0 \mathcal{D}_0^j \widetilde{M}_{0j} \cdot \nu = 0 & \text{on } \Gamma_m \times]0, T/\varepsilon^\alpha[, \\ \widetilde{M}_{1j}(\cdot, 0) = 0 & \text{in } Y_j, \\ \widetilde{M}_{1j} \text{ is } Y\text{-periodic}, \end{cases}$$

which, recalling that $\widetilde{M}_{0j}$ is a constant 4.28, simplifies to:

$$\begin{cases} -\mathrm{div}_{\mathbf{y}}\big(\mathcal{D}_0^j \nabla_{\mathbf{y}} \widetilde{M}_{1j} - \imath q_0 \mathbf{u_g} F_0 \mathcal{D}_0^j M_{\text{ini}}\big) = -\dfrac{\partial}{\partial \tau} \widetilde{M}_{1j} & \text{in } Y_j \times]0, T/\varepsilon^\alpha[\\ \mathcal{D}_0^j \nabla_{\mathbf{y}} \widetilde{M}_{1j} \cdot \nu - \imath q_0 \mathbf{u_g} F_0 \mathcal{D}_0^j M_{\text{ini}} \cdot \nu = 0 & \text{on } \Gamma_m \times]0, T/\varepsilon^\alpha[\\ \widetilde{M}_{1j}(\cdot, 0) = 0 & \text{in } Y_j \\ \widetilde{M}_{1j} \text{ is } Y\text{-periodic}. \end{cases} \tag{4.29}$$

It can be easily verified that $\widetilde{M}_{1j}$ is purely imaginary and the imaginary part of $\widetilde{M}_{1j}$, for each $j \in \{c, e\}$, can be decomposed into the sum of d functions, ω_l^j, $l = 1, \cdots, d$, where d is the spatial dimension,

$$\Im\left(\widetilde{M}_{1j}(\mathbf{x}, \mathbf{y}, \tau)\right) = \sum_{l=1}^{d} \left(q_0 M_{\text{ini}}\right) \omega_l^j(\mathbf{y}, \tau) \left(\mathbf{u_g} \cdot \mathbf{e}_l\right) \qquad \text{in } Y_j\,, \tag{4.30}$$

where the ω_l^j's do not depend on the gradient direction $\mathbf{u_g}$ or q_0 and are solutions of

$$\begin{cases} -\mathrm{div}_{\mathbf{y}}\big(\mathcal{D}_0^j \nabla_{\mathbf{y}} \omega_l^j - F_0 \mathcal{D}_0^j \mathbf{e}_l\big) = -\dfrac{\partial}{\partial \tau} \omega_l^j & \text{in } Y_j \times]0, T/\varepsilon^\alpha[, \\ \mathcal{D}_0^j \nabla_{\mathbf{y}} \omega_l^j \cdot \nu - F_0 \mathcal{D}_0^j \mathbf{e}_l \cdot \nu = 0 & \text{on } \Gamma_m \times]0, T/\varepsilon^\alpha[, \\ \omega_l^j(\cdot, 0) = 0 & \text{in } Y_j, \\ \omega_l^j \text{ is } Y\text{-periodic}. \end{cases}$$

Now we consider the periodicity box problem satisfied by $\widetilde{M}_{2j}$

$$\begin{cases} -\mathrm{div}_{\mathbf{y}}\big(\mathcal{D}_0^j \nabla_{\mathbf{y}} \widetilde{M}_{2j} + \mathcal{D}_0^j \nabla_{\mathbf{x}} \widetilde{M}_{1j} - \imath q_0 \mathbf{u_g} F_0 \mathcal{D}_0^j \widetilde{M}_{1j}\big) = -\dfrac{\partial}{\partial \tau} \widetilde{M}_{2j} & \text{in } Y_j \times]0, T/\varepsilon^\alpha[, \\ \qquad -q_0^2 F_0^2 \mathcal{D}_0^j \widetilde{M}_{0j} - \imath q_0 \mathbf{u_g} F_0 \mathcal{D}_0^j \nabla_{\mathbf{y}} \widetilde{M}_{1j} - \imath q_0 \mathbf{u_g} F_0 \mathcal{D}_0^j \nabla_{\mathbf{x}} \widetilde{M}_{0j} & \\ \qquad +\mathrm{div}_{\mathbf{x}}\big(\mathcal{D}_0^j \nabla_{\mathbf{y}} \widetilde{M}_{1j} + \mathcal{D}_0^j \nabla_{\mathbf{x}} \widetilde{M}_{0j} - \imath q_0 \mathbf{u_g} F_0 \mathcal{D}_0^j \widetilde{M}_{0j}\big) & \\ \mathcal{D}_0^j \nabla_{\mathbf{y}} \widetilde{M}_{2j} \cdot \nu + \mathcal{D}_0^j \nabla_{\mathbf{x}} \widetilde{M}_{1j} \cdot \nu - \imath q_0 \mathbf{u_g} F_0 \mathcal{D}_0^j \widetilde{M}_{1j} \cdot \nu = \kappa_0\big(\widetilde{M}_{0e} - \widetilde{M}_{0c}\big) & \text{on } \Gamma_m \times]0, T/\varepsilon^\alpha[, \\ \widetilde{M}_{2j}(\cdot, 0) = 0 & \text{in } Y_j, \\ \widetilde{M}_{2j} \text{ is } Y\text{-periodic}. \end{cases} \tag{4.31}$$

Recalling again that $\widetilde{M}_{0j} \equiv M_{\text{ini}}$ is constant in the whole domain, $\mathcal{D}_0^j$ is piecewise constant and $\widetilde{M}_{1j}$ is purely imaginary, we have that $\Im\left(\widetilde{M}_{2j}\right) = 0$ and using the the divergence theorem on the real part of Eq. (4.31) we obtain the compatibility condition for $\Re\left(\widetilde{M}_{2j}\right)$ ($j \in \{e, c\}$):

$$-\int_{Y_j} \frac{\partial}{\partial \tau} \Re\left(\widetilde{M}_{2j}\right) - \int_{Y_j} q_0^2 F_0^2 \mathcal{D}_0^j \widetilde{M}_{0j} + \int_{Y_j} q_0 \mathbf{u_g} F_0 \mathcal{D}_0^j \nabla_{\mathbf{y}} \Im\left(\widetilde{M}_{1j}\right) = 0\,.$$

Integrating in time we obtain

$$\int_{Y_j} \Re\left(\widetilde{M}_{2j}\right) = -q_0^2 \int_0^\tau F_0^2 \int_{Y_j} \mathcal{D}_0^j M_{\text{ini}} + q_0 \mathbf{u_g} \sum_{l=1}^{d} \int_0^\tau F_0 \int_{Y_j} \mathcal{D}_0^j \left(q_0 M_{\text{ini}}\right) \nabla_{\mathbf{y}} \omega_l^j \mathbf{u_g} \cdot \mathbf{e}_l\,. \tag{4.32}$$

We immediately remark that with the identical constant initial conditions for both compartments we lose the boundary term $\kappa_0(\widetilde{M}_{0e} - \widetilde{M}_{0c})$, which is the only information that we have on the membrane's permeability. This means that our model would not be applicable for situations where water exchange between the geometrical compartments is significant enough to affect the *ADC*, which is the first order moment with respect to q^2.

4.2.4 Asymptotic dMRI signal model and its *ADC*

In practice, in the case of PGSE, the dMRI signal is measured at $t = T_E = \Delta + \delta$, so our reference signal is

$$S_{ref}(q, \mathbf{u_g}) = \int M_\varepsilon(\mathbf{x}, T_E)\, d\mathbf{x}\,,$$

where M_ε is the solution of the Bloch-Torrey PDE (4.13). The volume of integration above is assumed large enough to contain the support of the solution (again, we remind that the voxel is large compared to diffusion displacement in dMRI). Then, remembering our ansatz (4.20) and the fact that we found the first three terms, the signal of our new asymptotic model inside the periodic box $|Y|$ is

$$\begin{aligned} S_{new}(q, \mathbf{u_g}) &:= \sum_{i=0}^{2} \varepsilon^i \Big(\int_{Y_e} \widetilde{M}_{ie}(\cdot, T_E/\varepsilon^2) + \int_{Y_c} \widetilde{M}_{ic}(\cdot, T_E/\varepsilon^2) \Big) \\ &= \int_{Y_e} \Big(M_{\text{ini}} + \varepsilon^2 \Re \widetilde{M}_{2e}(\cdot, T_E/\varepsilon^2) \Big) + \int_{Y_c} \Big(M_{\text{ini}} + \varepsilon^2 \Re \widetilde{M}_{2c}(\cdot, T_E/\varepsilon^2) \Big) \\ &= M_{\text{ini}} \left(|Y_e| + |Y_e| \right) + \int_{Y_e} \varepsilon^2 \Re \widetilde{M}_{2e}(\cdot, T_E/\varepsilon^2) + \int_{Y_c} \varepsilon^2 \Re \widetilde{M}_{2c}(\cdot, T_E/\varepsilon^2). \end{aligned} \tag{4.33}$$

We recall that $\widetilde{M}_{0j}(\mathbf{x}, \tau) = M_{\text{ini}}$ in Y_j for all τ and the real part of $\widetilde{M}_{1j}$ is equal to zero, $j \in \{e, c\}$. Thus, our new model approximates the reference model up to fourth order in ε (because the odd powers of ε are zero):

$$S_{ref}(q, \mathbf{u_g}) = S_{new}(q, \mathbf{u_g}) + O(\varepsilon^4).$$

Recalling Eq. (4.32), we define effective diffusion tensors in the geometrical compartments, $j \in \{c, e\}$, in the following way:

$$\left(\overline{D}_j^{\text{eff}}\right)_{il}(\tau) := \frac{1}{|Y_j|} \int_{Y_j} \mathcal{D}_0^j \left(\mathbf{e}_i \cdot \mathbf{e}_l - \frac{q_0^2 \int_0^\tau F_0 \frac{\partial}{\partial y_l} \omega_i^j}{b_0} \right), \quad i, l = 1, \ldots, d,$$

so that in more compact form,

$$\begin{aligned}\int_{Y_j} \Re\left(\widetilde{M}_{2j}\right) &= -q_0^2 \int_0^\tau F_0^2 \int_{Y_j} \mathcal{D}_0^j \, M_{\text{ini}} + q_0 \mathbf{u_g} \sum_{l=1}^{d} \int_0^\tau F_0 \int_{Y_j} \mathcal{D}_0^j q_0 M_{\text{ini}} \, \nabla_{\mathbf{y}} \omega_l^j \, (\mathbf{u_g} \cdot \mathbf{e}_l) \\ &= -M_{\text{ini}} b_0 \left(\int_{Y_j} \mathcal{D}_0^j - \mathbf{u_g} \sum_{l=1}^{d} \frac{q_0^2}{b_0} \int_0^\tau F_0 \int_{Y_j} \mathcal{D}_0^j \nabla_{\mathbf{y}} \omega_l^j \, (\mathbf{u_g} \cdot \mathbf{e}_l) \right) \\ &= -M_{\text{ini}} \, |Y_j| \, b_0 \, \overline{D}_j^{\text{eff}}(\tau) \mathbf{u_g} \cdot \mathbf{u_g} \, .\end{aligned}$$

Now we simplify the signal after the normalization

$$M_{\text{ini}} := \frac{1}{(|Y_c| + |Y_e|)},$$

$$S_{new}(q, \mathbf{u_g}) = 1 - \frac{\varepsilon^2 b_0 \, \left(|Y_c| \, \overline{D}_c^{\text{eff}}(\Delta_0 + \delta_0) + |Y_e| \, \overline{D}_e^{\text{eff}}(\Delta_0 + \delta_0) \right) \mathbf{u_g} \cdot \mathbf{u_g}}{(|Y_c| + |Y_e|)},$$

and put back the original variables,

$$S_{new}(q, \mathbf{u_g}) = 1 - b \, \frac{\left(|Y_c| \, \overline{D}_c^{\text{eff}}(\Delta + \delta) + |Y_e| \, \overline{D}_e^{\text{eff}}(\Delta + \delta) \right) \mathbf{u_g} \cdot \mathbf{u_g}}{(|Y_c| + |Y_e|)}, \tag{4.34}$$

where the effective diffusion tensors in compartment $j \in \{c, e\}$ are

$$\left(\overline{D}_j^{\text{eff}} \right)_{il}(t) := \frac{1}{|Y_j|} \int_{Y_j} \mathcal{D}_0^j \, \mathbf{e}_i \cdot \mathbf{e}_l - \frac{1}{\int_0^{\Delta+\delta} F^2} \int_0^t \left(F \frac{1}{|Y_j|} \int_{Y_j} \mathcal{D}_0^j \frac{\partial}{\partial y_l} \omega_i^j \right), \; i, l = 1, \ldots, d, \tag{4.35}$$

and the periodicity box problems to be solved are

$$\begin{cases} \dfrac{\partial}{\partial t} \omega_l^j - \operatorname{div}_{\mathbf{y}} \left(\mathcal{D}_0^j \nabla_{\mathbf{y}} \omega_l^j - F \mathcal{D}_0^j \mathbf{e}_l \right) = 0 & \text{in } Y_j \times]0, T[\\ \mathcal{D}_0^j \nabla_{\mathbf{y}} \omega_l^j \cdot \nu - F \mathcal{D}_0^j \mathbf{e}_l \cdot \nu = 0 & \text{on } \Gamma_m \times]0, T[, \\ \omega_l^j(\cdot, 0) = 0 & \text{in } Y_j, \\ \omega_l^j \text{ is } Y\text{-periodic.} \end{cases} \tag{4.36}$$

From this simplified expression we can identify the ADC_{new} for this new model as

$$ADC_{new} := v_e \overline{D}_e^{\text{eff}}(\Delta + \delta) \mathbf{u_g} \cdot \mathbf{u_g} + v_c \overline{D}_c^{\text{eff}}(\Delta + \delta) \mathbf{u_g} \cdot \mathbf{u_g}, \; v_c := \frac{|Y_c|}{|Y|} \, v_e := 1 - v_c, \tag{4.37}$$

where v_e and v_c are the extra-cellular and intra-cellular volume fractions respectively.

From (4.35) we immediately see that the definition of the effective diffusion tensor $\overline{D}_j^{\text{eff}}$, $j \in \{ e, c \}$, is dependent on Δ and δ. In particular, $\overline{D}_j^{\text{eff}}$ is defined as the sum of two terms: the first is the intrinsic diffusion coefficient, and the second depends on the magnetic field gradient time profile $f(t)$ (in addition to depending on the geometry) and is bounded between 0 and $\mathcal{D}_0^j$.

Our new asymptotic model matched terms up to and including $O(\varepsilon^2)$, and since by the choice of the scaling our b-value is also $O(\varepsilon^2)$, this means that our model explains first order effects of the b-value; it does not account for higher order effects of b.

4.3 Numerical results

In this section, we first validate the fourth order convergence of our model (see Equations (4.34), (4.35), (4.36)) in the signal and the second order convergence in the *ADC* (see Equation (4.37)) to the reference Bloch-Torrey model of Equation (4.13). Then we compare the *ADC* of our new model with the reference *ADC* as well as with two existing asymptotic models of the effective diffusion coefficient: the short time and long time models of (4.4) and (4.6).

In summary, the following quantities will be compared:

1. S_{ref} and ADC_{ref} from the reference Bloch-Torrey model.
2. S_{new} and ADC_{new} from our new asymptotic model.
3. ADC_{short}: the short time model of the effective diffusivity (4.4).
4. $\overline{D}_\infty \mathbf{u_g} \cdot \mathbf{u_g}$: the long time limit of the effective diffusivity (4.6).

The reference signal is the integral of the solution of (4.13) in a periodic geometry, where the domain is made up of copies of the periodicity box $Y = [0, L]^2$. As was already observed in [134], equivalently, one can obtain the reference signal by solving (4.14) subject to periodic boundary conditions on ∂Y. This was also our approach here. The initial condition M_{ini} is set to $M_{\text{ini}} = 1/L^2$ to normalize the signal to $S = 1$ at $b = 0$. The *ADC* of the reference signal was then obtained using a polynomial fit of the logarithm of the simulated signal at several b-values according to (4.12).

To obtain the signal due to our new asymptotic model (4.34) we solved the periodicity box problems (4.36) on Y. Then the *ADC* of our new model is computed according to (4.37).

To compute the long time model for the effective diffusivity according to (4.6), we solved the periodicity box problems (4.7).

The simulation of the reference model and the solution of the periodicity box problems were performed using FreeFem++ [155].

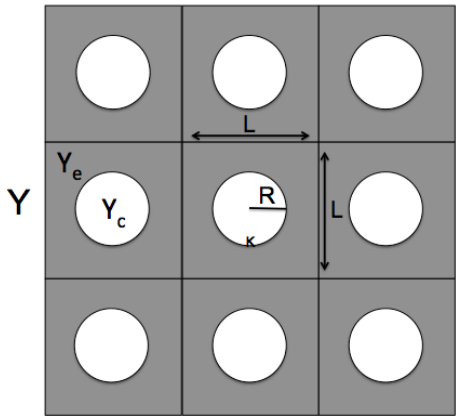

Figure 4.2 – Illustration of a periodic domain where there is a disk of radius R in the center of each periodicity box Y.

4.3.1 Convergence

We validate the convergence of the new model in a simple two-dimensional geometry. The periodicity box is $Y = [0, L]^2$, and we place in the center of Y a single disk of radius R (see 4.2). We fix L_0, κ_0, Δ_0, δ_0, and b_0 and vary ε while respecting the scalings:

$$L = \varepsilon L_0, \quad \kappa = \varepsilon \kappa_0, \quad \Delta = \varepsilon^2 \Delta_0, \quad \delta = \varepsilon^2 \delta_0 \quad q = \varepsilon^{-2} q_0.$$

We recall that the above choice implies the scaling of $b = O(\varepsilon^2)$ and $\Delta = O(L^2)$. We have chosen the gradient direction to be $\mathbf{u_g} = \mathbf{e}_x$. Furthermore, our choices of L_0, κ_0, Δ_0, δ_0, and b_0 are made in order to obtain physically reasonable parameters L, κ, Δ, δ, and b at $\varepsilon = 0.25$.

We obtained S_{ref} and S_{new} using a very fine finite element mesh for two disk radii: $R = 0.49\,L$ and $R = 0.4\,L$. The values of the intrinsic diffusivities, $\mathcal{D}_0^e = 3 \times 10^{-3} mm^2/s$, $\mathcal{D}_0^c = 1.6 \times 10^{-3} mm^2/s$, were chosen close to the values often used in the literature for dMRI numerical simulations [76, 190].

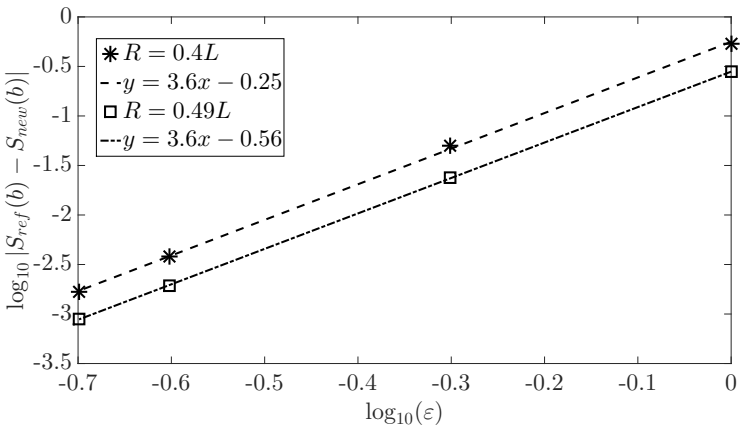

Figure 4.3 – Signal convergence for a single disk in a periodicity box with $\mathcal{D}_0^e = 3 \times 10^{-3} mm^2/s$, $\mathcal{D}_0^c = 1.6 \times 10^{-3} mm^2/s$, for two disk radii: $R = 0.49\,L$ and $R = 0.4\,L$. $L_0 = 20\mu m$, $\delta_0 = 8$ms, $\Delta_0 = 8$ms, $b_0 = 800$s/mm^2 and $\kappa_0 = 4 \times 10^{-5}$m/s.

In Fig. (4.3) we show the convergence of the signals $|S_{ref}(b) - S_{new}(b)|$ with the non-dimensional parameter ε for two different choices of R. We see that the convergence rate is about 4 (fitted to 3.6).

In Fig. (4.4) we show the convergence of the ADC with the non-dimensional parameter ε, where to compute the reference ADC, we use the linear fit:

$$ADC_{ref} \approx \frac{1 - S_{ref}(b)}{b}.$$

We see that the convergence rate is fitted to 1.6.

4.3.2 Time-dependent ADC

In this section we show some preliminary results on the ADC approximation of our new model (4.37) and compare with some other existing models.

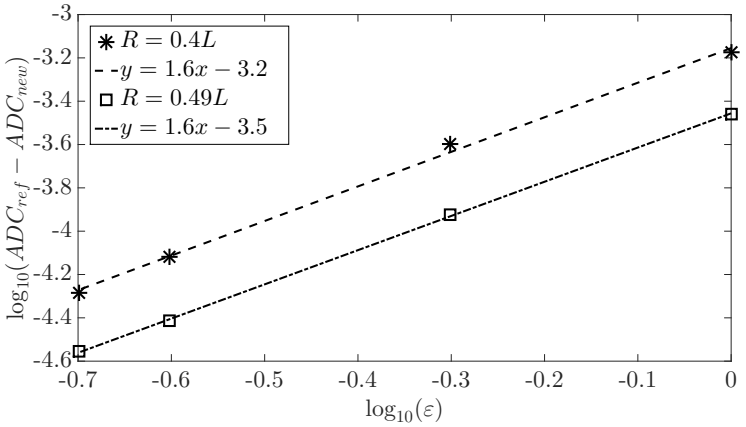

Figure 4.4 – *ADC* convergence for a single disk in a periodicity box with $\mathcal{D}_0^e = 3 \times 10^{-3} mm^2/s$, $\mathcal{D}_0^c = 1.6 \times 10^{-3} mm^2/s$, for two disk radii: $R = 0.49\,L$ and $R = 0.4\,L$. $L_0 = 20\mu m$, $\delta_0 = 8$ms, $\Delta_0 = 8$ms, $\kappa_0 = 4 \times 10^{-5}$m/s and fitted until $b_0 = 800\text{s/mm}^2$.

To compare the $ADCs$, we fixed $L = 5\mu m, \mathcal{D}_0^e = 3 \times 10^{-3} mm^2/s, \mathcal{D}_0^c = 1.6 \times 10^{-3} mm^2/s$ and $\kappa = 1 \times 10^{-5}$m/s and we varied δ and Δ over a wide range. The simulated (δ, Δ), expressed in ms, are $(1e^{-3}, 5e^{-3})$, $(1e^{-3}, 10e^{-3})$, $(1e^{-3}, 15e^{-3})$, $(0.3, 0.3)$, $(0.5, 0.5)$, $(1.0, 1.0)$, $(1.5, 1.5)$, $(2.5, 2.5)$, $(2.5, 5.0)$, $(2.5, 7.5)$, $(2.5, 10.0)$, $(2.5, 15.0)$, $(2.5, 20.0)$, $(2.5, 40.0)$, and $(2.5, 80.0)$. The geometry is again a single disk of different radii placed at the center of the periodicity box $Y = [0, L]^2$, and the gradient direction is $\mathbf{e}_x$. Two radii, $R = 0.49\,L$ and $R = 0.4\,L$, were simulated, in order to vary the volume fraction of the intra-cellular and extra-cellular compartment. The ADC_{ref} of the signal was obtained by a cubic fit using the logarithm of the signal at $b = 0, 10, 20, 40, 50\text{s/mm}^2$.

In Fig 4.5 is displayed a comparison of the $ADCs$ of the four different models as a function of the normalized diffusion displacement defined as

$$NDD := \frac{\sqrt{2(\Delta + \delta) ADC_{ref}}}{L/2}\,. \tag{4.38}$$

We immediately observe that the ADC_{new} of the new asymptotic model follows very well the the reference model (4.13) in the whole range of NDD. On the other hand, as we expected, the long time model works well only when $NDD \gg 1$ and the short-time model only for $NDD \ll 1$.

To validate our new asymptotic model in a more realistic geometry we simulated a large periodic box, with $L = 50\mu m$, that contains many cells of different shapes and sizes. There are 32 spheres of various radii in the range of $[2.5, 5]\mu m$ and 5 cylinders of various radii in the range of $[0.7, 2]\mu m$ (4.6a). The resulting external volume fraction is then $v_e = 0.4$. We fixed $\mathcal{D}_0^e = 3 \times 10^{-3}\, mm^2/s$, $\mathcal{D}_0^c = 2 \times 10^{-3}\, mm^2/s$, and $\kappa = 1 \times 10^{-5}$ m/s, and we varied δ and Δ over a wide range of times. The simulated (δ, Δ), expressed in ms, are $(0.1, 0.1)$, $(0.2, 0.2)$, $(0.3, 0.3)$, $(0.5, 0.5)$, $(1.0, 1.0)$, $(1.5, 1.5)$, $(2.5, 2.5)$, $(2.5, 5.0)$, $(2.5, 7.5)$, $(2.5, 10.0)$, $(2.5, 15.0)$, $(2.5, 20.0)$, $(2.5, 40.0)$, $(2.5, 80.0)$, $(2.5, 120.0)$ and $(2.5, 160.0)$. The gradient direction is $\mathbf{u_g} = [1/\sqrt{2}, 1/\sqrt{2}]$.

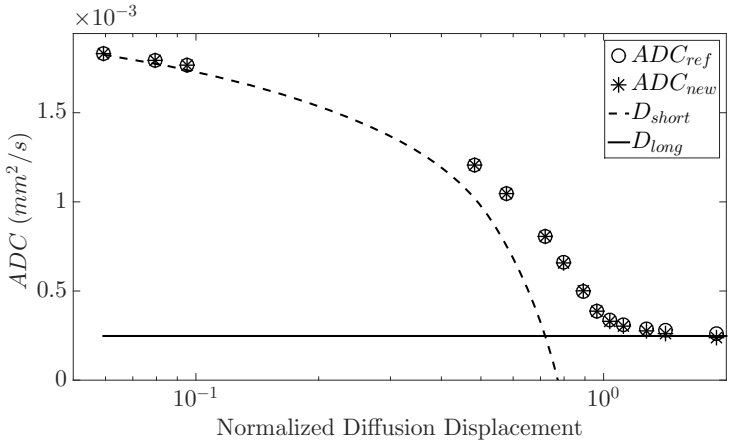

(a) $R = 0.49L$

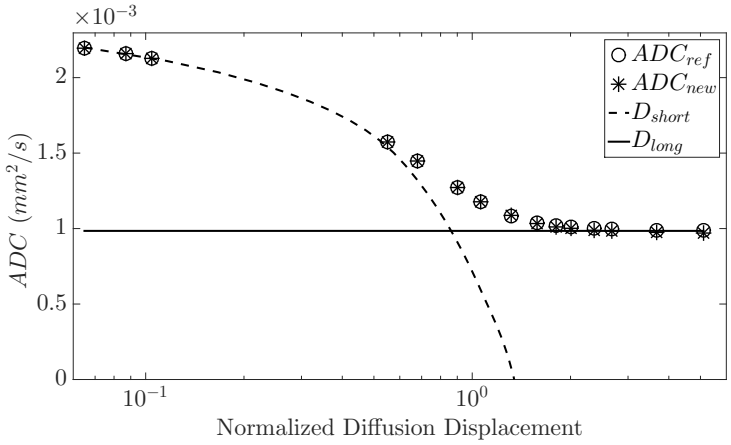

(b) $R = 0.4L$

Figure 4.5 – ADC approximation for a single disk in a periodicity box with $\kappa = 1 \times 10^{-5}$ m/s, $\mathcal{D}_0^e = 3 \times 10^{-3} mm^2/s$, $\mathcal{D}_0^c = 1.6 \times 10^{-3} mm^2/s$, for two disk radii: $R = 0.49\,L$ and $R = 0.4\,L$.

In Fig 4.6b is displayed a comparison of the $ADCs$ of the four different models as a function of the diffusion displacement. In this example, we did not normalize the diffusion displacement by $L/2$ because the characteristic length of this domain is not obvious, given the presence of several cell shapes and sizes. The ADC_{ref} of the signal was obtained by a cubic fit using the logarithm of the signal at $b = 0, 20, 40, 60, 80, 100\text{s/mm}^2$. We observe that the ADC_{new} of our new asymptotic model follows very well the reference model (4.13) in the whole range of diffusion displacement. On the contrary, as we expected, the short-time model works well only for small diffusion displacement and the long-time model only for large diffusion displacement. We see also that ADC_{ref} attains the long time limit at the diffusion displacement of around $10\mu m$, much smaller than $L/2$. This means the characteristic length of this medium is smaller than $L/2$, which is another reason we claim that the generality of our model is not limited by the original periodicity assumption on the domain when we performed the homogenization.

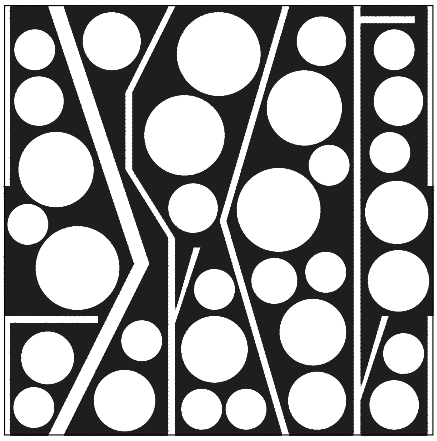

(a) Periodicity box $Y = [0, 50\mu m]^2$

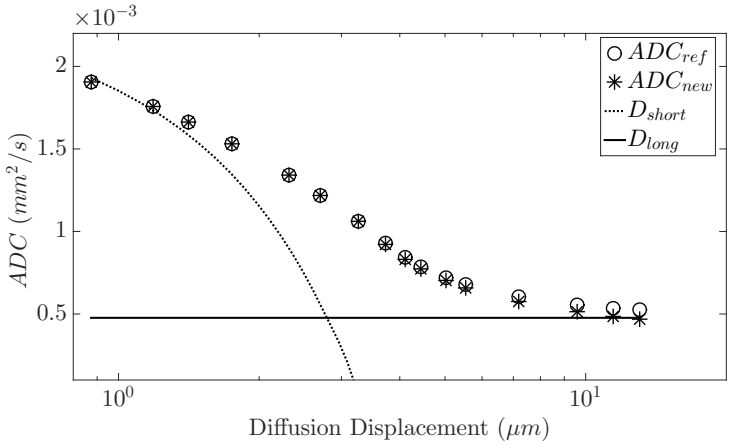

(b) Simulated *ADC*

Figure 4.6 – *ADC* approximation for a periodic domain where the periodicity box $Y = [0, 50\mu m]^2$ is shown above. The extra-cellular volume fraction is $v_e = 0.4$, with the membrane permeability $\kappa = 1 \times 10^{-5}$ m/s, and intrinsic diffusion coefficients: $\mathcal{D}_0^e = 3 \times 10^{-3} mm^2/s$ and $\mathcal{D}_0^c = 2 \times 10^{-3} mm^2/s$.

4.4 Comparison between the new asymptotic model and the linearized model

In Section 4.2 we derived a new asymptotic model using homogenization techniques along with a new time, gradient's intensity and permeability scalings. Now we want to show that, under some assumption on the initial magnetization and up to the first order in b, we could have achieved the same model using a linearization of the solution of the problem (4.14) considering the product of the gradient intensity and the integral of the time profile small along with the assumption that the permeability κ is also small.

More precisely, considering a periodic domain $\Omega = \Omega_e \bigcup \Omega_c$ (i.e. the union between an extracellular domain Ω_e and an intracellular domain Ω_c as in Figure) we suppose that there exists a non-dimensional parameter $\epsilon > 0$ such that

$$qF(t) = \epsilon \tilde{q} \tilde{F}(t) \quad \text{and} \quad \kappa = \epsilon \tilde{\kappa}\,. \tag{4.39}$$

We can thus rewrite the problem (4.14) as

$$\begin{cases} \dfrac{\partial}{\partial t}\widetilde{M}_\epsilon(\mathbf{x},t) - \operatorname{div}\big(\mathcal{D}_0\nabla\widetilde{M}_\epsilon(\mathbf{x},t) - \imath\epsilon\tilde{q}\mathbf{u_g}\tilde{F}(t)\mathcal{D}_0\widetilde{M}_\epsilon(\mathbf{x},t)\big) \\ \qquad\qquad + \imath\epsilon\tilde{q}\mathbf{u_g}\tilde{F}(t)\mathcal{D}_0\nabla\widetilde{M}_\epsilon(\mathbf{x},t) + \epsilon^2\tilde{q}^2\tilde{F}(t)^2\mathcal{D}_0\widetilde{M}_\epsilon(\mathbf{x},t) = 0, & \text{in } \Omega\times]0,T[, \\ \mathcal{D}_0\nabla\widetilde{M}_\epsilon\cdot\nu - \imath\epsilon\tilde{q}\mathbf{u_g}\tilde{F}(t)\mathcal{D}_0\widetilde{M}_\epsilon\cdot\nu = \epsilon\tilde{\kappa}[\![\widetilde{M}_\epsilon]\!]_{\Gamma_m^\epsilon}, & \text{on } \Gamma_m\times]0,T[, \\ [\![\mathcal{D}_0\nabla\widetilde{M}_\epsilon\cdot\nu - \imath\epsilon\tilde{q}\mathbf{u_g}\tilde{F}(t)\mathcal{D}_0\widetilde{M}_\epsilon\cdot\nu]\!]_{\Gamma_m} = 0, & \text{on } \Gamma_m\times]0,T[, \\ \widetilde{M}_\epsilon(\cdot,0) = M_{\text{ini}}, & \text{in } \Omega, \\ \widetilde{M}_\epsilon \text{ periodic on } \partial\Omega, \end{cases} \tag{4.40}$$

where $\mathcal{D}_0$ is the intrinsic diffusion coefficient (which is assumed to be piecewise constant and can assume different values in Ω_e and Ω_c like discussed in Section 4.1.2) and $\Gamma_m = \partial\Omega_c$. We remark that with $\widetilde{M}_\epsilon$ periodic on $\partial\Omega$ we mean that

$$\widetilde{M}_\epsilon|_{\partial\Omega_1} = \widetilde{M}_\epsilon|_{\partial\Omega_3} \quad \text{and} \quad \widetilde{M}_\epsilon|_{\partial\Omega_2} = \widetilde{M}_\epsilon|_{\partial\Omega_4}, \tag{4.41}$$

where $\bigcup_{i=1}^{4}\partial\Omega_i = \partial\Omega$ as defined in Figure 4.7.

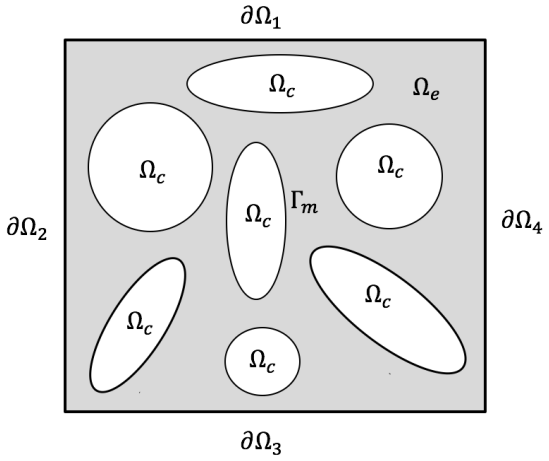

Figure 4.7 – Considered periodic domain.

As we did in Section 4.2.2, we also suppose that the solution $\widetilde{M}_\epsilon(\mathbf{x},t)$ of (4.40) admits a series expansion in terms of the power of ϵ like

$$\widetilde{M}_\epsilon(\mathbf{x},t) = \sum_{i=0}^{\infty}\epsilon^i M_i = \begin{cases} \displaystyle\sum_{i=0}^{\infty}\epsilon^i M_{ie} & \text{in } \Omega_e\times]0,T[, \\ \displaystyle\sum_{i=0}^{\infty}\epsilon^i M_{ic} & \text{in } \Omega_c\times]0,T[. \end{cases} \tag{4.42}$$

Substituting the expansion (4.42) in (4.40) and matching the terms in front the same power of

ϵ we obtain the following problems for the first three orders

$$\begin{cases} \dfrac{\partial}{\partial t} M_0 - \operatorname{div}\big(\mathcal{D}_0 \nabla M_0\big) = 0, & \text{in } \Omega\times]0,T[, \\ \mathcal{D}_0 \nabla M_0 \cdot \nu = 0, & \text{on } \Gamma_m\times]0,T[, \\ M_0(\mathbf{x},0) = M_{\text{ini}}, & \text{in } \Omega, \\ M_0 \text{ periodic on } \partial\Omega \end{cases} \tag{4.43}$$

$$\begin{cases} \dfrac{\partial}{\partial t} M_1 - \operatorname{div}\big(\mathcal{D}_0 \nabla M_1 - \imath\tilde{q}\mathbf{u_g}\tilde{F}\mathcal{D}_0 M_0\big) + \imath\tilde{q}\mathbf{u_g}\tilde{F}\mathcal{D}_0\nabla M_0 = 0, & \text{in } \Omega\times]0,T[, \\ \mathcal{D}_0\nabla M_1\cdot\nu - \imath\tilde{q}\mathbf{u_g}\tilde{F}\mathcal{D}_0 M_0\cdot\nu = \tilde{\kappa}[\![M_0]\!]_{\Gamma_m}, & \text{on } \Gamma_m\times]0,T[, \\ M_1(\mathbf{x},0) = 0, & \text{in } \Omega, \\ M_1 \text{ periodic on } \partial\Omega \end{cases} \tag{4.44}$$

and

$$\begin{cases} \dfrac{\partial}{\partial t} M_2 - \operatorname{div}\big(\mathcal{D}_0 \nabla M_2 - \imath\tilde{q}\mathbf{u_g}\tilde{F}\mathcal{D}_0 M_1\big) + \imath\tilde{q}\mathbf{u_g}\tilde{F}\mathcal{D}_0\nabla M_1 + \tilde{q}^2\tilde{F}(t)^2\mathcal{D}_0 M_0 = 0, & \text{in } \Omega\times]0,T[, \\ \mathcal{D}_0\nabla M_2\cdot\nu - \imath\tilde{q}\mathbf{u_g}\tilde{F}\mathcal{D}_0 M_1\cdot\nu = \tilde{\kappa}[\![M_1]\!]_{\Gamma_m}, & \text{on } \Gamma_m\times]0,T[, \\ M_2(\mathbf{x},0) = 0, & \text{in } \Omega, \\ M_2 \text{ periodic on } \partial\Omega. \end{cases} \tag{4.45}$$

We immediately observe that the problem (4.43) is the same as the problem (4.27) and then, since Ω_c is a closed domain and Ω_e is assumed to be periodic, $M_0(\mathbf{x},t) = M_{\text{ini}}$ in $\Omega\times]0,T[$. Regarding the problem (4.44) we observe that it has the same PDE and initial condition as the problem (4.29), but a different Neumann boundary condition on the interface. However, in the case of M_{ini} piecewise constant (standard assumption as we have discussed in Chapter 1) we have that $[\![M_0]\!]_{\Gamma_m} = 0$. So we obtain the same problem as (4.29) and then the solution is the same. For (4.45) we have again that the PDE and initial conditions coincide with the ones in (4.31) but not the Neumann boundary conditions. Nevertheless, as we are only interested in the real part of M_2, we use the fact that the real part of M_1 is equal to zero and then the Neumann boundary conditions for the real part of M_2 is $[\![M_1]\!]_{\Gamma_m} = 0$, i.e. we have the same problem as (4.31). Finally defining the dMRI signal as

$$S(\mathbf{x},q) = \int_\Omega \sum_{i=0}^{\infty} \epsilon^i M_i(\mathbf{x},T_E)\, d\mathbf{x}$$

and truncating it at $i=2$, we obtain the same expression as the one in (4.33).

We derived the new model also in this way for two reasons: the physical meaning of the chosen scalings can be better understood and it is easier to furnish the analytical convergence analysis between the solution of the derived model and the Bloch-Torrey one. Regarding the choice of scalings, indeed, say that the product $qF(t)$ and the permeability κ must be small, immediately tells us in which physical regime our model holds. Indeed, it is more clear than before where we related space, time, gradient strength and permeability to the same parameter.

4.4.1 Convergence

The convergence analysis is based on classical energy identities for the heat equation. Let us first specify the natural solution space for (4.40). Using standard theory for the parabolic problems one can easily show that, for $M_{\text{ini}} \in \mathrm{L}^2(\Omega)$, the problem (4.40) has a unique solution

$$\widetilde{M}_\epsilon \in C^0\left([0,T],\mathrm{L}^2(\Omega)\right)\bigcap \mathrm{L}^2\left([0,t],\tilde{\mathrm{H}}^1(\Omega)\right), \tag{4.46}$$

where

$$\tilde{\mathrm{H}}^1(\Omega) = \{\, u \in \mathrm{H}^1(\Omega_e \bigcup \Omega_c) : u \text{ is periodic in } \partial\Omega \,\}.$$

We observe that also the solutions of (4.43), (4.44) and (4.45) lies in the same space of $\widetilde{M}_\epsilon$. To prove the convergence, we define a new function

$$\mathrm{e}_\epsilon(\mathbf{x},t) = |\widetilde{M}_\epsilon(\mathbf{x},t) - \overline{M}_\epsilon(\mathbf{x},t)|, \quad \mathbf{x}\in\Omega, t\in[0,T] \tag{4.47}$$

where $\overline{M}_\epsilon(\mathbf{x},t) := \sum_{i=1}^{2}\epsilon^i M_i$. $\mathrm{e}_\epsilon(\mathbf{x},t)$ represents the error between the solution $\widetilde{M}_\epsilon$ of the linearized Bloch-Torrey system (4.40) and the solution $\overline{M}_\epsilon(\mathbf{x},t)$ obtained with the two-scales expansion (4.42) truncated at $i=2$ (i.e. expressed by the sum of the solutions of (4.43), (4.44) and (4.45) weighted by the correct power of ϵ). This function solves

$$\begin{cases}
\dfrac{\partial}{\partial t}\mathrm{e}_\epsilon(\mathbf{x},t) - \operatorname{div}\left(\mathcal{D}_0\nabla \mathrm{e}_\epsilon(\mathbf{x},t) - \imath\epsilon\tilde{q}\mathbf{u_g}\tilde{F}(t)\mathcal{D}_0\mathrm{e}_\epsilon(\mathbf{x},t)\right) & \\
\qquad +\imath\epsilon\tilde{q}\tilde{F}(t)\mathcal{D}_0\mathbf{u_g}\cdot\nabla\mathrm{e}_\epsilon(\mathbf{x},t) + \epsilon^2\tilde{q}^2\tilde{F}^2(t)\mathcal{D}_0\mathrm{e}_\epsilon(\mathbf{x},t) & \\
\qquad\quad = -\epsilon^3\imath\tilde{q}\tilde{F}(t)\mathcal{D}_0\mathbf{u_g}\cdot\nabla M_2(\mathbf{x},t) - \epsilon^3\imath\tilde{q}\tilde{F}(t)\mathcal{D}_0\operatorname{div}\left(\mathbf{u_g}M_2(\mathbf{x},t)\right) & \\
\qquad\quad -\epsilon^3\tilde{q}^2\tilde{F}^2(t)\mathcal{D}_0 M_1(\mathbf{x},t) - \epsilon^4\tilde{q}^2\tilde{F}^2(t)\mathcal{D}_0 M_0(\mathbf{x},t), & \text{in } \Omega\times]0,T[,\\
\mathcal{D}_0\nabla\mathrm{e}_\epsilon(\mathbf{x},t)\cdot\nu - \imath\epsilon\tilde{q}\tilde{F}(t)\mathcal{D}_0\mathrm{e}_\epsilon(\mathbf{x},t)\mathbf{u_g}\cdot\nu - \epsilon\tilde{\kappa}[\![\mathrm{e}_\epsilon]\!]_{\Gamma_m} & \\
\qquad\quad = -\epsilon^3\imath\tilde{q}\tilde{F}(t)\mathcal{D}_0 M_2(\mathbf{x},t)\mathbf{u_g}\cdot\nu - \epsilon^4\tilde{\kappa}[\![M_2]\!]_{\Gamma_m}, & \text{on } \Gamma_m\times]0,T[,\\
[\![\mathcal{D}_0\nabla\mathrm{e}_\epsilon(\mathbf{x},t)\cdot\nu - \imath\epsilon\tilde{q}\tilde{F}(t)\mathcal{D}_0\mathrm{e}_\epsilon(\mathbf{x},t)\mathbf{u_g}\cdot\nu]\!]_{\Gamma_m} = 0, & \text{on } \Gamma_m\times]0,T[,\\
\mathrm{e}_\epsilon(\mathbf{x},0) = 0, & \text{in } \Omega,\\
\mathrm{e}_\epsilon \text{ periodic on } \partial\Omega.
\end{cases} \tag{4.48}$$

The idea is to use the energy estimate to prove that the solution e_ϵ depends continuously on the source terms and the boundary condition and that the rate of convergence is of $O(\epsilon^3)$.

To lighter the notation, we write $[\![]\!]$ instead of $[\![]\!]_{\Gamma_m}$. Multiplying (4.48) by e_ϵ and using the Green theorem, we have that for all $t\in[0,T]$

$$\begin{aligned}
\frac{1}{2}\int_\Omega \frac{\partial}{\partial t}|\mathrm{e}_\epsilon|^2 + \int_\Omega \mathcal{D}_0|\nabla\mathrm{e}_\epsilon|^2 + \epsilon^2\int_\Omega \tilde{q}^2\tilde{F}^2\mathcal{D}_0|\mathrm{e}_\epsilon|^2 + \epsilon\tilde{k}\int_{\Gamma_m}|[\![\mathrm{e}_\epsilon]\!]|^2 = \\
+\epsilon^3\int_\Omega\left(-\imath\tilde{q}\tilde{F}\mathcal{D}_0\mathbf{u_g}\cdot\nabla M_2 - \imath\tilde{q}\tilde{F}\mathcal{D}_0\operatorname{div}\left(\mathbf{u_g}M_2\right) - \tilde{q}^2\tilde{F}^2\mathcal{D}_0 M_1 - \epsilon\tilde{q}^2\tilde{F}^2\mathcal{D}_0 M_0\right)\mathrm{e}_\epsilon \\
+\epsilon^3\int_{\Gamma_m}\left(-\imath\tilde{q}\tilde{F}\mathcal{D}_0 M_2\mathbf{u_g}\cdot\nu - \epsilon\tilde{k}[\![M_2]\!]\right)\mathrm{e}_\epsilon
\end{aligned} \tag{4.49}$$

which integrating in time from 0 to t becomes

$$\frac{1}{2}\int_\Omega |\mathrm{e}_\epsilon|^2 + \int_0^t\int_\Omega \mathcal{D}_0|\nabla \mathrm{e}_\epsilon|^2 + \epsilon^2\int_0^t\int_\Omega \tilde{q}^2\tilde{F}^2\mathcal{D}_0|\mathrm{e}_\epsilon|^2 + \epsilon\int_0^t\int_{\Gamma_m}\tilde{k}|[\![\mathrm{e}_\epsilon]\!]|^2 =$$
$$+\epsilon^3\int_0^t\int_\Omega\left(-\imath\tilde{q}\tilde{F}\mathcal{D}_0\mathbf{u_g}\cdot\nabla M_2 - \imath\tilde{q}\tilde{F}\mathcal{D}_0\mathrm{div}\,(\mathbf{u_g}M_2) - \tilde{q}^2\tilde{F}^2\mathcal{D}_0M_1 - \epsilon\tilde{q}^2\tilde{F}^2\mathcal{D}_0M_0\right)\mathrm{e}_\epsilon$$
$$+\epsilon^3\int_0^t\int_{\Gamma_m}\left(-\imath\tilde{q}\tilde{F}\mathcal{D}_0M_2\mathbf{u_g}\cdot\nu - \epsilon\tilde{k}[\![M_2]\!]\right)\mathrm{e}_\epsilon. \quad (4.50)$$

Using the fact that $\mathrm{e}_\epsilon(t)\in \mathrm{L}^2(\Omega)$ and the Cauchy-Schwarz inequality we obtain that for all $t\in[0,T]$

$$\frac{1}{2}\|\mathrm{e}_\epsilon\|^2_{\mathrm{L}^2(\Omega)} + \int_0^t \mathcal{D}_0\|\nabla\mathrm{e}_\epsilon\|^2_{\mathrm{L}^2(\Omega)} + \epsilon^2\int_0^t\tilde{q}^2\tilde{F}^2\mathcal{D}_0\|\mathrm{e}_\epsilon\|^2_{\mathrm{L}^2(\Omega)} + \epsilon\int_0^t\tilde{k}\|[\![\mathrm{e}_\epsilon]\!]\|^2_{\mathrm{L}^2(\Gamma_m)} \leqslant$$
$$\epsilon^3\int_0^T\|-\imath\tilde{q}\tilde{F}\mathcal{D}_0\mathbf{u_g}\cdot\nabla M_2 - \imath\tilde{q}\tilde{F}\mathcal{D}_0\mathrm{div}\,(\mathbf{u_g}M_2) - \tilde{q}^2\tilde{F}^2\mathcal{D}_0M_1 - \epsilon\tilde{q}^2\tilde{F}^2\mathcal{D}_0M_0\|_{\mathrm{L}^2(\Omega)}\|\mathrm{e}_\epsilon\|_{\mathrm{L}^2(\Omega)}$$
$$+\epsilon^3\int_0^t\|-\imath\tilde{q}\tilde{F}\mathcal{D}_0M_2\mathbf{u_g}\cdot\nu - \epsilon\tilde{k}[\![M_2]\!]\|_{\mathrm{L}^2(\Gamma_m)}\|\mathrm{e}_\epsilon\|_{\mathrm{L}^2(\Gamma_m)}. \quad (4.51)$$

We observe that

$$\|\mathrm{e}_\epsilon\|_{\mathrm{L}^2(\Gamma_m)} \leqslant \left(\|\mathrm{e}_\epsilon\|_{\mathrm{L}^2(\Omega)} + \|\nabla\mathrm{e}_\epsilon\|_{\mathrm{L}^2(\Omega)}\right). \quad (4.52)$$

Using this property and completing the squares we obtain that for all $t\in[0,T]$

$$\frac{1}{2}\|\mathrm{e}_\epsilon\|^2_{\mathrm{L}^2(\Omega)} + \int_0^t\mathcal{D}_0\left(\|\nabla\mathrm{e}_\epsilon\|_{\mathrm{L}^2(\Omega)} - \frac{\epsilon^3}{2}\|-\imath\tilde{q}\tilde{F}M_2\mathbf{u_g}\cdot\nu - \epsilon\tilde{k}[\![M_2]\!]\|_{\mathrm{L}^2(\Gamma_m)}\right)^2$$
$$+\epsilon^2\int_0^t\tilde{q}^2\tilde{F}^2\mathcal{D}_0\|\mathrm{e}_\epsilon\|^2_{\mathrm{L}^2(\Omega)} + \epsilon\int_0^t\tilde{k}\|[\![\mathrm{e}_\epsilon]\!]\|^2_{\mathrm{L}^2(\Gamma_m)} \leqslant +\frac{\epsilon^6}{4}\int_0^t\|-\imath\tilde{q}\tilde{F}\mathcal{D}_0M_2\mathbf{u_g}\cdot\nu - \epsilon\tilde{k}[\![M_2]\!]\|^2_{\mathrm{L}^2(\Gamma_m)}$$
$$\epsilon^3\int_0^t\Big[\|-\imath\tilde{q}\tilde{F}\mathcal{D}_0\mathbf{u_g}\cdot\nabla M_2 - \imath\tilde{q}\tilde{F}\mathcal{D}_0\mathrm{div}\,(\mathbf{u_g}M_2) - \tilde{q}^2\tilde{F}^2\mathcal{D}_0M_1 - \epsilon\tilde{q}^2\tilde{F}^2\mathcal{D}_0M_0\|_{\mathrm{L}^2(\Omega)}$$
$$+\|-\imath\tilde{q}\tilde{F}\mathcal{D}_0M_2\mathbf{u_g}\cdot\nu - \epsilon\tilde{k}[\![M_2]\!]\|_{\mathrm{L}^2(\Gamma_m)}\Big]\|\mathrm{e}_\epsilon\|_{\mathrm{L}^2(\Omega)}. \quad (4.53)$$

If we call

$$a := \frac{\epsilon^6}{4}\int_0^t\|-\imath\tilde{q}\tilde{F}\mathcal{D}_0M_2\mathbf{u_g}\cdot\nu - \epsilon\tilde{k}[\![M_2]\!]\|^2_{\mathrm{L}^2(\Gamma_m)}, \quad (4.54)$$

$$b(s) := \Big[\epsilon^3\|-\imath\tilde{q}\tilde{F}\mathcal{D}_0\mathbf{u_g}\cdot\nabla M_2 - \imath\tilde{q}\tilde{F}\mathcal{D}_0\mathrm{div}\,(\mathbf{u_g}M_2) - \tilde{q}^2\tilde{F}^2\mathcal{D}_0M_1\|_{\mathrm{L}^2(\Omega)}$$
$$+\epsilon^4\|-\tilde{q}^2\tilde{F}^2\mathcal{D}_0M_0\|_{\mathrm{L}^2(\Omega)} + \epsilon^3\|-\imath\tilde{q}\tilde{F}\mathcal{D}_0M_2\mathbf{u_g}\cdot\nu - \epsilon\tilde{k}[\![M_2]\!]\|_{\mathrm{L}^2(\Gamma_m)}\Big] \quad (4.55)$$

and

$$z^2(t) := \frac{1}{2}\|\mathrm{e}_\epsilon\|^2_{\mathrm{L}^2(\Omega)} + \int_0^t\mathcal{D}_0\left(\|\nabla\mathrm{e}_\epsilon\|_{\mathrm{L}^2(\Omega)} - \frac{\epsilon^3}{2}\|-\imath\tilde{q}\tilde{F}M_2\mathbf{u_g}\cdot\nu - \epsilon\tilde{k}[\![M_2]\!]\|_{\mathrm{L}^2(\Gamma_m)}\right)^2$$
$$+\epsilon^2\int_0^t\tilde{q}^2\tilde{F}^2\mathcal{D}_0\|\mathrm{e}_\epsilon\|^2_{\mathrm{L}^2(\Omega)} + \epsilon\int_0^t\tilde{k}\|[\![\mathrm{e}_\epsilon]\!]\|^2_{\mathrm{L}^2(\Gamma_m)}, \quad (4.56)$$

since all the quantities are positive, we have that $\|\mathrm{e}_\epsilon\|_{\mathrm{L}^2(\Omega)}\leqslant z(t)$ for all $t\in[0,T]$.

Remark 4.4.1. *We observe that if*

$$z^2(t) \leqslant a + \int_0^t b(s)z(s)ds. \tag{4.57}$$

and, if we call

$$\tilde{z}(t) := a + \int_0^t b(s)z(s)ds \tag{4.58}$$

we have that

$$\frac{d}{dt}\tilde{z}(t) = b(t)z(t) \leqslant b(t)\sqrt{\tilde{z}(t)} \tag{4.59}$$

and thus integrating in time

$$\sqrt{\tilde{z}(t)} \leqslant \frac{1}{2}\int_0^t b(s)ds + \sqrt{a}, \tag{4.60}$$

because $a = \tilde{z}(0)$. *As a consequence we obtain that*

$$z(t) \leqslant \sqrt{\tilde{z}(t)} \leqslant \frac{1}{2}\int_0^t b(s)ds + \sqrt{a}. \tag{4.61}$$

Now, remembering the definition of z, a and b and applying (4.61) of the above Remark, we obtain

$$\begin{aligned}\frac{1}{2}\|\mathrm{e}_\epsilon\|^2_{\mathrm{L}^2(\Omega)} + \int_0^t \mathcal{D}_0 \left(\|\nabla \mathrm{e}_\epsilon\|_{\mathrm{L}^2(\Omega)} - \frac{\epsilon^3}{2}\|-\imath\tilde{q}\tilde{F}M_2\mathbf{u_g}\cdot\nu - \epsilon\tilde{k}[\![M_2]\!]\|_{\mathrm{L}^2(\Gamma_m)}\right)^2 \\ + \epsilon^2\int_0^t \tilde{q}^2\tilde{F}^2\mathcal{D}_0\|\mathrm{e}_\epsilon\|^2_{\mathrm{L}^2(\Omega)} + \epsilon\int_0^t \tilde{k}\|[\![\mathrm{e}_\epsilon]\!]\|^2_{\mathrm{L}^2(\Gamma_m)} \leqslant \\ \frac{\epsilon^3}{2}\int_0^t \Big[\|-\imath\tilde{q}\tilde{F}\mathcal{D}_0\mathbf{u_g}\cdot\nabla M_2 - \imath\tilde{q}\tilde{F}\mathcal{D}_0\mathrm{div}\,(\mathbf{u_g}M_2) - \tilde{q}^2\tilde{F}^2\mathcal{D}_0M_1 - \epsilon\tilde{q}^2\tilde{F}^2\mathcal{D}_0M_0\|_{\mathrm{L}^2(\Omega)} \\ + \|-\imath\tilde{q}\tilde{F}\mathcal{D}_0M_2\mathbf{u_g}\cdot\nu - \epsilon\tilde{k}[\![M_2]\!]\|_{\mathrm{L}^2(\Gamma_m)}\Big] + \frac{\epsilon^3}{2}\sqrt{\int_0^t \|-\imath\tilde{q}\tilde{F}\mathcal{D}_0M_2\mathbf{u_g}\cdot\nu - \epsilon\tilde{k}[\![M_2]\!]\|^2_{\mathrm{L}^2(\Gamma_m)}}.\end{aligned} \tag{4.62}$$

From this inequality we then have that

$$\begin{aligned}\|\mathrm{e}_\epsilon\|^2_{\mathrm{L}^2(\Omega)} \leqslant \epsilon^3\int_0^t \Big[\|-\imath\tilde{q}\tilde{F}\mathcal{D}_0\mathbf{u_g}\cdot\nabla M_2 - \imath\tilde{q}\tilde{F}\mathcal{D}_0\mathrm{div}\,(\mathbf{u_g}M_2) - \tilde{q}^2\tilde{F}^2\mathcal{D}_0M_1 - \epsilon\tilde{q}^2\tilde{F}^2\mathcal{D}_0M_0\|_{\mathrm{L}^2(\Omega)} \\ + \|-\imath\tilde{q}\tilde{F}\mathcal{D}_0M_2\mathbf{u_g}\cdot\nu - \epsilon\tilde{k}[\![M_2]\!]\|_{\mathrm{L}^2(\Gamma_m)}\Big] + \epsilon^3\sqrt{\int_0^t \|-\imath\tilde{q}\tilde{F}\mathcal{D}_0M_2\mathbf{u_g}\cdot\nu - \epsilon\tilde{k}[\![M_2]\!]\|^2_{\mathrm{L}^2(\Gamma_m)}}.\end{aligned} \tag{4.63}$$

i.e.

$$\|\mathrm{e}_\epsilon\|^2_{\mathrm{L}^2(\Omega)} \leqslant \epsilon^3 C(t), \tag{4.64}$$

where $C(t)$ is a quantity that does not depend on ϵ. This proves that the error between the Bloch-Torrey solution and our model is of $O(\epsilon^3)$, which confirms what we claimed before (since we stopped the asymptotic expansion at M_2) and what we got in the simulation in Section 4.3.

4.5 Conclusions

We have formulated a new asymptotic model of the dMRI signal from the Bloch-Torrey PDE using homogenization with a particular choice of scaling for the time, the biological cell membrane permeability, the diffusion-encoding magnetic field gradient strength, and a periodicity length of the cellular geometry. The apparent diffusion coefficient (ADC) of the resulting model is diffusion time-dependent, a property observed in *in-vivo* imaging experiments of the brain. We numerically validated the new asymptotic model in two dimensional geometrical configurations and showed that its ADC is close to the ADC of the reference Bloch-Torrey PDE model over a wide range of diffusion times. The derived model is valid for all dimensions. Numerical implementation in three dimensions, though most likely time-consuming, should be straightforward. We also derived the model using linearization instead of homogenization techniques and we proved the convergence between the Bloch-Torrey solution and the new approximation. Deeper analysis of this new model and adapting it to estimate model parameters from the dMRI signal data will be the subject of the Chapter 6.

Chapter 5

Other scalings for small b-values

Contents

5.1 General equations 96
5.2 Parameters limitations 98
5.3 Diffusion time scale comparable with the cell size $\alpha = 1$ 99
5.4 Diffusion time scale shorter than the cell size $\alpha = 2$ 101
5.4.1 Moderate intensity: $\gamma = 0$ 102
5.4.2 Relatively strong intensity: $\gamma = 1$ 103
5.4.3 Very strong intensity: $\gamma = 3$ 105
5.5 M_{ini} space dependent for $\alpha = 2$ 106

In the previous Chapter, using homogenization techniques along with particular scalings for the membrane permeability, the time of the experiment and the gradient intensity, we derived a family of models from the Bloch-Torrey PDE problem [180]. A priori all these models can be used to approximate the solution of the Bloch-Torrey PDE under the regime specified by the choice of parameters. Our purpose is to approximate the apparent diffusion coefficient for relatively small values of the membrane permeability so, according to the definition (2.42) in Chapter 1, we mostly investigate the choice of parameters which gives us a small b-value, (i.e. $O(g^2)$). If one is interested in other quantities, like the Kurtosis terms or terms of higher order in g, or different regime of permeability, other choices of scalings may be more appropriate but this goes beyond the scope of this Thesis and could be part of future investigations. We just remark that an analysis of other possible choices for κ and standard homogenization can be found in [41].

In this Chapter we recall how we derive a general family of models imposing particular scalings on L, κ, t and g. We then explain why we decided that the choice $L = \varepsilon L_0$, $\kappa = \varepsilon\kappa_0$, $t = \varepsilon^2\tau$ and $g = \varepsilon^{-2}g_0$ was appropriate to give a good estimates for ADC. To do so, we describe other choices of parameters and we identify in which physical regime they hold. In particular, we use the definition of b-value in terms of t and g and we find mathematical limitations for the time and the gradient intensity parameters which yield to small b-values. We show that, if $t = (\varepsilon^1)$ for possible choices of scaling on g which respects the constraint of giving small b-values, we obtain an expression of ADC that coincides with the FPK model. In the same vein, we show that if $t = O(\varepsilon^2)$, for every possible choice of scaling on g (which respects the constraint of giving small b-values), we obtain an expression of ADC that coincides with the H-ADC model derived in Chapter 4. This help us in better understanding the regime of physical parameters for which the homogenised models hold. Finally we investigate what changes mathematically if the initial value of the magnetization is not constant but is piecewise constant in the two compartments (intra and extra-cellular). We show that, while the PDEs to be solved to get the asymptotic

functions M_i are different, the expression of the signal remains the same. We remark that all the presented models hold also if $\mathcal{D}_0$ depends on the space variable $\mathbf{y}$.

The Chapter is organized as follows. In Section 5.1, we recall how we derived the family of models in Chapter 4 after having imposed some specific scalings for the periodic cell, the permeability coefficient, the time and the gradient's intensity. In Section 5.2 we impose some mathematical constraints on the scaling's parameters in order to obtain models for small b-values. In Section 5.3 we show the results obtained for $t = O(\varepsilon^1)$. In Section 5.4 we show the results obtained for $t = O(\varepsilon^2)$ and various intensity gradient scalings. In Section 5.5 we show the results for the space dependent initial condition.

5.1 General equations

We recall that in Section 4.2, after having applied the change of variable

$$\widetilde{M}_\varepsilon(\mathbf{x},t) = M_\varepsilon(\mathbf{x},t)e^{\imath q\mathbf{u_g}\cdot\mathbf{x}F(t)} \tag{5.1}$$

to the standard Bloch-Torrey equation for $M_\varepsilon(\mathbf{x},t)$ (where $q=\gamma g$), we obtained the new PDE system

$$\begin{cases} \dfrac{\partial}{\partial t}\widetilde{M}_\varepsilon(\mathbf{x},t) - \operatorname{div}\big(\hat{\mathcal{D}}_{0\varepsilon}\nabla\widetilde{M}_\varepsilon(\mathbf{x},t) - \imath q\mathbf{u_g}F(t)\hat{\mathcal{D}}_{0\varepsilon}\widetilde{M}_\varepsilon(\mathbf{x},t)\big) & \\ \qquad + \imath q\mathbf{u_g}F(t)\hat{\mathcal{D}}_{0\varepsilon}\nabla\widetilde{M}_\varepsilon(\mathbf{x},t) + q^2F(t)^2\hat{\mathcal{D}}_{0\varepsilon}\widetilde{M}_\varepsilon(\mathbf{x},t) = 0 & \text{in } \Omega^\varepsilon_{ext}\times]0,T[, \\ \hat{\mathcal{D}}_{0\varepsilon}\nabla\widetilde{M}_\varepsilon\cdot\nu - \imath q\mathbf{u_g}F(t)\hat{\mathcal{D}}_{0\varepsilon}\widetilde{M}_\varepsilon\cdot\nu = \kappa^\varepsilon[\![\widetilde{M}_\varepsilon]\!]_{\Gamma^\varepsilon_m} & \text{on } \Gamma^\varepsilon_m\times]0,T[, \\ [\![\hat{\mathcal{D}}_{0\varepsilon}\nabla\widetilde{M}_\varepsilon\cdot\nu - \imath q\mathbf{u_g}F(t)\hat{\mathcal{D}}_{0\varepsilon}\widetilde{M}_\varepsilon\cdot\nu]\!]_{\Gamma^\varepsilon_m} = 0 & \text{on } \Gamma^\varepsilon_m\times]0,T[, \\ \widetilde{M}_\varepsilon(\cdot,0) = M_{\text{ini}} & \text{in } \Omega^\varepsilon_{ext}, \end{cases} \tag{5.2}$$

for which we want to apply the homogenization theory.

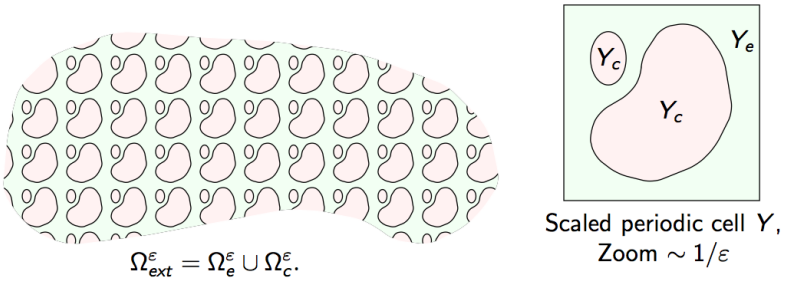

Figure 5.1 – Illustration of a periodic domain and the periodicity box Y.

As explained in Section 4.2.2, we have chosen the scaling of the periodicity length to be:

$$L = \varepsilon L_0,$$

where L_0 has the unit of *length* and ε is without dimension.

We keep the same scaling of the membrane permeability as was used in [42]:

$$\kappa = \varepsilon\kappa_0,$$

where κ_0 has the unit of *length/time*. We observe that other scalings of permeability may be chosen (and lead to other asymptotic models), but because biological cell membranes impede the movement of water, the permeability should be "small". In [41] detailed mathematical derivations with the other possible choices of scaling for κ can be found. Here we were not interested in this particular aspect and then we fixed one reasonable value.

We set the scaling of time to be:

$$t = \varepsilon^{\alpha}\tau,$$

which implies that F becomes

$$F_{\varepsilon}(t) = \int_0^t f(s)ds = \varepsilon^{\alpha}\int_0^{\tau} f(\xi)d\xi = \varepsilon^{\alpha}F_0(\tau)\,,$$

where we made the change of variable $\xi = s/\varepsilon^{\alpha}$ and $\tau = t/\varepsilon^{\alpha}$. We note that τ and ξ have the unit of *time*. In particular, for PGSE, this choice implies

$$\delta = \varepsilon^{\alpha}\delta_0, \quad \text{and} \quad \Delta = \varepsilon^{\alpha}\Delta_0. \tag{5.3}$$

We set the scaling of the gradient strength to be

$$q = \frac{q_0}{\varepsilon^{\gamma}},$$

and q_0 has the unit of $\frac{1}{length\times time}$ [1]. In consequence, the scaling on b is

$$b = q^2\int_0^{T_E} F^2(t)dt = \frac{q_0^2}{\varepsilon^{2\gamma}}\varepsilon^{3\alpha}\int_0^{\widetilde{T_E}} F_0^2\left(\tau\right)d\tau = \varepsilon^{3\alpha-2\gamma}b_0\,. \tag{5.4}$$

We use the periodic homogenization techniques [22], to develop $\widetilde{M}_{\varepsilon}$ using two-scale asymptotic expansions for Ω_e^{ε} and Ω_c^{ε}, along with the new time scaling, for general α and γ:

$$\widetilde{M}_{\varepsilon}(\mathbf{x},t) = \begin{cases} \widetilde{M}_{\varepsilon}^{e}(\mathbf{x},t) = \displaystyle\sum_{i=0}^{\infty}\varepsilon^{i}\widetilde{M}_{ie}(\mathbf{x},\mathbf{y},\tau) & \text{in } Y_e\times[0,T_E] \\ \widetilde{M}_{\varepsilon}^{c}(\mathbf{x},t) = \displaystyle\sum_{i=0}^{\infty}\varepsilon^{i}\widetilde{M}_{ic}(\mathbf{x},\mathbf{y},\tau) & \text{in } Y_c\times[0,T_E] \end{cases} \tag{5.5}$$

where

$$\mathbf{y} = \frac{\mathbf{x}}{\varepsilon} \qquad \text{and} \qquad \tau = \frac{t}{\varepsilon^{\alpha}}$$

and the functions $\widetilde{M}_{ie}(\mathbf{x},\mathbf{y},\tau)$ and $\widetilde{M}_{ic}(\mathbf{x},\mathbf{y},\tau)$ are defined on $\Omega\times Y_e\times+\infty[$ and $\Omega\times Y_c\times]0,+\infty[$ respectively, and the $\widetilde{M}_{ij}$ are assumed Y-periodic in $\mathbf{y}$. The aim of this ansatz is to obtain a new problem in which the different scales are linked.

1. Again, here γ is a positive exponent used to introduce a scaling on q and it should not be confuse with the gyro-magnetic ratio introduced before.

Finally, for $j \in \{ c, e \}$, we obtained the following PDE:

$$\begin{aligned} 0 = &\sum_{i=0}^{\infty} \varepsilon^{i-\alpha} \frac{\partial}{\partial \tau} \widetilde{M}_{ij} + \varepsilon^{i+2\alpha-2\gamma} q_0^2 \mathbf{u_g} \cdot \mathbf{u_g} F_0(\tau)^2 \mathcal{D}_0^j \widetilde{M}_{ij} \\ &+ \varepsilon^{i+\alpha-\gamma} \imath q_0 \mathbf{u_g} F_0(\tau) \mathcal{D}_0^j (\nabla_{\mathbf{x}} \widetilde{M}_{ij} + \varepsilon^{-1} \nabla_{\mathbf{y}} \widetilde{M}_{ij}) - \varepsilon^i \mathrm{div}_{\mathbf{x}} (\mathcal{D}_0^j \nabla_{\mathbf{x}} \widetilde{M}_{ij}) \\ &- \varepsilon^{i-1} \mathrm{div}_{\mathbf{x}} (\mathcal{D}_0^j \nabla_{\mathbf{y}} \widetilde{M}_{ij}) - \varepsilon^{i-1} \mathrm{div}_{\mathbf{y}} (\mathcal{D}_0^j \nabla_{\mathbf{x}} \widetilde{M}_{ij}) - \varepsilon^{i-2} \mathrm{div}_{\mathbf{y}} (\mathcal{D}_0^j \nabla_{\mathbf{y}} \widetilde{M}_{ij}) \\ &+ \varepsilon^{i+\alpha-\gamma} \mathrm{div}_{\mathbf{x}} (\imath q_0 \mathbf{u_g} F_0(\tau) \mathcal{D}_0^j \widetilde{M}_{ij}) + \varepsilon^{i+\alpha-\gamma-1} \mathrm{div}_{\mathbf{y}} (\imath q_0 \mathbf{u_g} F_0(\tau) \mathcal{D}_0^j \widetilde{M}_{ij}) \quad \text{in } Y_j \times]0, +\infty[, \end{aligned} \tag{5.6}$$

with boundary conditions given by

$$\begin{aligned} \sum_{i=0}^{\infty} \varepsilon^{i+1} \kappa_0 \Big(\widetilde{M}_{ie} - \widetilde{M}_{ic} \Big) = &\ \varepsilon^{-1} \mathcal{D}_0^j \nabla_{\mathbf{y}} \widetilde{M}_{0j} \cdot \nu \\ &+ \varepsilon^0 \Big(\mathcal{D}_0^j \nabla_{\mathbf{y}} \widetilde{M}_{1j} + \mathcal{D}_0^j \nabla_{\mathbf{x}} \widetilde{M}_{0j} - \varepsilon^{\alpha-\gamma} \imath q_0 \mathbf{u_g} F_0 \mathcal{D}_0^j \widetilde{M}_{0j} \Big) \cdot \nu \\ &+ \sum_{i=1}^{\infty} \varepsilon^i \Big(\mathcal{D}_0^j \nabla_{\mathbf{y}} \widetilde{M}_{i+1j} + \mathcal{D}_0^j \nabla_{\mathbf{x}} \widetilde{M}_{ij} - \varepsilon^{\alpha-\gamma} \imath q_0 \mathbf{u_g} F_0 \mathcal{D}_0^j \widetilde{M}_{ij} \Big) \cdot \nu \quad \text{on } \Gamma_j \times]0, +\infty[, \end{aligned} \tag{5.7}$$

and

$$\sum_{i=0}^{\infty} \Big[\!\Big[\mathcal{D}_0^j \Big(\varepsilon^i \nabla_x \widetilde{M}_{ij} + \varepsilon^{i-1} \nabla_y \widetilde{M}_{ij} - \varepsilon^{i+\alpha-\gamma} \imath q_0 F_0(\tau) \widetilde{M}_{ij} \mathbf{u_g} \Big) \cdot \nu \Big]\!\Big] = 0 \quad \text{on } \Gamma_m \times]0, +\infty[, \tag{5.8}$$

and initial conditions

$$\widetilde{M}_{0j}(\cdot, \cdot, 0) = M_{\mathrm{ini}}, \quad \text{and} \quad \widetilde{M}_{ij}(\cdot, \cdot, 0) = 0 \qquad \forall i > 0 \tag{5.9}$$

where we recall that M_{ini} is a real constant (see Chapter 1).

Using the asymptotic expansion of $\widetilde{M}_\varepsilon$ in (5.5), the signal attenuation for the periodicity box can be written as

$$\overline{S}(T_E, q, \mathbf{u_g}) := \frac{S(T_E, q, \mathbf{u_g})}{S(0, q, \mathbf{u_g})} = \frac{\displaystyle\sum_{i=0}^{\infty} \varepsilon^i \left(\int_{Y_e} \widetilde{M}_{ie}(\mathbf{x}, \widetilde{T_E}) d\mathbf{x} + \int_{Y_c} \widetilde{M}_{ic}(\mathbf{x}, \widetilde{T_E}) d\mathbf{x} \right)}{S_0}, \tag{5.10}$$

where $S_0 = \displaystyle\int_{Y_e} M_{\mathrm{ini}} + \int_{Y_c} M_{\mathrm{ini}}$.

5.2 Parameters limitations

As our purpose is to find an accurate approximation of the (time-dependent) *ADC* for low b-values, whose scaling is

$$b = \varepsilon^{3\alpha-2\gamma} b_0 \,, \tag{5.11}$$

where b_0 is independent from ε, we require

$$3\alpha - 2\gamma > 0. \tag{5.12}$$

We also want the time to be small since for long-time a sufficiently good model was already retrieved using the same techniques (the FPK model [42]). Hence we require that

$$\alpha > 0. \tag{5.13}$$

We recall that the choice that corresponds to the FPK model in [42], is $\alpha = \gamma = 0$ and it gives a constant ADC.

Since if b is too small it is possible to end up again with the microscopic model given by the Bloch-Torrey PDE (5.2) (see Section 5.4.3), we impose the intensity of the gradient to be strong, i.e.

$$\gamma \geqslant 0. \tag{5.14}$$

Looking at (5.6) and (5.7) we observe that, in order to have a well defined system of PDE we also need

$$\alpha \leqslant 2. \tag{5.15}$$

Indeed, if $\alpha \geqslant 2$, the term $\mathcal{D}_0 \nabla_{\mathbf{y}} M_{0j} \cdot \nu$ in the boundary condition (5.7) will appear in a different problem with respect to the corresponding term $\mathrm{div}_{\mathbf{y}} (\mathcal{D}_0 \nabla_{\mathbf{y}} M_{0j})$ in the PDE (5.6). Thus, for the problem containing the term $\mathrm{div}_{\mathbf{y}} (\mathcal{D}_0 \nabla_{\mathbf{y}} M_{0j})$ we would not have the appropriate boundary conditions and the system would not make sense mathematically.

Using (5.12), (5.14) and (5.15) we obtain that

$$\begin{cases} 0 \leqslant \gamma < \frac{3}{2} & \text{if } \alpha = 1, \\ 0 \leqslant \gamma < 3 & \text{if } \alpha = 2. \end{cases} \tag{5.16}$$

We observe that a priori $\alpha, \gamma \in \mathbb{Q} \bigcap [0, +\infty[$ plus the constraints (5.13-5.16). Thus, also $i \in \mathbb{Q} \bigcap [0, +\infty[$. In particular, the numerator of i varies always in $\mathbb{N}$ and the denominator is chosen according to the values of α and γ to be able to match all the combinations of these two parameters present in (5.6-5.7).

5.3 Diffusion time scale comparable with the cell size $\alpha = 1$

The first idea is to consider $\alpha = 1$ and find γ that respects (5.16) and lead to a time dependent ADC. A reasonable choice appears to be $\gamma = 1$. In this way $b = \varepsilon b_0$. Repeating the same computations in Section 4.2.3, one finds that M_{0j} solves

$$\begin{cases} -\mathrm{div}_{\mathbf{y}} (\mathcal{D}_0 \nabla_{\mathbf{y}} M_{0j}) = 0 & \text{in } Y_j \\ \mathcal{D}_0 \nabla_{\mathbf{y}} M_{0j} \cdot \nu = 0 & \text{on } \Gamma_m \\ M_{0e} \text{ is } Y - \text{periodic.} \end{cases} \tag{5.17}$$

This implies that M_{0j}, $j \in \{e, c\}$ does not depend on $\mathbf{y}$. Going on, M_{1j} solves

$$\begin{cases} -\mathrm{div}_{\mathbf{y}} (\mathcal{D}_0 \nabla_{\mathbf{y}} M_{1j} + \mathcal{D}_0 \nabla_{\mathbf{x}} M_{0j} - \imath q_0 F_0 \mathcal{D}_0 \mathbf{u_g} M_{0j}) = \\ \qquad -\mathrm{div}_{\mathbf{x}} (\mathcal{D}_0 \nabla_{\mathbf{y}} M_{0j}) + \frac{\partial}{\partial \tau} M_{0j} + \imath q_0 F_0 \mathcal{D}_0 \mathbf{u_g} \cdot \nabla_{\mathbf{y}} M_{0j} = 0 & \text{in } Y_j \\ \mathcal{D}_0 \nabla_{\mathbf{y}} M_{1j} \cdot \nu + \mathcal{D}_0 \nabla_{\mathbf{x}} M_{0j} \cdot \nu - \imath q_0 F_0 \mathcal{D}_0 M_{0j} \mathbf{u_g} \cdot \nu = 0 & \text{on } \Gamma_m \\ M_{1e} \text{ is } Y - \text{periodic.} \end{cases} \tag{5.18}$$

Since M_{0j}, $j \in \{e, c\}$ does not depend on $\mathbf{y}$, the above problem simplifies to

$$\begin{cases} -\mathrm{div}_{\mathbf{y}}\left(\mathcal{D}_0\nabla_{\mathbf{y}}M_{1j} + \mathcal{D}_0\nabla_{\mathbf{x}}M_{0j} - \imath q_0 F_0 \mathcal{D}_0\mathbf{u_g}M_{0j}\right) = -\frac{\partial}{\partial\tau}M_{0j} & \text{in } Y_j \\ \mathcal{D}_0\nabla_{\mathbf{y}}M_{1j}\cdot\nu + \mathcal{D}_0\nabla_{\mathbf{x}}M_{0j}\cdot\nu - \imath q_0 F_0\mathcal{D}_0\mathbf{u_g}M_{0j} = 0 & \text{on } \Gamma_m \\ M_{1e} \text{ is } Y-\text{periodic.} \end{cases} \tag{5.19}$$

Applying the Green's theorem we get that there exists a unique solution only if

$$-\int_{Y_j}\frac{\partial}{\partial\tau}M_{0j} = 0, \tag{5.20}$$

which, since M_{0j}, $j \in \{e, c\}$, does not depend on $\mathbf{y}$, implies that M_{0j} does not depend on time. Thus, using (5.9),

$$M_{0j}(\mathbf{x}, \mathbf{y}, \tau) = M_{\mathrm{ini}}. \tag{5.21}$$

Using the cell problem introduced in [42], we can also write, for $j \in \{e, c\}$,

$$M_{1j}(\mathbf{x}, \mathbf{y}, \tau) = (\nabla_{\mathbf{x}}M_{0j}(\mathbf{x}, \mathbf{y}, \tau) - \imath q_0 F_0 M_{0j}(\mathbf{x}, \mathbf{y}, \tau)\mathbf{u_g})\cdot\rho^j(\mathbf{y}), \tag{5.22}$$

where for $k = 1, \ldots, d$ (with d the dimension of the problem)

$$\begin{cases} -\mathrm{div}\left(\mathcal{D}_0^j\nabla\rho_k^j + \mathcal{D}_0\mathbf{e}_k\right) = 0 & \text{in } Y_j \\ \mathcal{D}_0^j\nabla\rho_k^j\cdot\nu + \mathcal{D}_0\mathbf{e}_k\cdot\nu = 0 & \text{on } \Gamma_m, \end{cases} \tag{5.23}$$

and is such that

$$\int_{Y_j}\rho_k^j(\mathbf{y})d\mathbf{y} = 0. \tag{5.24}$$

Moreover, if we assume that M_{ini} is constant as we discussed in Chapter 1, we also have that M_{0j} is independent from $\mathbf{x}$. Going on, M_{2j} is solution of

$$\begin{cases} -\mathrm{div}_{\mathbf{y}}\left(\mathcal{D}_0\nabla_{\mathbf{y}}M_{2j} + \mathcal{D}_0\nabla_{\mathbf{x}}M_{1j} - \imath q_0 F_0\mathcal{D}_0\mathbf{u_g}M_{1j}\right) = \\ \quad -\mathrm{div}_{\mathbf{x}}\left(\mathcal{D}_0\nabla_{\mathbf{y}}M_{1j} + \mathcal{D}_0\nabla_{\mathbf{x}}M_{0j} - \imath q_0 F_0\mathcal{D}_0\mathbf{u_g}M_{0j}\right) \\ \quad\quad +\frac{\partial}{\partial\tau}M_{1j} + \imath q_0 F_0\mathcal{D}_0\mathbf{u_g}\cdot(\nabla_{\mathbf{y}}M_{1j} + \nabla_{\mathbf{x}}M_{0j}) + q_0^2F_0^2\mathcal{D}_0\mathbf{u_g}\cdot\mathbf{u_g}M_{0j} = 0 & \text{in } Y_j \\ \mathcal{D}_0\nabla_{\mathbf{y}}M_{2j}\cdot\nu + \mathcal{D}_0\nabla_{\mathbf{x}}M_{1j}\cdot\nu - \imath q_0 F_0\mathcal{D}_0M_{1j}\mathbf{u_g}\cdot\nu = \kappa_0[\![M_{0j}]\!] & \text{on } \Gamma_m \\ M_{2e} \text{ is } Y-\text{periodic.} \end{cases} \tag{5.25}$$

Applying again the Green's theorem and remembering that $M_{0j}(\mathbf{x}, \mathbf{y}, \tau) = M_{\mathrm{ini}}$, thus $[\![M_{0j}]\!] = 0$, we obtain

$$\int_{Y_j}\left(\frac{\partial}{\partial\tau}M_{1j} + \imath q_0 F_0\mathcal{D}_0\mathbf{u_g}\cdot\nabla_{\mathbf{y}}M_{1j} + q_0^2F_0^2\mathcal{D}_0\mathbf{u_g}\cdot\mathbf{u_g}M_{0j}\right) = 0. \tag{5.26}$$

Using the above expression and (5.22) we get

$$\frac{1}{|Y_j|}\int_{Y_j}M_{1j}(\mathbf{x}, \mathbf{y}, \tau) = -q_0^2\overline{\mathbf{D}}^j\mathbf{u_g}\cdot\mathbf{u_g}M_{\mathrm{ini}}\int_0^\tau F_0^2(\xi)d\xi \tag{5.27}$$

where

$$\overline{\mathbf{D}}^j_{kl} := \frac{1}{|Y_j|}\int_{Y_j}\left(\nabla\rho^j_k(\mathbf{y})\cdot\mathbf{e}_l + \mathbf{e}_k\cdot\mathbf{e}_l\right)d\mathbf{y} \tag{5.28}$$

with $\mathbf{e}_i$ the i-th vector of the canonical basis of $\mathbb{R}^d$. The resulting signal attenuation is then

$$\begin{aligned}\overline{S}(T_E,q,\mathbf{u_g}) &= \frac{1}{S_0}\sum_{j=e,c}\left(\int_{Y_j}M_{0j}(\mathbf{x},\mathbf{y},\tau)+\varepsilon\int_{Y_j}M_{1j}(\mathbf{x},\mathbf{y},\tau)\right)+O(\varepsilon^2)\\ &= \sum_{j=e,c}v_j\left(1-\varepsilon q_0^2\int_0^{\widetilde{T_E}}F_0^2(\xi)d\xi\,\overline{\mathbf{D}}^j\mathbf{u_g}\cdot\mathbf{u_g}\right)+O(\varepsilon^2)\\ &= \sum_{j=e,c}v_j\left(1-b\overline{\mathbf{D}}^j\mathbf{u_g}\cdot\mathbf{u_g}\right)+O(\varepsilon^2).\end{aligned}$$

where v_e and v_c are the volume fractions of the compartments Y_e and Y_c respectively. We observe that the resulting apparent diffusion coefficient,

$$ADC = v_e\overline{\mathbf{D}}^e\mathbf{u_g}\cdot\mathbf{u_g} + v_c\overline{\mathbf{D}}^c\mathbf{u_g}\cdot\mathbf{u_g}, \tag{5.29}$$

is the same as the one in the FPK model ([42]) described in Section 2.2.3. In particular, it is time-independent.

Keeping $\alpha = 1$, we also tried other values of γ which respected the conditions in Section 5.2. We do not report the result here because we always obtained a time-independent effective diffusion coefficient. Inspired by the classical definition of short-time regime (see Section 2.1.2), my conjecture was then that, if we consider a scaling in time which is comparable with the length scaling, all the obtained models describe the phenomenon when diffusion is already Gaussian and the apparent diffusion coefficient is constant. The obvious consequence was then to increase the value of α.

5.4 Diffusion time scale shorter than the cell size $\alpha = 2$

Among the values of $\alpha > 1$ that satisfy the conditions (5.15) and (5.16), the most convenient choice to render the equation for M_{0j} time dependent is $\alpha = 2$ as we had for the model in Chapter 4. Mathematically, this choice of α guarantees the coupling between the derivation in time and the divergence operator in $\mathbf{y}$ in equation (5.6). Indeed, we can rewrite (5.6) as

$$\begin{aligned}0 = &\sum_{i=0}^{\infty}\varepsilon^{i-2}\frac{\partial}{\partial\tau}\widetilde{M}_{ij} + \varepsilon^{i+4-2\gamma}q_0^2\mathbf{u_g}\cdot\mathbf{u_g}F_0(\tau)^2\mathcal{D}_0^j\widetilde{M}_{ij}\\ &+\varepsilon^{i+2-\gamma}\imath q_0\mathbf{u_g}F_0(\tau)\mathcal{D}_0^j(\nabla_{\mathbf{x}}\widetilde{M}_{ij}+\varepsilon^{-1}\nabla_{\mathbf{y}}\widetilde{M}_{ij}) - \varepsilon^i\mathrm{div}_{\mathbf{x}}(\mathcal{D}_0^j\nabla_{\mathbf{x}}\widetilde{M}_{ij})\\ &-\varepsilon^{i-1}\mathrm{div}_{\mathbf{x}}(\mathcal{D}_0^j\nabla_{\mathbf{y}}\widetilde{M}_{ij}) - \varepsilon^{i-1}\mathrm{div}_{\mathbf{y}}(\mathcal{D}_0^j\nabla_{\mathbf{x}}\widetilde{M}_{ij}) - \varepsilon^{i-2}\mathrm{div}_{\mathbf{y}}(\mathcal{D}_0^j\nabla_{\mathbf{y}}\widetilde{M}_{ij})\\ &+\varepsilon^{i+2-\gamma}\mathrm{div}_{\mathbf{x}}(\imath q_0\mathbf{u_g}F_0(\tau)\mathcal{D}_0^j\widetilde{M}_{ij}) + \varepsilon^{i+1-\gamma}\mathrm{div}_{\mathbf{y}}(\imath q_0\mathbf{u_g}F_0(\tau)\mathcal{D}_0^j\widetilde{M}_{ij}) \quad \text{in } Y_j\times]0,T_E/\varepsilon^2[,\end{aligned} \tag{5.30}$$

and (5.7) as

$$\sum_{i=0}^{\infty}\varepsilon^{i+1}\kappa_0\Big(\widetilde{M}_{ie}-\widetilde{M}_{ic}\Big) = \varepsilon^{-1}\mathcal{D}_0^j\nabla_{\mathbf{y}}\widetilde{M}_{0j}\cdot\nu + \varepsilon^0\Big(\mathcal{D}_0^j\nabla_{\mathbf{y}}\widetilde{M}_{1j}+\mathcal{D}_0^j\nabla_{\mathbf{x}}\widetilde{M}_{0j}-\varepsilon^{2-\gamma}\imath q_0\mathbf{u_g}F_0\mathcal{D}_0^j\widetilde{M}_{0j}\Big)\cdot\nu + \sum_{i=1}^{\infty}\varepsilon^i\Big(\mathcal{D}_0^j\nabla_{\mathbf{y}}\widetilde{M}_{i+1j}+\mathcal{D}_0^j\nabla_{\mathbf{x}}\widetilde{M}_{ij}-\varepsilon^{2-\gamma}\imath q_0\mathbf{u_g}F_0\mathcal{D}_0^j\widetilde{M}_{ij}\Big)\cdot\nu \quad \text{on } \Gamma_j\times]0,T_E/\varepsilon^2[, \tag{5.31}$$

Now for $\gamma=2$ we obtain the same model as Chapter 4 but, for our assumptions in Section 5.2, $\gamma\in[0,3[$, so it is interesting to see what happens in the limit cases $\gamma=0$, $\gamma=1$ and $\gamma=3$ which identifies three regimes of strength for the applied magnetic field: moderate intensity, relatively strong intensity and very strong intensity.

5.4.1 Moderate intensity: $\gamma=0$

With this choice of parameters the scaling on b-value is

$$b=\varepsilon^6 b_0 \tag{5.32}$$

and the asymptotic PDE problem takes the form

$$\begin{cases}
\sum_{i=0}^{\infty}\varepsilon^i\frac{\partial}{\partial\tau}\widetilde{M}_{ij}+\varepsilon^{i+6}q_0^2\mathbf{u_g}\cdot\mathbf{u_g}F_0(\tau)^2\mathcal{D}_0^j\widetilde{M}_{ij}-\varepsilon^{i+2}\mathrm{div}_{\mathbf{x}}(\mathcal{D}_0^j\nabla_{\mathbf{x}}\widetilde{M}_{ij}) & \\
\quad -\varepsilon^{i+1}\mathrm{div}_{\mathbf{x}}(\mathcal{D}_0^j\nabla_{\mathbf{y}}\widetilde{M}_{ij})-\varepsilon^{i+1}\mathrm{div}_{\mathbf{y}}(\mathcal{D}_0^j\nabla_{\mathbf{x}}\widetilde{M}_{ij})-\varepsilon^{i}\mathrm{div}_{\mathbf{y}}(\mathcal{D}_0^j\nabla_{\mathbf{y}}\widetilde{M}_{ij}) & \\
\quad +\varepsilon^{i+4}\mathrm{div}_{\mathbf{x}}(\imath q_0\mathbf{u_g}F_0(\tau)\mathcal{D}_0^j\widetilde{M}_{ij})+\varepsilon^{i+3}\mathrm{div}_{\mathbf{y}}(\imath q_0\mathbf{u_g}F_0(\tau)\mathcal{D}_0^j\widetilde{M}_{ij}) & \\
\quad +\varepsilon^{i+4}\imath q_0\mathbf{u_g}F_0(\tau)\mathcal{D}_0^j(\nabla_{\mathbf{x}}\widetilde{M}_{ij}+\varepsilon^{-1}\nabla_{\mathbf{y}}\widetilde{M}_{ij})=0 & \text{in } Y_j\times]0,T_E/\varepsilon^2[,\\
\sum_{i=0}^{\infty}\varepsilon^i\Big(\mathcal{D}_0^j\nabla_{\mathbf{y}}\widetilde{M}_{ij}+\varepsilon^{i+1}\mathcal{D}_0^j\nabla_{\mathbf{x}}\widetilde{M}_{ij}-\varepsilon^{i+3}\imath q_0\mathbf{u_g}F_0\mathcal{D}_0^j\widetilde{M}_{ij}\Big)\cdot\nu = & \\
\qquad \sum_{i=0}^{\infty}\varepsilon^{i+2}\kappa_0\Big(\widetilde{M}_{ie}-\widetilde{M}_{ic}\Big) & \text{on } \Gamma_j\times]0,T_E/\varepsilon^2[,\\
\sum_{i=0}^{\infty}\Big[\!\Big[\mathcal{D}_0^j\Big(\varepsilon^{i+1}\nabla_x\widetilde{M}_{ij}+\varepsilon^i\nabla_y\widetilde{M}_{ij}-\varepsilon^{i+3}\imath q_0F_0(\tau)\widetilde{M}_{ij}\mathbf{u_g}\Big)\cdot\nu\Big]\!\Big]=0 & \text{on } \Gamma_m\times]0,T_E/\varepsilon^2[,\\
\widetilde{M}_{0j}(\cdot,\cdot,0)=M_{\mathrm{ini}},\quad\text{and}\quad \widetilde{M}_{ij}(\cdot,\cdot,0)=0\qquad\forall i>0 & \text{in } Y_j\\
M_{ie}\text{ is } Y-\text{periodic }\forall i. &
\end{cases} \tag{5.33}$$

Matching the powers of ε, for $j=e,c$, we obtain

$$\begin{aligned}
M_{0j}(\mathbf{x},\mathbf{y},\tau) &= M_{\mathrm{ini}},\\
M_{1j}(\mathbf{x},\mathbf{y},\tau) &= M_{2j}(\mathbf{x},\mathbf{y},\tau)=0\\
M_{3j}(\mathbf{x},\mathbf{y},\tau) &= \imath\sum_{l=1}^{d}q_0M_{\mathrm{ini}}\,\omega_l^j(\mathbf{y})(\mathbf{e}_l\cdot\mathbf{u_g})\\
M_{4j}(\mathbf{x},\mathbf{y},\tau) &= 0,
\end{aligned}$$

and $M_{5j}(\mathbf{x}, \mathbf{y}, \tau)$ solves

$$\begin{cases} \dfrac{\partial}{\partial \tau} M_{5j} - \operatorname{div}_{\mathbf{y}} \left(\mathcal{D}_0 \nabla_{\mathbf{y}} M_{5j} \right) = 0 & \text{in } Y_j \times [0, T_E/\varepsilon^2] \\ \mathcal{D}_0 \nabla_{\mathbf{y}} M_{5j} \cdot \nu = \kappa_0 [\![M_{3j}]\!] & \text{om } \Gamma_m \times [0, T_E/\varepsilon^2] \end{cases}$$

with $\int_{Y_j} M_{5j} = 0$. For $M_{6j}(\mathbf{x}, \mathbf{y}, \tau)$ we obtain the following compatibility condition

$$\int_{Y_j} \left(\frac{\partial}{\partial \tau} M_{6j}(\mathbf{x}, \mathbf{y}, \tau) + \imath q_0 F_0 \mathcal{D}_0 \nabla_{\mathbf{y}} M_{3j}(\mathbf{x}, \mathbf{y}, \tau) + q_0^2 \mathbf{u_g} \cdot \mathbf{u_g} F_0(\tau)^2 \mathcal{D}_0^j M_{\text{ini}} \cdot \mathbf{u_g} \right) d\mathbf{y} = 0,$$

where $\mathbf{e}_l$ is the l-th element of the $\mathbb{R}^d$ canonical basis and $\omega_l^j(\mathbf{y}, \tau)$, for $l = 1, \ldots, d$ is solution of

$$\begin{cases} \dfrac{\partial}{\partial \tau} \omega_l^j - \operatorname{div}_{\mathbf{y}} \left(\mathcal{D}_0 \nabla_{\mathbf{y}} \omega_l^j - F_0 \mathcal{D}_0 \mathbf{e}_l \right) = 0 & \text{in } Y_j \times [0, T_E/\varepsilon^2] \\ \mathcal{D}_0 \nabla_{\mathbf{y}} \omega_l^j \cdot \nu - F_0 \mathcal{D}_0 \mathbf{e}_l \cdot \nu = 0 & \text{on } \Gamma_m \times [0, T_E/\varepsilon^2]. \end{cases} \tag{5.34}$$

We can thus write the signal attenuation as

$$\begin{aligned} \overline{S}(T_E, q, \mathbf{u_g}) &= \frac{1}{S_0} \sum_{j=e,c} \sum_{i=1}^{6} \varepsilon^i \int_{Y_j} M_{ij}(\mathbf{x}, \mathbf{y}, \tau) + O(\varepsilon^7) \\ &= \sum_{j=e,c} v_j \left(1 - \varepsilon q_0^2 \int_0^{\widetilde{T_E}} F_0^2(\xi) d\xi \, \overline{\mathbf{D}}^j(\widetilde{T_E}) \mathbf{u_g} \cdot \mathbf{u_g} \right) + O(\varepsilon^7) \\ &= \sum_{j=e,c} v_j \left(1 - b \overline{\mathbf{D}}^j(\widetilde{T_E}) \mathbf{u_g} \cdot \mathbf{u_g} \right) + O(\varepsilon^7), \end{aligned}$$

where v_e and v_c are the volume fractions of the compartments Y_e and Y_c respectively and

$$\overline{\mathbf{D}}^j(\widetilde{T_E})_{kl} = \frac{1}{|Y_j|} \int_{Y_j} \mathcal{D}_0^j \, \mathbf{e}_k \cdot \mathbf{e}_l - \frac{1}{\int_0^{\widetilde{T_E}} F_0^2} \int_0^{\widetilde{T_E}} \left(F_0 \frac{1}{|Y_j|} \int_{Y_j} \mathcal{D}_0^j \frac{\partial}{\partial y_l} \omega_k^j \right), \; k, l = 1, \ldots, d \tag{5.35}$$

is the apparent diffusion tensor. We observe that this model corresponds to the one with $\alpha = \gamma = 2$ derived in Chapter 4 but its regime of validity is for smaller b-values because the scaling in the gradient intensity is smaller.

5.4.2 Relatively strong intensity: $\gamma = 1$

With this choice of parameters the scaling on b-value is

$$b = \varepsilon^4 b_0 \tag{5.36}$$

and the asymptotic PDE problem takes the form

$$\begin{cases} \sum_{i=0}^{\infty} \varepsilon^i \frac{\partial}{\partial \tau} \widetilde{M}_{ij} + \varepsilon^{i+4} q_0^2 \mathbf{u_g} \cdot \mathbf{u_g} F_0(\tau)^2 \mathcal{D}_0^j \widetilde{M}_{ij} - \varepsilon^{i+2} \mathrm{div}_{\mathbf{x}}(\mathcal{D}_0^j \nabla_{\mathbf{x}} \widetilde{M}_{ij}) \\ \quad -\varepsilon^{i+1} \mathrm{div}_{\mathbf{x}}(\mathcal{D}_0^j \nabla_{\mathbf{y}} \widetilde{M}_{ij}) - \varepsilon^{i+1} \mathrm{div}_{\mathbf{y}}(\mathcal{D}_0^j \nabla_{\mathbf{x}} \widetilde{M}_{ij}) - \varepsilon^i \mathrm{div}_{\mathbf{y}}(\mathcal{D}_0^j \nabla_{\mathbf{y}} \widetilde{M}_{ij}) \\ \quad +\varepsilon^{i+3} \mathrm{div}_{\mathbf{x}}(\imath q_0 \mathbf{u_g} F_0(\tau) \mathcal{D}_0^j \widetilde{M}_{ij}) + \varepsilon^{i+2} \mathrm{div}_{\mathbf{y}}(\imath q_0 \mathbf{u_g} F_0(\tau) \mathcal{D}_0^j \widetilde{M}_{ij}) \\ \quad +\varepsilon^{i+3} \imath q_0 \mathbf{u_g} F_0(\tau) \mathcal{D}_0^j (\nabla_{\mathbf{x}} \widetilde{M}_{ij} + \varepsilon^{-1} \nabla_{\mathbf{y}} \widetilde{M}_{ij}) = 0 & \text{in } Y_j \times]0, T_E/\varepsilon^2[, \\ \sum_{i=0}^{\infty} \varepsilon^i \Big(\mathcal{D}_0^j \nabla_{\mathbf{y}} \widetilde{M}_{ij} + \varepsilon^{i+1} \mathcal{D}_0^j \nabla_{\mathbf{x}} \widetilde{M}_{ij} - \varepsilon^{i+2} \imath q_0 \mathbf{u_g} F_0 \mathcal{D}_0^j \widetilde{M}_{ij} \Big) \cdot \nu = \\ \qquad \sum_{i=0}^{\infty} \varepsilon^{i+2} \kappa_0 \Big(\widetilde{M}_{ie} - \widetilde{M}_{ic} \Big) & \text{on } \Gamma_j \times]0, T_E/\varepsilon^2[, \\ \sum_{i=0}^{\infty} \Big[\!\Big[\mathcal{D}_0^j \left(\varepsilon^{i+1} \nabla_x \widetilde{M}_{ij} + \varepsilon^i \nabla_y \widetilde{M}_{ij} - \varepsilon^{i+2} \imath q_0 F_0(\tau) \widetilde{M}_{ij} \mathbf{u_g} \right) \cdot \nu \Big]\!\Big] = 0 & \text{on } \Gamma_m \times]0, T_E/\varepsilon^2[, \\ \widetilde{M}_{0j}(\cdot, \cdot, 0) = M_{\mathrm{ini}}, \quad \text{and} \quad \widetilde{M}_{ij}(\cdot, \cdot, 0) = 0 \qquad \forall i > 0 & \text{in } Y_j \\ M_{ie} \text{ is } Y - \text{periodic } \forall i. \end{cases} \tag{5.37}$$

Matching the powers of ε, for $j = e, c$, we obtain

$$\begin{aligned} M_{0j}(\mathbf{x}, \mathbf{y}, \tau) &= M_{\mathrm{ini}}, \\ M_{1j}(\mathbf{x}, \mathbf{y}, \tau) &= 0 \\ M_{2j}(\mathbf{x}, \mathbf{y}, \tau) &= \imath \sum_{l=1}^{d} q_0 M_{\mathrm{ini}}\, \omega_l^j(\mathbf{y})(\mathbf{e}_l \cdot \mathbf{u_g}) \\ M_{3j}(\mathbf{x}, \mathbf{y}, \tau) &= 0 \end{aligned}$$

and the compatibility condition

$$\int_{Y_j} \left(\frac{\partial}{\partial \tau} M_{4j}(\mathbf{x}, \mathbf{y}, \tau) + \imath q_0 F_0 \mathcal{D}_0 \nabla_{\mathbf{y}} M_{2j}(\mathbf{x}, \mathbf{y}, \tau) + q_0^2 \mathbf{u_g} \cdot \mathbf{u_g} F_0(\tau)^2 \mathcal{D}_0^j M_{\mathrm{ini}} \cdot \mathbf{u_g} \right) d\mathbf{y} = 0,$$

where $\mathbf{e}_l$ is the l-th element of the $\mathbb{R}^d$ canonical basis and $\omega_l^j(\mathbf{y}, \tau)$, for $l = 1, \ldots, d$ and $j = e, c$, is solution of the cell problem in (5.34). For the signal attenuation we thus obtain

$$\begin{aligned} \overline{S}(T_E, q, \mathbf{u_g}) &= \frac{1}{S_0} \sum_{j=e,c} \sum_{i=1}^{4} \varepsilon^i \int_{Y_j} M_{ij}(\mathbf{x}, \mathbf{y}, \tau) + O(\varepsilon^5) \\ &= \sum_{j=e,c} v_j \left(1 - \varepsilon q_0^2 \int_0^{\widetilde{T_E}} F_0^2(\xi) d\xi\, \overline{\mathbf{D}}^j(\widetilde{T_E}) \mathbf{u_g} \cdot \mathbf{u_g} \right) + O(\varepsilon^5) \\ &= \sum_{j=e,c} v_j \left(1 - b \overline{\mathbf{D}}^j(T_E) \mathbf{u_g} \cdot \mathbf{u_g} \right) + O(\varepsilon^5), \end{aligned}$$

where v_e and v_c are the volume fractions of the compartments Y_e and Y_c respectively and $\overline{\mathbf{D}}^j(\widetilde{T_E})$ is defined in (5.35). This model corresponds again to the one derived for $\alpha = \gamma = 2$ in Chapter

4 but is valid for smaller b-values because the scaling in the gradient intensity is smaller. It is then interesting to see what happens in the limit case of very strong gradient $\gamma = 3$.

5.4.3 Very strong intensity: $\gamma = 3$

With this choice of parameters the scaling on b-value is

$$b = \varepsilon^0 b_0 \tag{5.38}$$

and the asymptotic PDE problem takes the form

$$\begin{cases}
\sum_{i=0}^{\infty} \varepsilon^i \frac{\partial}{\partial \tau} \widetilde{M}_{ij} + \varepsilon^i q_0^2 \mathbf{u_g} \cdot \mathbf{u_g} F_0(\tau)^2 \mathcal{D}_0^j \widetilde{M}_{ij} - \varepsilon^{i+2} \mathrm{div}_{\mathbf{x}}(\mathcal{D}_0^j \nabla_{\mathbf{x}} \widetilde{M}_{ij}) \\
\quad -\varepsilon^{i+1} \mathrm{div}_{\mathbf{x}}(\mathcal{D}_0^j \nabla_{\mathbf{y}} \widetilde{M}_{ij}) - \varepsilon^{i+1} \mathrm{div}_{\mathbf{y}}(\mathcal{D}_0^j \nabla_{\mathbf{x}} \widetilde{M}_{ij}) - \varepsilon^i \mathrm{div}_{\mathbf{y}}(\mathcal{D}_0^j \nabla_{\mathbf{y}} \widetilde{M}_{ij}) \\
\quad +\varepsilon^{i+1} \mathrm{div}_{\mathbf{x}}(\imath q_0 \mathbf{u_g} F_0(\tau) \mathcal{D}_0^j \widetilde{M}_{ij}) + \varepsilon^i \mathrm{div}_{\mathbf{y}}(\imath q_0 \mathbf{u_g} F_0(\tau) \mathcal{D}_0^j \widetilde{M}_{ij}) \\
\quad +\varepsilon^{i+1} \imath q_0 \mathbf{u_g} F_0(\tau) \mathcal{D}_0^j (\nabla_{\mathbf{x}} \widetilde{M}_{ij} + \varepsilon^{-1} \nabla_{\mathbf{y}} \widetilde{M}_{ij}) = 0 & \text{in } Y_j \times]0, T_E/\varepsilon^2[, \\
\sum_{i=0}^{\infty} \varepsilon^i \Big(\mathcal{D}_0^j \nabla_{\mathbf{y}} \widetilde{M}_{ij} + \varepsilon^{i+1} \mathcal{D}_0^j \nabla_{\mathbf{x}} \widetilde{M}_{ij} - \varepsilon^i \imath q_0 \mathbf{u_g} F_0 \mathcal{D}_0^j \widetilde{M}_{ij} \Big) \cdot \nu = \\
\qquad \sum_{i=0}^{\infty} \varepsilon^{i+2} \kappa_0 \Big(\widetilde{M}_{ie} - \widetilde{M}_{ic} \Big) & \text{on } \Gamma_j \times]0, T_E/\varepsilon^2[, \\
\sum_{i=0}^{\infty} \Big[\!\Big[\mathcal{D}_0^j \Big(\varepsilon^{i+1} \nabla_x \widetilde{M}_{ij} + \varepsilon^i \nabla_y \widetilde{M}_{ij} - \varepsilon^i \imath q_0 F_0(\tau) \widetilde{M}_{ij} \mathbf{u_g} \Big) \cdot \nu \Big]\!\Big] = 0 & \text{on } \Gamma_m \times]0, T_E/\varepsilon^2[, \\
\widetilde{M}_{0j}(\cdot, \cdot, 0) = M_{\mathrm{ini}}, \quad \text{and} \quad \widetilde{M}_{ij}(\cdot, \cdot, 0) = 0 \qquad \forall i > 0 & \text{in } Y_j \\
M_{ie} \text{ is } Y - \text{periodic } \forall i.
\end{cases}$$

Now if we write the problem for $\widetilde{M}_{0j}$ we find exactly the one in (5.2) with $\kappa = 0$. This means that this scaling corresponds exactly to the microscopic model, i.e. with this choice of parameters the homogenization does not help in simplifying the problem.

Our conjecture is then that, after having fixed the scaling of time $\alpha = 2$, for all choice of γ which gives us a small scaling in b-value (i.e. $\gamma < 3$) we retrieve the same model as in Chapter 4. Physically, this means that, for a scaling on time which is twice smaller than the scaling on space, we find the same models for every choice of the strength of the gradient which maintain us in a small regime of b-value (that is the regime under which we defined the ADC in Section 2.1.5).

Furthermore, we observe that this new model is also valid for relatively long time. Indeed, if $\widetilde{T_E}$ is sufficiently long, the problem in (5.34) can be approximated with the steady state problem (5.23) and thus we find the same diffusion tensor as in the FPK model (5.28) which is time-independent ([42]). This consists in a mathematical reason of why the H-ADC is valid also for relatively long time. Moreover, we observe that, all the model described in Section 5.4 that give and expression of ADC which coincides with the H-ADC, verify also the property $gF(t) = O(\varepsilon)$ that was used in Section 4.4 to recover the H-ADC trough linearization. Thus, all these models are equivalent to describe the ADC but they better identify in which regime the H-ADC is valid.

As discussed in Chapter 4, the models obtained with $\alpha = 2$ are independent from the membrane permeability. This happens because, considering M_{ini} a constant independent from space, in the asymptotic model, we loose the information on the surface, since $[\![M_{\text{ini}}]\!]_{\Gamma_m} = 0$. Hereafter, we report the results in which M_{ini} is piecewise constant and assumes two different values in the intra-cellurar and extra-cellular space. We shall see that even if the asymptotic model depend on κ_0, the signal model remains independent from κ_0.

5.5 M_{ini} space dependent for $\alpha = 2$

We consider $\alpha = 2$ because it is the choice for which we have a coupling between the derivative in time and the divergence with respect to the $\mathbf{y}$ variable in (5.6). This is a case for which we are sure that we can obtain a time dependent ADC. Nevertheless, if one is interested, a similar analysis could be done also for the other choices of α.

We define M_{ini} piecewise constant, i.e.

$$M_{\text{ini}}(\mathbf{x}) = \widetilde{M}_{\text{ini}}(\mathbf{x},\mathbf{y}) = \begin{cases} c_e & \text{if } \mathbf{y} \in Y_e \\ c_c & \text{if } \mathbf{y} \in Y_c, \end{cases} \tag{5.39}$$

where c_e and c_c are two different positive constants. We then consider the asymptotic equation given in (5.30) along with the boundary conditions in (5.31) and the new initial conditions

$$\widetilde{M}_{0j}(\mathbf{x},\mathbf{y},0) = c_j \quad \text{and} \quad \widetilde{M}_{ij}(\mathbf{x},\mathbf{y},0) = 0 \quad \forall i > 0. \tag{5.40}$$

If we impose $\gamma = 2$, then we have

$$\begin{aligned} \widetilde{M}_{0j}(\mathbf{x},\mathbf{y},\tau) &= c_j \\ \widetilde{M}_{1j}(\mathbf{x},\mathbf{y},\tau) &= \imath \sum_{l=1}^{d} q_0 c_j\, \omega_l^j(\mathbf{y},\tau)(\mathbf{e}_l \cdot \mathbf{u_g}) \end{aligned}$$

and $\widetilde{M}_{2j}(\mathbf{x},\mathbf{y},\tau)$ solves,

$$\begin{cases} -\text{div}_{\mathbf{y}}\left(\mathcal{D}_0^j \nabla_{\mathbf{y}} \widetilde{M}_{2j} - \imath q_0 \mathbf{u_g} F_0 \mathcal{D}_0^j \widetilde{M}_{1j}\right) = -\dfrac{\partial}{\partial \tau}\widetilde{M}_{2j} & \\ \qquad\qquad -q_0^2 F_0^2 \mathcal{D}_0^j \widetilde{M}_{0j} - \imath q_0 \mathbf{u_g} F_0 \mathcal{D}_0^j \nabla_{\mathbf{y}} \widetilde{M}_{1j} & \text{in } Y_j \times]0, T/\varepsilon^2[, \\ \mathcal{D}_0^j \nabla_{\mathbf{y}} \widetilde{M}_{2e} \cdot \nu - \imath q_0 \mathbf{u_g} F_0 \mathcal{D}_0^e \widetilde{M}_{1e} \cdot \nu = \kappa_0 (c_e - c_c) & \text{on } \Gamma_m \times]0, T/\varepsilon^2[, \\ \mathcal{D}_0^c \nabla_{\mathbf{y}} \widetilde{M}_{2c} \cdot \nu - \imath q_0 \mathbf{u_g} F_0 \mathcal{D}_0^c \widetilde{M}_{1c} \cdot \nu = \kappa_0 (c_c - c_e) & \text{on } \Gamma_m \times]0, T/\varepsilon^2[, \\ \widetilde{M}_{2j}(\cdot, 0) = 0 & \text{in } Y_j, \\ \widetilde{M}_{2j} \text{ is } Y\text{-periodic.} & \end{cases} \tag{5.41}$$

Thus, the imaginary part of $\widetilde{M}_{2j}$ remains equal to 0, but for the real part, applying the Green's theorem we obtain

$$\begin{aligned} \int_{Y_e} \left(\frac{\partial}{\partial \tau}\widetilde{M}_{2e} + q_0^2 F_0^2 \mathcal{D}_0^e \widetilde{M}_{0e} + \imath q_0 \mathbf{u_g} F_0 \mathcal{D}_0^e \nabla_{\mathbf{y}} \widetilde{M}_{1e} \right) &= \int_{\Gamma_m} \kappa_0 (c_e - c_c), \\ \int_{Y_c} \left(\frac{\partial}{\partial \tau}\widetilde{M}_{2c} + q_0^2 F_0^2 \mathcal{D}_0^c \widetilde{M}_{0c} + \imath q_0 \mathbf{u_g} F_0 \mathcal{D}_0^c \nabla_{\mathbf{y}} \widetilde{M}_{1c} \right) &= \int_{\Gamma_m} \kappa_0 (c_c - c_e). \end{aligned}$$

Integrating in time, and remembering the expression of $\widetilde{M}_{1j}(\mathbf{x}, \mathbf{y}, \tau)$, the above equations become

$$\int_{Y_e} \widetilde{M}_{2e} = \int_0^t \int_{Y_e} \left(-q_0^2 F_0^2 \mathcal{D}_0^e c_e - q_0^2 \mathbf{u_g} F_0 \mathcal{D}_0^e \nabla_{\mathbf{y}} \omega^e(\mathbf{y}, \tau) \cdot \mathbf{u_g} c_e\right) + t \int_{\Gamma_m} \kappa_0 \left(c_e - c_c\right),$$
$$\int_{Y_c} \widetilde{M}_{2c} = \int_0^t \int_{Y_c} \left(-q_0^2 F_0^2 \mathcal{D}_0^c c_c - q_0^2 \mathbf{u_g} F_0 \mathcal{D}_0^c \nabla_{\mathbf{y}} \omega^c(\mathbf{y}, \tau) \cdot \mathbf{u_g} c_c\right) - t \int_{\Gamma_m} \kappa_0 \left(c_e - c_c\right).$$

Since the two boundary conditions have opposite signs, writing the signal attenuation we obtain again

$$\overline{S}(T_E, q, \mathbf{u_g}) = \sum_{j=e,c} \theta_j \left(1 - b \overline{\mathbf{D}}^j(T_E) \mathbf{u_g} \cdot \mathbf{u_g}\right) + O(\varepsilon^3), \quad \theta_j = \frac{c_j |Y_j|}{c_e |Y_e| + c_c |Y_c|}$$

where $\overline{\mathbf{D}}^j(T_E)$ is defined in (5.35). We therefore obtain the same expression as in the case $M_{\text{ini}} = M_0$.

If we impose $\gamma = 1$, then we obtain

$$\begin{aligned}
&M_{0j}(\mathbf{x}, \mathbf{y}, \tau) = c_j, \\
&M_{1j}(\mathbf{x}, \mathbf{y}, \tau) = 0 \\
&M_{2j}(\mathbf{x}, \mathbf{y}, \tau) = \imath \sum_{l=1}^{d} q_0 c_j \, \omega_l^j(\mathbf{y}, \tau)(\mathbf{e}_l \cdot \mathbf{u_g}) + \psi^j(\mathbf{x}, \mathbf{y}, \tau) \\
&M_{3j}(\mathbf{x}, \mathbf{y}, \tau) = 0
\end{aligned}$$

where $\psi^j(\mathbf{x}, \mathbf{y})$ solves

$$\begin{cases}
\dfrac{\partial}{\partial \tau} \psi^j - \operatorname{div}_{\mathbf{y}} \left(\mathcal{D}_0 \nabla_{\mathbf{y}} \psi^j\right) = 0 & \text{in } Y_j \times]0, T/\varepsilon^2[\\
\mathcal{D}_0 \nabla_{\mathbf{y}} \psi^e \cdot \nu = \kappa_0 \left(M_{0e} - M_{0c}\right) & \text{on } \Gamma_m \times]0, T/\varepsilon^2[\\
\mathcal{D}_0 \nabla_{\mathbf{y}} \psi^c \cdot \nu = \kappa_0 \left(M_{0c} - M_{0e}\right) & \text{on } \Gamma_m \times]0, T/\varepsilon^2[\\
\psi^j(\mathbf{y}, 0) = 0 & \text{in } Y_j
\end{cases} \tag{5.42}$$

and for $M_{4j}(\mathbf{x}, \mathbf{y}, \tau)$ we obtain

$$\int_{Y_e} \widetilde{M}_{4e} = \int_0^t \int_{Y_e} \left(-q_0^2 F_0^2 \mathcal{D}_0^e c_e - \imath q_0 \mathbf{u_g} F_0 \mathcal{D}_0^e \nabla_{\mathbf{y}} M_{2e} \cdot \mathbf{u_g}\right) + \int_0^t \int_{\Gamma_m} \kappa_0 \left(M_{2e} - M_{2c}\right),$$
$$\int_{Y_c} \widetilde{M}_{4c} = \int_0^t \int_{Y_c} \left(-q_0^2 F_0^2 \mathcal{D}_0^c c_c - \imath q_0 \mathbf{u_g} F_0 \mathcal{D}_0^c \nabla_{\mathbf{y}} M_{2c} \cdot \mathbf{u_g}\right) - \int_0^t \int_{\Gamma_m} \kappa_0 \left(M_{2e} - M_{2c}\right).$$

However, since the boundary conditions containing the jumps have opposite signs, ω^j has zero Y_j-mean, $\int_{Y_e} \psi^e = t \int_{\Gamma_m} \kappa_0 \left(M_{0e} - M_{0c}\right)$ and $\int_{Y_c} \psi^c = -t \int_{\Gamma_m} \kappa_0 \left(M_{0e} - M_{0c}\right)$ we end up with the same signal attenuation

$$\overline{S}(T_E, q, \mathbf{u_g}) = \sum_{j=e,c} \theta_j \left(1 - b \overline{\mathbf{D}}^j(T_E) \mathbf{u_g} \cdot \mathbf{u_g}\right) + O(\varepsilon^5), \quad \theta_j = \frac{c_j |Y_j|}{c_e |Y_e| + c_c |Y_c|},$$

where $\overline{\mathbf{D}}^j(T_E)$ is defined in (5.35).

If we impose $\gamma = 0$, then we obtain

$$\begin{aligned}
M_{0j}(\mathbf{x},\mathbf{y},\tau) &= c_j,\\
M_{1j}(\mathbf{x},\mathbf{y},\tau) &= 0\\
M_{2j}(\mathbf{x},\mathbf{y},\tau) &= \imath \sum_{l=1}^{d} q_0 c_j\, \omega_l^j(\mathbf{y},\tau)(\mathbf{e}_l\cdot\mathbf{u_g}) + \psi^j(\mathbf{x},\mathbf{y},\tau)\\
M_{3j}(\mathbf{x},\mathbf{y},\tau) &= 0\\
M_{4j}(\mathbf{x},\mathbf{y},\tau) &= \phi^j(\mathbf{x},\mathbf{y},\tau)
\end{aligned}$$

where ψ^j is defined in (5.42), $\phi^j(\mathbf{x},\mathbf{y},\tau)$ solves

$$\begin{cases}
\dfrac{\partial}{\partial\tau}\phi^j - \operatorname{div}_{\mathbf{y}}\left(\mathcal{D}_0\nabla_{\mathbf{y}}\phi^j\right) = 0 & \text{in } Y_j\times]0,T/\varepsilon^2[\\
\mathcal{D}_0\nabla_{\mathbf{y}}\phi^e\cdot\nu = \kappa_0\left(M_{2e}-M_{2c}\right) & \text{on } \Gamma_m\times]0,T/\varepsilon^2[\\
\mathcal{D}_0\nabla_{\mathbf{y}}\phi^c\cdot\nu = \kappa_0\left(M_{2c}-M_{2e}\right) & \text{on } \Gamma_m\times]0,T/\varepsilon^2[\\
\psi^j(\mathbf{y},0) = 0 & \text{in } Y_j
\end{cases} \tag{5.43}$$

$M_{5j}(\mathbf{x},\mathbf{y},\tau)$ solves

$$\begin{cases}
\dfrac{\partial}{\partial\tau}M_{5j} - \operatorname{div}_{\mathbf{y}}\left(\mathcal{D}_0\nabla_{\mathbf{y}}M_{5j} - \imath q_0F_0\mathcal{D}_0M_{2j}\mathbf{u_g}\right) = 0 & \text{in } Y_j\times[0,T_E/\varepsilon^2]\\
\mathcal{D}_0\nabla_{\mathbf{y}}M_{5j}\cdot\nu - \imath q_0F_0\mathcal{D}_0M_{2j}\mathbf{u_g}\cdot\nu = \kappa_0[\![M_{3j}]\!] & \text{on } \Gamma_m\times[0,T_E/\varepsilon^2]
\end{cases} \tag{5.44}$$

and for $M_{6j}(\mathbf{x},\mathbf{y},\tau)$ we obtain the following conditions

$$\begin{aligned}
\int_{Y_e}\widetilde{M}_{6e} &= \int_0^t\int_{Y_e}\left(-q_0^2F_0^2\mathcal{D}_0^ec_e - \imath q_0\mathbf{u_g}F_0\mathcal{D}_0^e\nabla_{\mathbf{y}}M_{3e}\cdot\mathbf{u_g}\right) + \int_0^t\int_{\Gamma_m}\kappa_0\left(M_{4e}-M_{4c}\right),\\
\int_{Y_c}\widetilde{M}_{6c} &= \int_0^t\int_{Y_c}\left(-q_0^2F_0^2\mathcal{D}_0^cc_c - \imath q_0\mathbf{u_g}F_0\mathcal{D}_0^c\nabla_{\mathbf{y}}M_{3c}\cdot\mathbf{u_g}\right) - \int_0^t\int_{\Gamma_m}\kappa_0\left(M_{4e}-M_{4c}\right).
\end{aligned}$$

However applying the Green's theorem to their systems of definition we obtain

$$\begin{aligned}
\int_{Y_e}\psi^e &= t\int_{\Gamma_m}\kappa_0\left(M_{0e}-M_{0c}\right)\\
\int_{Y_c}\psi^c &= -t\int_{\Gamma_m}\kappa_0\left(M_{0e}-M_{0c}\right)\\
\int_{Y_e}\phi^e &= \int_0^t\int_{\Gamma_m}\kappa_0\left(M_{2e}-M_{2c}\right)\\
\int_{Y_c}\phi^c &= -\int_0^t\int_{\Gamma_m}\kappa_0\left(M_{2e}-M_{2c}\right)\\
\int_{Y_e}M_{5e} &= \int_0^t\int_{\Gamma_m}\kappa_0\left(M_{3e}-M_{3c}\right)\\
\int_{Y_c}M_{5c} &= -\int_0^t\int_{\Gamma_m}\kappa_0\left(M_{3e}-M_{3c}\right)
\end{aligned}$$

and thus we get again

$$\overline{S}(T_E, q, \mathbf{u_g}) = \sum_{j=e,c} \theta_j \left(1 - b\overline{\mathbf{D}}^j(T_E)\mathbf{u_g} \cdot \mathbf{u_g}\right) + O(\varepsilon^7), \quad \theta_j = \frac{c_j|Y_j|}{c_e|Y_e| + c_c|Y_c|}$$

where $\overline{\mathbf{D}}^j(T_E)$ is defined in (5.35).

This tells us that even if we take a piecewise constant initial condition with two different values in the intracellular and extracellular space, and even if the single functions which compose the signal have a different expression we end up with the same model for the signal attenuation.

Chapter 6

Time-dependent ADC inside cells

Contents

6.1 Effective diffusion coefficient in finite domains 113
6.2 Solution of the model 114
6.2.1 Eigenfunctions representation (finite pulse long-time formula, FPLT) 114
6.2.2 Layer potential representation (short pulse short-time formula, SPST) . . . 116
6.2.3 Mixed approximation (short pulse long-time formula, SPLT) 121
6.3 Averaging D^{eff} over multiple diffusion directions 123
6.4 Numerical results 124
6.5 Conclusions 128

In Chapter 2, we have seen that we can define the apparent diffusion coefficient (ADC), or effective diffusion coefficient D^{eff}, in terms of the mean square displacement (MSD). In particular, to adapt the definition of the apparent diffusion coefficient to the non-narrow pulse case, in Section 2.1.5, we made the following mathematical definition:

$$ADC_{\mathbf{u_g}} := -\frac{1}{\gamma^2 \int_0^{TE} F(t)^2 dt} \frac{\partial}{\partial g^2} \ln\left(\frac{S(T_E)}{S_0}\right)\Bigg|_{g=0}. \tag{6.1}$$

We have also seen that, in the dMRI community, the above quantity is fitted using the experimental MRI signal at several b (see Section 2.1.5). We remark again that the $ADC_{\mathbf{u_g}}$ defined in the above formula depends on the gradient direction $\mathbf{u_g}$ and the temporal profile $f(t)$ but not on the gradient amplitude. In this Chapter we restrict ourselves to PGSE time profile defined in Section 2.1 and, with the phrase "diffusion time-dependent", we actually mean dependent on both the PGSE parameters Δ and δ.

The motivation of our work is the experimentally observed phenomenon (see [160] and the references contained there) that the ADC depends on Δ (and δ in the non-narrow pulse case), leading to the need to characterize the time-dependent ADC in terms of tissue-related quantities over a wide range of diffusion time regimes. The ultimate goal is of course the estimation of these tissue-related quantities from the measured dMRI signal.

In this Chapter, we focus on the case of finite domains, where the membrane permeability is small enough to have negligible effect on the effective diffusion coefficient, which is related to the first order moment of the dMRI signal in the b-value. We note that this does not exclude the permeability from having an effect on the higher order moments of the signal. For the case where the permeability does affect the ADC, the analysis is more difficult and we refer the reader to [37, 77, 102, 175, 179] for results on periodic media and to [29, 55, 138, 139, 140] on more general heterogeneous media, not necessarily periodic.

As we have seen in Chapter 1, there exist several results concerning the apparent diffusion coefficient for finite domains where the membrane permeability is negligible. In the short time regime, the effective diffusion coefficient for a single domain is reduced from the free diffusion coefficient $\mathcal{D}_0$ by the presence of the cell membranes that affects only the molecules in the adjacent layer. The thickness of this layer is of the order of the diffusion length $\sqrt{\mathcal{D}_0 t}$ [99], where $\mathcal{D}_0$ is the bulk diffusion coefficient. Calculations in [129, 130] show

$$D^{\text{eff}}_{short}(t) = \mathcal{D}_0 \left(1 - \frac{4}{3\sqrt{\pi}} \frac{S}{dV} \sqrt{\mathcal{D}_0 t}\right), \tag{6.2}$$

where d is the spatial dimension and S/V is the surface to volume ratio. This result was extended to include higher order terms accounting for permeable membranes, surface relaxation and mean curvature [103, 138]. It was also shown that, in the case of anisotropic media subjected to a linear gradient with direction $\mathbf{u_g}$, one should replace $\frac{S}{dV}$ above by $\frac{\int_{\partial\Omega}(\mathbf{u_g}\cdot\nu)^2 d\mathbf{x}}{|\Omega|}$ [11, 63]. In the long time limit, the spins explore the whole available space of the finite domain and then their mean square displacement saturates while the effective diffusion coefficient decreases as Δ increases. For an isolated cell of a typical size R the diffusion becomes Gaussian as was shown in [133, 162]. In the case of the PGSE sequence in the narrow pulse limit one gets

$$D^{\text{eff}}_{long}(\Delta) \approx C \frac{R^2}{\Delta}, \tag{6.3}$$

where C is a geometrical constant (for example, $C = 1/4$ for the reflecting cylinder and $C = 1/12$ for a 1D configuration [30, 63]).

Finally, an approach that is closely related to the work of this Chapter is the "matrix formalism" approach used to describe restricted diffusion in bounded domains [15, 63, 64, 65]. There one considers the applied diffusion-encoding magnetic field as a perturbation of the Laplace operator and the magnetization is decomposed on the basis of Laplacian eigenfunctions. In contrast, our model in Chapter 4 was derived using a certain scaling of the membrane permeability with respect to other physical parameters and thus is not limited to impermeable domains . Our derivation justifies neglecting the membrane permeability for the choice of scaling that we have made. In addition, since we have formulated the time-dependent effective diffusion coefficient as the solution of a diffusion equation rather than directly in the eigenfunction basis, we have the freedom to analyze the solution of the resulting diffusion equation using both the eigenfunction representation as well as the layer potential representation according the relevant time regime under consideration.

The major result of this Chapter is the derivation of the new short time short pulse formula (SPST) that account for the duration of the pulses. This formula is derived using the single layer potential to rewrite the solution of the homogeneous diffusion equation in the H-*ADC* model. In particular, using an approximation of the single layer potential that is valid at short time, we find a formula which depends on both the duration of the pulses and the delay between them. This formula extend then the well known short-time formula in [130] to the case of not narrow pulses. Using the eigenfunctions expansion to represent the solution of the homogeneous diffusion equation in the H-*ADC* model, we recover instead the same expression of the "matrix formalism". We call it finite pulse long time (FPLT) formula because form the simulations we see that it approximates very well the solution with a limited number of eigenvalues when the

pulses and the delay between them are both long. Finally, supposing the pulses sufficiently short and the time delay between them long, we mix the two approximations using the single layer potential during the pulses and the eigenfunctions approximations between them and we call it short pulse long-time formula (SPLT). This last formula is particularly interesting because it contains a term that depends on the surface over volume ratio and terms that depend on the eigenvalues and first moment of the eigenfunctions. It gives then more information on the geometry than the SPST which contains only the surface over volume ration or the FPLT which contains only the eigenvalues and the first moment of the eigenfunctions.

This Chapter is organized as follows. In Section 6.1 we summarize the model of the effective diffusion coefficient derived in Chapter 4. In Section 6.2 we represent the solution of the resulting diffusion equation using the eigenfunction basis (FPLT), the single layer potential (SPST), or a mix of single layer potential and eigenfunctions (SPLT), and discuss the regime where each representation is advantageous. In Section 6.3 we provide the formulas for the average of the effective diffusion coefficient when the dMRI signal is measured along multiple diffusion-encoding gradient directions. In Section 6.4 we validate our analytical results with numerical simulations on two-dimensional geometries. Section 6.5 contains our conclusions.

6.1 Effective diffusion coefficient in finite domains

In Chapter 4, we obtained an homogenized model by starting from the Bloch-Torrey equation using the following scaling relationship between the time (Δ and δ), the biological cell membrane permeability (κ), the diffusion-encoding magnetic field gradient strength (g), and a periodicity length of the cellular geometry (L):

$$L = O(\epsilon),\ \kappa = O(\epsilon),\ g = O(\epsilon^{-2}),\ \{\Delta, \delta\} = O(\epsilon^2),$$

where ϵ is a non-dimensional parameter. It was shown that with this choice, there is no coupling between the different geometrical compartments in the g^2 term which gives rise to the effective diffusion coefficient. The total effective diffusion coefficient is the sum of the effective diffusion coeffcient in each geometrical compartment weighted by its volume fraction. Thus, in this Chapter we are justified in considering each compartment separately.

According to our model, the effective diffusion coefficient in the compartment Ω can be obtained in the following way:

$$D_{\mathbf{u_g}}^{\text{eff}} = \mathcal{D}_0 - \frac{\mathcal{D}_0}{\int_0^{T_E} F(t)^2 dt} \int_0^{T_E} F(t)\ h(t)\ dt, \tag{6.4}$$

where

$$h(t) = \frac{1}{|\Omega|} \int_\Omega \mathbf{u_g} \cdot \nabla \omega(\mathbf{x}, t) \tag{6.5}$$

is a quantity related to the directional gradient of a function ω that is the solution of the homogeneous diffusion equation with Neumann boundary condition and zero initial condition:

$$\frac{\partial}{\partial t}\omega(\mathbf{x}, t) - \nabla\left(\mathcal{D}_0 \nabla \omega(\mathbf{x}, t)\right) = 0, \qquad \mathbf{x} \in \Omega, \tag{6.6}$$

$$\mathcal{D}_0 \nabla \omega(\mathbf{x}, t) \cdot \nu(\mathbf{x}) = \mathcal{D}_0 F(t) \mathbf{u_g} \cdot \nu(\mathbf{x}), \quad \mathbf{x} \in \partial\Omega, \tag{6.7}$$

$$\omega(\mathbf{x}, t) = 0, \qquad \mathbf{x} \in \Omega, \tag{6.8}$$

ν is the outward normal and $t \in [0, T_E]$. We can see that if $h(t)$ is close to $F(t)$, then $D^{\text{eff}}_{\mathbf{u_g}}$ is close to 0.

In Chapter 4, we imposed periodic boundary conditions on the boundary of the voxel. In this Chapter, we are interested in analyzing (6.6) for spatially finite compartments, which is relevant to diffusion inside biological cells. It is not necessary to impose periodic boundary conditions on the sides of the imaging voxel if we consider only cells that do not touch the sides. In addition, in this Chapter, we will focus on the PGSE time profile.

6.2 Solution of the model

Defining the right hand side of the Neumann boundary condition as

$$\beta(\mathbf{y}, t) := \mathcal{D}_0 F(t)\ \mathbf{u_g} \cdot \nu(\mathbf{y}), \tag{6.9}$$

we will use the following two equivalent expressions for $h(t)$:

$$h(t) = \frac{1}{|\Omega|} \int_\Omega \mathbf{u_g} \cdot \nabla \omega(\mathbf{x}, t) d\mathbf{x} = \frac{1}{|\Omega|} \int_\Gamma \omega(\mathbf{y}, t)\, (\mathbf{u_g} \cdot \nu(\mathbf{y}))\, ds_{\mathbf{y}}, \tag{6.10}$$

where the second expression can be obtained by applying the divergence theorem to (6.5). We observe that the first expression uses values of the gradient of ω inside the domain while the second uses the values of ω on the boundary. Each expression will have advantages depending on whether we use the eigenfunctions of the Laplace operator or layer potentials to represent ω.

6.2.1 Eigenfunctions representation (finite pulse long-time formula, FPLT)

Writing ω as the sum

$$\omega(\mathbf{x}, t) = \widetilde{\omega}(\mathbf{x}, t) + F(t)\ \mathbf{x} \cdot \mathbf{u_g}, \tag{6.11}$$

where $\widetilde{\omega}(\mathbf{x}, t)$ satisfied the diffusion equation with a forcing term and homogeneous boundary condition:

$$\frac{\partial}{\partial t}\widetilde{\omega}(\mathbf{x}, t) - \nabla\left(\mathcal{D}_0 \nabla \widetilde{\omega}(\mathbf{x}, t)\right) = -f(t)\mathbf{x} \cdot \mathbf{u_g}, \qquad \mathbf{x} \in \Omega, \tag{6.12}$$

$$\mathcal{D}_0 \nabla \widetilde{\omega}(\mathbf{x}, t) \cdot \nu(\mathbf{x}) = 0, \qquad \mathbf{x} \in \Gamma, \tag{6.13}$$

$$\widetilde{\omega}(\mathbf{x}, t) = 0, \qquad \mathbf{x} \in \Omega, \tag{6.14}$$

it is well-known that $\widetilde{\omega}(\mathbf{x}, t)$ can be expanded in the basis of Laplace eigenfunctions. Let $\phi_n(\mathbf{x})$ and λ_n be the eigenfunctions and eigenvalues associated to the Laplace operator with homogeneous Neumann boundary conditions:

$$\begin{aligned} -\nabla \mathcal{D}_0 \left(\nabla \phi_n(\mathbf{x})\right) &= \lambda_n \phi_n(\mathbf{x}), && \mathbf{x} \in \Omega, \\ \mathcal{D}_0 \nabla \phi_n(\mathbf{x}) \cdot \nu(\mathbf{x}) &= 0, && \mathbf{x} \in \Gamma. \end{aligned}$$

We can write $\widetilde{\omega}(\mathbf{x}, t)$ in the basis of the eigenfunctions as

$$\widetilde{\omega}(\mathbf{x}, t) = -a_0 F(t) + \sum_{n=1}^{\infty} (-a_n) \phi_n(\mathbf{x}) \int_0^t e^{-\mathcal{D}_0 \lambda_n (t-s)} f(s) ds, \tag{6.15}$$

where the coefficients are

$$a_0 = \int_\Omega \mathbf{x}\cdot\mathbf{u_g} d\mathbf{x}, \quad a_n = \int_\Omega \mathbf{x}\cdot\mathbf{u_g}\phi_n(\mathbf{x}) d\mathbf{x},$$

which coincide with the first moments of the eigenfunctions in the $\mathbf{u_g}$ direction.

Finally, the solution to the diffusion equation is

$$\omega(\mathbf{x},t) = (\mathbf{x}\cdot\mathbf{u_g} - a_0)\, F(t) + \sum_{n=1}^{\infty}(-a_n)\phi_n(\mathbf{x})\int_0^t e^{-\mathcal{D}_0\lambda_n(t-s)} f(s) ds \tag{6.16}$$

and using properties of the eigenfunctions:

$$\int_\Omega \phi_n(\mathbf{x}) d\mathbf{x} = \begin{cases} |\Omega|, & n = 0 \\ 0, & n \geqslant 1, \end{cases} \tag{6.17}$$

and the divergence theorem:

$$\int_\Omega \lambda_n\phi_n\,(\mathbf{u_g}\cdot\mathbf{x})\, d\mathbf{x} = \int_\Omega \nabla\phi_n(\mathbf{x})\cdot\mathbf{u_g}\, d\mathbf{x} - \int_\Gamma \mathcal{D}_0\nabla\phi_n(\mathbf{x})\cdot\nu\mathbf{u_g}\cdot\nu ds_{\mathbf{x}} = \int_\Omega \nabla\phi_n(\mathbf{x})\cdot\mathbf{u_g}\, d\mathbf{x}, \tag{6.18}$$

we obtain

$$h(t) = F(t) + \sum_{n=1}^{\infty} -\frac{(a_n)^2\lambda_n}{|\Omega|}\int_0^t e^{-\mathcal{D}_0\lambda_n(t-s)} f(s) ds. \tag{6.19}$$

This leads to the final formula:

$$D^{\text{eff}}_{\mathbf{u_g}} = \sum_{n=1}^{\infty} \frac{(a_n)^2\mathcal{D}_0\lambda_n}{|\Omega|\int_0^{TE} F^2(t)dt}\int_0^{TE} F(t)\left(\int_0^t e^{-\mathcal{D}_0\lambda_n(t-s)} f(s) ds\right) dt. \tag{6.20}$$

We remark that this formula is the same as the one obtained with the matrix formalism in [63]. In particular, if we consider PGSE sequence, we can rewrite (6.4) using the contribution of each of the three intervals as

$$D^{\text{eff}}_{\mathbf{u_g}} = \mathcal{D}_0 - \left(\underbrace{\frac{\mathcal{D}_0}{A}\int_0^\delta t\; h(t)\; dt}_{I} + \underbrace{\frac{\mathcal{D}_0}{A}\int_\delta^\Delta \delta\; h(t)\; dt}_{II} + \underbrace{\frac{\mathcal{D}_0}{A}\int_\Delta^{\Delta+\delta} (\Delta+\delta-t)\; h(t)\; dt}_{III}\right), \tag{6.21}$$

where

$$A = \int_0^{T_E} F^2(t)dt = \delta^2\left(\Delta - \frac{\delta}{3}\right), \tag{6.22}$$

and in the first pulse

$$I = \frac{\mathcal{D}_0\delta^3}{3A} + \frac{1}{|\Omega|A}\sum_{n=1}^{\infty}(a_n)^2\left(-\frac{\delta^2}{2} - \frac{\delta e^{-\mathcal{D}_0\lambda_n\delta}}{\mathcal{D}_0\lambda_n} - \frac{e^{-\mathcal{D}_0\lambda_n\delta} - 1}{(\mathcal{D}_0\lambda_n)^2}\right), \tag{6.23}$$

between the pulses

$$II = \frac{\mathcal{D}_0\delta^2(\Delta-\delta)}{A} + \frac{1}{|\Omega|A}\sum_{n=1}^{\infty}\frac{-\delta(a_n)^2}{\mathcal{D}_0\lambda_n}\left(e^{-\mathcal{D}_0\lambda_n\Delta} - e^{-\mathcal{D}_0\lambda_n(\Delta-\delta)} - e^{-\mathcal{D}_0\lambda_n\delta} + 1\right), \tag{6.24}$$

and in the second pulse

$$III = \frac{\mathcal{D}_0\delta^3}{3A} + \sum_{n=1}^{\infty} \frac{-(a_n)^2}{\mathcal{D}_0\lambda_n A|\Omega|}\left(\delta - \frac{\delta^2\mathcal{D}_0\lambda_n}{2} - \delta e^{-\mathcal{D}_0\lambda_n\Delta} + \delta e^{-\mathcal{D}_0\lambda_n(\Delta-\delta)} + \frac{2e^{-\mathcal{D}_0\lambda_n\Delta} - 1 + e^{-\mathcal{D}_0\lambda_n\delta} - e^{-\mathcal{D}_0\lambda_n(\Delta+\delta)} - e^{-\mathcal{D}_0\lambda_n(\Delta-\delta)}}{\mathcal{D}_0\lambda_n}\right). \quad (6.25)$$

In the end, we obtain

$$D_{\mathbf{u_g}}^{\text{eff}} = \sum_{n=1}^{\infty} \frac{-(a_n)^2}{\mathcal{D}_0^2\lambda_n^2\delta^2\left(\Delta - \frac{\delta}{3}\right)|\Omega|}\left[e^{-\mathcal{D}_0\lambda_n(\Delta+\delta)} + e^{-\mathcal{D}_0\lambda_n(\Delta-\delta)} - 2\left(\mathcal{D}_0\lambda_n\delta + e^{-\mathcal{D}_0\lambda_n\delta} + e^{-\mathcal{D}_0\lambda_n\Delta} - 1\right)\right] \quad (6.26)$$

and from now on we refer to it as finite pulse long-time formula (FPLT). We observe that in the narrow pulse case ($\delta \ll \Delta$), we obtain

$$D_{\mathbf{u_g}}^{\text{eff}} \approx \sum_{n=1}^{\infty} \frac{(a_n)^2}{\Delta}\left(1 - e^{-\mathcal{D}_0\lambda_n\Delta}\right), \quad (6.27)$$

which confirms that $D_{\mathbf{u_g}}^{\text{eff}}$ approach its long time limit as $1/\Delta$ inside finite domains. In particular, for a 1D configuration of length L, $a_1 = \frac{L^2}{12}$ and for a reflecting cylinder of radius R, $a_1 = \frac{R^2}{4}$, which confirm the results in [30, 63].

6.2.2 Layer potential representation (short pulse short-time formula, SPST)

The solution of the diffusion equation can be also represented using layer potentials [70]. This representation is more efficient than the eigenfunction representation at short diffusion times. Since the PDE has a Neumann boundary condition, we choose to represent the solution $\omega(\mathbf{x}, t) = S[\mu](\mathbf{x}, t)$ as a single layer potential with a density μ defined on Γ,

$$S[\mu](\mathbf{x}, t) = \int_0^t \frac{1}{\sqrt{4\pi(t-\tau)}} B_S[\mu](\mathbf{x}, t, \tau)d\tau \quad (6.28)$$

where we separated out the part of the integrand,

$$B_S[\mu](\mathbf{x}, t, \tau) \equiv \int_\Gamma \mathcal{D}_0\, G(\mathbf{x} - \mathbf{y}, t - \tau)\mu(\mathbf{y}, \tau)ds_{\mathbf{y}}, \quad (6.29)$$

that is analytic in $(t - \tau)$. The $G(\mathbf{x}, t)$ in the above equation is the fundamental solution of the heat equation in free space given by

$$G(\mathbf{x}, t) = (4\pi\mathcal{D}_0 t)^{-d/2} \exp\left(\frac{-\|\mathbf{x}\|^2}{4\mathcal{D}_0 t}\right), \quad \mathbf{x} \in \Omega, t \in [0, T_E], \quad (6.30)$$

where d is the dimension of the problem. Automatically, the single layer potential satisfies

$$\frac{\partial}{\partial t}S[\mu](\mathbf{x}, t) - \nabla\big(\mathcal{D}_0\nabla S[\mu](\mathbf{x}, t)\big) = 0, \qquad \mathbf{x} \in \Omega, t \in [0, T_E], \quad (6.31)$$

$$S[\mu, 0](\mathbf{x}) = 0, \qquad \mathbf{x} \in \Omega. \quad (6.32)$$

The density μ will be chosen to satisfy the Neumann boundary condition:

$$\lim_{\mathbf{x}\to\mathbf{x}^0\in\Gamma} \mathcal{D}_0 \nabla S[\mu](\mathbf{x},t)\cdot\nu(\mathbf{x}) = \beta(\mathbf{x}^0,t), \quad \mathbf{x}^0\in\Gamma, t\in[0,T_E],$$

where $\beta(\mathbf{x}^0,t)$ is defined in (6.9).

Given the jump discontinuity of the normal derivative of the single layer potential, the integral equation to be solved for μ is the following:

$$\frac{\mathcal{D}_0}{2}\mu(\mathbf{x}^0,t) + \mathcal{D}_0 K^*[\mu](\mathbf{x}^0,t) = \beta(\mathbf{x}^0,t), \quad \mathbf{x}^0\in\Gamma, t\in[0,T_E], \tag{6.33}$$

where

$$K^*[\mu](\mathbf{x}^0,t) = \int_0^t \frac{1}{\sqrt{4\pi(t-\tau)}} B_K[\mu](\mathbf{x}^0,t,\tau)d\tau. \tag{6.34}$$

with

$$B_K[\mu](\mathbf{x}^0,t,\tau) \equiv \int_\Gamma \frac{-2(\mathbf{x}^0-\mathbf{y})\cdot\nu(\mathbf{y})}{4\mathcal{D}_0(t-\tau)} \mathcal{D}_0 G(\mathbf{x}^0-\mathbf{y},t-\tau)\mu(\mathbf{y},\tau)ds_{\mathbf{y}} \tag{6.35}$$

being analytic in $(t-\tau)$.

To compute $h(t)$ from (6.10) we only need to evaluate $\omega(\mathbf{x}^0,t) = S[\mu](\mathbf{x}^0,t)$ on the boundary Γ. We write the density μ as the solution of (6.33):

$$\mu(\mathbf{x}^0,t) = \frac{2}{\mathcal{D}_0}\left(1+2K^*\right)^{-1}\beta(\mathbf{x}^0,t), \quad \mathbf{x}^0\in\Gamma, t\in[0,T_E], \tag{6.36}$$

and expand the operator $(1+2K^*)^{-1}$:

$$\mu(\mathbf{x}^0,t) = \frac{2}{\mathcal{D}_0}\left(1-2K^*+4(K^*)^2+\dots\right)\beta(\mathbf{x}^0,t), \tag{6.37}$$

to obtain

$$\mu(\mathbf{x}^0,t) = \frac{2}{\mathcal{D}_0}\beta(\mathbf{x}^0,t) - \frac{4}{\mathcal{D}_0}K^*[\beta](\mathbf{x}^0,t) + \text{higher order terms}, \tag{6.38}$$

which means

$$S[\mu](\mathbf{x}^0,t) = S\left[\frac{2}{\mathcal{D}_0}\beta\right](\mathbf{x}^0,t) + S\left[-\frac{4}{\mathcal{D}_0}K^*[\beta]\right](\mathbf{x}^0,t) + \text{higher order terms}. \tag{6.39}$$

We will now compute the first term on the right hand side of the above equation to get an approximate expression for $\omega(\mathbf{x}^0,t) = S[\mu](\mathbf{x}^0,t)$ and we will compute the second term to get an expression for the error. To do this we will use the following results concerning $S[\mu]$ and $K^*[\mu]$ for small values of $(t-\tau)$ obtained (in 2 dimensions) in [69, 114] for the operator S :

$$B_S[\mu](\mathbf{x}^0,t,\tau) = \mu(\mathbf{x}^0,t) + \left(\frac{k(\mathbf{x}^0)^2}{4}\mu(\mathbf{x}^0,t) + \mu_t(\mathbf{x}^0,t) - \mu_{ss}(\mathbf{x}^0,t)\right)(t-\tau) + O\left((t-\tau)^2\right) \tag{6.40}$$

and for the operator K^* :

$$\begin{aligned} B_K[\mu](\mathbf{x}^0,t,\tau) = \frac{k(\mathbf{x}^0)}{2}\mu(\mathbf{x}^0,t) + \frac{1}{8}\Big[16\gamma_{sss}(\mathbf{x}^0)\mu_s(\mathbf{x}^0,t) + 12\gamma_{ss}(\mathbf{x}^0)\mu_{ss}(\mathbf{x}^0,t) \\ +4k(\mathbf{x}^0)\mu_t(\mathbf{x}^0,t) + \left(6\gamma_{ssss}(\mathbf{x}^0) - 15k(\mathbf{x}^0)^3\right)\mu(\mathbf{x}^0,t)\Big](t-\tau) \\ +O\left((t-\tau)^2\right), \end{aligned} \tag{6.41}$$

where Γ is parametrised around $\mathbf{x}^0$ in the arc length parameter s,

$$y(s) = \frac{1}{2}\gamma_{20}s^2 + \frac{1}{6}\gamma_{30}s^3 + \frac{1}{24}\gamma_{40}s^4 + \dots. \tag{6.42}$$

In the above, we have translated and rotated the x and y-axes so that the origin is at $\mathbf{x}^0$ and the tangent of Γ at $\mathbf{x}^0$ is parallel to the x-axis. Specifically $k(\mathbf{x}^0) = \gamma_{ss}$ is the curvature of Γ at the point $\mathbf{x}^0$.

For the PGSE sequence, $\beta(\mathbf{x}^0,t)$ assumes the following three expressions in the three time intervals:

$$\beta(\mathbf{x}^0,t) = \mathcal{D}_0\mathbf{u_g}\cdot\nu(\mathbf{x}^0)\begin{cases} t & 0<t\leqslant\delta, \\ \delta & \delta<t\leqslant\Delta, \\ \Delta+\delta-t & \Delta<t\leqslant\Delta+\delta. \end{cases} \tag{6.43}$$

First, using the definition (6.40) and the result (6.28) we obtain

$$\begin{aligned} S\left[\frac{2}{\mathcal{D}_0}\beta\right](\mathbf{x}^0,t) = \frac{4(\mathcal{D}_0)^{1/2}}{3\sqrt{\pi}}\mathbf{u_g}\cdot\nu(\mathbf{x}^0)\begin{cases} t^{3/2} \\ t^{3/2}-(t-\delta)^{3/2} \\ t^{3/2}-(t-\delta)^{3/2}-(t-\Delta)^{3/2} \end{cases} \\ +O\begin{cases} t^{5/2} & \text{if } 0<t\leqslant\delta \\ t^{5/2}-(t-\delta)^{5/2} & \text{if } \delta<t\leqslant\Delta \\ t^{5/2}-(t-\delta)^{5/2}-(t-\Delta)^{5/2} & \text{if } \Delta<t\leqslant\Delta+\delta \end{cases}. \end{aligned} \tag{6.44}$$

Similarly, using the definition (6.34) and the result (6.41) we obtain

$$\begin{aligned} -\frac{4}{\mathcal{D}_0}K^*[\beta](\mathbf{x}^0,t) = -\frac{4}{\mathcal{D}_0}\frac{(\mathcal{D}_0)^{3/2}k(\mathbf{x}^0)}{3\sqrt{\pi}}\left(\mathbf{u_g}\cdot\nu(\mathbf{x}^0)\right)\begin{cases} t^{3/2} \\ t^{3/2}-(t-\delta)^{3/2} \\ t^{3/2}-(t-\delta)^{3/2}-(t-\Delta)^{3/2} \end{cases} \\ +O\begin{cases} t^{5/2} & \text{if } 0<t\leqslant\delta \\ t^{5/2}-(t-\delta)^{5/2} & \text{if } \delta<t\leqslant\Delta \\ t^{5/2}-(t-\delta)^{5/2}-(t-\Delta)^{5/2} & \text{if } \Delta<t\leqslant\Delta+\delta \end{cases}. \end{aligned} \tag{6.45}$$

To compute $S[K^*[\beta]](\mathbf{x}^0,t)$ we cannot use the result (6.28) because $K^*[\beta](\mathbf{x}^0,t)$ does not admit a Taylor expansion in t. Instead, we use the definition of the single layer (6.29) applied to the

density (6.45) and directly integrate to obtain

$$S\left[-\frac{4}{\mathcal{D}_0}K^*[\beta]\right](\mathbf{x}^0,t) = -\frac{4}{\mathcal{D}_0}\frac{\mathcal{D}_0^2}{16}k(\mathbf{x}^0)(\mathbf{u_g}\cdot\nu(\mathbf{x}^0))\begin{cases}t^2\\ t^2-(t-\delta)^2\\ t^2-(t-\delta)^2-(t-\Delta)^2.\end{cases}$$
$$+O\begin{cases}t^3 & \text{if } 0<t\leqslant\delta,\\ t^3-(t-\delta)^3 & \text{if } \delta<t\leqslant\Delta,\\ t^3-(t-\delta)^3-(t-\Delta)^3 & \text{if } \Delta<t\leqslant\Delta+\delta.\end{cases} \tag{6.46}$$

Replacing the various expressions in (6.39) with the calculations we did above, we obtain the approximation with the error bound:

$$S[\mu](\mathbf{x}^0,t) = \frac{4(\mathcal{D}_0)^{1/2}}{3\sqrt{\pi}}\mathbf{u_g}\cdot\nu(\mathbf{x}^0)\begin{cases}t^{3/2}\\ t^{3/2}-(t-\delta)^{3/2}\\ t^{3/2}-(t-\delta)^{3/2}-(t-\Delta)^{3/2}\end{cases}$$
$$-\frac{\mathcal{D}_0}{16}k(\mathbf{x}^0)(\mathbf{u_g}\cdot\nu(\mathbf{x}^0))\begin{cases}t^2 & \text{if } 0<t\leqslant\delta\\ t^2-(t-\delta)^2 & \text{if } \delta<t\leqslant\Delta\\ t^2-(t-\delta)^2-(t-\Delta)^2 & \text{if } \Delta<t\leqslant\Delta+\delta\end{cases} \quad +\text{higher order terms.} \tag{6.47}$$

Now using (6.47) we compute the approximate expressions of $h(t)$ in each time-interval with the corresponding errors in time. In the first interval we obtain

$$h(t) = \frac{1}{|\Omega|}\int_\Gamma \omega(\mathbf{x},t)\,(\mathbf{u_g}\cdot\nu(\mathbf{x}))\,ds_{\mathbf{x}} = P\,t^{3/2} + O\left(P_{\text{err}}t^2\right), \tag{6.48}$$

where

$$P = \frac{1}{|\Omega|}\int_\Gamma\left(\frac{4}{3\sqrt{\pi}}\sqrt{\mathcal{D}_0}(\mathbf{u_g}\cdot\nu(\mathbf{x}))^2\right)ds_{\mathbf{x}} \tag{6.49}$$

$$P_{\text{err}} = -\frac{\mathcal{D}_0}{4|\Omega|}\int_\Gamma k(\mathbf{x})(\mathbf{u_g}\cdot\nu(\mathbf{x}))^2 ds_{\mathbf{x}} \tag{6.50}$$

and

$$I = \frac{\mathcal{D}_0}{\delta^2\left(\Delta-\frac{\delta}{3}\right)}\int_0^\delta t\,h(t)\,dt = \frac{2\mathcal{D}_0P}{7\left(\Delta-\frac{\delta}{3}\right)}\delta^{7/2} + O\left(\mathcal{D}_0P_{\text{err}}\frac{\delta^2}{4\left(\Delta-\frac{\delta}{3}\right)}\right). \tag{6.51}$$

Between the pulses, we obtain

$$h(t) = \frac{1}{|\Omega|}\int_\Gamma \omega(\mathbf{x},t)\,(\mathbf{u_g}\cdot\nu(\mathbf{x}))\,ds_{\mathbf{x}} = P\left(t^{3/2}-(t-\delta)^{3/2}\right) + O\left(P_{\text{err}}(t^2-(t-\delta)^2)\right) \tag{6.52}$$

and

$$II = \frac{\mathcal{D}_0}{\delta^2\left(\Delta-\frac{\delta}{3}\right)}\int_\delta^\Delta \delta\,h(t)\,dt$$
$$= -\frac{2}{5}\frac{\mathcal{D}_0P\left(\delta^{7/2}-\Delta^{5/2}\delta+(\Delta-\delta)^{5/2}\,\delta\right)}{\delta^2\left(\Delta-\frac{\delta}{3}\right)} + O\left(\mathcal{D}_0P_{\text{err}}\frac{-\delta(\Delta-\delta)+\Delta^2-\delta^2}{\Delta-\frac{\delta}{3}}\right) \tag{6.53}$$

with P and P_{err} defined in (6.49) and (6.50) respectively. During the second pulse, we find

$$\begin{aligned} h(t) &= \frac{1}{|\Omega|}\int_\Gamma \omega(\mathbf{x},t)\,(\mathbf{u_g}\cdot\nu(\mathbf{x}))\,ds_{\mathbf{x}} \\ &= P\left(t^{3/2}-(t-\delta)^{3/2}-(t-\Delta)^{3/2}\right)+O\left(P_{\text{err}}(t^2-(t-\delta)^2-(t-\Delta)^2)\right) \end{aligned} \tag{6.54}$$

and

$$\begin{aligned} III &= \frac{\mathcal{D}_0}{\delta^2\left(\Delta-\frac{\delta}{3}\right)}\int_\Delta^{\Delta+\delta}(\Delta+\delta-t)\,h(t)\,dt \\ &= \frac{2}{35}\frac{\mathcal{D}_0 P}{\delta^2\left(\Delta-\frac{\delta}{3}\right)}\Big(\left(2\Delta^3+\Delta^2\delta-8\Delta\delta^2+5\delta^3\right)\sqrt{\Delta-\delta}+2\left(\Delta+\delta\right)^{7/2} \\ &\qquad -4\Delta^{7/2}-7\Delta^{5/2}\delta-2\delta^{7/2}\Big)+O\left(\mathcal{D}_0 P_{\text{err}}\frac{\Delta\delta-\frac{1}{4}\delta^2}{\left(\Delta-\frac{\delta}{3}\right)}\right). \end{aligned} \tag{6.55}$$

with P and P_{err} defined in (6.49) and (6.50) respectively. Finally, adding up the above expressions, we obtain that using the layer potentials representation,

$$\begin{aligned} D^{\text{eff}}_{\mathbf{u_g}} = \mathcal{D}_0\Bigg[1-\frac{4}{35}P\frac{1}{\delta^2\left(\Delta-\frac{\delta}{3}\right)}\Big(-2\left(\delta^{7/2}+\Delta^{7/2}\right) \\ +\left(\Delta-\delta\right)^{7/2}+\left(\Delta+\delta\right)^{7/2}\Big)\Bigg]+O\left(\mathcal{D}_0 P_{\text{err}}\frac{\Delta^2}{\Delta-\frac{\delta}{3}}\right), \end{aligned} \tag{6.56}$$

where P_{err} is defined in (6.50). From now on we will refer to this formula as short pulse short-time formula (SPST).

We observe that, in the narrow pulse limit, $\delta \ll \Delta$, the expression (6.56) reduces to the formula given in [11, 63]:

$$\begin{aligned} D^{\text{eff}}_{\mathbf{u_g}} &= \mathcal{D}_0\left(1-P\sqrt{\Delta}\right)+O(\mathcal{D}_0 P_{\text{err}}\Delta) \\ &= \mathcal{D}_0\left(1-\frac{4}{3\sqrt{\pi}}\sqrt{\mathcal{D}_0\Delta}\frac{\int_\Gamma(\mathbf{u_g}\cdot\nu)^2 ds_{\mathbf{x}}}{|\Omega|}\right)+O(\mathcal{D}_0 P_{\text{err}}\Delta), \end{aligned}$$

and if Ω is an isotropic domain, we have

$$\frac{\int_\Gamma(\mathbf{u_g}^i\cdot\nu)^2 ds_{\mathbf{x}}}{|\Omega|}=\frac{|\Gamma|}{d|\Omega|}, \tag{6.57}$$

which is the surface over volume divided by the space dimension d, exactly the quantity obtained in [130]. Hence our new formula in (6.56) is a correction of the results in [11, 63, 130] because it takes into account the contribution of δ. This makes the new formula applicable for cases where the narrow pulse assumption $\delta \ll \Delta$ does not hold. Of course, this description still hold only for short times due to the nature of the asympotic expansions for layer potentials.

6.2.3 Mixed approximation (short pulse long-time formula, SPLT)

When the pulses are short but the delay between the pulses is not short (with respect to diffusion in the finite domain), we use potential representation in the first and third intervals and eigenfunction representation between the pulses.

In the first pulse, $t \in [0, \delta]$, we have the same results as in the previous section, i.e. $\omega(\mathbf{x}, t) = S\left[\frac{2}{\mathcal{D}_0}\beta\right](\mathbf{x}, t) + O(t^2) = S\left[2t\mathbf{u_g} \cdot \nu\right](\mathbf{x}, t) + O(t^2)$, and thus

$$I = \frac{8}{21A|\Omega|\sqrt{\pi}}\mathcal{D}_0^{3/2}\delta^{7/2}\int_\Gamma (\mathbf{u_g} \cdot \nu)^2 ds_{\mathbf{x}} + O\left(\frac{\delta^2}{(\Delta - \frac{\delta}{3})}\right). \tag{6.58}$$

Between the pulses, $t \in [\delta, \Delta]$, the Neumann boundary condition in (6.9) is

$$\mathcal{D}_0 \nabla\omega(\mathbf{x}, t) \cdot \nu = \mathcal{D}_0 \delta \mathbf{u_g} \cdot \nu, \quad \text{on } \Gamma \times [\delta, \Delta] \tag{6.59}$$

and the initial condition is

$$\omega(\mathbf{x}, \delta) = S\left[2\delta\mathbf{u_g} \cdot \nu\right](\mathbf{x}, t) + O(\delta^2), \quad \mathbf{x} \text{ in } \Omega. \tag{6.60}$$

The function $\widetilde{\omega}(\mathbf{x}, t) = \omega(\mathbf{x}, t) - \delta\mathbf{x} \cdot \mathbf{u_g}$ satisfies homogeneous Neumann boundary condition and the initial condition

$$\widetilde{\omega}(\mathbf{x}, \delta) = S\left[(2\delta\mathbf{u_g} \cdot \nu)\right](\mathbf{x}, \delta) - \delta\mathbf{x} \cdot \mathbf{u_g}. \tag{6.61}$$

This means

$$\widetilde{\omega}(\mathbf{x}, t) = c_0 + \sum_{n=1}^{\infty} c_n e^{-\lambda_n \mathcal{D}_0 (t-\delta)}\phi_n(\mathbf{x}) \tag{6.62}$$

where

$$c_0 = -\delta a_0 + b_0 = -\delta\int_\Omega \mathbf{x} \cdot \mathbf{u_g} d\mathbf{x} + \int_\Omega \omega(\mathbf{x}, \delta) d\mathbf{x}, \tag{6.63}$$

$$c_n = -\delta a_n + b_n = -\delta\int_\Omega \mathbf{x} \cdot \mathbf{u_g}\phi_n(\mathbf{x}) d\mathbf{x} + \int_\Omega \omega(\mathbf{x}, \delta)\phi_n(\mathbf{x}) d\mathbf{x} \tag{6.64}$$

with again ϕ_n and λ_n the Neumann eigenfunctions and eigenvalues associated to the Laplace operator ($n = 1, 2, \dots$). Thus, for $t \in [\delta, \Delta]$,

$$\omega(\mathbf{x}, t) = c_0 + \sum_{n=1}^{\infty} c_n e^{-\lambda_n \mathcal{D}_0 (t-\delta)}\phi_n(\mathbf{x}) + \delta\mathbf{x} \cdot \mathbf{u_g} + O(\delta^2), \tag{6.65}$$

and

$$h(t) = \sum_{n=1}^{\infty} \frac{c_n \lambda_n a_n}{|\Omega|} e^{-\lambda_n \mathcal{D}_0 (t-\delta)} + \delta + O\left(\frac{\delta^2}{A}\right), \tag{6.66}$$

and

$$II = \frac{1}{A}\sum_{n=1}^{\infty} \frac{c_n a_n}{|\Omega|}\left(1 - e^{-\lambda_n \mathcal{D}_0 (\Delta - \delta)}\right) + \frac{\mathcal{D}_0 \delta^2 (\Delta - \delta)}{A} + O\left(\frac{\delta(\Delta - \delta)}{(\Delta - \frac{\delta}{3})}\right). \tag{6.67}$$

During the second pulse, $t \in [\Delta, \Delta+\delta]$, we keep the solution from the previous interval in Eq. (6.65) which satisfies homogeneous boundary conditions and just add a single layer potential to match the Neumann boundary condition. We obtain

$$\omega(\mathbf{x},t) = c_0 + \sum_{n=1}^{\infty} c_n e^{-\lambda_n \mathcal{D}_0 (t-\delta)} \phi_n(\mathbf{x}) + \delta \mathbf{x}\cdot\mathbf{u_g} + S\left[(-2\tau \mathbf{u_g}\cdot\nu)\right](\mathbf{x}, t-\Delta) + O((t-\Delta)^2), \quad (6.68)$$

where $t \in [\Delta, \Delta+\delta]$, while $\tau \in [0,\delta]$ because we operate a shift in time $t \to t-\Delta$ to be able to keep the definition of the single layer potential in (6.29) (for which the interval of integration is $t-\Delta$). Using the definition of the single layer potential (6.29) we obtain

$$S\left[(-2\tau \mathbf{u_g}\cdot\nu)\right](\mathbf{x}, t-\Delta) = -\frac{4}{3\sqrt{\pi}|\Omega|}\sqrt{\mathcal{D}_0}\,(t-\Delta)^{3/2}\int_\Gamma (\mathbf{u_g}\cdot\nu) + O((t-\Delta)^{5/2}),$$

which leads to

$$h(t) = \sum_{n=1}^{\infty} \frac{c_n}{|\Omega|} e^{-\lambda_n \mathcal{D}_0 (t-\delta)} \lambda_n a_n - \frac{4}{3\sqrt{\pi}|\Omega|}\sqrt{\mathcal{D}_0}\,(t-\Delta)^{3/2}\int_\Gamma (\mathbf{u_g}\cdot\nu)^2 ds_{\mathbf{x}} + \delta + O\left(\frac{(t-\Delta)^2}{A}\right), \quad (6.69)$$

and

$$III = \frac{\mathcal{D}_0}{2A}\delta^3 + \sum_{n=1}^{\infty} \frac{c_n a_n}{\mathcal{D}_0 \lambda_n A|\Omega|}\left(e^{-\lambda_n \mathcal{D}_0(\Delta-\delta)}(\mathcal{D}_0\lambda_n\delta - 1) + e^{-\lambda_n \mathcal{D}_0 \Delta}\right) - \frac{16}{105\sqrt{\pi}A|\Omega|}\mathcal{D}_0^{3/2}\left(\int_\Gamma (\mathbf{u_g}\cdot\nu)^2 ds_{\mathbf{x}}\right)\delta^{7/2} + O\left(\frac{\delta^2}{(\Delta - \frac{\delta}{3})}\right). \quad (6.70)$$

The effective diffusion coefficient for the compartment Ω assumes thus the form

$$D^{\text{eff}}_{\mathbf{u_g}} = \frac{\mathcal{D}_0\delta}{6(\Delta-\frac{\delta}{3})} - \frac{8\mathcal{D}_0^{3/2}\delta^{3/2}}{35\sqrt{\pi}|\Omega|(\Delta-\frac{\delta}{3})}\int_\Gamma (\mathbf{u_g}\cdot\nu)^2 ds_{\mathbf{x}} + - \sum_{n=1}^{\infty} \frac{-\delta(a_n)^2 + a_n b_n}{|\Omega|\delta^2(\Delta-\frac{\delta}{3})}\left(\delta - \frac{e^{-\lambda_n\mathcal{D}_0\Delta}(1-e^{\lambda_n\mathcal{D}_0\delta})}{\lambda_n\mathcal{D}_0}\right) + O\left(\max\left\{\frac{\delta^2}{(\Delta-\frac{\delta}{3})}, \frac{\delta(\Delta-\delta)}{(\Delta-\frac{\delta}{3})}\right\}\right) \quad (6.71)$$

and from now on we will refer to it as short pulse long-time formula (SPLT).

In the narrow pulse limit, we get

$$D^{\text{eff}}_{\mathbf{u_g}} = -\sum_{n=1}^{\infty} \frac{(-\delta a_n + b_n)a_n}{|\Omega|\delta(\Delta-\frac{\delta}{3})}\left(1 - e^{-\lambda_n\mathcal{D}_0\Delta}\right) + O(\delta^{1/2}), \quad (6.72)$$

which again tells us that $D^{\text{eff}}_{\mathbf{u_g}}$ approaches its long time limit as $1/\Delta$, because $b_n = O(\delta^{3/2})$ for all $n \geqslant 1$ due to the maximum principle for heat equation applied to $\omega(\mathbf{x},t)$ in the first pulse:

$$\|\omega(\mathbf{x},t)\| \leqslant \|\omega(\mathbf{x}^0,t)\| \approx O(t^{3/2}) \quad \forall \mathbf{x}\in\Omega, \mathbf{x}^0\in\Gamma, t\in[0,\delta]. \quad (6.73)$$

6.3 Averaging D^{eff} over multiple diffusion directions

If we average the effective diffusion coefficient $D^{\text{eff}}_{\mathbf{u_g}}$ over all the possible gradient directions $\mathbf{u_g}$, we can obtain a new formula that is independent of the orientation of the biological cells. We define the orientionally averaged effective diffusion coefficient as

$$\frac{\widetilde{D}^{\text{eff}}}{\mathcal{D}_0} := \frac{\int_{\mathbb{S}^{d-1}} D^{\text{eff}}_{\mathbf{u_g}} d\mathbf{u}}{\mathcal{D}_0 \int_{\mathbb{S}^{d-1}} d\mathbf{u}}. \tag{6.74}$$

We recall that

$$D^{\text{eff}}_{\mathbf{u_g}} = \mathcal{D}_0 - \frac{\mathcal{D}_0}{A|\Omega|} \int_0^{TE} F(t) \int_\Omega \mathbf{u_g} \cdot \nabla \omega_{\mathbf{u_g}}(\mathbf{x}, t) d\mathbf{x}\, dt \tag{6.75}$$

where $\omega_{\mathbf{u_g}}(\mathbf{x}, t)$ solves the problem (6.6). Because of the linearity of the Neumann problem, for every direction $\mathbf{u_g} = [u_1, \ldots, u_d]$ we have that

$$\omega_{\mathbf{u_g}}(\mathbf{x}, t) = \sum_{i=1}^{d} u_i \omega_{\mathbf{e}_i}(\mathbf{x}, t), \tag{6.76}$$

where $\mathbf{e}_i$ is the i-th vector of the canonical basis of $\mathbb{R}^d$. As a consequence

$$\begin{aligned} D^{\text{eff}}_{\mathbf{u_g}} &= \mathcal{D}_0 - \frac{\mathcal{D}_0}{A|\Omega|} \int_0^{TE} F \int_\Omega (u_1 \mathbf{e}_1 + \cdots + u_d \mathbf{e}_d) \cdot (u_1 \nabla \omega_{\mathbf{e}_1} + \cdots + u_d \nabla \omega_{\mathbf{e}_i})\, d\mathbf{x}\, dt \\ &= \mathcal{D}_0 - \frac{\mathcal{D}_0}{A|\Omega|} \int_0^{TE} F \left(\sum_{i=1}^{d} u_i^2 \int_\Omega \mathbf{e}_i \cdot \nabla \omega_{\mathbf{e}_i} d\mathbf{x} + \sum_{\substack{i \neq j \\ i,j=1}}^{d} u_i u_j \int_\Omega \mathbf{e}_i \cdot \nabla \omega_{\mathbf{e}_j} d\mathbf{x} \right) dt \end{aligned}$$

and thus, if we want to average over all the possible directions, we are interested in the integrals

$$\frac{\int_{\mathbb{S}^{d-1}} u_i^2 d\mathbf{u}}{\int_{\mathbb{S}^{d-1}} d\mathbf{u}},\ i = 1, \ldots, d \quad \text{and} \quad \frac{\int_{\mathbb{S}^{d-1}} u_i u_j d\mathbf{u}}{\int_{\mathbb{S}^{d-1}} d\mathbf{u}},\ i, j = 1, \ldots, d, i \neq j. \tag{6.77}$$

We observe that, for all $i, j = 1, \ldots, d$ and $i \neq j$,

$$\int_{\mathbb{S}^{d-1}} u_i u_j d\mathbf{u} = 0. \tag{6.78}$$

Indeed to prove this results it is sufficient to pass into spherical coordinates and every time we have the product $u_i u_j$ with $i \neq j$ we have also an integral of the type $\int_0^\pi \sin(\theta)\cos(\theta) d\theta = 0$ or $\int_0^{2\pi} \sin(\theta)\cos(\theta) d\theta = 0$ or $\int_0^{2\pi} \cos(\theta) d\theta = 0$ or $\int_0^{2\pi} \sin(\theta) d\theta = 0$. Therefore, what remains in the average are just the terms

$$\sum_{i=1}^{d} \frac{\int_{\mathbb{S}^{d-1}} u_i^2 d\mathbf{u}}{\int_{\mathbb{S}^{d-1}} d\mathbf{u}} \int_\Omega \mathbf{e}_i \cdot \nabla \omega_{\mathbf{e}_i} d\mathbf{x} \tag{6.79}$$

i.e. simply the average over d perpendicular directions and then

$$\frac{\widetilde{D}^{\text{eff}}}{\mathcal{D}_0} = 1 - \sum_{i=1}^{d} \frac{1}{dA|\Omega|} \int_0^{TE} F(t) \int_\Omega \mathbf{u_g}^i \cdot \nabla \omega_{\mathbf{u_g}^i}(\mathbf{x}, t) d\mathbf{x}\, dt \tag{6.80}$$

where ${\mathbf{u_g}}^i, i = 1, \ldots, d$ are d orthogonal directions. Then averaging over all the possible directions is equivalent to average only over d orthogonal normalized directions.

We use the fact that

$$\sum_{i=i}^{d} \frac{\int_\Gamma ({\mathbf{u_g}}^i \cdot \nu)^2 ds_{\mathbf{x}}}{d} = \frac{|\Gamma|}{d} \tag{6.81}$$

and we define

$$k_n := \sum_{i=1}^{d} \frac{-(a_n^i)^2}{d|\Omega|} = \sum_{i=1}^{d} \frac{-\left(\int_\Omega \mathbf{x} \cdot {\mathbf{u_g}}^i \phi_n(\mathbf{x}) d\mathbf{x}\right)^2 d\mathbf{u_g}}{d|\Omega|}, \tag{6.82}$$

i.e. the mean over d orthogonal directions of the square of the first moment along these directions, and

$$j_n := \sum_{i=1}^{d} \frac{b_n^i a_n^i}{d|\Omega|} = \sum_{i=1}^{d} \frac{\left(\int_\Omega \omega_{{\mathbf{u_g}}^i}(\mathbf{x}, \delta)\phi_n(\mathbf{x}) d\mathbf{x}\right)\left(\int_\Omega \mathbf{x} \cdot {\mathbf{u_g}}^i \phi_n(\mathbf{x}) d\mathbf{x}\right)}{d|\Omega|}. \tag{6.83}$$

The finite pulse long-time formula in (6.26) gives

$$\frac{\widetilde{D}^{\text{eff}}}{\mathcal{D}_0} = \sum_{n=1}^{\infty} \frac{k_n}{\mathcal{D}_0^3 {\lambda_n}^2 \delta^2 \left(\Delta - \frac{\delta}{3}\right)} \Big[e^{-\mathcal{D}_0\lambda_n(\Delta+\delta)} + e^{-\mathcal{D}_0\lambda_n(\Delta-\delta)} - 2\left(\mathcal{D}_0\lambda_n\delta + e^{-\mathcal{D}_0\lambda_n\delta} + e^{-\mathcal{D}_0\lambda_n\Delta} - 1\right)\Big] \tag{6.84}$$

The short pulse short-time formula in (6.56) gives

$$\frac{\widetilde{D}^{\text{eff}}}{\mathcal{D}_0} = 1 - \frac{16}{35} \frac{\mathcal{D}_0^{1/2}}{\delta^2 (3\,\Delta - \delta)\sqrt{\pi}} \Big[-2\left(\delta^{7/2} + \Delta^{7/2}\right) + (\Delta - \delta)^{7/2} + (\Delta + \delta)^{7/2} \Big] \frac{|\Gamma|}{d|\Omega|} + O(\Delta). \tag{6.85}$$

The short pulse long-time formula in (6.71) gives

$$\frac{\widetilde{D}^{\text{eff}}}{\mathcal{D}_0} = \frac{\delta}{6(\Delta - \frac{\delta}{3})} - \frac{8\mathcal{D}_0^{1/2}\delta^{3/2}}{35\sqrt{\pi}(\Delta - \frac{\delta}{3})} \frac{|\Gamma|}{d|\Omega|} - \sum_{n=1}^{\infty} \frac{\delta k_n + j_n}{\mathcal{D}_0 \delta^2 (\Delta - \frac{\delta}{3})} \left(\delta - \frac{e^{-\lambda_n\mathcal{D}_0\Delta}(1 - e^{\lambda_n\mathcal{D}_0\delta})}{\lambda_n\mathcal{D}_0}\right) + O\left(\max\left\{\frac{\delta^2}{(\Delta - \frac{\delta}{3})}, \frac{\delta(\Delta - \delta)}{(\Delta - \frac{\delta}{3})}\right\}\right) \tag{6.86}$$

6.4 Numerical results

In this Section we numerically validate the accuracy of the approximate formulas we derived in the diffusion regimes claimed. To compute the reference *ADC* we solved the homogenized model using the Matlab PDEToolbox. The eigenvalues and eigenfunctions of the Laplace equation with Neumann boundary conditions were also computed with the same software.

First we show the goodness of the three approximations of $h(t)$ for a simple impermeable domain. We consider a 2D geometry of one vertically orientated ellipse with semi-axes of 19μm and 9μm. The intrinsic diffusion coefficient is set to $\mathcal{D}_0 = 1e^{-3}\text{mm}^2/\text{s}$ and we vary the values of

δ, Δ and $\mathbf{u_g}$. To compute the reference solution $h(t)$ we solved the problem (6.6) on the finite element mesh shown in Fig. 6.1. The eigenvalues and eigenfunctions are also computed on the same finite element mesh. The projections a_n and b_n are computed according the the formulas (6.64). For this particular geometry the first four non-zero eigenvalues are

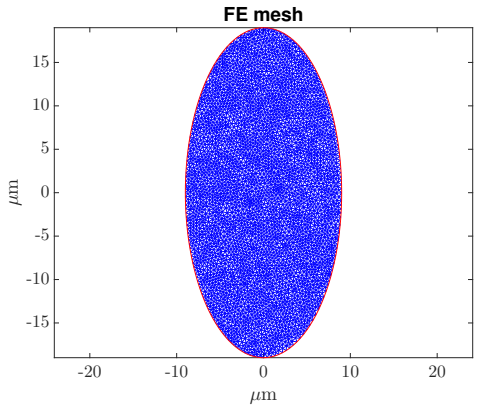

Figure 6.1 – Finite elements mesh of an ellipse with semiaxes of 19μm and 9μm, orientated vertically along the y-axis.

$$\lambda_1 = 0.0097, \quad \lambda_2 = 0.0325, \quad \lambda_3 = 0.0383, \quad \lambda_4 = 0.0644,$$

and their projections a_i are reported in the table below.

$\mathbf{u_g}$	a_1	a_2	a_3	a_4
$[1,0]$	38.9	-25.7	$-4.62e^{+5}$	-0.97
$[0,1]$	$1.07e^{+6}$	1.75	-4.49	-5.58

Table 6.1 – Eigenfunction first moments obtained for the first four non-zero eigenvalues in the two directions $\mathbf{u_g} = [1,0]$ and $\mathbf{u_g} = [0,1]$.

It is important to observe that in the direction $\mathbf{u_g} = [1,0]$ the first two non-zero eigenvalues have a contribution a_n which is negligible compared to a_3. Thus, in the eigen-expansion formula, in the direction $\mathbf{u_g} = [1,0]$, the dominant eigenvalue we consider is λ_3. On the other hand, in the direction $\mathbf{u_g} = [0,1]$, the most significant contribution comes from the first eigenvalue and thus we only consider dominant eigenvalue λ_1 in the eigen-expansion.

To characterize the short-time regime, we use the well-known formula defined in Section 2.1.2

$$t \ll t_{short}^{lim} = \frac{L^2}{2\mathcal{D}_0},$$

where L is the characteristic length of the geometry along the direction perpendicular to $\mathbf{u_g}$ (see for example [138]). To characterize the long-time limit we use the normal diffusion displacement defined in Section 2.1.2 as

$$\frac{\sqrt{2(\Delta+\delta)\mathcal{D}_0}}{(L/2)} = NDD \gg 1.$$

For the chosen geometry and effective diffusion coefficient $\mathcal{D}_0$, the short-time limit is

$$t_{short}^{lim} = \frac{(9 \times 2)^2}{2e^{-3}} = 162\text{ms},$$

in the direction $[0, 1]$. In the direction $[1, 0]$, we have

$$t_{short}^{lim} = \frac{(19 \times 2)^2}{2e^{-3}} = 722\text{ms}.$$

In the following plots we always indicate the reference solution with a line, the potential approximation with squares, the eigenfunction approximation with circles and the mixed approximation with asterisks.

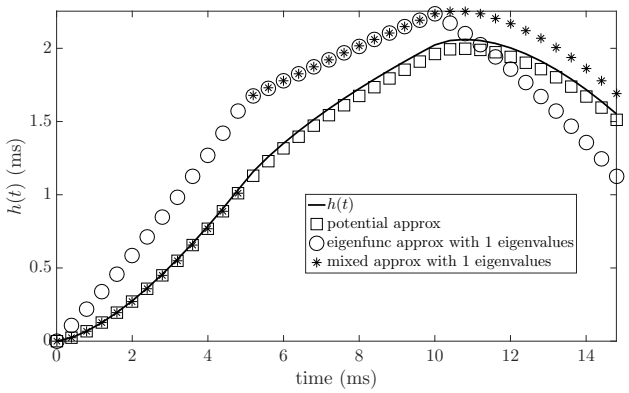

Figure 6.2 – $h(t)$ and its approximation (using the three different formulas found) with respect to the gradient directions $\mathbf{u_g} = [1, 0]$ for an ellipse of semi-axes 19μm and 9μm. Intrinsic diffusion coefficients $\mathcal{D}_0 = 1 \times 10^{-3}\text{mm}^2/\text{s}$, pulses duration $\delta = 5$ms and time-delay between pulses $\Delta = 10$ms.

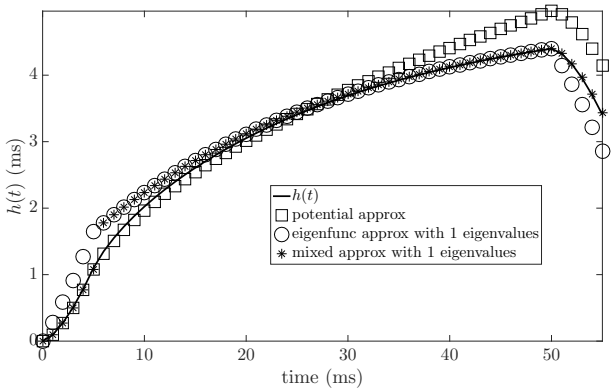

Figure 6.3 – $h(t)$ and its approximation (using the three different formulas found) with respect to the gradient directions $\mathbf{u_g} = [1, 0]$ for an ellipse of semiaxes 19μm and 9μm. Intrinsic diffusion coefficients $\mathcal{D}_0 = 1 \times 10^{-3}\text{mm}^2/\text{s}$, pulses duration $\delta = 5$ms and time-delay between pulses $\Delta = 50$ms.

In Figure 6.2 we considered $\delta = 5$ms, $\Delta = 10$ms and $\mathbf{u_g} = [1, 0]$. This means that we are considering short pulses and short delay between them but we are not in narrow pulse hypothesis.

As we can see the potential approximation (square) fits very well the reference (continuous line) in all the three time interval. We also notice that the mixed approximation (asterisks) works sufficiently well during the two pulses but not between them. Since the time is too short for considering just one eigenvalue contribution for the eigenfunctions approximation, the fit using this formula is far from the true solution.

In Figure 6.3 we considered $\delta = 5$ms, $\Delta = 50$ms and $\mathbf{u_g} = [1, 0]$. This means that we are considering short pulses and long delay between them. As we can see the layer potential approximation fits well the reference only during the first pulse and until $t \approx 25$ms but then it goes far away. The eigenfunction approximation appears not good during the pulses but it becomes very good at the end of the interval between them. The mixed approximation instead fits well during the pulses and it is a bit off just at the beginning of the second interval.

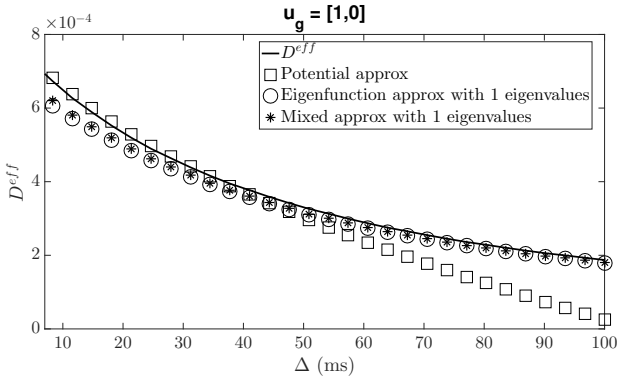

(a) Gradient direction $\mathbf{u_g} = [1, 0]$

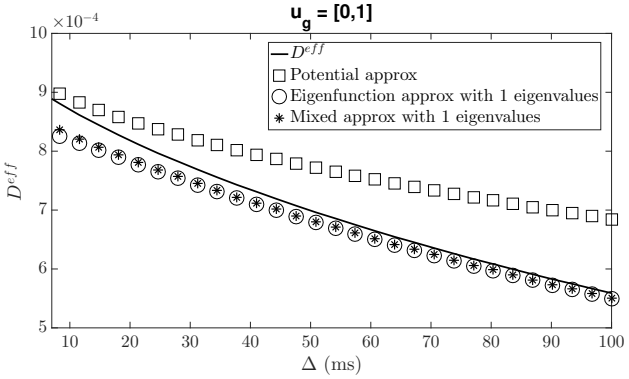

(b) Gradient direction $\mathbf{u_g} = [0, 1]$

Figure 6.4 – D^{eff} and its approximation (using the three different formulas found) with respect to two different gradient directions for an ellipse of semiaxes 19μm and 9μm. Intrinsic diffusion coefficients $\mathcal{D}_0 = 1 \times 10^{-3}$mm^2/s, pulses duration $\delta = 5$ms and thirty different values of the time-delay between pulses in the interval $[8, 80]$ms.

In Figures 6.4a and 6.4b we show the behaviour of D^{eff} computed for two different directions of the gradient ($\mathbf{u_g} = [1, 0]$ and $\mathbf{u_g} = [0, 1]$) but the same parameters ($\delta = 5$ms and thirty different values of Δ equally distributed in the interval $[8, 80]$ms). The potential formula works well for short $\Delta + \delta$, the eigenfunctions formula for long $\Delta + \delta$. Looking at these plots we can also say that the short time limits in which one should use the potential approximation is

$\Delta + \delta <$ 25ms for the $\mathbf{u_g} = [1, 0]$ direction and $\Delta + \delta <$ 10ms for the $\mathbf{u_g} = [0, 1]$ direction. On the contrary the long time limits in which one should use the eigenfunctions approximation is $\Delta + \delta >$ 55ms for the $\mathbf{u_g} = [1, 0]$ direction and $\Delta + \delta >$ 70ms for the $\mathbf{u_g} = [0, 1]$ direction.

In Figure 6.5 we show the approximations we found for the average of $D^{\text{eff}}/\mathcal{D}_0$ along two perpendicular directions. Here we considered $\delta = 5$ms and again thirty values of Δ in the interval $[8, 80]$ms. We observe that the potential approximation works well for small $\Delta + \delta$, the eigenfunction approximations for long $\Delta + \delta$.

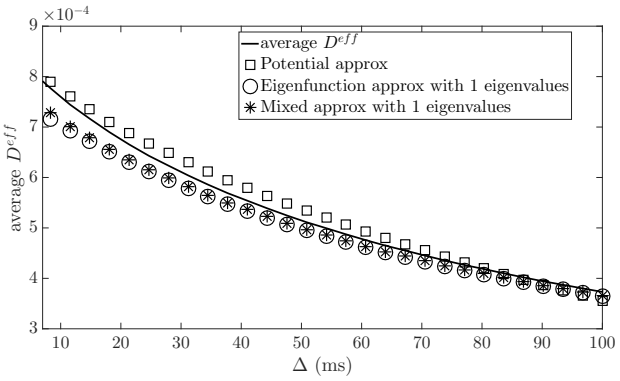

Figure 6.5 – $\tilde{D}^{\text{eff}}/\mathcal{D}_0$ and its approximation (using the three different formulas found) for an ellipse of semiaxes 19μm and 9μm. Intrinsic diffusion coefficients $\mathcal{D}_0 = 1 \times 10^{-3}\text{mm}^2/\text{s}$, pulses duration $\delta = 5$ms and thirty different values of the time-delay between pulses in the interval $[8, 80]$ms.

To conclude in Figure 6.6 we report the absolute error

$$|D^{\text{eff}} - D^{approx}|$$

for the same parameters as before and the two orthogonal directions. As we can see from the plots, as $\Delta + \delta$ grows, the error for the eigenfunctions and mixed approximations goes to zero while the error of the potential approximation grows.

6.5 Conclusions

Diffusion magnetic resonance imaging (dMRI) can be used to measure a time and direction dependent effective diffusion coefficient which can in turn reveal information about the tissue structure. In Chapter 4, a new mathematical model for the effective diffusion coefficient was obtained using homogenization techniques after imposing a certain scaling relationship between the physical parameters. An analytical formula for this coefficient was found that depends on the solution of a diffusion equation subject to time-dependent Neumann boundary conditions.

In this Chapter, we analysed the formula in the case of finite sub-domains. In particular, we obtained three representations of the effective diffusion coefficient that are appropriate in different time regimes. In the short time regime, we proposed using a representation based on the single layer potential and we call it SPST formula. In the long time regime when the pulse duration is not short, we proposed using a representation based on the eigenfunctions expansion of the Neumann Laplace operator and we call it FPLT formula. In the long time regime when

the pulse duration is short, we proposed a representation that combines the single layer during the pulses with the eigenfunctions expansion between the pulses and we call it SPLT formula.

In particular, the SPST formula corrects the existing Mitra formula [130] by correctly accounting for the pulse duration. This work helped to clarify how parameters of the tissue microstructure such as the surface to volume ratio or the dominant eigenvalues affect the effective diffusion coefficient.

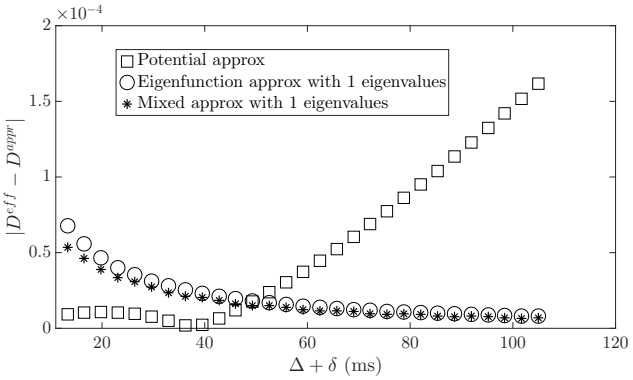

(a) Gradient direction $\mathbf{u_g} = [1, 0]$

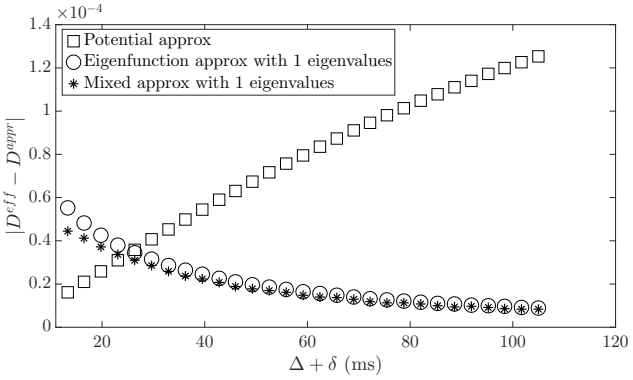

(b) Gradient direction $\mathbf{u_g} = [0, 1]$

Figure 6.6 – Absolute error $|D^{\text{eff}} - D^{approx}|$ using the three different formulas found with respect to two different gradient directions for an ellipse of semi-axes 19μm and 9μm. Intrinsic diffusion coefficients $\mathcal{D}_0 = 1 \times 10^{-3}\text{mm}^2/\text{s}$, pulses duration $\delta = 5$ms and thirty different values of the time-delay between pulses in the interval $[8, 80]$ms.

Chapter 7

On the inverse problem

Contents

7.1 Analysis based on the new formulas for *ADC* 132
7.1.1 Finding the surface over volume ratio in the short-time limit using SPST . 132
7.1.2 Finding the surface over volume ratio and the eigenvalues 136
7.2 On the determination of radii distributions 140
7.3 On the detection of the fibers orientations 146

In this final Chapter we want to give some indications about the final goal of the signal modelling, i.e. the inverse problem. Indeed, as we have observed many times in Chapter 2, the ambition of this field of research is to use the dMRI signal to recover as much information as possible on the microstructure. Possible questions are for example:

— find the surface over volume ratio,

— find distribution of cell sizes,

— find fiber orientations.

Many works in these directions are present in the literature (see for example [8, 13, 45, 101, 177, 185, 193, 195] and references therein) and here we do very preliminary work to investigate these tasks using the short pulse short-time (SPST), and the short pulse long-time (SPLT) formulas found from the H-*ADC* model as well as from the dMRI signal obtained solving the Bloch-Torrey equation at multiple g-values. Unfortunately we did not have sufficient time to properly investigate all the tasks so here we report our first investigations and we leave a deeper analysis (especially including the extra-cellular space) as a future direction of research. In particular, we give some mathematical hints regarding the use of the *ADC* or the dMRI signal to answer to these questions. We set up three simple problems:

— after having defined simple geometries we compute the reference *ADC* coming from the interior domain using the signal obtained from the solution of the Bloch-Torrey PDE at $b = 0,20\text{s/mm}^2$, and we try to fit geometrical parameters like the surface over volume ratio, the eigenvalues and the mean first moments of the eigenfunctions, using the SPST or the SPLT formulas derived in Chapter 6;

— supposing the domain composed by only circles, we develop an algorithm to estimate the radii distribution from the signal obtained solving the Bloch-Torrey PDE at multiple Δ and g;

— supposing the domain composed by only ellipses of the same size, we try to estimate the distribution of the ellipses orientations from the *ADC* obtained from the solution of the Bloch-Torrey PDE at $b = 0,20\text{s/mm}^2$ for several gradient directions.

To solve these tasks we always set up the least square problem between the reference data and our formulas and we try to determine a solution using different algorithms according to the application.

The Chapter is organized as follows. In Section 7.1.1 we show how we can estimate the surface over volume ratio, using the short pulse short-time formula obtained in Chapter 6. In particular, we show that with this formula we are not limited to the narrow pulse approximation and we compare the results with the well known Mitra model [130]. In Section 7.1.2 we report the results obtained using the short pulse long-time formula found in Chapter 6 and we show that the estimates on the eigenvalues and their contributions are sufficiently good while the surface over volume ratio cannot be well estimated. In Section 7.2 we investigate the use of the "Uzawa" algorithm ([183]) to solve the detection of radii distribution using the dMRI signal at multiple b-values or just the ADC. With this approach one does not need to define, a priori, a type of distribution (Gaussian, Gamma, Watson, etc.), but just be able to overestimate the total number of circles that are contributing to the measure inside the fix volume. Employing this algorithm we find that the problem is severely ill posed if we use only the values of ADC as data as it is extremely sensitive to noise. On the contrary, if we use the dMRI signal at multiple values of g and Δ, we obtain good results for a noise up to 5% (multiplicative random Gaussian noise). Finally, in Section 7.3, we investigate the detection of the fiber orientations using data coming from ADC or the entire dMRI signal. We suppose that we can decompose the measurements as sum of measurements coming from many 2D ellipses of the same size but different orientations. We prove that, contrary to the case of size distributions, it is not possible to determine a general distribution of orientations from given data. We in fact prove that the data can determine at most three significant parameters.

7.1 Analysis based on the SPST and SPLT formulas for ADC

In Chapter 6 we used the new model for time-dependent ADC derived in Chapter 4 and we approximated its expression using the eigenfunctions expansion and the single layer potential for the diffusion equation. We found three different formulas according to the duration of the pulses and the delay between them. In the case of both the duration of the pulses, and the time-delay between them long, we have already observed that the obtained formula coincides with the well known matrix formalism (see for example [15, 63, 64, 65]). For this reason we do not investigate this case but we concentrate ourselves in recovering the surface over volume ratio and/or the first non-zero and most contributive eigenvalues and their contributions using the potential or mixed approximations.

7.1.1 Finding the surface over volume ratio in the short-time limit using SPST

As we have already seen, for a closed domain Ω with a small permeability coefficient that negligible influence on the ADC, the short-time limit is achieved if the diffusion time is much shorter than $\frac{L^2}{2\mathcal{D}_0}$ where L^2 is the characteristic length of the domain. Considering the PGSE

sequence and narrow pulse approximation a well known formula ([11, 130]) is

$$D^{\text{eff}}_{\text{short}}(\Delta) = \mathcal{D}_0 \left(1 - \frac{4\sqrt{\mathcal{D}_0 \Delta}}{3\sqrt{\pi}} \frac{\int_\Gamma (\mathbf{u_g} \cdot \nu)^2 ds_{\mathbf{x}}}{|\Omega|} \right). \tag{7.1}$$

In Chapter 6, using the single layer potential ([70]) we have generalized this formula for the case of non narrow pulses but still short-time and we have found that we can write

$$\tilde{D}^{\text{eff}}_{\text{SPST}} = \mathcal{D}_0 - \frac{16}{35} \frac{\mathcal{D}_0^{3/2}}{\delta^2 (3\,\Delta - \delta)\sqrt{\pi}} \left[-2 \left(\delta^{7/2} + \Delta^{7/2} \right) + (\Delta - \delta)^{7/2} + (\Delta + \delta)^{7/2} \right] \frac{\int_\Gamma (\mathbf{u_g} \cdot \nu)^2 ds_{\mathbf{x}}}{|\Omega|}. \tag{7.2}$$

In particular, if we take the mean over d perpendicular dimensions (with d the dimension of the problem), the above formulas reduce to

$$\tilde{D}^{\text{eff}}_{\text{short}}(\Delta) = \mathcal{D}_0 \left(1 - \frac{4\sqrt{\mathcal{D}_0 \Delta}}{3\sqrt{\pi}} \frac{|\Gamma|}{d|\Omega|} \right) \tag{7.3}$$

and

$$\tilde{D}^{\text{eff}}_{\text{SPST}} = \mathcal{D}_0 - \frac{16}{35} \frac{\mathcal{D}_0^{3/2}}{\delta^2 (3\,\Delta - \delta)\sqrt{\pi}} \left[-2 \left(\delta^{7/2} + \Delta^{7/2} \right) + (\Delta - \delta)^{7/2} + (\Delta + \delta)^{7/2} \right] \frac{|\Gamma|}{d|\Omega|}. \tag{7.4}$$

Thanks to these formulas, by acquiring measurements in just d orthogonal directions and over several values of Δ, we can try to access the surface to volume fraction $\frac{|\Gamma|}{|\Omega|}$. Indeed, for simplicity, we consider the intrinsic diffusion coefficient $\mathcal{D}_0$ as known, and, in order to find $\frac{|\Gamma|}{|\Omega|}$, we can vary the delay between the pulses Δ for the Mitra's formula and varying both Δ and δ for the SPST formula. These formulas are especially convenient for sufficiently big geometries configurations for which the short-time limit can be achieved on the current dMRI scanners, for example for the neurons of the Alypsia (see [32, 112]).

We consider as examples a 2D geometry composed by two ellipses of semi-axes 75μm and 50μm, and 80μm and 55μm rotated respectively by 90° and 40° with respect to the x-axis, as illustrated in Figure 7.1. For this geometry, we have that the correct surface to volume ratio, computed using the finite element mesh in Figure 7.1, is equal to $0.0322\mu\text{m}^{-1}$. We suppose that the intrinsic diffusion coefficient is $\mathcal{D}_0 = 1.5e^{-3}\text{mm}^2/\text{s}$ for both ellipses. Thus, the short-time limit is achieved for $\Delta + \delta << 833\text{ms}$ (where to compute this limit we used the shortest axis of the ellipses, i.e. 100μm, as a characteristic length).

To compute the reference solution, we use the matlab pdetool to solve the Bloch-Torrey equation, and we obtain the *ADC* using a linear fit of the logarithm of the dMRI signal at two small b-values ($b = 0, 10\,\text{s/mm}^2$). We run the simulations for two different cases:

— under NPA, i.e. we consider $\delta = 2\text{ms}$ and ten values of Δ in $[8, 60]\text{ms}$,

— non-NPA, i.e. we consider $\delta = 8\text{ms}$ and ten values of Δ in $[8, 60]\text{ms}$.

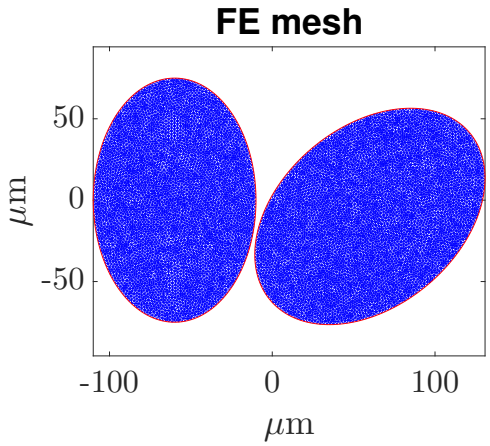

Figure 7.1 – Considered finite element mesh: two ellipses rotated by 90° and 40° with respect to the x-axis, and of semi-axis 75μm and 55μm, and 80μm and 55μm respectively.

In both cases, we consider the two orthogonal directions $\mathbf{u_g}^1 = [1, 0]$ and $\mathbf{u_g}^2 = [0, 1]$ and we average the resulting *ADC*s. We test the SPST formula (7.4) and the well known Mitra's one (7.3). Moreover, since in Chapter 3 we found that the evaluation time to consider for the Kärger model is $\Delta - \delta/3$ and not Δ, we also test (7.3) in which we replace Δ with $\Delta - \delta/3$, i.e. $\widetilde{D}^{\text{eff}}_{\text{short}}(\Delta - \delta/3)$. In Figure 7.2a and 7.2c we show how these three formulas approach the reference. We can see that in 7.2a all the formulas are superposed: this is because, since the pulses are narrow and Δ is sufficiently large, the value of δ does not influence the *ADC* too much. On the contrary, in 7.2c only the SPST formula (red crosses) approaches the reference in the whole time interval considered. Indeed, we see that the SPST formula fits better the data than the usual Mitra's formula (7.3) (purple stars). We also notice that the $\widetilde{D}^{\text{eff}}_{\text{short}}(\Delta - \delta/3)$ formula (black squares) give bad results so it should never been used.

		$\frac{\lvert\Gamma\rvert}{\lvert\Omega\rvert}$ (μm^{-1})	Estimated value (μm^{-1})	Relative Error %
NPA		0.0322		
	Old Formula 1		0.0341	5.9%
	Old Formula 2		0.0345	7.1%
	New Formula		0.0336	4.3%
not NPA		0.0322		
	Old Formula 1		0.0356	10.6%
	Old Formula 2		0.0371	15.2%
	New Formula		0.0336	4%

Table 7.1 – Estimated surface over volume ratio using the short time formula two ellipses of semi-axes 75μm and 50μm, and 80μm and 55μm rotated respectively by 90° and 40° with respect to the x-axis. Physical parameters $\mathcal{D}_0 = 1.5e-3\text{mm}^2/\text{s}$ and several values of Δ below 60ms.

To fit the surface over volume ratio, $\frac{|\Gamma|}{|\Omega|}$, we use the Matlab routine "lsqnonlin". This routine

employs the Levenberg-Marquardt algorithm to solve the minimization problem

$$\min_{\frac{|\Gamma|}{|\Omega|}} \|\widetilde{D}^{BT}(\delta,\Delta) - \widetilde{D}^{\text{eff}}(\delta,\Delta)\|_2$$

where $\widetilde{D}^{BT}(\delta,\Delta)$ is the reference *ADC* obtained after solving the Bloch-Torrey PDE and $\widetilde{D}^{\text{eff}}(\delta,\Delta)$ is either the SPST formula (7.3), either the Mitra formula (7.4). We run 1000 simulations each time choosing a random initial value in the interval $\left[0, 2\frac{|\Gamma|}{|\Omega|}\right]$. For each simulation we obtained the same minimum which means that this problem is well posed and has a unique solution. The resulting fits are reported in Figure 7.2b and 7.2d. As we can see, the fitting in Figure 7.2b is very good for all the three formulas, while in Figure 7.2d only the new formula is able to correctly fit the data. In Table 7.1 we report the values of the estimated surface over volume ratio along with their relative errors. These values confirms that the new formula allows us to estimate sufficiently well (less than 4% of relative error) the surface over volume ratio under the only hypothesis of short times. We clearly see that also in NPA gives a very accurate response.

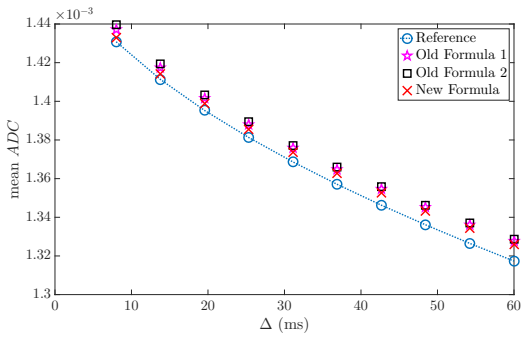

(a) Mean *ADC* under NPA

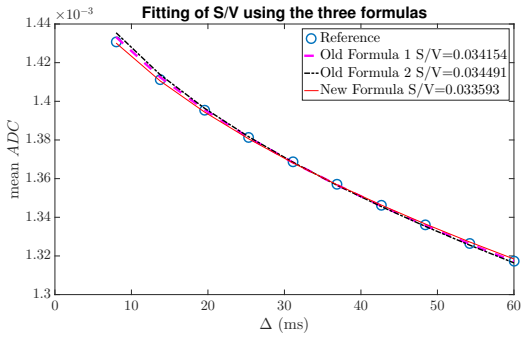

(b) Fitting with the three formulas under NPA

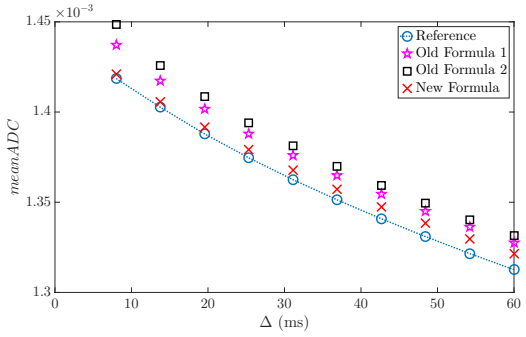

(c) Mean *ADC* without NPA

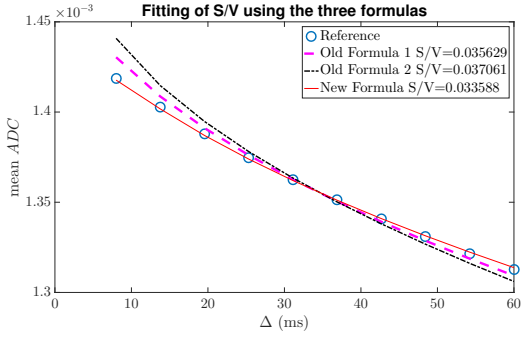

(d) Fitting with the three formulas without NPA

Figure 7.2 – Mean *ADC* over two orthogonal directions obtained with three different formulas and fitting of the surface over volume ratio under the narrow pulse hypothesis and not. With purple stars we indicate the results using Formula (7.3), with black square results using Formula (7.3) but replacing Δ with $\Delta - \frac{\delta}{3}$ and with red crosses results using Formula (7.4).

In conclusion, the short pulse short-time formula (SPST) is preferred over the Mitra formula for the non-NPA case. In particular, the SPST formula results very accurate and could be used

in practice to determine the surface over volume ratio in configurations for which the short-time limit can be achieved by the dMRI scanner (i.e. big cells like for example the Aplysia neurons). Indeed we showed that the SPST formula corrects the well known Mitra formula accounting for the finite pulses that are easier to achieve in practice.

7.1.2 Finding the surface over volume ratio and the eigenvalues

If the pulses are short enough, and the time delay between them is sufficiently long, we can use the SPLT formula founded in Chapter 6 and see if we can invert it considering only a small number of eigenvalues. We suppose that each domain in the defined geometry has the same intrinsic diffusion coefficient $\mathcal{D}_0$ and for each domain Ω_l, we consider the formula obtained averaging over d-orthogonal directions

$$\frac{\widetilde{D}^l_{\text{SPLT}}}{\mathcal{D}_0} = \frac{\delta}{6(\Delta - \frac{\delta}{3})} - \frac{8\mathcal{D}_0^{1/2}\delta^{3/2}}{35\sqrt{\pi}(\Delta - \frac{\delta}{3})}\frac{|\Gamma_l|}{d|\Omega_l|} - \sum_{n=1}^{\infty} \frac{\delta k_n + j_n}{\mathcal{D}_0\delta^2(\Delta - \frac{\delta}{3})}\left(\delta - \frac{e^{-\lambda_n\mathcal{D}_0\Delta}(1 - e^{\lambda_n\mathcal{D}_0\delta})}{\lambda_n\mathcal{D}_0}\right). \tag{7.5}$$

where

$$k_n := \sum_{i=1}^{d} \frac{-(a_n^i)^2}{d|\Omega_l|} = \sum_{i=1}^{d} \frac{-\left(\int_{\Omega_j} \mathbf{x}\cdot{\mathbf{u_g}}^i\phi_n(\mathbf{x})d\mathbf{x}\right)^2 d\mathbf{u_g}}{d|\Omega_l|}, \tag{7.6}$$

i.e. the mean over d orthogonal directions of the first moment square of the n-th eigenfunction along these directions ($a_n^i = \int_{\Omega_l}(\mathbf{x}\cdot{\mathbf{u_g}}^i)\phi_n(\mathbf{x})d\mathbf{x}$), and

$$j_n := \sum_{i=1}^{d} \frac{b_n^i a_n^i}{d|\Omega_l|} = \sum_{i=1}^{d} \frac{\left(\int_{\Omega_l}\omega_{{\mathbf{u_g}}^i}(\mathbf{x},\delta)\phi_n(\mathbf{x})d\mathbf{x}\right)\left(\int_{\Omega_l}\mathbf{x}\cdot{\mathbf{u_g}}^i\phi_n(\mathbf{x})d\mathbf{x}\right)}{d|\Omega_l|} \tag{7.7}$$

with $b_n^i = \int_{\Omega_l}\omega^i(\mathbf{x},\delta)\phi_n(\mathbf{x})d\mathbf{x}$, i.e. the integral of the solution of the cellular problem (6.6) evaluated at time δ multiplied by the n-th Laplace eigenfunction $\phi_n(\mathbf{x})$ (See Section 6.2 for more details). We then average the two effective diffusion coefficients obtaining:

$$\frac{\widetilde{D}^{\text{eff}}_{\text{SPLT}}}{\mathcal{D}_0} = \sum_l \frac{|\Omega_l|}{|\Omega|}\frac{\widetilde{D}^l_{\text{SPLT}}}{\mathcal{D}_0}, \tag{7.8}$$

where $\Omega = \bigcup_l \Omega_l$. Thus the formula we want to invert is

$$\frac{\widetilde{D}^{\text{eff}}_{\text{SPLT}}}{\mathcal{D}_0} = \frac{\delta}{6(\Delta - \frac{\delta}{3})} - \frac{8\mathcal{D}_0^{1/2}\delta^{3/2}}{35\sqrt{\pi}(\Delta - \frac{\delta}{3})}\frac{|\Gamma|}{d|\Omega|} - \sum_l \frac{|\Omega_l|}{|\Omega|}\sum_{n=1}^{\infty} \frac{\delta k_n + j_n}{\mathcal{D}_0\delta^2(\Delta - \frac{\delta}{3})}\left(\delta - \frac{e^{-\lambda_n\mathcal{D}_0\Delta}(1 - e^{\lambda_n\mathcal{D}_0\delta})}{\lambda_n\mathcal{D}_0}\right) \tag{7.9}$$

where $|\Gamma| = \sum_l |\Gamma_l|$. In order to investigate the invertibility we a-dimensionalize the above formula and the unknown parameters as follows

$$\frac{\widetilde{D}^{\text{eff}}}{\mathcal{D}_0} = \mathcal{C} - \mathcal{C}_1\mathcal{P}_1 + \sum_{\substack{n=2 \\ n\in 2\mathbb{N}}}^{\infty} \mathcal{C}_2\mathcal{P}_n\left(1 - \frac{e^{-\mathcal{C}_3\mathcal{P}_{n+1}}(1 - e^{\mathcal{P}_{n+1}})}{\mathcal{P}_{n+1}}\right), \tag{7.10}$$

where

$$\mathcal{C} = \frac{\delta}{6\left(\Delta - \frac{\delta}{3}\right)}, \quad \mathcal{C}_1 = -\frac{8\delta}{35\sqrt{\pi}\left(\Delta - \frac{\delta}{3}\right)}, \quad \mathcal{C}_2 = -\frac{\delta}{\left(\Delta - \frac{\delta}{3}\right)}, \quad \mathcal{C}_3 = \frac{\Delta}{\delta},$$

are the known constants and

$$\mathcal{P}_1 = \sqrt{\mathcal{D}_0\delta}\frac{|\Gamma|}{d|\Omega|}, \quad \mathcal{P}_n = \frac{\delta k_n^2 + j_n}{\mathcal{D}_0\delta^2}, \quad \mathcal{P}_{n+1} = \lambda_n \mathcal{D}_0 \delta$$

are the non dimensional parameters to be estimated. In the previous Chapter, we have already observed that, since δ is small, $b_n^i \approx O(\delta^{3/2})$ and thus j_n is smaller then δk_n^2 thus we can neglect its contribution and estimate k_n. Thus, from the estimate on $\mathcal{P}_1$ we can recover the surface over volume ratio, from the estimate on $\mathcal{P}_n$ we can recover k_n (i.e. the square root of the mean over d orthogonal directions of the first moment square along these directions of the n-th eigenfunction) and from $\mathcal{P}_{n+1}$ the n-th Laplace eigenvalue.

Here we report the results obtained fitting the first five parameters $(\mathcal{P}_1, \ldots, \mathcal{P}_5)$ for a 2D geometry consisted of two impermeable ellipses of semi-axes 4μm and 1μm, and 3μm and 1μm, rotated respectively by 60° and 120° with respect to the x-axis as illustrated in Figure 7.3. We consider just 5 parameters because, as we have seen in the numerical section of Chapter 6, we can well approximate the data using just one non-zero eigenvalue and its contribution for each domain in the geometry.

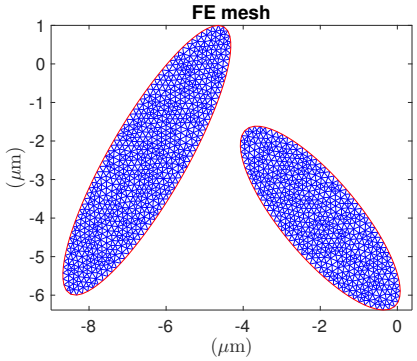

Figure 7.3 – Considered finite element mesh: two ellipses rotated by 60° and 120° with respect to the x-axis, and of semi-axis 4μm and 1μm, and 3μm and 1μm respectively.

To create the data we solved the Bloch-Torrey equation with zero Neumann boundary conditions in the two orthogonal directions $\mathbf{u_g}^1 = [1, 0]$ and $\mathbf{u_g}^2 = [0, 1]$, using the Matlab "pdetool" and the mesh in Figure 7.3. For each ellipse, we calculate the average effective diffusion coefficient ($\widetilde{D}^{BT}$) for fixed δ and fifteen values of Δ equally distributed in the interval $[5, 18]$ms. We then averaged the effective diffusion coefficients over the two domains to get a total of 15 data points as inputs in our fitting procedure. We keep just two terms in the infinite sum in (7.10) in order to estimate the total surface over volume ratio, the first eigenvalue of each ellipse (i.e. the smallest one for each ellipse) and their contributions. To fit the data we used the Matlab routine "lsqnonlin" which employees the algorithm "trust-region-reflective" to find the minimum of the least square problem

$$\min_{\mathcal{P}_1 \ldots \mathcal{P}_5} \left\| \frac{\widetilde{D}^{BT}(\Delta)}{\mathcal{D}_0} - \frac{\widetilde{D}^{\text{eff}}(\Delta)}{\mathcal{D}_0} \right\|_2 \tag{7.11}$$

with tolerance of $1e^{-8}$. In particular, we made a statistical analysis using 1000 random normal initial guesses in the interval $[\frac{1}{2}, \frac{3}{2}] \times$ (true parameter) and as limits for the estimate parameters we considered the interval $[0, 2 \times$ (true parameter)$]$.

In Figure 7.4 we report the plots of the data and the fitting obtained for three different values of δ. The black circles are the simulated data and the dotted line is the obtained fitting using as parameters the mean values of the obtained results in the 1000 simulations. In blue we plot the results we would obtain employing the formula in (7.10) and using the exact parameters. As we can see, the formula with the exact parameters fits very well the data at the end of the considered time interval, while is a bit off at the beginning. This is because, as we have seen in Chapter 6 the SPLT formula with a small number of eigenvalues works better when Δ is sufficiently long. Thus we expect to lose something in the approximation of the parameters because the fitting eliminates this gap between the data and the formula.

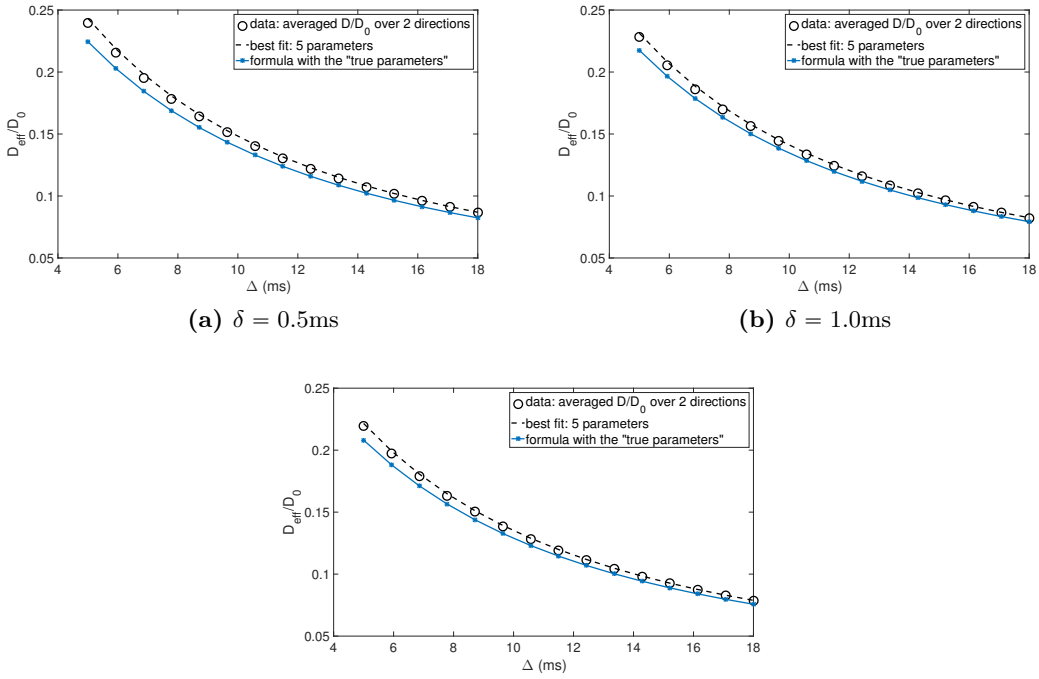

(a) $\delta = 0.5$ms **(b)** $\delta = 1.0$ms

(c) $\delta = 1.5$ms

Figure 7.4 – Fitting of the average ADC in two orthogonal directions coming from a geometry composed by two ellipses of semi-axes 4μm and 1μm, and 3μm and 1μm, rotated respectively by 60° and 120° with respect to the x-axis and of intrinsic diffusion coefficient $\mathcal{D}_0 = 1e^{-3}\text{mm}^2/\text{s}$.

In Table 7.2 we report the numerical results of the inversion. As we can see the eigenvalues (λ_1 and λ_2) and their contributions (k_1 and k_2) are sufficiently well estimated, indeed we have a relative error less then 16%. We also observe that we obtain the best estimates for the eigenvalues for the biggest $\delta = 1.5$ms and for their contribution for δ considered, i.e. 1.0ms. On the contrary, the surface over volume ratio is not well estimated, indeed the relative error is always between 30% and 42%. Taking a closer look at the data in Table 7.2 the best estimates for this parameter is obtained for the shortest δ. This means that for the other choices the approximation during

the pulses fails because we are considering too long pulses (see Chapter 6). Another explanation for this failure is that if we take the derivative of the expression in (7.10) with respect to $\mathcal{P}_1$ we obtain $\mathcal{C}_1$. This is a constant for the estimate but it depends on Δ and in particular it tends to 0 as Δ grows. This means that to well estimate $\mathcal{P}_1$ we should consider just points for small Δ but (from Chapter 6) we know that for these points the mixed formula is not appropriate unless we consider an higher numbers of eigenvalues to better approximate the solution between the pulses. But this would imply more parameters to be estimated. We also observe that, on contrast of what we found in the previous Section for the SPST formula, here the problem is not well posed and for every different initial guess we end up in a different minimum. This is the reason for which in Table 7.2 we report also the values of the relative standard deviations for each estimated parameter.

		$\frac{\lvert\Gamma\rvert}{d\lvert\Omega\rvert}$ (mm^{-1})	λ_1 (mm^{-2})	k_1 (mm)	λ_2 (mm^{-2})	k_2 (mm)
	True Parameters	1.37	0.22	7.03	0.39	4.57
$\delta = 0.5$ms						
	Estimations	0.96 ± 0.46	0.216 ± 0.02	6.85±0.71	0.45±0.06	4.53±0.69
	Relative error	30.3%	2.7%	2.5%	15.6%	0.8%
	Relative std	33.5%	8.2%	10.1%	15.3%	15%
$\delta = 1.0$ms						
	Estimations	0.80±0.41	0.21±0.01	6.56± 0.72	0.42±0.06	4.25±0.68
	Relative error	41.6%	2%	6.8%	6%	7%
	Relative std	30%	6.8%	10.3%	16.7%	15%
$\delta = 1.5$ms						
	Estimations	0.85±0.22	0.22±0.01	6.32± 0.75	0.39±0.07	4.01±0.70
	Relative error	38.2%	0%	10.1%	0%	12.2%
	Relative std	15.9%	6.4%	10.6%	18.4%	15.4%

Table 7.2 – Estimated parameters using the mixed formula for two ellipses of semi-axes 4μm and 1μm, and 3μm and 1μm, rotated respectively by 60° and 120° with respect to the x-axis. Physical parameters: $\mathcal{D}_0 = 1e-3\text{mm}^2/\text{s}$ and fifteen values of Δ in $[5, 18]$ms.

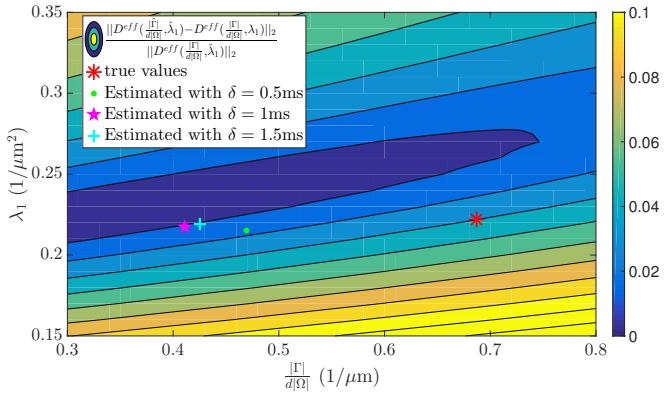

Figure 7.5 – Sensitivity of the method using SPLT formula with five parameters.

Finally in Figure 7.5 we show a contour plot which underlines the sensitivity of our approach

for $\frac{|\Gamma|}{|\Omega|}$ and λ_1 assuming that we know the exact values of the other three parameters. As we can see the method is more accurate to estimate λ_1 than $\frac{|\Gamma|}{|\Omega|}$ which confirms the results obtained in Table 7.2. Moreover, here we can see that the SPLT formula with the correct values of parameters has already an error of about 4% (red star) while the fitting with different δ gives us results with errors around 1%. This means that part of the error that we commit in the estimation is due to the error of the formula.

In conclusion, this formula helps us to better understand the behaviour of ADC but its use for the inverse problem is complicated and more investigations are need. From the obtained results, we cannot hope to well approximate the surface over volume ratio with the current approach. On the contrary, the estimates of the eigenvalues and their contributions are already satisfactory even if we cannot keep the number of parameters small if the geometry is not sufficiently simple. Anyhow, for simple geometries already the values of the eigenvalues and their first moments can tell us something about the configuration.

7.2 On the determination of radii distributions

To investigate this question we suppose the domain to be composed of only N impermeable circles. We do not consider the contribution of the extra-cellular compartment (which is left for future investigations) and we use the PGSE sequence. We also suppose that δ is fixed and we vary Δ and $q = \gamma g$ to obtain the signals or just Δ to obtain the effective diffusion tensors. Furthermore, since we investigate the signal coming from only circles which are symmetric, we fix $\mathbf{u_g} = [1, 0]$, because, without the contribution of the extra-cellular space, the signal is the same in all the directions.

With these assumptions we can write the signal coming from a voxel as

$$S(q, \Delta) \approx \sum_{R_i} \mathbf{n}_{R_i} S(R_i, q, \Delta), \tag{7.12}$$

where $\mathbf{n}_{R_i}$ is the number of circles of radius R_i that contribute to the signal and $S(R_i, q, \Delta)$ represents the signal obtained by one circle of radius R_i subjected to a gradient of intensity q and Δ parameter for PGSE. The idea is to discretize Δ and q in two intervals to obtain a vector of data

$$S^T = [S(q_1, \Delta_1), \dots, S(q_1, \Delta_M), \dots, S(q_L, \Delta_1), \dots, S(q_L, \Delta_M)] \tag{7.13}$$

and discretize also R to obtain the 2D reference matrix

$$A = \begin{pmatrix} S(R_1, q_1, \Delta_1) & \dots & S(R_N, q_1, \Delta_1) \\ \vdots & \vdots & \vdots \\ S(R_1, q_1, \Delta_M) & \dots & S(R_N, q_1, \Delta_M) \\ \vdots & \vdots & \vdots \\ S(R_1, q_L, \Delta_1) & \dots & S(R_N, q_L, \Delta_1) \\ \vdots & \vdots & \vdots \\ S(R_1, q_L, \Delta_M) & \dots & S(R_N, q_L, \Delta_M) \end{pmatrix}. \tag{7.14}$$

We can thus rewrite the inverse problem as finding solutions to the linear system

$$S = A\mathbf{x} \tag{7.15}$$

where the components of $\mathbf{x} = (n_{R_1}, \dots, n_{R_N})$ represent the number of circles of the corresponding radius present in the geometry and is the parameter we want to recover. Since A is in general not a square matrix (but a priori $\text{rank}(A) = N$), we can define the solution as

$$\mathbf{x}^* = \underset{\mathbf{x}}{\text{argmin}} \|A\mathbf{x} - S\|^2. \tag{7.16}$$

Usually A is ill-conditioned, and there may be noise in the data S, thus one should rely on some regularization techniques to solve the least square problem (7.16). We choose to use Tikhonov regularization technique ([98]) since a reasonable statistical form of noise is Gaussian. Let S^ϵ be the noisy measurements, i.e.

$$\|S^\epsilon - S\| \leqslant \epsilon \tag{7.17}$$

where ϵ is an upper bound for the noise level. We solve for $\mathbf{x}^\epsilon$ solution of

$$\mathbf{x}^\epsilon = \min_{\mathbf{x}} J^\epsilon(\mathbf{x}) = \min_{\mathbf{x}} \frac{1}{2}\|A\mathbf{x} - S^\epsilon\|^2 + \frac{1}{2}\alpha(\epsilon)\|\mathbf{x}\|^2, \tag{7.18}$$

where the parameter $\alpha(\epsilon)$ is determined using the Morozov's Discrepancy Principle (see for example [98]), i.e. $\alpha(\epsilon)$ is such that

$$\|A\mathbf{x}^\epsilon - S^\epsilon\| = \epsilon. \tag{7.19}$$

For our problem, the components of $\mathbf{x}^\epsilon$ cannot have any values in $\mathbb{R}$. Indeed, we have the constraints

$$\sum_{i=1}^{N} x_i^\epsilon \leqslant N_{\max} \quad \text{and} \quad x_i^\epsilon \geqslant 0 \quad \forall i = 1, \dots, N. \tag{7.20}$$

What we need to solve is then a minimization of $J^\epsilon(\mathbf{x})$ in the subspace F identified by the constraints (7.20). We can rewrite these constraints as $F(\mathbf{x}^\epsilon) = C\mathbf{x}^\epsilon - \mathbf{f} \leqslant 0$ where

$$C = \begin{pmatrix} 1 & \dots & \dots & 1 \\ -1 & 0 & \dots & 0 \\ 0 & \ddots & \ddots & \vdots \\ \vdots & \ddots & \ddots & 0 \\ 0 & \dots & 0 & -1 \end{pmatrix} \quad \text{and} \quad \mathbf{f} = \begin{pmatrix} N_{\max} \\ 0 \\ \vdots \\ \vdots \\ 0 \end{pmatrix}. \tag{7.21}$$

The idea is then to use an algorithm that solves

$$\begin{cases} \min_{\mathbf{x}} J^\epsilon(\mathbf{x}) = \min_{\mathbf{x}} \frac{1}{2}\|A\mathbf{x} - S^\epsilon\|^2 + \frac{1}{2}\alpha(\epsilon)\|\mathbf{x}\|^2, \\ F(\mathbf{x}) \leqslant 0. \end{cases} \tag{7.22}$$

We know that if $\mathbf{x}^\epsilon$ is a minimum for $J^\epsilon(\mathbf{x})$ on the convex set $F(\mathbf{x})$ then there exists $\lambda \in (\mathbb{R}^+)^{N+1}$ such that

$$\mathcal{L}(\mathbf{x}^\epsilon, \lambda) = \nabla J^\epsilon(\mathbf{x}^\epsilon) + \lambda \nabla F(\mathbf{x}^\epsilon) = 0 \tag{7.23}$$

$$C\mathbf{x}^\epsilon \leqslant f, \quad \langle \lambda, C\mathbf{x}^\epsilon - \mathbf{f} \rangle = 0, \tag{7.24}$$

where $\langle ., . \rangle$ indicates the $\mathbb{R}^{N+1}$ scalar product. Assuming that the number of data that we can acquire is bigger than N (i.e. $M + L \geqslant N$), a way to solve this problem is to use the Uzawa algorithm ([183]) summarized in the pseudo-code below.

Algorithm 1 Uzawa algorithm

procedure
  $\lambda \leftarrow$ parameter for the Uzawa iteration
  $\rho \leftarrow$ step of Uzawa
  $\eta \leftarrow$ precision
  $J(\mathbf{x}) = \frac{1}{2}(\|A\mathbf{x} - S\|^2 + \alpha\|\mathbf{x}\|^2)$
  $F(\mathbf{x}) = C\mathbf{x} - \mathbf{f}$
  $\mathcal{L}(\mathbf{x}, \lambda) \leftarrow J(\mathbf{x}) + \lambda F(\mathbf{x})$
  while $||\lambda_{n+1} - \lambda_n|| > \eta$ **do**
    $\alpha(\epsilon) \leftarrow$ Tikhonov parameter for regularization
    $\mathbf{x}^\epsilon_{n+1} \leftarrow \mathcal{L}(\mathbf{x}^\epsilon_n, \lambda_n)$ + Tikhonov
    $\lambda_{n+1} \leftarrow \max(0, \lambda_n + \rho(C\mathbf{x}^\epsilon_n - \mathbf{f}))$
  end while
end procedure

In particular, one needs to choose a step ρ, a precision η and, at each iteration, solve the problem (7.23) and update the values of λ_{n+1} using

$$\lambda_{n+1} = \max(\lambda_n + \rho F(\mathbf{x}^\epsilon), 0). \tag{7.25}$$

We apply Tikhonov regularization to (7.23). We factorize the matrix A using the singular values decomposition (SVD [98])

$$A = U\Sigma V^T \tag{7.26}$$

and at each iteration we update $\mathbf{x}^\epsilon_n$ as follows

$$(\alpha_n(\epsilon) + \sigma_i^2)(x^\epsilon_n)_i = \sigma_i(S^\epsilon \cdot u_i) - \lambda_n \cdot (Cv_i), \tag{7.27}$$

$$\mathbf{x}_n = \sum_i (x^\epsilon_n)_i v_i, \tag{7.28}$$

where σ_i are the singular values of A (i.e. the components of the diagonal matrix Σ), and u_i and v_i are the column vectors of U and V respectively. The parameter $\alpha_n(\epsilon)$ is determined by (7.19) and is therefore the zero of the function

$$\phi(\alpha) := \sum_i \left(\frac{\alpha^2}{(\alpha + \sigma_i^2)^2} - \epsilon^2 \right) \langle S^\epsilon, u_i \rangle^2 , \tag{7.29}$$

inside the interval $\left[\frac{\epsilon \min \sigma_i}{1 - \epsilon}, \frac{\epsilon \max \sigma_i}{1 - \epsilon} \right]$.

For our numerical simulations, we implemented the Uzawa algorithm in Matlab and we used the function "svd" to factorize the matrix A. To create the data we simulated the signal using the formula (7.12). This means in particular that we do not take into account modelling error.

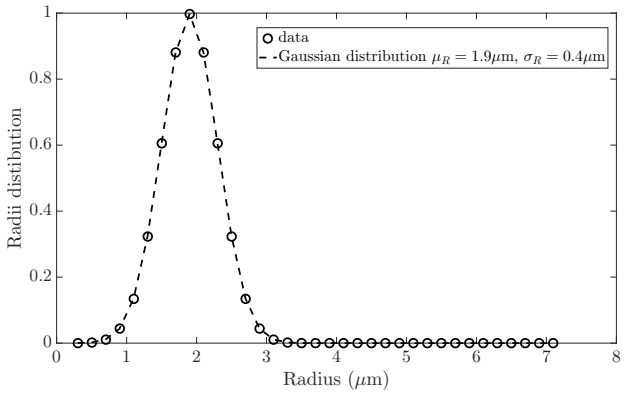

Figure 7.6 – Radii distribution used for the simulations.

We consider a set of 100 circles distributed as a Normal of $\mu_R = 1.9\mu$m and $\sigma = 0.4$ as shown in Figure 7.6. We assume that the radii of the circles are discretized uniformly in $[0.3, 7.1]\mu$m with a discretization step of 0.2μm (see radii distribution in Figure 7.6). We also impose the intrinsic diffusion coefficient to be $\mathcal{D}_0 = 1e-3\text{mm}^2/\text{s}$ and we generated the vector of the signals with $\delta = 0.5$ms, $\mathbf{u_g} = [1, 0]$, six values of $q = \gamma g$ in $[2.5e-3, 5e-3]$ and nineteen values of Δ in $[0.5, 5]$ms. To create the matrix A we discretize the radii in the interval $[0.25, 7]\mu$m with a step of discretization of 0.25μm and we generate the components of the matrix using the signals obtained with $\delta = 0.5$ms, $\mathbf{u_g} = [1, 0]$, six values of γg in $[2.5e-3, 5e-3]$ and nineteen values of Δ in $[0.5, 5]$ms. For the inverse problem we also imposed $N_{\max} = 100$ and $\lambda_0 = 0$.

The results obtained using the Uzawa algorithm are shown in Figure 7.7. In Figure 7.7a we show how we were able to recover the number of circles of a precise radius without noise affecting the data. For this case we choose the parameters

$$\rho = 1e^{-4}, \quad \eta = 1e^{-4} \quad \text{and} \quad \alpha = 1e^{-5}, \tag{7.30}$$

and the Uzawa algorithm converges to the shown solution in just one iteration and the total radii found are 100, while the estimate mean an standard deviation are $\mu_R = 1.8998$ and $\sigma_R = 0.4129$. To make an analysis for the case of noisy data we set ρ to be equal to the added noise, and to choose α we use the Morozov's Discrepancy Principle introduced before. In Figure 7.7b we show the results obtained adding a 1% Gaussian noise to our data before applying the inversion algorithm. In this case, the Uzawa algorithm converges in 155193 iterations and the total radii found are 99, while the estimate mean an standard deviation are $\mu_R = 1.8725$ and $\sigma_R = 0.4358$. In Figure 7.7c we show the results obtained adding 5% Gaussian noise and using the same routine. The algorithm converged after 178744 iterations and the total radii found are 96, the estimate mean an standard deviation are $\mu_R = 1.8067$ and $\sigma_R = 0.4934$. Finally, in Figure 7.7d we show the sensitivity of our approach. We show a contour plot of the relative residual

$$\frac{||S(\hat{\mu}_R, \hat{\sigma}_R, \delta, \Delta, g) - S(\mu_R, \sigma_R, \delta, \Delta, g)||_2}{||S(\hat{\mu}_R, \hat{\sigma}_R, \delta, \Delta, g)||_2}$$

where $\hat{\mu}_R = 1.9$, and $\hat{\sigma}_R = 0.4$ are the parameters of the simulated Normal distribution to create the data and we have discretized μ_R and σ_R around these values to obtain the level curves. As

we can see, this approach results to be very accurate for the mean μ_R and less for the variance σ_R. In particular, the behaviour of the levels lines explain why we have a slow convergence and highlights the fact that if the noise is not Gaussian we could have much more sensitivity to noise for the parameter σ_R.

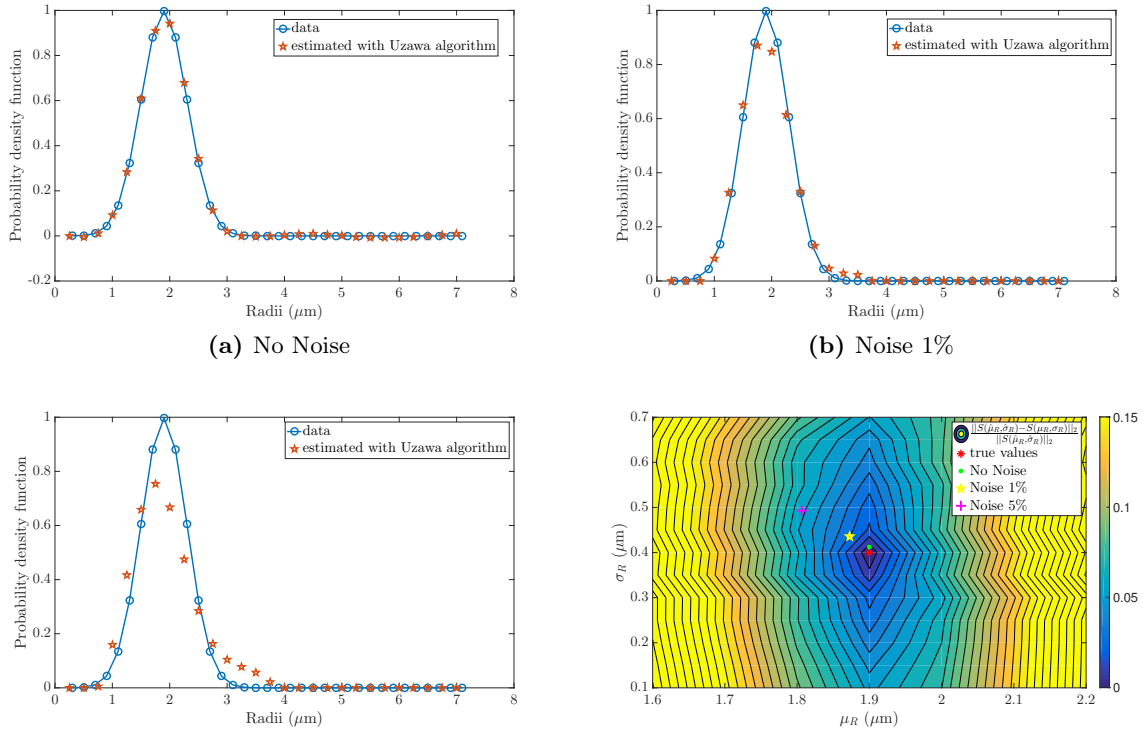

(a) No Noise **(b)** Noise 1%

(c) Noise 5% **(d)** Sensitivity

Figure 7.7 – Radii distribution estimation using the dMRI signal coming from 25 radii distributed as a Normal of $\mu_R = 1.9\mu$m and $\sigma = 0.4$ with intrinsic diffusion coefficient $\mathcal{D}_0 = 1e-3\text{mm}^2/\text{s}$. The signal was generated with $\delta = 0.5$ms, $\mathbf{u_g} = [1, 0]$, six values of γg in $[2.5e-3, 5e-3]$ and nineteen values of Δ in $[0.5, 5]$ms.

We now try to apply the same procedure to *ADC* data and not to the entire signal. We always assume that δ and $\mathbf{u_g}$ are fixed and we acquire measurements varying only Δ. With these assumptions we can write the effective diffusion tensor as

$$D^{\text{eff}}(\Delta) = \sum_{R_i} \mathbf{n}_{R_i} D(\Delta, R_i), \tag{7.31}$$

where $\mathbf{n}_{R_i}$ is the number of circles of radii R_i and $D(\Delta, R_i)$ is the effective diffusion coefficient computed multiplied by the volume of the circle πR_i^2 for an impermeable circle of radius R_i subjected to two pulses of a linear diffusion gradient with a time delay between them equal to Δ. Again this problem can be rewritten using the formulation in (7.22) where $A = D(\Delta_j, R_i)$, $S = D^{\text{eff}}(\Delta_j)$ and F is the same as before, i.e. the constraints can be written using (7.20). For the simulations we fix$\delta = 0.5$ms and $\mathbf{u_g} = [1, 0]$. We use again the radii distribution in Figure 7.6, but to generate enough data without the employ of g, we used thirty-eight values of Δ in the in $[0.75, 10]$ms. For the inverse problem we also impose $N_{\max} = 100$ and $\lambda_0 = 0$.

In Figure 7.8 we show the results obtained using the Uzawa algorithm with parameters $\rho = \eta = 1e^{-4}$ and $\alpha = 1e^{-20}$. Here the data were simulated without noise and we see that the inversion works sufficiently well and the method converges in 1 iteration. In particular, the recovered mean is $\mu_R = 1.9\mu$m and the standard deviation is $\sigma_R = 0.4131$.

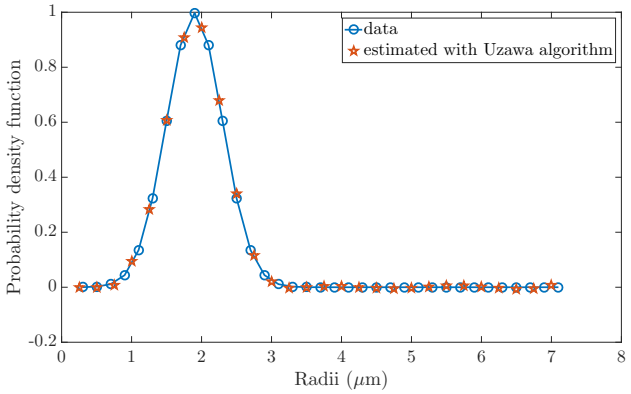

Figure 7.8 – Radii distribution estimation using the dMRI signal coming from 25 radii distributed as a Normal of $\mu_R = 1.9\mu$m and $\sigma = 0.4$ with intrinsic diffusion coefficient $\mathcal{D}_0 = 1e-3\text{mm}^2/\text{s}$. The signal was generated with $\delta = 0.5$ms, $\mathbf{u_g} = [1, 0]$, six values of γg in $[2.5e-3, 5e-3]$ and nineteen values of Δ in $[0.75, 10]$ms.

We tried to use the same routine also for noisy data and we started adding 1% Gaussian noise. Unfortunately, for this type of data, setting $\rho = 0.01$ and choosing α according to the Morozov's Discrepancy Principle the method did not converge. In our investigations to try to understand the reasons of this failure, we thought about two possibilities

— the founded α was not correct,

— the choice of ρ was not appropriate.

We tried to investigate these two possible reasons but what we get was that, incrementing the value of ρ, the Uzawa method did not converge either. On the contrary taking a smaller ρ we obtained that the stopping criteria was verified after only one iteration but the result was not respecting the constraints (in particular we had some negative values for the entries). The reason for that could be that α was not well chosen because we notice that taking a smaller value of α the amount of negative contributions was less and the reconstructed distribution was better. On the other hand, only one iteration seems to be not enough to converge to a good solution in case of noisy data, so maybe the stopping criterion and/or the value of ρ were not well chosen. An idea to overcome this problem could be to adapt the value of ρ at each iteration. A way to do that could be to add a loop on ρ and say that while $J(\mathbf{x}_n) < J(\mathbf{x}_{n+1})$, we need to replace ρ by $a * \rho_{n-1}$ (with $a \in [0.5, 1[$), and recompute $\mathbf{x}_{n+1}$. In this case, we guarantee that the values of the functional we want to minimize, are decreasing at each iteration. Nevertheless, looking at the singular values of the matrix A for this case we found that only one value was bigger than 0.01 and all the others were going to zero very quickly. This means that the problem is extremely bad conditioned and we do not believe that the adapting method for ρ would significantly improve the results. This means, in particular, that the chosen parameters for collecting the data (varying Δ) do not provide sufficient sensitivity of ADC to radial distributions. Exploiting other type of parameters with different other signals, may be helpful, but this is yet to be investigate.

In conclusion, with our simulations we get that inverting the signal using linear convex minimization with constraints appear feasible and very stable with respect to noise. This is in accordance with the results obtained by Daducci et. al [45] with "AMICO" (Accelerated Microstructure Imaging via Convex Optimization), in which they used Tikhonov regularization along with the employment of the ordinary least-squares procedure implemented in Matlab. Here we propose a new algorithm to solve this inverse problem which seems to be stable to noise but of course validation on real data adding a modelling for the extra-compartment should be done. We also highlighted the difficulties encountered when using just *ADC* but further investigations should be also done for this case.

7.3 On the detection of the fibers orientations

A classical question in the dMRI of the white matter in the brain, is to find the orientations distributions of the fibers. To investigate this task we consider the contribution to the *ADC* coming just from the intra-cellular compartment. For simplicity we also suppose the geometry to be compose by only 2D ellipses of the same shape but with different orientations and they represent our model of fibers. For simplicity we also assume the ellipses to be impermeable and we use PGSE sequence. With the model found in Chapter 4, the resulting diffusion tensor can be the written as

$$D^{\text{eff}}(\alpha,\delta,\Delta)=\sum_{\beta^i} n(\beta^i)D^{\text{eff}}_{\beta^i}(\alpha,\delta,\Delta)=\sum_{\beta^i} n(\beta^i)\mathbf{u_g}(\alpha)^T D^{\beta^i}(\delta,\Delta)\mathbf{u_g}(\alpha), \tag{7.32}$$

where α is the angle identified by the gradient direction $\mathbf{u_g}$ and the x-axis, β is the angle identified by the major axis of an ellipse and the x-axis (as illustrated in Figure 7.9) and $n(\beta^i)$ is the number of the ellipses orientated along the direction β^i.

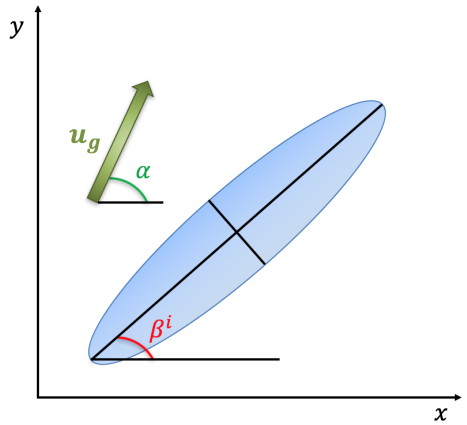

Figure 7.9 – Definition of the angles which determine the orientation of an ellipse and of the gradient direction.

From simple simulations, one can notice how, using the same values of Δ, δ and gradient direction $\mathbf{u_g}$, the values of *ADC* changes if we consider all the ellipses oriented in the same direction or many different directions. An example is shown in Figure 7.10a. To generate this data we considered 2D impermeable ellipses of semi-axes 5μm and 2μm with intrinsic diffusion

coefficient $\mathcal{D}_0 = 1e-3\text{mm}^2/\text{s}$ and we fixed $\delta = 0.5\text{ms}$ and fifteen values of Δ evenly distributed in the interval $[1, 25]\text{ms}$. In Figure 7.10a we report the results when all the 200 ellipses are orientated at $\beta = 100°$, in Figure 7.10b when 100 ellipses are orientated at $\beta = 80°$ and 100 at $\beta = 120°$, and in Figure 7.10c when 100 ellipses are orientated at $\beta = 70°$ and 100 at $\beta = 130°$. In all the cases, the "mean" direction is 100° but, as we can see, the values of D^{eff} are different. In particular, as the crossing angle between the ellipses becomes bigger, D^{eff} becomes smaller. Seeing this difference gives one hope that it may be possible to find the dominant orientation, detect if there is a crossing or not and if there is of how many degrees.

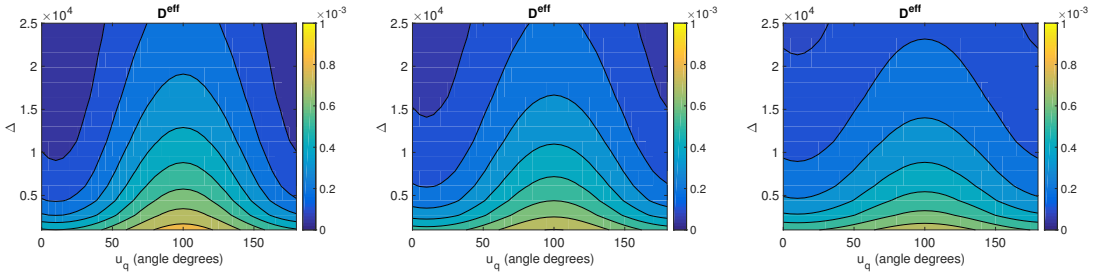

(a) 200 ellipses at $\beta = 100°$. **(b)** 100 ellipses at $\beta = 80°$ and 100 ellipses at $\beta = 120°$. **(c)** 100 ellipses at $\beta = 70°$ and 100 ellipses at $\beta = 130°$.

Figure 7.10 – D^{eff} of 200 ellipses of semi-axes 5μm and 2μm, intrinsic diffusion coefficient $\mathcal{D}_0 = 1e-3\text{mm}^2/\text{s}$, $\delta = 0.5\text{ms}$ and fifteen values of Δ evenly distributed in the interval $[1, 25]\text{ms}$.

For our preliminary analysis, we consider the formula (7.32) in 2D and we try to simplify it. We observe that, since $\mathbf{u_g}$ is the gradient direction vector and $\|\mathbf{u_g}\| = 1$, we can always write it as

$$\mathbf{u_g}(\alpha) = [\cos(\alpha), \sin(\alpha)]. \tag{7.33}$$

Moreover, for fixed δ and Δ, D^{β^i} is a squared matrix and, using the eigendecomposition, can be decomposed as

$$D^{\beta^i} = V_{\beta^i} \Lambda V_{\beta^i}^T \tag{7.34}$$

where V is a square matrix whose j-th column is the eigenvector $v_j^{\beta^i}$ of D^{β^i} and Λ is the diagonal matrix whose diagonal elements are the corresponding eigenvalues λ_1 and λ_2. We notice that the eigenvalues does not depends on the orientation β^i because the just depends on the shape of the considered ellipses (thus since we are considering copies of the same ellipse they assume only one value). Furthermore, since we supposed that D^{β^i} is the effective diffusion tensor of an ellipse orientated in direction β^i, and the vectors $[\cos(\beta), -\sin(\beta)]$ and $[\sin(\beta), \cos(\beta)]$ form a basis for this space, we have that

$$V_{\beta^i} = \begin{pmatrix} \cos(\beta^i) & \sin(\beta^i) \\ -\sin(\beta^i) & \cos(\beta^i) \end{pmatrix} \quad \text{and} \quad \Lambda = \begin{pmatrix} \lambda_1(\delta, \Delta) & 0 \\ 0 & \lambda_2(\delta, \Delta)) \end{pmatrix}. \tag{7.35}$$

Using this decomposition and making few computations, we can rewrite (7.32) as

$$D^{\text{eff}}(\alpha,\delta,\Delta) = \sum_{\beta^i} n(\beta^i)[\cos(\alpha),\sin(\alpha)]V_{\beta^i}\Lambda V_{\beta^i}^T[\cos(\alpha),\sin(\alpha)] \tag{7.36}$$

$$= \sum_{\beta^i} n(\beta^i)\left(\lambda_1(\delta,\Delta)\cos^2(\alpha-\beta^i) + \lambda_2(\delta,\Delta)\sin^2(\alpha-\beta^i)\right). \tag{7.37}$$

A natural way to find how many ellipses are orientated in a specific direction is to discretize the gradient direction α and collect the data for N different directions α_j. In this way we can rewrite the above equation as

$$D^{\text{eff}}(\alpha_j,\delta,\Delta) = \sum_{i=1}^{M} \mathcal{A}_{j,i} n(\beta_i), \tag{7.38}$$

where the entries of the matrix $\mathcal{A}$ are

$$\mathcal{A}_{j,i} = \lambda_1(\delta,\Delta)\cos^2(\alpha_j-\beta^i) + \lambda_2(\delta,\Delta)\sin^2(\alpha_j-\beta^i). \tag{7.39}$$

The matrix $\mathcal{A}_{j,i}$ is constructed with reference values of the D^{eff} obtained by measuring ADC for ellipses orientated along the direction β_i subjected to a gradient in the direction α_j. What is important is that $N \leqslant M$. Once the matrix $\mathcal{A}$ is constructed, one can proceed to recover the $n(\beta_i)$ by solving the linear system. Unfortunately the matrix $\mathcal{A}$ has just three non trivial singular eigenvalues, i.e. (neglecting the constants) it can be decomposed in a basis formed by the following vectors

$$\begin{aligned} v_1 &= \cos^2(\alpha_j), \quad v_2 = \cos(\alpha_j)\sin(\alpha_j), \quad v_3 = \sin^2(\alpha_j) \\ u_1 &= \cos^2(\beta_i), \quad u_2 = \cos(\beta_i)\sin(\beta_i), \quad u_3 = \sin^2(\beta_i) \end{aligned}$$

as

$$\mathcal{A}_{j,i} = a_1 u_1 v_1^T + a_2 u_2 v_2^T + a_3 u_3 v_3^T. \tag{7.40}$$

where a_i are constants. This proves that we cannot hope to recover $n(\beta_i)$ in this way. A natural idea would be then to consider not only the effective diffusion tensor but the whole dMRI signal varying also the values of g. Repeating the same argument as before, for a fixed direction of the gradient $\mathbf{u_g}$ we can write the signal as

$$S(\mathbf{g},\mathbf{u_g}) = \sum_{\beta^i} n(\beta_i) S(\mathbf{g},\mathbf{u_g},\beta^i) \tag{7.41}$$

where β^i are the direction along which the ellipses are oriented. However, for elongated shapes like the ellipses, one can easily see that

$$S(\mathbf{g},\mathbf{u_g},\beta^i) = S(\mathbf{g},\mathcal{R}\mathbf{u_g},\mathcal{R}\beta^i), \tag{7.42}$$

for every rotation matrix $\mathcal{R}$. This means that making the hypothesis that the signal is obtained as sum of different separated ellipses is not a good assumption to solve the problem of fibres orientation. It would be better to investigate the problem using a different approach and maybe try to retrieve just the mean direction and a measure of dispersion and not the exact number of ellipses pointing in each direction.

Conclusions and Perspectives

The problems studied in this thesis provide a rich spectrum of further research directions, which will be mentioned here after a brief recall of the mains results.

In Chapter 3 we analysed deeply two existing macroscopic models: the Finite Pulse Kärger (FPK) [42] and the Kärger model [94]. The principal difference between these two is that the FPK model was derived mathematically by applying homogenization techniques to the microscopic Bloch-Torrey equation, while the second was obtained heuristically by physicists. We rigorously proved that the Kärger model is a particular case of the FPK model when we assume narrow pulses. We show that if we use the PGSE sequence and we evaluate the Kärger model at $t = \Delta - \frac{\delta}{3}$, the order of convergence of the Kärger model to the FPK model is $O(\delta^6)$ (or $O(b^3)$), whereas for other choices of the evaluation time, $t = \Delta$ or $\Delta + \delta$, for example, the order of convergence is at most $O(\delta^3)$. All the proofs were done for the PGSE sequence, but we suggested a way to extend all the results to the trapezoidal PGSE sequence and supported our assertion with numerical examples. These results are particularly interesting for the investigation of certain porous media to which the Kärger model is applicable. One future direction on this topic would be deriving the best evaluation time for the Kärger model for other time-profiles.

In Chapter 4, we used homogenization techniques that were employed to derive the FPK model to derive a new model for the time-dependent ADC. First, we introduced a new set of scalings that, in contrast to the scaling used to derive the FPK model, coupled the time variable and the gradient intensity to the the space variable and the permeability through the non-dimensional homogenization parameter ε. We obtained thus a new family of models. To recover a model valid for the time-dependent ADC (i.e. $O(g^2)$ term), we determined that we must impose a scaling such that the b-value is sufficiently small. Using the following particular choice of the scaling that results in $b = O(\varepsilon^2)$,

$$L = O(\varepsilon),\ \kappa = O(\varepsilon),\ g = O(\varepsilon^{-2}),\ t = O(\varepsilon^2),$$

we obtained a new homogenized model for the time-dependent ADC that we called the H-ADC model. The H-ADC model relates the ADC to the value of the solution of a homogeneous diffusion equation on the set of interfaces within the volume. This diffusion equation is subject to zero initial condition and time-dependent Neumann interface conditions that are related to the time profile and direction of the diffusion gradient. We also furnish a result of convergence of $O(\varepsilon^3)$ in the signal for the H-ADC model, using the energy theorem. In Chapter 5 we analysed some other homogenized models obtained using other choices of scalings in time and gradient intensity, while respecting the constraint that b goes to zero as ε goes to zero. We found that if we set $t = O(1)$ or $t = O(\varepsilon^1)$, no matter which scaling we chose for g, we obtained a model whose ADC is time-independent and coincides with the one found with the FPK model. Similarly, if we set $t = O(\varepsilon^2)$, no matter which scaling we chose for g, we obtained a model whose ADC is time-dependent and coincides with the H-ADC model. On the topic of homogenized models, an interesting future direction would be to obtain asymptotic models in higher orders of ε. For example, models that contain the $O(\varepsilon^4)$ term may be used to produce a closed term expression for the Kurtosis of the signal.

In Chapter 6 we restricted ourselves to the case of closed geometries (which is relevant to diffusion inside biological cells) and the PGSE sequence. We analysed the H-ADC model obtained in Chapter 4 using different techniques according to the duration of the gradient pulses and the delay between them. In particular, we concentrated our attention on the solution of the homogeneous diffusion equation with time-dependent Neumann boundary condition and zero initial condition. If we consider short-time regime, we used potential theory and wrote the solution using a single layer potential. In this way, we found a new explicit formula for the ADC which generalises the well known Mitra's formula ([130]) for short-time by accounting for the duration of the pulses. We call it short pulse short-time (SPST) formula. If the duration of the pulses and the time delay between them are both long, we used the eigenfunction expansion to write the solution of the diffusion equation. We obtained an approximation of ADC which coincide with the one from the well known matrix formalism approach [63]. We call it finite pulse long-time (FPLT) formula. If the duration of the pulses is small while the time delay between them is long, we used the single layer potential during the pulses and the eigenfunction expansion between them. We call it short pulse long-time (SPLT) formula. An interesting future direction would be to use potential theory to analyse the short-time regime for the OGSE sequence and see if it gives a correction of existing formulas. A next step should be to analyse the H-ADC model in the extra-cellular compartment by considering the solution of the relevant diffusion equation in unbounded domains. It would be a challenge to extend our procedure to non-periodic domains.

In Chapter 7 we just made a preliminary study of the inverse problem of finding information about the microstructure starting from 1) the above obtained formulas of the ADC or 2) the dMRI signal at multiple values of g. This work is far from complete and opens many different future directions.

The most important result of this Chapter is the successful use of the SPST formula. We showed that with this new formula we can go beyond the narrow pulse assumption and find the surface to volume ratio for sufficiently big domains for which the short-time limit can be achieved at standard dMRI diffusion times. To be used in practice, a behaviour for the extracellular compartment should be added. On the contrary, fitting using the SPLT formula, we were not able to estimate well the surface to volume ratio but we were able to estimate well the dominant eigenvalues and the first moment of the related eigenfunctions. The dominant eigenvalues and first moment of eigenfunctions can give useful information about the geometry.

We also investigated the problem of finding the radii distribution of a geometry composed of 2D circles. Neglecting the signal contribution coming from the extracellular compartment, we solved the least squares problem by applying Tikhonov regularization [178] and the Uzawa algorithm [183] to find the radii distribution, with the data being the dMRI signal at multiple values of the diffusion gradient intensity g and multiple values of Δ, the delay between the pulses. We also showed the difficulties encountered using the same method with the data being the ADC at multiple values of Δ rather than the dMRI signal at multiple values of g and Δ. Further investigations still need to be conducted for this case. For example, a better stopping criteria should be considered and maybe an optimization of the parameters of the Uzawa algorithm should be done.

Finally, analysing the problem of finding the fiber orientations using both the ADC and the dMRI signal, we furnished a mathematical proof according which is not possible to recover an

arbitrary distribution of the fiber orientations.

In conclusion, with this thesis we first answered an often-asked question about how to choose the best evaluation time to be used for the Kärger model in the case of the non-narrow pulse PGSE sequence. Then we showed that homogenization techniques applied to the microscopic Bloch-Torrey equation resulted in a simplified model of the apparent diffusion coefficient from which the dependence on the geometry is more clear. Using classical mathematical analysis for the diffusion equation, we were able to find mathematical formulas for the ADC in long and short-time regimes in the case of finite domains. We deeply investigated the case of the PGSE sequence but repeating the derivations for other type of sequences would be really interesting and useful for the practical applications. Moreover, what is missing in this thesis is the validation of these results for more complex geometries and/or real experimental data. We note that all the numerical validations we made were on 2D geometries but the results we presented are expected to generalize to 3D.

Appendix A

Physical background

Contents

A.1 Spatial and Contrast resolution . . . 154
A.1.1 Nuclear Magnetic Resonance . . . 154
A.1.2 Spin angular momentum . . . 156
A.1.3 Energy Levels . . . 157
A.2 Generating the signal . . . 158
A.2.1 Resonance . . . 158
A.2.2 Relaxation . . . 158
A.2.3 Contrast . . . 160
A.3 Gradient magnetic field . . . 161
A.3.1 Slice selection . . . 162
A.3.2 Frequency and Phase encoding . . . 163
A.4 Diffusion MRI . . . 164

Diffusion magnetic resonance imaging (dMRI) or diffusion weighted imaging (DWI) is a non-invasive technique which is extensively applied in material science to investigate structural and transport properties of porous media (such as sedimentary rocks or concrete), as well as in medicine and neuroscience to study anatomical, physiological and functional properties gives uctuual of biological tissues and organs such as brain, skin, lungs, heart and bone [30, 63, 91, 108, 159, 182]. In biological tissues, the image contrast in water proton diffusion magnetic resonance imaging is given by the difference in the average water displacement due to the difference in diffusion between imaged tissues at different spatial positions [106]. A major clinical application of dMRI has been in detecting acute cerebral ischemia minutes after stroke [131, 187]. DMRI has been also used to detect and differentiate a wide range of physiological and pathological conditions in the brain, including tumors [125, 174, 181] and myelination abnormalities (for a review, see [108]). Recently, it also has been used to study brain connectivity (for a review, see [105]) and in functional imaging [111], as well as in cardiac applications [35, 36, 163].

DMRI is limited by the range of diffusion times that can be measured, due to biological and technical reasons. In the brain, diffusion times in the range of 1ms-100ms can be measured, associated to average diffusion distances of 2.5μm-25μm. This distance is averaged over all water molecules, and the actual diffusion distance varies depending on whether the water molecules started in the neuronal bodies, the neurites (dendrites and axons) or the extra-cellular space. The resolution of dMRI is of the order of 1mm^3 in the clinical scanner (about 200μm^3 in research scanner), meaning each pixel in the image displays the averaged diffusion characteristics of a tissue volume (voxel) of 1mm^3 (or 200μm^3). This is very large compared to cell features, which in the brain, vary from sub-micron (diameter of neurites) to tens of microns (neuronal bodies and

glial cells). To simulate the dMRI signal attenuation in a voxel Ω, one would have to simulate the magnetization inside Ω and compute its integral at a fixed time. At physically realistic dMRI diffusion times of tens of milliseconds, the average diffusion distance is no more than 25μm. It follows that the microscopic components of the tissues are not visible at the spatial resolution of dMRI, rather their geometric features are aggregated into the macroscopic signal coming from the voxels. Measuring the signal at different diffusion times and gradients, one aims to infer the morphological structure of a sample and to characterize the dynamics of the system. Despite of the numerous applications of dMRI for both clinical and research purposes, and more than sixty years of theoretical works, this inverse problem has not been fully solved yet.

This Appendix will deal with describing the basic physical phenomena behind the dMRI image. The aim is to give the reader a better understanding of the physical restrictions with which we have to deal, and clarify the physical meaning of all the quantities we shall introduce. Our exposition is indeed not exhaustive and, for more details about MRI and dMRI, we refer for example to the following books [28, 79, 90, 118] around which these sections are structured. I have also personally enjoyed the online course "Introducing MRI" of Dr. Michael Lipton provided by the Albert Einstein College of Medicine (https://www.youtube.com/playlist?list=PLPcImQzEnTpz-5TzxyyoYSbiAa9xdd89l). The course helps in understanding may aspects of MRI.

A.1 Spatial and Contrast resolution

The aim of MRI is to differentiate two adjacent tissues based on their different MR signals. To accomplish this the image must have sufficient resolution both spatially and in contrast.

The system must be physically capable to distinguish between two different types of tissues in the same region of interest assigning them different positions within the image; that is, the image must have sufficient spatial resolution. In particular, an MR image represents a slice of tissue with a defined thickness. This slice is then divided into a two-dimensional array that we call *voxels* (for "volume elements"). Each voxel is sampled as a single MRI signal that is an average of the signal arising from all of the tissue within the voxel.

The MRI acquisition must also bring out a different signal from each of the tissues we wish to separate. That is, the image must have sufficient contrast resolution. To maximize the difference in signal between tissues, one modulates the measured signal by adjusting the parameters of the MR acquisition.

A.1.1 Nuclear Magnetic Resonance

Nuclear Magnetic Resonance (NMR) is a physical phenomenon in which atomic nuclei in a magnetic field absorb and re-emit electromagnetic radiation. In particular, it results in a method to "label" or "encode" the Brownian trajectories of particles by using magnetic fields. NMR is then the process by which the signal detected in MRI is generated. With this technique we cannot image all the elements in nature, indeed an element shows NMR if it has non-zero spin, which is a quantum mechanics feature of the nucleus. Without entering into details, it is sufficient to know that this happens when the number of protons or neutrons in an atom is odd. Although many nuclei can undergo NMR (Hydrogen, Carbon, Sodium, Potassium, Calcium, etc.), we will confine our discussion to the hydrogen nucleus (^{1}H) for two reasons: in the human

tissue it is the most prevalent (because the tissues are mostly composed of water, H_2O); and the strength of NMR response of hydrogen isotope is much higher than that of any other elements [118].

If we look at the nucleus of hydrogen, it has a simple structure, indeed it is just a single positively charged particle (a proton). It turns out that the presence of charge in this nucleus leads to a phenomenon called nuclear magnetism (NM). NM tells us that this nucleus, with its charge, behaves as a small magnet which has magnetic field lines (see Figure A.1). Even though it is tempting to think of such nuclear magnetism in terms of classic electromagnetic phenomena, with spinning charges generating a magnetic field based on Faraday's law of induction, we cannot because nuclear magnetism is indeed a quantum mechanical phenomenon, and not an electromagnetic one, as such nuclear particles do not, as currently understood, actually spin in the physical sense [118]. Nevertheless, it turns out that we can describe its magnetic field as a vector, where the length is the magnitude of the magnetic field generated by the proton, and the orientation is the orientation of the magnetic field (see Figure A.1).

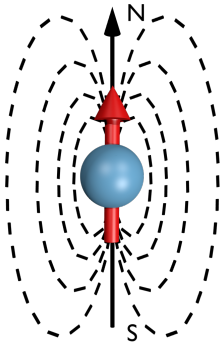

Figure A.1 – Proton with its magnetic field lines and the magnetic field represented by a vector.

In the absence of any magnetic field external to the nucleus, the orientation of the nuclear magnetic field is random. It is also important to observe that we cannot look at a single proton, but we will always look at a population of atoms, and thus we will always talk about the resultant vector sum $\mathbf{M}$. Since we have said that, in the absence of any magnetic field external to the nucleus, the orientation of each nucleus is random, the vector sum of a large sample will be always equal to zero. On the other hand, if we apply a strong enough magnetic field with a well defined orientation, we will generate a net magnetization with the same direction as the applied magnetic field, but opposite orientation. Nevertheless, the magnitude of the resulting magnetization vector $\mathbf{M}$ will not be equal to the sum of the magnitudes of all the spins. This is due to the fact that there are two possible orientations along which the spins can align themselves: parallel or anti-parallel to the applied field. This is in contrast with classical electromagnetism, and is a result of the quantistic nature of the spins, which we will briefly discuss later. Overall the distribution of the spins will be only slightly in favour of the anti-parallel orientation, resulting in a small net magnetization. At standard field strengths of 1.5 Tesla, only about 6 in every 10000 spins will align parallel to the external field. Such a small difference is not sufficient to be detectable, as it is covered by the strong field used to induce it. It is nonetheless this signal that we wish to measure.

A.1.2 Spin angular momentum

Nuclear magnetism is not the only property of the nucleus which is relevant to MRI experiments, the so called "spin angular momentum" also play a role. Spin angular momentum can be considered as analogous of angular momentum in standard physics. When an external magnetic field $\mathbf{B}_0$ is applied to a particle with spin angular momentum, the particle will tend to align with the field, but, because of its spin it will settle out of alignment with the external magnetic field. Its magnetic vector will then rotate in a cone shape trajectory around the axis identified by $\mathbf{B}_0$ (Figure A.2). This particular rotation movement is called "precession" (see [28, 79, 118] for more details). There exists a parameter that we call the *gyromagnetic ratio* (γ), which is unique for each element that can be studied by NMR (Hydrogen or Carbon or Nitrogen etc.), and that determines the frequency at which the proton precesses around the applied magnetic field. This parameter has units of frequency divided by the field strength (MHz/T). In particular, it depends on the applied magnetic field, and, more precisely, the frequency at which the spins precess is given by

$$w_0 = \gamma \mathbf{B}_0 \tag{A.1}$$

which is called Larmor equation. The frequency w_0 is thus known as "Larmor frequency". Equation (A.1) gives the key relation between frequency and applied magnetic field which allows us to create the images.

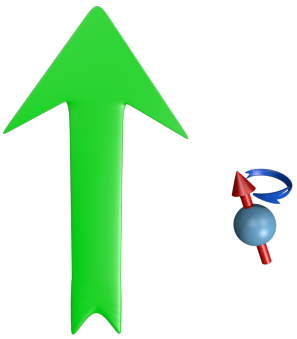

Figure A.2 – Proton subjected to a magnetic field starts to precess around it

As the particle precesses around the external applied magnetic filed, its magnetic vector can be decomposed in a longitudinal, M_l, and a transversal, M_t, component. When dealing with a population of identical particles, the characteristic frequency of precession around an applied $\mathbf{B}_0$ will be the same for all of them. However, they will not be all at the same point in their precession, i.e. they will all have a different phase. That is, the transverse components are not all pointing in the same direction at any point in time. Indeed, the arrangement of the spins along the path of precession is completely random. We call this "random phase". As a consequence, given a large sample of spins (remember that we are always dealing in average with several trillions of spins), we find that the transverse component of the vector sum is zero. Random phase thus means that all transverse components cancel each other.

The net magnetization can then be correctly represented as a static vector parallel to $\mathbf{B}_0$ with opposite direction and a magnitude equal to the sum of the longitudinal component vectors. As

we have already noted, though, the net magnetization of the sample is of the order of 6/10000 protons, much smaller than the external applied magnetic field, making it impossible to be measured. In order to find a solution to this problem we are then forced to introduce energy levels and a quantistic approach to the system.

A.1.3 Energy Levels

Until now we have used a classical approach to explain how the particles in our system react to an external magnetic field, and have somewhat ignored the quantistic aspects involved. Particles which obey quantum mechanics can only access a discrete number of states, their energy is thus quantized, hence the name quantum mechanics. The particles can, however, exist in a combination of two or more different states. Moreover the uncertainty principle states that it is impossible to determine the exact state of a single particle at an exact moment in time. As a result, measurements on a system provide the probability of finding particles in the available states [118]. So we will always talk about the state of the entire system and not of a single proton.

Quantum mechanics identifies a discrete number of states for a given nucleus. These states are known as energy levels, and the number of energy levels varies with the type of nucleus. In the case of ^{1}H, there are only two energy levels ($+\frac{1}{2}$ and $-\frac{1}{2}$), making it a relatively simple system to discuss. So it is possible for a hydrogen proton to exist in any linear combination of the two different energy states.

It turns out that the state of the system is not frozen, and protons can fluctuate between energy levels. This jump from one state to the other requires some energy ΔE to be provided to the particle (in order for the particle to move to a higher energy level), or to leave it (when a particle falls to a lower energy state).

If we are considering a random population of protons at the equilibrium there will be a relative greater occupancy of the lower energy state, but we observe that the upper level will never be completely empty, due to thermal energy always being present in the sample. If we take the sample and we place it into an external magnetic field, which acts as a source of energy for the system, we increase the relative occupancy of our spins in the higher energy state. This is equivalent to what we have described in the above sections, i.e. giving energy to the system we align the spins, forcing the protons in a higher energy state, and creating a net magnitude which has the same orientation as the magnetic field and opposite direction. The greater amount of the energy we give to the system, the greater the occupancy of the upper state will be and thus and the greater the net magnitude of the system will be. When we turn off the magnetic field the protons return to their initial states keeping their angular momentum and releasing energy.

Another reason for which it is convenient to talk about the total energy is that, if one puts enough of it into the system, the phase of the spins starts to become relatively coherent, i.e. not only the spins are precessing at the same frequency (given by the Larmor equation (A.1)), but they are also pointing in the same direction, and, as a consequence, the transverse component of the net magnetization will not be 0.

A.2 Generating the signal

As energy is provided to the system, and the phase of the spins aligns, M_t will progressively grow, at the expense of M_l. As a result, the magnetization vector $\mathbf{M}$ will form an angle with $\mathbf{B}_0$, as it rotates towards its transverse plane. This operation is called “flipping" the nuclear magnetic vector, and, as we will see, is the solution to the problem of measuring the signal.

Once we have flipped the nuclear magnetic vector into the plane transverse to $\mathbf{B}_0$ we are actually able to measure the transverse magnetization. This is because it is not static, as the spins are continuously precessing around the $\mathbf{B_0}$ direction. Indeed, if the magnetization were static we would not be able to measure its contribution because it would still be much too small compared to the magnitude of $\mathbf{B}_0$. However, since it is not static we can use the Faraday law of induction and, simply adding a voltmeter, we are able to measure the amplitude of the difference in voltage which is proportional to the magnitude of the transverse magnetization. The intensity measured by the voltmeter will be our signal.

A.2.1 Resonance

To efficiently transfer energy onto the spins in the sample, we discuss the concept of resonance. For our purpose resonance can be simplified as a process by which energy is transferred from one system to another. The basis of resonance is that everything has a unique “natural frequency" at which it will oscillate under a given set of ambient conditions. In the case of the precessing protons, the resonating frequency is in fact the Larmor frequency ω_0 in (A.1).

To give energy to the system (in order to flip the nuclear magnetic vector), the idea is to turn on another magnetic field $\mathbf{B}_1$ in the direction perpendicular to $\mathbf{B}_0$. We can then apply an oscillating magnetic field, in the plane perpendicular to $\mathbf{B}_0$ with frequency ω_0 to give energy to the system, and to flip the nuclear magnetic vector. Because the resonating frequency is in the same frequency range as those used in FM radio, it is also referred to as radiofrequency (RF). If we were, on the other hand, to use a static field, without making use of resonance, we would only obtain a slight change in the orientation of the sum vector, but would not cause any phase coherence in the nuclear magnetic vectors associated with the spin. In contrast, by applying an oscillating field we managed to have a large amount of energy very efficiently transferred into the system of spins which drives it towards a higher energy configuration. In addition we introduced coherence of the transversal components of almost all spins. As $\mathbf{B}_1$ is applied the system will progressivelly align perpendicular to $\mathbf{B}_0$, becoming detectable by the antenna. The angle of rotation is called “flip angle” and depends on how long $\mathbf{B}_1$ is kept turned on and on the magnitude of $\mathbf{B}_1$. Indeed, taking a greater $\mathbf{B}_1$ will imply that we need to wait less time to achieve the same flip angle for the same system. Usually one takes a flip angle of 90° (indicated by RF 90°) because in this direction the longitudinal magnetization is 0 and the detectable magnetization is maximized.

A.2.2 Relaxation

When $\mathbf{B_1}$ is turner off, the spins, now in a high energy state, will tend to return to their initial lower energy state. As we have mentioned before this will necessarily result in some energy being transferred outside of the system. Since the energy of a system must always be

conserved, we need to understand where this energy is transferred to. Moreover, the spins do not go back to their initial position in the same way as they where flipped, because the change in the longitudinal NMR has a different rate with respect to the change in the transversal NMR. This phenomena is called "relaxation" and is the origin of the contrast in MRI.

The relaxation of the transversal component M_t is described by a time constant called T_2. This constant represents the amount of time it takes for the system to lose 37% of the starting signal. During this relaxation the energy is transferred from the spins in the higher energy states to the other spins and thus it happens through interaction between spins. For this reason it is also called "spin-spin" relaxation. A small T_2 means that the interactions of the spins occur with an high probability.

The relaxation of the longitudinal component M_l is governed by a time constant called T_1. This constant represents the amount of time it takes for the system to lose 63% of the starting signal. This process represents the loss of energy of the spins in favour of the lattice, i.e. all the other component into the system other than the spins. In contrast to the spin-spin relaxation, it is called "spin-lattice" relaxation. In particular, this is a much slower process than the one determined by T_2.

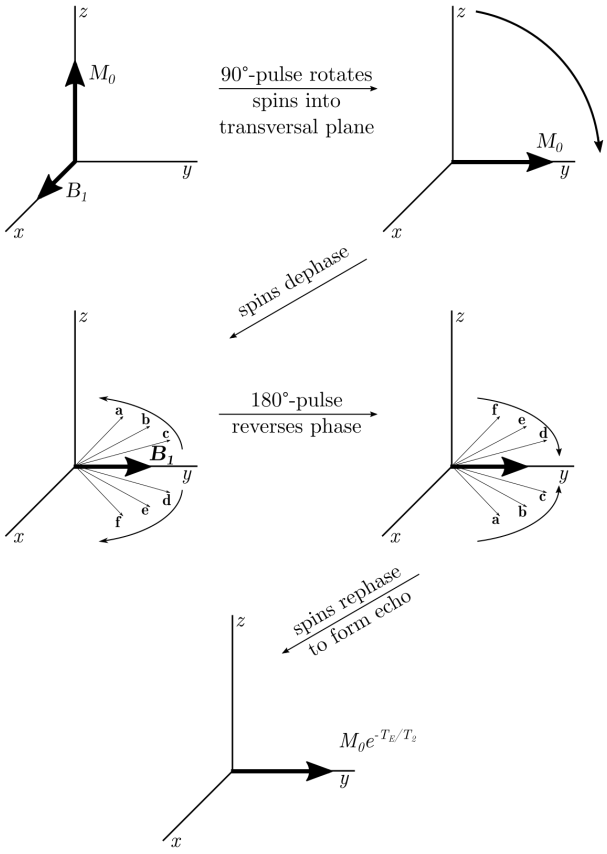

Figure A.3 – A simulation of an ensemble of spins in the rotating reference frame during a spin echo experiment. A 90°-pulse rotates the spins, around the x-axis, into the transverse plane where they begin to precess. The spins accumulate extra phase, until this accumulation is inverted by the 180°-pulse. The spins continue to collect extra phase at the same rate and, at a later time, all spins return to the positive y-axis together, forming an echo. The echo amplitude is still reduced, however, by the intrinsic T_2 decay (This figure was inspired by [28]).

In general, signals would suffer additional suppression due to dephasing from external field inhomogeneities (T_2 would be replaced by a smaller relaxation time $T_2^* < T_2$). But a rephasing or echoing of this source of dispersion can be achieved by an additional RF pulse application, where the basic idea is to flip all the spins 180° in the transverse plane (Figure A.3). Following the 180° flip the dephasing is reversed, and the phases refocus at what is called echo time T_E. The value of T_E can be set by varying the time interval between the initial 90° pulse and the 180° pluse. A longer wait time will result in a larger T_E, while a short interval between the two pulses will give a small T_E.

Different tissues will have different values of T_1 and T_2 and what we actually measure during MRI is the decrease in the signal amplitude, called the free induction decay (FID), of the signal at the echo time T_E. In particular we find that the FID is governed by T_2.

A.2.3 Contrast

MRI's ability to differentiate between material is given, among other things, by its sensitivity to proton densities, relaxation times, temperature, proton motion, the chemical shift in the Larmor frequencies, and tissue heterogeneity. This large set of variables allows images to be generated with different levels of contrast based upon the desired usage. Here we briefly mention what $T2$ contrast means as it is the one used to obtain the reference signal for dMRI, for the other cases we refer to [28, 79, 118].

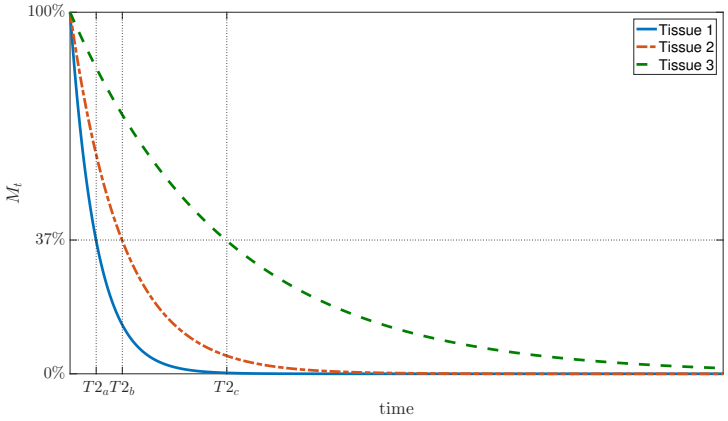

Figure A.4 – T_2 decay for different tissues

Looking at Figure A.4, we see that the three tissues whose transverse relaxation curves are shown lose net M_t, at different rates. The tissue with the shorter T_2 will lose M_t, faster. If we set T_E to occur immediately after the RF is turned off (making T_E as close to 0 as possible), we will detect very little difference in the M_t, (read signal intensity) from the two tissues. As a result, we will be unable to distinguish the tissue in our image. A longer T_E, however, will reveal a large difference in signal from these tissues. That signal difference (read image contrast) is entirely dependent on differences in T_2. Thus, $T2$ contrast is modulated by T_E and one has maximal $T2$ contrast for long T_E and minimal for short.

A.3 Gradient magnetic field

It is not sufficient to apply the two magnetic vectors $\mathbf{B}_0$ and $\mathbf{B}_1$, and correctly chose the contrast of the image to obtain an MRI. It is also necessary to be able to image selective regions within the sample. This can be done by introducing gradient magnetic field. It is the magnetic gradient which allows us to obtain slices of the system we wish to analyse.

The "gradient" is a linear change in magnetic field strength along one linear direction within the scanner. Gradient magnetic fields are generated using resistive electromagnets that are turned on and off rapidly during MRI. A powerful property of MRI is that by carefully varying the configuration of the gradient coils it is possible to adjust the direction of the gradient at will. This removes the necessity of physically rotating the subject in order to acquire images in different directions, as a simple change in the gradient direction results in the desired effect.

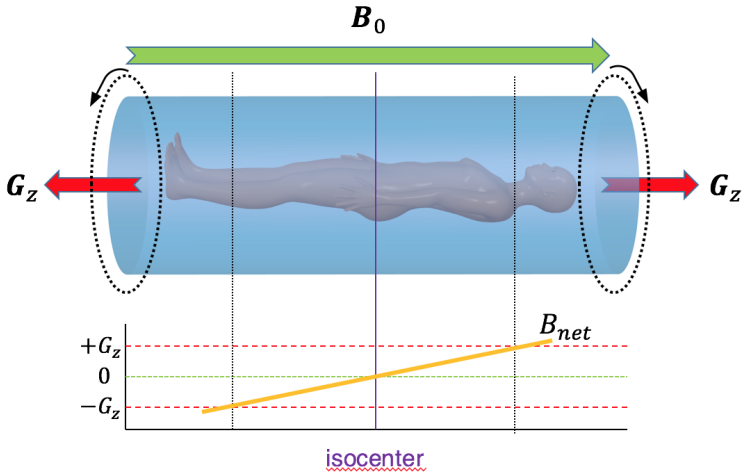

Figure A.5 – Application of a gradient $\mathbf{G}_z$ along the z-direction and resulting magnetic field $\mathbf{B}_{net}$

Spatial localization of the MR signal requires gradient magnetic fields in three orthogonal directions. Let's consider for example the standard x,y and z directions where $\mathbf{B}_0$ is applied along the z direction. We start applying a gradient in the z direction (parallel to $\mathbf{B}_0$). As shown in Figure A.5, two circular coils are used to do that, one at each end of the scanner, equidistant from a point called "isocenter". Without going into the details of how the coils work, let just simply say that when current is run through both coils simultaneously, but in opposite directions, two magnetic fields are generated of equal magnitude, but of opposite direction [118]. Because magnetic field strength declines with distance from the source of the magnetic field, the field strength is higher near the coils and lower near isocenter. At the isocenter, the vectors describing the field generated by the two coils are equal in magnitude but point in opposite directions. Thus, the vector sum $\mathbf{G}_z$ of the gradient magnetic fields is 0 at isocenter. As we move from isocenter along the same direction as $\mathbf{B}_0$ (to the right in Fig. A.5), $\mathbf{G}_z$ increases in magnitude with the same direction as $\mathbf{B}_0$. We have two magnetic fields, $\mathbf{G}_z$ and $\mathbf{B}_0$, with identical direction. Their vector sum $\mathbf{B}_{net}$ is $\mathbf{B}_0 + \mathbf{G}_z$ which is greater than $\mathbf{B}_0$. If we now measure the field strength an equal distance from isocenter, but in the opposite direction along $\mathbf{B}_0$ (to the left in Fig. A.5), $\mathbf{G}_z$ has now the same magnitude but opposite direction. Thus,

$\mathbf{B}_{net}$ is less than $\mathbf{B}_0$. The graph in Figure A.5 shows that when we measure $\mathbf{B}_{net}$ at any location along the z dimension, we find a linear change in $\mathbf{B}_{net}$ due to a linear change in $\mathbf{G}_z$, such that $\mathbf{B}_{net}$ is equal to $\mathbf{B}_0$, at isocenter.

In a similar fashion it is possible to create magnetic fields which induce a gradient along the other two directions, $\mathbf{G_x}$ and $\mathbf{G_y}$ in order to obtain three independent magnetic field gradients in the three orthogonal directions. While the basic principle is the same, a few more physical principles of magnetic fields are need in order to do so without varying the direction of $\mathbf{B}_{net}$. As this goes beyond the scope of the manuscript we encourage you to look at [28, 79, 118] for a more in depth explanation.

A.3.1 Slice selection

We have shown how resistive magnets can be used to create a gradient in any direction inside the MRI machine, we will now explain how this enables us to image a single slice along the sample. With the gradient magnetic field $\mathbf{G}_z$ on, protons will experience a different $\mathbf{B}_{net}$ and therefore, a different frequency w depending on their location along $\mathbf{G}_z$. If $\mathbf{B}_1$ is transmitted with a frequency of w_0 while $\mathbf{G}_z$ is on, only protons with $w = w_0$ (i.e. those located at isocenter and experiencing only $\mathbf{B}_0$) will have resonance with $\mathbf{B}_1$. Because $\mathbf{G}_z$ varies along the z dimension, but not along the x or y dimensions, all spins on the plane of the isocenter of $\mathbf{G}_z$ achieve resonance with the applied $\mathbf{B}_1$.

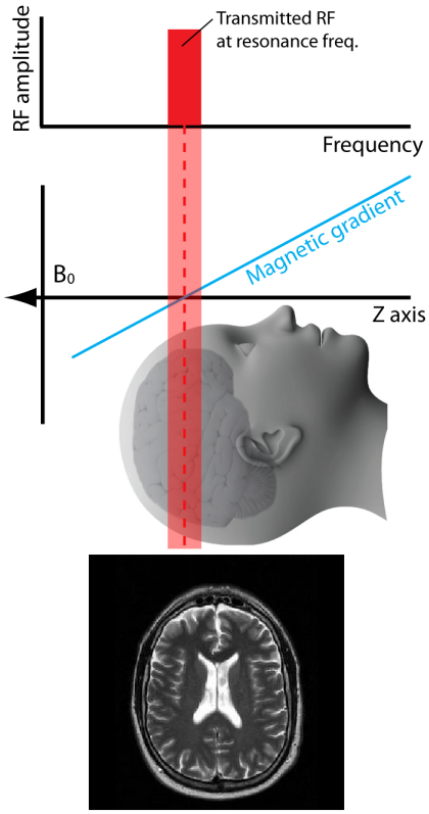

Figure A.6 – Slice selection using a magnetic field gradient and the 2D resultant image after the entire acquisition with $T2$-contrast. This image was inspired by the one present at *http://neurosurgerysurvivalguide.com/roundy/*

We observe that a slice has real thickness. Measurement of signal only arising from spins lying on a plane (i.e., infinitely thin) is an impossibility. Similarly, it is physically impossible to transmit $\mathbf{B}_1$ at a single frequency. The RF transmitter hardware is not that precise. $\mathbf{B}_1$ is always transmitted as a limited range of frequencies or RF bandwidth. When a range of frequencies centred on w_0 is transmitted as the RF pulse, all spins resonant with any of those frequencies will become excited. This group of excited spins represents a range of frequencies residing on either side of isocenter. Each image contains then the resultant magnetization of a slice of sample which has a certain thickness (see Figure A.6).

A.3.2 Frequency and Phase encoding

What we have described up to now allows us to obtain a single value of intensity from a slice of the sample, but we have no way to localise information within this slice. What we need is a way to differentiate the signal coming from within the slice, and correctly place it within a 2D image. This is where frequency and phase encoding come into play.

Once the spins within the slice have been excited, the slice select gradient is turned off. The spins are now precessing, at least in part, in the transverse plane with a precessional frequency of w_0. Their precessional frequency is w_0 because, with no gradient magnetic field on, the only magnetic field they experience at this time is $\mathbf{B}_0$. While the spins in the slice still have net transverse magnetization (and before we record any signal), a magnetic gradient is create along a direction perpendicular to the original one, either x or y. Suppose the gradient is applied along the x direction. At this point the difference in magnitude of $\mathbf{B}_{net}$ will cause a variation in the precession speed of the particles based on their position along the x axis. The resulting signal can than be decomposed through Fourier analysis, and amplitudes can be assigned to positions in the x direction based on the resonant frequency. We are now left with a 1D image, and we say that the signal is now “frequency encoded".

A process called “phase encoding” is used to expand the frequency encoded signal, and obtain a 2D image of the slice we are analysing. A gradient along the y axis is used to impart a specific phase angle to a transverse magnetization vector. While the phase encoding gradient is on the spins at different locations along the y axis begin to precess at different Larmor frequencies. When the phase encoding gradient is turned off the net magnetization vectors return to precess at the same rate, but possess different phases. The phase being determined by the duration and magnitude of the phase encoding gradient pulse. Once the phase encoding gradient pulse is turned off a frequency encoding gradient pulse is turned on. In this example the frequency encoding gradient is in the x direction. The frequency encoding gradient causes spin packets to precess at rates dependent on their x location. At this point one simply apply the Fourier transformation to correctly localize in space. We observe that there needs to be one phase encoding gradient step for each location in the phase encoding gradient direction. So to create the final image these steps must be repeated several times where every time one changes the magnitude of the applied phase encoding gradient. These processes are usually sketched in a diagram called “pulse sequence” diagram which describes the timeline of what we do in order to generate the measurable MR signal (see Figure A.7a).

A.4 Diffusion MRI

Now that we have introduced how the MRI works we see what it means to make the experiment sensitive to diffusion. The goal of diffusion MRI is to detect how rapidly the molecules can move, i.e. measure the diffusion tensor described before.

We have seen that any time we apply a gradient magnetic field, after having flipped our spins in the transverse plane, they will experience different strengths of $\mathbf{B}_{net}$ based on their position along the gradient, and therefore they will precess at different frequencies. During the time this gradient is on there is some amount of phase change which leads to less net transverse magnetization. This is true for stationary spins, but even more so for spins moving along the gradient, leading to a greater loss of signal for those particles which are moving compared to those which are stationary. This is the exact principle on which dMRI is based on. We turn on gradient magnetic fields and look at the amount of signal loss that occurs while those gradient magnetic fields are on. That amount of signal is going to be proportional to the rate of diffusion (diffusion tensor).

If we look at any MR pulse sequence (Figure A.7a), we start with the 90° RF pulse and the application of the slice selective gradient G_{sl}, then we have phase encode gradient G_y, then frequency encode G_x and in the middle of the frequency encode period we have T_E (the echo time at which the phases of the spins refocus). When G_{sl} or G_y or G_x are on, we know that some spins are stationary and other are moving through the tissue in all different directions (diffusion is a random process); but, whenever there is a movement along a gradient magnetic field, there is going to be an accumulation of phase proportional to the amount of the movement along that direction and it will result in a loss of signal. The signal in the MRI is thus influenced by diffusion. With dMRI (or DWI diffusion weighted imaging) we are interested in detecting that diffusion specifically. It is important to remark that the reference image for diffusion MRI (those without the addition of diffusion sensibility) are acquired using $T2$ contrast.

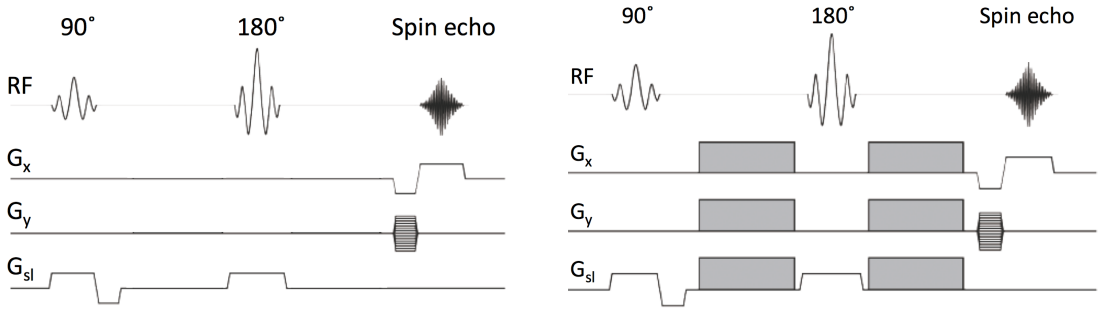

(a) MRI **(b)** Diffusion MRI

Figure A.7 – Schema of the sequence applied in MRI and dMRI.

The change of signal intensity that occurs as a result of diffusion is dependent on the rate of diffusion (diffusion tensor), the time observation (how long we let this occurs) and on the strength of the applied gradient magnetic field. If the magnetic gradient is stronger, then, over the same period of time, particles with the same speed will experience a greater change in phase In our experiment we want to determine the diffusion tensor by adjusting the duration and

the strength of the magnetic gradient. If we want to make the pulse sequence (Figure A.7a) sensitive to diffusion what we do is turn on a strong bipolar magnetic gradient (the direction of the gradient is inverted after the 180° RF pulse). In such a way all stationary particle will not feel the effect of the gradient, and the signal becomes sensitive to movement in the direction of the magnetic gradient (in Figure A.7b the bipolar magnetic gradient is applied to all three directions, making the signal sensitive to diffusion along any axis). We thus obtain that the signal from moving particles will be attenuated based on their diffusion speed: a faster moving particle will have a more attenuated signal compared to a slower moving one (See Figure A.8).

With this section we wanted to introduce how we realize the dMRI experiment and specifically we wanted to distinguish between the imaging gradients (G_{sl}, G_y and G_x) and the diffusion gradient that we add to make the image sensitive to diffusion. In the rest of the thesis, the imaging gradients are ignored since, for the mathematical modelling of dMRI signal, one considers just the contribution of the diffusion gradient.

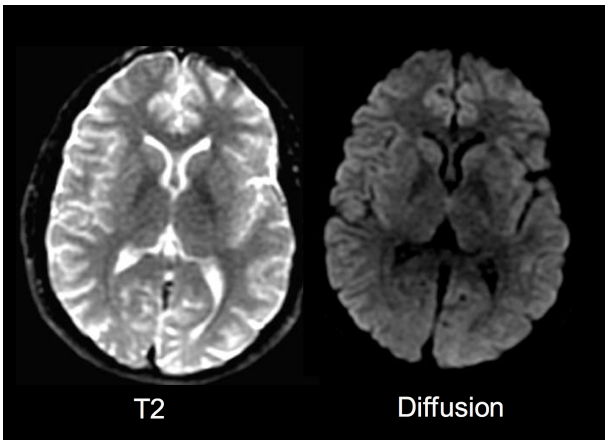

Figure A.8 – Example of MRI obtained with $T2$-contrast and Diffusion weighted MRI image. We can see the loss of signal in dMRI. Image taken from a 2014 CENIR's course *Diffusion: Applications au cerveau*.

Acknowledgements / Remerciements / Ringraziamenti

I would like to start by thanking my two advisors Houssem and Jing. Houssem, cela a été un très grand plaisir de travailler avec vous. Je vous remercie beaucoup pour toutes les choses que vous m'avez apprises, de m'avoir toujours guidée et de m'avoir donné confiance pendant tout mon parcours. Jing I have really enjoyed working with you and especially our great discussions. I especially thank you for having pushed me in every occasion and the many opportunities you gave me to learn new things and present our work.

I would like to thank the two reviewers Prof. Gary Hui Zhang and Prof. Evren Özarslan for having accepted to review my thesis. It is an honor for me having you as reviewers. In particular, I would like to thank Prof. Gary Hui Zhang for the interest he showed for our work, his attention on the details and for the great time we spent in Lisbon. I would also like to thank Prof. Evren Özarslan for the interesting discussions we had in Lisbon about the physics behind the dMRI signal, which helped me get a better understanding of the phenomena.

Je tiens à remercier chaleureusement les trois membres du jury Prof. Rachid Deriche, Prof. Maher Moakher et Prof. Bertrand Thirion d'avoir accepté d'être présents en ce jour très important pour moi. En particulier, je voudrais remercier Prof. Rachid Deriche pour le grand intérêt montré pour notre travail et pour m'avoir présentée à son groupe de recherche avec qui j'ai pu discuter en plusieurs occasions. Je remercie Prof. Maher Moakher d'avoir fait un long voyage afin d'être présent et de m'avoir donné l'opportunité de travailler avec son étudiante Marwa. Enfin je remercie Prof. Bertrand Thirion pour sa disponibilité et son aide pour trouver une bonne date pour la soutenance.

These three years of thesis where also a good opportunity for me to know great people from or related to my field. In particular, I would like to greatly thank Prof. Denis Grebenkov for his availability and our really interesting and useful discussions. I would also like to thank Luisa for giving me the opportunity to assist her in a small project at NeuroSpin. I have really learned a lot from this experience. Infine ci tengo a ringraziare il Prof. Michele Piana con cui tutto è iniziato. Senza di lui probabilmente non avrei raggiunto tutti questi successi. In particolare lo ringrazio ancora per tutte le opportunità che continua a offrirmi.

Pendant ma thèse, j'ai aussi fait partie d'une équipe magnifique : DeFi ! Je tiens à remercier, à nouveau, notre directeur d'équipe Houssem parce qu'il a su créer un groupe très uni. Sur ce point j'aimerais adresser des remerciements tout particuliers à notre magnifique gestionnaire Jessica ! Je ne sais pas comment j'aurai pu faire sans toi durant ces trois ans ! Tu as toujours eu les bonnes réponses à toutes mes questions administratives et tu as été une fabuleuse organisatrice de pique-niques et de goûters ! Je remercie tous les membres du groupe : Prof. Grégoire Allaire pour nos intéressantes discussions sur l'homogénéisation ; Lucas pour n'avoir pas raté une occasion de se moquer de moi (tu ne trouveras pas d'erreurs de français dans ce texte parce que je l'ai fait corriger !) ; Lorenzo pour avoir été un très bon ami depuis le début ; Zixian pour m'avoir aidé à comprendre l'algorithme EM et pour ses incroyables gâteaux ; Camille pour sa sympathie durant les mois où elle est restée avec nous ; Thi Phong et Mohammed pour avoir partagé avec

moi toutes les joies et les douleurs de ce parcours (votre soutenance va arriver bientôt, courage !) ; Kevish, même si tu viens d'arriver, tu t'es déjà fait une belle place dans la meilleure équipe de foot (allez l'A.S. Saint Hessienne) ; Hang Tuan et Van Dang pour m'avoir introduit l'IRMD et le modèle FPK ; Tobias pour ses photos de l'équipe de foot ; Federico perché non so come avrei fatto i primi mesi senza il tuo supporto; Irene for showing me that you have always a reason to be in a good mood; Shixu for showing me that there exist people who have never seen a musical; and finally Jake who is a very good friend (I am sorry I have no better words to describe you but I have really enjoyed the time we spent together and I am really glad that I had the opportunity to meet you!). Even if she is not really a member of DeFI group, I would like to thank Prof. Fioralba Cakoni for bringing always a good spirit when she is around. Au sein de l'INRIA je tiens aussi à remercier vivement Valérie Berthou pour toute l'aide qu'elle m'a apportée avant mon arrivée en France puis pendant mes trois ans ici !

Pendant ces trois ans au CMAP l'ambiance a été magnifique ! Je tiens à remercier tout le monde parce que le CMAP est une très grande famille dont tous les membres (permanents, équipe administrative, post-docs et thésards) sont très gentils et disponibles. Je tiens à remercier, en particulier, toute l'équipe administrative : Nasséra parce que personne ne pourra jamais être comme elle ; Alexandra pour son amitié et les cafés à 8 heures ; Manoëlla, Vincent et Wilfried pour avoir complété au mieux cette équipe !

Je tiens à remercier tous les doctorants, les post-docs et les permanents qui ont partagé avec moi ces trois ans ou une partie de cette période. Tout d'abord mes irremplaçables collègues de bureau, le bureau des pauses, des moments "maths questions" et de la bonne humeur : Gwenael pour tous les beaux moments passés ensemble et pour être même venu aujourd'hui (merci à Tatiana aussi pour son amitié) ; Matteo perché in questi tre anni abbiamo condiviso davvero tutto insieme e spero che la nostra amicizia continui a lungo ; Luca per aver portato tanta allegria e freschezza nell'ufficio ; Geneviève, enfin une autre fille présente tous les jours dans le bureau ; Esther, Rémi et Belhal qui viennent de s'installer mais qui font déjà partie du meilleur bureau du premier étage ! Je voudrais remercier aussi les deux stagiaires que je n'oublierai jamais Marco et Carole avec qui j'ai passé de très bons moments ! Enfin, même s'il ne faisait officiellement pas partie de mon bureau, je tiens à remercier Etienne pour nos magnifiques pauses de 8 heures et pour m'avoir fait goûter la véritable tartiflette, même s'il ne connaissait pas le bon fromage pour la préparer !

Je tiens à remercier les membres des deux équipes magiques de foot du CMAP, le Real Matrice et l'A.S. Sainte Hessienne (plus connues sous les noms d'équipe A et B) et mes partenaires d'entrainement de foot : la capitaine Hélène pour avoir partagé avec moi les très dures séances du dimanche matin (et pour être une grande amie que j'espère ne jamais perdre malgré la distance) ; l'entraineur Aymeric pour avoir su être gentil mais aussi intransigeant quand il faut (et pour m'avoir tolérée et surtout soutenue pendant ces trois ans, j'espère vraiment que notre amitié durera très longtemps) ; Lucas parce que personne n'est comme toi sur le terrain et lors des pauses dans la salle café (je n'oublierai jamais le "finger football" et j'espère revenir pour ton HDR) ; Benji pour les magnifiques places du quart de final de l'Euro 2016 et pour m'avoir ramené après chaque entrainement (même si tu n'as pas supporté l'Italie à la fan zone, tu restes un bon ami) ; Cormac pour avoir toujours été le plus motivé sur le terrain ; Alain et Claire pour avoir partagé les séances du dimanche ; Gaoyue pour ton dessin magnifique ; Charline pour ta sympathie ; Alexey pour avoir été un bon ami sur le terrain et à l'extérieur ; Etienne pour être le

Prof. le plus aimé du labo ; Gustaw et Jean-Bernard pour nos discussions sur le sport ; Gaëtan pour avoir toujours été le plus gentil ; et tous les autres Alex, Cédric, Jérémy, Martin, Massil, Mathieu, Raphaël, Thomas, Shahrzad, Tony, Daniel, Yoann, Yuan, Giulio et Mauro (sempre forza Roma per voi due).

Je tiens à remercier aussi les autres doctorants avec qui j'ai passé de très bons moments : Aline qui m'a sauvée en se chargant du café ; Ludovic même si on n'a pas réussi à trouver le nom des insectes de ma cuisine ; Raphaël pour ses gâteaux du séminaire des doctorants ; Antoine, Hadrien, Perle et Tristan pour les blagues dans la salle café ; Pedro il mio migliore amico cileno-italiano; Alessandro il miglior nerd e patito di Heroes III che potessi mai incontrare (non potrò mai ringraziarti abbastanza per le mille risate dei miei primi mesi a Polytechnique e per aver detto che le nostre lasagne erano buone)!

A very special thanks goes to the lab's English speaker group! Many people have become members of it during these three years but among them I would like to thank Helle and Atte for always being ready to organize amazing evenings or days together and Adi because you really became as a sister to me and I will never forget you and your shatshuka!

Ed ora... dopo tre lunghi anni... il momento di scrivere di nuovo in italiano! Vorrei ringraziare la mia migliore amica Rosy per essermi sempre stata accanto in questi anni, perché nonostante la lontananza noi un modo per essere vicine lo troviamo sempre! Vorrei ringraziare Francesca perché il nostro periodo di convivenza è stato davvero fantastico e ho riscoperto una persona speciale su cui si può sempre contare. Un grazie speciale va anche a Giamma per avermela portata in Francia (prima o poi ti ripagherò di questo fantastico regalo). Un grazie anche alle mie due amiche Ali e Marti, perché, anche se per un motivo o per l'altro non siamo mai riuscite a sentirci spesso, abbiamo sempre recuperato alla grande a ogni mia visita in Liguria. Un grazie speciale anche a Iulia e Torio per aver finalmente coronato il sogno di tutti e perché, nonostante la lontananza, non abbiamo perso il vizio di scherzare insieme. Grazie a Simon, anche se sto ancora aspettando il nostro aperitivo sulla Tour Eiffel. Un enorme grazie a Michi che da buon fratellino acquisito è pure venuto a trovarmi nell'impervia capitale Gallica! Una piazza d'onore se la merita Nick che, anche se probabilmente una cosa non me la regalerà mai, non smette mai di stupirmi e regalarmi momenti di complicità unici a casa (speriamo di averne un'altra insieme prima o poi!). Credo di poter dire che un legame così è qualcosa che non si vede tutti i giorni e sono davvero fortunata, perciò grazie di tutto (soprattutto del super viaggio che stiamo per fare)! E grazie anche ai suoi genitori Luisa e Antonio per non farci mai mancare il loro supporto nelle varie scelte e per la bellissima vacanza in Bretagna.

Vorrei ringraziare la mia famiglia e, in particolare, i miei genitori per avermi sempre sostenuta anche in scelte che so che non hanno condiviso, ma non mi hanno mai fatto mancare il loro affetto! Vorrei ringraziare Sonia e Elven per avermi donato la prima nipotina e essersi pure fatti 1000km perché io potessi stare qualche giorno con lei. Se la prima nipotina che avete fatto è stata un piccolo capolavoro, non oso immaginare il secondo che, per esperienza, si sa che riesce sempre meglio! Vorrei ringraziare zii e cugini perché nonostante tutte le difficoltà che la vita ci mette di fronte la nostra famiglia resterà sempre unita e alla mal parata il nostro 26 dicembre non ce lo toglierà mai nessuno! Infine vorrei ringraziare i miei tre mitici nonni coi quali sono cresciuta. Purtroppo una delle nonne non ha neanche potuto vedermi partire per questa esperienza ma so che sarebbe stata fiera di me e di questo successo, l'altra nonna invece non ha mai smesso di dirmi quanto mi stima e mi vuole bene e questo non può che rendermi orgogliosa. Le mie ultime

parole di ringraziamento vanno a colui che per me è sempre stata una persona di riferimento e che sarà sempre nel mio cuore. Grazie di cuore per tutti i tuoi insegnamenti, per avermi sempre supportato in questi anni francesi con le nostre chiacchierate serali e scusami per non esserti potuta stare accanto come avrei voluto alla fine.

J'espère n'avoir oublié personne, mais si tu es en train de lire ces pages et que tu n'as pas trouvé ton nom, s'il te plait, pardonne-moi, parce que si tu es là aujourd'hui, c'est sûr que tu as eu un rôle important pendant ces trois ans et je t'en remercie beaucoup !

I hope I haven't forgotten anybody, but if you are reading these pages and you have not found your name, please forgive me, because if you are here today, it means that you had an important role in these three years and so I thank you a lot!

Spero di non aver dimenticato nessuno, ma se stai leggendo queste pagine e non hai trovato il tuo nome, ti prego perdonami, perché se sei qui oggi, vuol dire che hai avuto un ruolo importante in questi tre anni e perciò ti ringrazio tanto!

Bibliography

[1] Daniel C. Alexander. An Introduction to Computational Diffusion MRI: the Diffusion Tensor and Beyond, pages 83–106. Springer Berlin Heidelberg, Berlin, Heidelberg, 2006. (Cited on page 35.)

[2] Daniel C Alexander. A general framework for experiment design in diffusion MRI and its application in measuring direct tissue-microstructure features. Magnetic Resonance in Medicine, 60(2):439–448, 2008. (Cited on pages 49 and 50.)

[3] Daniel C Alexander, Penny L Hubbard, Matt G Hall, Elizabeth A Moore, Maurice Ptito, Geoff J M Parker, and Tim B Dyrby. Orientationally invariant indices of axon diameter and density from diffusion MRI. NeuroImage, 52(4):1374–1389, 2010. (Cited on page 50.)

[4] Todd Arbogast. Gravitational forces in dual-porosity systems: I. Model derivation by homogenization. Transport in Porous Media, 13(2):179–203, 1993. (Cited on page 73.)

[5] Todd Arbogast. Gravitational forces in dual-porosity systems: II. Computational validation of the homogenized model. Transport in Porous Media, 13(2):205–220, 1993. (Cited on page 73.)

[6] Ingrid Åslund, Agnieszka Nowacka, Markus Nilsson, and Daniel Topgaard. Filter-exchange PGSE NMR determination of cell membrane permeability. Journal of Magnetic Resonance, 200(2):291–295, 2009. (Cited on page 51.)

[7] Yaniv Assaf and Peter J Basser. Composite hindered and restricted model of diffusion (CHARMED) MR imaging of the human brain. NeuroImage, 27(1):48–58, 2005. (Cited on pages 25, 49, and 50.)

[8] Yaniv Assaf, Tamar Blumenfeld-Katzir, Yossi Yovel, and Peter J Basser. AxCaliber: A method for measuring axon diameter distribution from diffusion MRI. Magn. Reson. Med., 59(6):1347–1354, 2008. (Cited on pages 49, 71, and 131.)

[9] Yaniv Assaf, Raisa Z Freidlin, Gustavo K Rohde, and Peter J Basser. New modeling and experimental framework to characterize hindered and restricted water diffusion in brain white matter. Magnetic Resonance in Medicine, 52(5):965–978, 2004. (Cited on page 25.)

[10] Yaniv Assaf and Ofer Pasternak. Diffusion Tensor Imaging (DTI)-based White Matter Mapping in Brain Research: A Review. Journal of Molecular Neuroscience, 34(1):51–61, 2008. (Cited on pages 24 and 25.)

[11] Scott Axelrod and Pabitra N Sen. Nuclear magnetic resonance spin echoes for restricted diffusion in an inhomogeneous field: Methods and asymptotic regimes. The Journal of Chemical Physics, 114:6878, 2001. (Cited on pages 41, 112, 120, and 133.)

[12] Balin Balinov, B Jonsson, Per Linse, and O Soderman. The NMR self-diffusion method applied to restricted diffusion. Simulation of echo attenuation from molecules in spheres and between planes. Journal of Magnetic Resonance, Series A, 104(1):17–25, 1993. (Cited on page 35.)

[13] Daniel Barazany, Peter J. Basser, and Yaniv Assaf. In vivo measurement of axon diameter distribution in the corpus callosum of rat brain. Brain, 132(5):1210–1220, 2009. (Cited on pages 49, 50, and 131.)

[14] Alexandre V Barzykin. Exact solution of the Torrey-Bloch equation for a spin echo in restricted geometries. Physical Review B, 58(21):14171, 1998. (Cited on page 34.)

[15] Alexandre V Barzykin. Theory of spin echo in restricted geometries under a step-wise gradient pulse sequence. Journal of Magnetic Resonance, 139(2):342–353, 1999. (Cited on pages 35, 112, and 132.)

[16] P J Basser, J Mattiello, and D LeBihan. MR diffusion tensor spectroscopy and imaging. Biophysical Journal, 66(1):259–267, 1994. (Cited on page 24.)

[17] Peter J Basser, Sinisa Pajevic, Carlo Pierpaoli, Jeffrey Duda, and Akram Aldroubi. In vivo fiber tractography using DT-MRI data. Magnetic Resonance in Medicine, 44(4):625–632, 2000. (Cited on page 25.)

[18] P. G. Batchelor, M. Moakher, D. Atkinson, F. Calamante, and A. Connelly. A rigorous framework for diffusion tensor calculus. Magnetic Resonance in Medicine, 53(1):221–225, 2005. (Cited on page 24.)

[19] T.E.J. Behrens, M.W. Woolrich, M. Jenkinson, H. Johansen-Berg, R.G. Nunes, S. Clare, P.M. Matthews, J.M. Brady, and S.M. Smith. Characterization and propagation of uncertainty in diffusion-weighted MR imaging. Magnetic Resonance in Medicine, 50(5):1077–1088, 2003. (Cited on page 49.)

[20] Kevin M. Bennett, James S. Hyde, and Kathleen M. Schmainda. Water diffusion heterogeneity index in the human brain is insensitive to the orientation of applied magnetic field gradients. Magnetic Resonance in Medicine, 56(2):235–239, 2006. (Cited on page 47.)

[21] Kevin M. Bennett, Kathleen M. Schmainda, Raoqiong Bennett (Tong), Daniel B. Rowe, Hanbing Lu, and James S. Hyde. Characterization of continuously distributed cortical water diffusion rates with a stretched-exponential model. Magnetic Resonance in Medicine, 50(4):727–734, 2003. (Cited on page 47.)

[22] Alain Bensoussan, Jacques-Louis Lions, and George Papanicolaou. Asymptotic analysis for periodic structures, volume 5 of Studies in Mathematics and its Applications. North-Holland Publishing Co., Amsterdam, 1978. (Cited on pages 45, 46, 78, and 97.)

[23] David J. Bergman and Keh-Jim Dunn. NMR of diffusing atoms in a periodic porous medium in the presence of a nonuniform magnetic field. Phys. Rev. E, 52:6516–6535, Dec 1995. (Cited on page 36.)

[24] Sachin Bhalekar, Varsha Daftardar-Gejji, Dumitru Baleanu, and Richard Magin. Generalized fractional order Bloch equation with extended delay. International Journal of Bifurcation and Chaos, 22(04):1250071, 2012. (Cited on pages 47 and 71.)

[25] Martin H Blees. The effect of finite duration of gradient pulses on the pulsed-field-gradient NMR method for studying restricted diffusion. Journal of Magnetic Resonance, Series A, 109(2):203–209, 1994. (Cited on page 35.)

[26] Jean-Philippe Bouchaud and Antoine Georges. Anomalous diffusion in disordered media: Statistical mechanisms, models and physical applications. Physics Reports, 195(4):127 – 293, 1990. (Cited on page 47.)

[27] Robert Brown. A brief account of microscopical observations made in the months of june, july and august 1827, on the particles contained in the pollen of plants; and on the general existence of active molecules in organic and inorganic bodies. The Philosophical Magazine, or Annals of Chemistry, Mathematics, Astronomy, Natural History and General Science, 4(21):161–173, 1828. (Cited on page 19.)

[28] Robert W Brown, Y-C Norman Cheng, E Mark Haacke, Michael R Thompson, and Ramesh Venkatesan. Magnetic resonance imaging: physical principles and sequence design. John Wiley & Sons, 2014. (Cited on pages 9, 18, 19, 22, 154, 156, 159, 160, and 162.)

[29] Lauren M. Burcaw, Els Fieremans, and Dmitry S. Novikov. Mesoscopic structure of neuronal tracts from time-dependent diffusion. NeuroImage, 114:18 – 37, 2015. (Cited on pages 42 and 111.)

[30] P T Callaghan, A Coy, D MacGowan, K J Packer, and F O Zelaya. Diffraction-like effects in NMR diffusion studies of fluids in porous solids. Nature, 351(6326):467–469, 1991. (Cited on pages 1, 11, 19, 25, 33, 36, 38, 42, 44, 112, 116, and 153.)

[31] P.T. Callaghan. Pulsed-gradient spin-echo NMR for planar, cylindrical, and spherical pores under conditions of wall relaxation. Journal of Magnetic Resonance, Series A, 113(1):53 – 59, 1995. (Cited on page 36.)

[32] Dave Cash and Thomas J. Carew. A quantitative analysis of the development of the central nervous system in juvenile Aplysia californica. Journal of Neurobiology, 20(1):25–47, 1989. (Cited on page 133.)

[33] Thomas L Cbenevert, Charles R Meyer, Bradford A Moffat, Alnawaz Rehemtulla, Suresh K Mukherji, Stephen S Gebarski, Douglas J Quint, Patricia L Robertson, Theodore S Lawrence, Larry Junck, et al. Diffusion MRI: a new strategy for assessment of cancer therapeutic efficacy. Molecular imaging, 1(4), 2002. (Cited on pages 1, 11, and 19.)

[34] Steren Chabert, Nicolas Molko, Yann Cointepas, Patrick Le Roux, and Denis Le Bihan. Diffusion tensor imaging of the human optic nerve using a non-CPMG fast spin echo sequence. J. Magn. Reson. Imaging, 22(2):307–310, 2005. (Cited on pages 42, 43, and 71.)

[35] Junjie Chen, Wei Liu, Huiying Zhang, Liz Lacy, Xiaoxia Yang, Sheng-Kwei Song, Samuel A. Wickline, and Xin Yu. Regional ventricular wall thickening reflects changes in cardiac fiber and sheet structure during contraction: quantification with diffusion tensor MRI. American Journal of Physiology - Heart and Circulatory Physiology, 289(5):H1898–H1907, 2005. (Cited on pages 25 and 153.)

[36] Junjie Chen, Sheng-Kwei Song, Wei Liu, Mark McLean, J. Stacy Allen, Jie Tan, Samuel A. Wickline, and Xin Yu. Remodeling of cardiac fiber structure after infarction in rats quantified with diffusion tensor MRI. American Journal of Physiology - Heart and Circulatory Physiology, 285(3):H946–H954, 2003. (Cited on pages 25 and 153.)

[37] H Cheng and S Torquato. Effective Conductivity of Periodic Arrays of Spheres with Interfacial Resistance. Proceedings: Mathematical, Physical and Engineering Sciences, 453(1956):145–161, 1997. (Cited on pages 46, 72, and 111.)

[38] Chih-Liang Chin, Felix W Wehrli, Scott N Hwang, Masaya Takahashi, and David B Hackney. Biexponential diffusion attenuation in the rat spinal cord: computer simulations based on anatomic images of axonal architecture. Magnetic resonance in medicine, 47(3):455–460, 2002. (Cited on page 35.)

[39] Chris A Clark and Denis Le Bihan. Water diffusion compartmentation and anisotropy at high b values in the human brain. Magn. Reson. Med., 44(6):852–859, 2000. (Cited on pages 25, 42, 43, and 71.)

[40] Chris A Clark and David J Werring. Diffusion tensor imaging in spinal cord: methods and applications–a review. NMR in Biomedicine, 15(7-8):578–586, 2002. (Cited on pages 1, 11, and 19.)

[41] Julien Coatléven. Mathematical justification of macroscopic models for diffusion MRI through the periodic unfolding method. Asymptotic Analysis, 93(3):219–258, 2015. (Cited on pages 78, 95, and 97.)

[42] Julien Coatléven, Houssem Haddar, and Jing-Rebecca Li. A Macroscopic Model Including Membrane Exchange for Diffusion MRI. SIAM Journal on Applied Mathematics, 74(2):516–546, 2014. (Cited on pages 5, 7, 15, 16, 42, 45, 51, 52, 63, 64, 66, 73, 74, 77, 78, 80, 96, 99, 100, 101, 105, and 149.)

[43] Andrew Coy and Paul T Callaghan. Pulsed gradient spin echo nuclear magnetic resonance for molecules diffusing between partially reflecting rectangular barriers. The Journal of chemical physics, 101:4599, 1994. (Cited on pages 35 and 36.)

[44] Francis Crick. Diffusion in Embryogenesis. Nature, 225:420–422, 1970. (Cited on pages 41 and 42.)

[45] Alessandro Daducci, Erick J. Canales-Rodríguez, Hui Zhang, Tim B. Dyrby, Daniel C. Alexander, and Jean-Philippe Thiran. Accelerated Microstructure Imaging via Convex Optimization (AMICO) from diffusion MRI data. NeuroImage, 105:32 – 44, 2015. (Cited on pages 131 and 146.)

[46] Thomas M. de Swiet and Pabitra N. Sen. Time dependent diffusion coefficient in a disordered medium. The Journal of Chemical Physics, 104(1):206–209, 1996. (Cited on pages 41 and 42.)

[47] Wendy DeMartini, Constance Lehman, and Savannah Partridge. Breast MRI for cancer detection and characterization: a review of evidence-based clinical applications. Academic radiology, 15(4):408–416, 2008. (Cited on pages 1, 11, and 19.)

[48] Rachid Deriche. Computational brain connectivity mapping: A core health and scientific challenge. Medical Image Analysis, 33:122 – 126, 2016. 20th anniversary of the Medical Image Analysis journal (MedIA). (Cited on page 25.)

[49] D.A.T. Dick. The permeability coefficient of water in the cell membrane and the diffusion coefficient in the cell interior. Journal of Theoretical Biology, 7(3):504 – 531, 1964. (Cited on page 44.)

[50] Mark D Does, Edward C Parsons, and John C Gore. Oscillating gradient measurements of water diffusion in normal and globally ischemic rat brain. Magn. Reson. Med., 49(2):206–215, 2003. (Cited on page 30.)

[51] Dean C. Douglass and David W. McCall. Diffusion in paraffin hydrocarbons. The Journal of Physical Chemistry, 62(9):1102–1107, 1958. (Cited on page 49.)

[52] Albert Einstein. Über die von der molekularkinetischen theorie der wärme geforderte bewegung von in ruhenden flüssigkeiten suspendierten teilchen. Annalen der physik, 322(8):549–560, 1905. (Cited on page 19.)

[53] Albert Einstein. Investigations on the Theory of the Brownian Movement. Dover Publications Inc., New York, 1926. (Cited on page 19.)

[54] Uran Ferizi, Torben Schneider, Eleftheria Panagiotaki, Gemma Nedjati-Gilani, Hui Zhang, Claudia A. M. Wheeler-Kingshott, and Daniel C. Alexander. A ranking of diffusion MRI compartment models with in vivo human brain data. Magnetic Resonance in Medicine, 72(6):1785–1792, 2014. (Cited on page 49.)

[55] Els Fieremans, Lauren M. Burcaw, Hong-Hsi Lee, Gregory Lemberskiy, Jelle Veraart, and Dmitry S. Novikov. In vivo observation and biophysical interpretation of time-dependent diffusion in human white matter. NeuroImage, 129:414 – 427, 2016. (Cited on pages 42 and 111.)

[56] Els Fieremans, Dmitry S Novikov, Jens H Jensen, and Joseph A Helpern. Monte Carlo study of a two-compartment exchange model of diffusion. NMR in Biomedicine, 23(7):711–724, 2010. (Cited on pages 44 and 45.)

[57] J Chetley Ford and David B Hackney. Numerical model for calculation of apparent diffusion coefficients (ADC) in permeable cylinders–comparison with measured ADC in spinal cord white matter. Magnetic resonance in medicine, 37(3):387–394, 1997. (Cited on page 35.)

[58] Lawrence R. Frank. Anisotropy in high angular resolution diffusion-weighted MRI. Magnetic Resonance in Medicine, 45(6):935–939, 2001. (Cited on page 25.)

[59] Lawrence R. Frank. Characterization of anisotropy in high angular resolution diffusion-weighted MRI. Magnetic Resonance in Medicine, 47(6):1083–1099, 2002. (Cited on page 25.)

[60] A. Ghosh, R. Deriche, and M. Moakher. Ternary Quartic approach for positive 4th order diffusion tensors revisited. In 2009 IEEE International Symposium on Biomedical Imaging: From Nano to Macro, pages 618–621, June 2009. (Cited on page 25.)

[61] Aurobrata Ghosh and Rachid Deriche. A survey of current trends in diffusion MRI for structural brain connectivity. Journal of Neural Engineering, 13(1):14, February 2016. (Cited on page 25.)

[62] D S Grebenkov, G Guillot, and B Sapoval. Restricted diffusion in a model acinar labyrinth by NMR: theoretical and numerical results. Journal of Magnetic Resonance, 184(1):143–156, 2007. (Cited on page 35.)

[63] Denis Grebenkov. NMR survey of reflected Brownian motion. Reviews of Modern Physics, 79(3):1077–1137, 2007. (Cited on pages 21, 27, 30, 32, 33, 35, 39, 40, 41, 42, 112, 115, 116, 120, 132, 150, and 153.)

[64] Denis Grebenkov. Laplacian eigenfunctions in NMR. I. A numerical tool. Concepts in Magnetic Resonance Part A, 32A(4):277–301, 2008. (Cited on pages 35, 112, and 132.)

[65] Denis S Grebenkov. Laplacian eigenfunctions in NMR. II. Theoretical advances. Concepts Magn. Reson., 34A(5):264–296, 2009. (Cited on pages 35, 112, and 132.)

[66] Denis S Grebenkov. Use, misuse, and abuse of apparent diffusion coefficients. Concepts Magn. Reson., 36A(1):24–35, 2010. (Cited on pages 43 and 47.)

[67] Denis S Grebenkov. From the microstructure to diffusion MRI, and back. 2016. (Cited on pages 27, 28, 29, 32, 37, 39, 40, 41, 42, 43, and 45.)

[68] Denis S Grebenkov, Hang Tuan Nguyen, and Jing-Rebecca Li. A fast random walk algorithm for computing diffusion-weighted NMR signals in multiscale porous media: a feasibility study for a Menger sponge. Microporous & Mesoporous Materials, 2013. (Cited on page 35.)

[69] Leslie Greengard and John Strain. A fast algorithm for the evaluation of heat potentials. Comm. Pure Appl. Math., 43(8):949–963, 1990. (Cited on page 117.)

[70] Ronald B Guenther and John W Lee. Partial differential equations of mathematical physics and integral equations. Prentice Hall, Inglewood Cliffs, New Jersey, 1988. (Cited on pages 116 and 133.)

[71] Bengi Gürses, Neslihan Kabakci, Arzu Kovanlikaya, Zeynep Firat, Ali Bayram, Aziz Müfit Uluð, and İlhami Kovanlikaya. Diffusion tensor imaging of the normal prostate at 3 tesla. European Radiology, 18(4):716–721, 2008. (Cited on page 25.)

[72] Houssem Haddar, Jing Rebecca Li, and Simona Schiavi. Adapting the Kärger model to account for finite diffusion-encoding pulses in diffusion MRI. IMA Journal of Applied Mathematics, 2016. (Cited on page 52.)

[73] Houssem Haddar, Jing-Rebecca Li, and Simona Schiavi. A Macroscopic Model for the Diffusion MRI Signal Accounting for Time-Dependent Diffusivity. SIAM Journal on Applied Mathematics, 76(3):930–949, 2016. (Cited on page 74.)

[74] Masoom A. Haider, Theodorus H. Van Der Kwast, Jeff Tanguay, Andrew J. Evans, Ali-Tahir Hashmi, Gina Lockwood, and John Trachtenberg. Combined T2-Weighted and Diffusion-Weighted MRI for Localization of Prostate Cancer. American Journal of Roentgenology, 2(189):323–328, 2007. (Cited on page 25.)

[75] Matt G. Hall and Thomas R. Barrick. From diffusion-weighted mri to anomalous diffusion imaging. Magnetic Resonance in Medicine, 59(3):447–455, 2008. (Cited on page 47.)

[76] Kevin D Harkins, Jean-Philippe Galons, Timothy W Secomb, and Theodore P Trouard. Assessment of the effects of cellular tissue properties on ADC measurements by numerical simulation of water diffusion. Magn. Reson. Med., 62(6):1414–1422, 2009. (Cited on page 85.)

[77] D P H Hasselman and Lloyd F Johnson. Effective Thermal Conductivity of Composites with Interfacial Thermal Barrier Resistance. Journal of Composite Materials, 21(6):508–515, 1987. (Cited on pages 47, 73, and 111.)

[78] J.W. Haus and K.W. Kehr. Diffusion in regular and disordered lattices. Physics Reports, 150(5-6):263 – 406, 1987. (Cited on pages 41 and 42.)

[79] Joseph P. Hornak. Basics of NMR, 1997. (Cited on pages 9, 18, 19, 154, 156, 160, and 162.)

[80] Mark A Horsfield and Derek K Jones. Applications of diffusion-weighted and diffusion tensor MRI to white matter diseases, a review. NMR Biomed., 15(7-8):570–577, 2002. (Cited on pages 1, 11, 19, and 23.)

[81] Edward S. Hui. Diffusion magnetic resonance imaging of ischemic stroke. Journal of Neuroscience and Neuroengineering, 1(1):48–53, 2012. (Cited on pages 1, 11, 19, and 24.)

[82] Edward S. Hui, Els Fieremans, Jens H. Jensen, Ali Tabesh, Wuwei Feng, Leonardo Bonilha, Maria V. Spampinato, Robert Adams, and Joseph A. Helpern. Stroke Assessment With Diffusional Kurtosis Imaging. Stroke, 43(11):2968–2973, 2012. (Cited on page 24.)

[83] Scott N Hwang, Chih-Liang Chin, Felix W Wehrli, and David B Hackney. An image-based finite difference model for simulating restricted diffusion. Magnetic Resonance in Medicine, 50(2):373–382, 2003. (Cited on page 35.)

[84] B.A. Inglis, E.L. Bossart, D.L. Buckley, E.D. Wirth, and T.H. Mareci. Visualization of neural tissue water compartments using biexponential diffusion tensor MRI. Magnetic Resonance in Medicine, 45(4):580–587, 2001. (Cited on page 25.)

[85] Kalvis M Jansons and Daniel C Alexander. Persistent angular structure: new insights from diffusion magnetic resonance imaging data. Inverse Problems, 19(5):1031, 2003. (Cited on page 25.)

[86] Jens H Jensen and Joseph A Helpern. MRI Quantification of Non-Gaussian Water Diffusion by Kurtosis Analysis. NMR Biomed., 23(7):698–710, 2010. (Cited on page 40.)

[87] Jens H Jensen and Joseph A Helpern. Progress in diffusion-weighted imaging: concepts, techniques and applications to the central nervous system. NMR Biomed., 23(7):659–660, 2010. (Cited on page 63.)

[88] Jens H Jensen, Joseph A Helpern, Anita Ramani, Hanzhang Lu, and Kyle Kaczynski. Diffusional kurtosis imaging: The quantification of non-Gaussian water diffusion by means of magnetic resonance imaging. Magnetic Resonance in Medicine, 53(6):1432–1440, 2005. (Cited on pages 25, 40, 42, 43, 63, and 71.)

[89] Sune N Jespersen, Christopher D Kroenke, Leif Astergaard, Joseph J H Ackerman, and Dmitriy A Yablonskiy. Modeling dendrite density from magnetic resonance diffusion measurements. NeuroImage, 34(4):1473–1486, 2007. (Cited on page 71.)

[90] H Johansen-Berg and T E J Behrens. Diffusion MRI: From Quantitative Measurement to In vivo Neuroanatomy. Elsevier Science, 2013. (Cited on pages 1, 9, 11, 18, 19, 22, and 154.)

[91] D K Jones. Diffusion MRI: Theory, Methods, and Applications. Oxford University Press, USA, 2010. (Cited on pages 1, 11, 19, and 153.)

[92] Derek K. Jones and Alexander Leemans. Diffusion Tensor Imaging, pages 127–144. Humana Press, Totowa, NJ, 2011. (Cited on page 24.)

[93] J Kärger, H Pfeifer, and W Heinik. Principles and application of self-diffusion measurements by nuclear magnetic resonance. Advances in magnetic resonance, 12:1–89, 1988. (Cited on page 44.)

[94] Jörg Kärger. NMR self-diffusion studies in heterogeneous systems. Advances in Colloid and Interface Science, 23:129–148, 1985. (Cited on pages 5, 7, 15, 16, 44, 51, 54, 55, 72, and 149.)

[95] V Kenkre. Simple solutions of the Torrey-Bloch equations in the NMR study of molecular diffusion. Journal of Magnetic Resonance, 128(1):62–69, 1997. (Cited on pages 33, 34, and 38.)

[96] Chelsea S Kidwell, Jeffry R Alger, Francesco Di Salle, Sidney Starkman, Pablo Villablanca, John Bentson, and Jeffrey L Saver. Diffusion MRI in patients with transient ischemic attacks. Stroke, 30(6):1174–1180, 1999. (Cited on page 24.)

[97] Sungheon Kim, Gloria Chi-Fishman, Alan S Barnett, and Carlo Pierpaoli. Dependence on diffusion time of apparent diffusion tensor of ex vivo calf tongue and heart. Magn. Reson. Med., 54(6):1387–1396, 2005. (Cited on page 25.)

[98] Andreas Kirsch. An introduction to the mathematical theory of inverse problems, volume 120. Springer Science & Business Media, 2011. (Cited on pages 141 and 142.)

[99] Valerij G Kiselev. The cumulant expansion: an overarching mathematical framework for understanding diffusion NMR. Diffusion MRI: Theory, Methods, and Applications: Theory, Methods, and Applications, page 152, 2010. (Cited on pages 27, 39, 40, 41, and 112.)

[100] Tristan Anselm Kuder and Frederik Bernd Laun. Nmr-based diffusion pore imaging by double wave vector measurements. Magnetic Resonance in Medicine, 70(3):836–841, 2013. (Cited on pages 30 and 36.)

[101] Nicolas Kunz, Hui Zhang, Lana Vasung, Kieran R O'Brien, Yaniv Assaf, François Lazeyras, Daniel C Alexander, and Petra S Hüppi. Assessing white matter microstructure of the newborn with multi-shell diffusion MRI and biophysical compartment models. Neuroimage, 96:288–299, 2014. (Cited on page 131.)

[102] L L Latour, K Svoboda, P P Mitra, and C H Sotak. Time-dependent diffusion of water in a biological model system. Proceedings of the National Academy of Sciences, 91(4):1229–1233, 1994. (Cited on pages 47, 73, and 111.)

[103] Lawrence L Latour, Partha P Mitra, Robert L Kleinberg, and Christopher H Sotak. Time-dependent diffusion coefficient of fluids in porous media as a probe of surface-to-volume ratio. Journal of Magnetic Resonance, Series A, 101(3):342–346, 1993. (Cited on pages 41, 42, and 112.)

[104] Frederik Bernd Laun, Tristan Anselm Kuder, Wolfhard Semmler, and Bram Stieltjes. Determination of the defining boundary in nuclear magnetic resonance diffusion experiments. Phys. Rev. Lett., 107:048102, Jul 2011. (Cited on page 36.)

[105] Mariana Lazar. Mapping brain anatomical connectivity using white matter tractography. NMR Biomed., 23(7):821–835, 2010. (Cited on pages 23, 25, and 153.)

[106] D Le Bihan, E Breton, D Lallemand, P Grenier, E Cabanis, and M Laval-Jeantet. MR imaging of intravoxel incoherent motions: application to diffusion and perfusion in neurologic disorders. Radiology, 161(2):401–407, 1986. (Cited on pages 23 and 153.)

[107] Denis Le Bihan and E. Breton. Imagerie de diffusion in-vivo par resonance magnetique nucleaire. Comptes-Rendus de l'Academie des Sciences, 93(5):27–34, December 1985. (Cited on pages 23, 33, and 39.)

[108] Denis Le Bihan and Heidi Johansen-Berg. Diffusion MRI at 25: Exploring brain tissue structure and function. NeuroImage, 61(2):324–341, 2012. (Cited on pages 23, 25, 39, and 153.)

[109] Denis Le Bihan, Jean-François Mangin, Cyril Poupon, Chris A Clark, Sabina Pappata, Nicolas Molko, and Hughes Chabriat. Diffusion tensor imaging: concepts and applications. Journal of magnetic resonance imaging, 13(4):534–546, 2001. (Cited on page 24.)

[110] Denis LeBihan, Cyril Poupon, Alexis Amadon, and Franck Lethimonnier. Artifacts and pitfalls in diffusion MRI. Journal of Magnetic Resonance Imaging, 24(3):478–488, 2006. (Cited on page 23.)

[111] Denis LeBihan, Shin-ichi Urayama, Toshihiko Aso, Takashi Hanakawa, and Hidenao Fukuyama. Direct and fast detection of neuronal activation in the human brain with diffusion MRI. PNAS, 103(21):8263–8268, 2006. (Cited on pages 23 and 153.)

[112] Choong H. Lee, Jeremy J. Flint, Brian Hansen, and Stephen J. Blackband. Investigation of the subcellular architecture of L7 neurons of Aplysia californica using magnetic resonance microscopy (MRM) at 7.8 microns. Scientific Reports, 5, 2015. (Cited on page 133.)

[113] Jing-Huei Lee and Charles S Springer. Effects of equilibrium exchange on diffusion-weighted NMR signals: The diffusigraphic shutter-speed? Magn. Reson. Med., 49(3):450–458, 2003. (Cited on page 51.)

[114] Jing-Rebecca Li and Leslie Greengard. High order accurate methods for the evaluation of layer heat potentials. SIAM J. Sci. Comput., 31(5):3847–3860, 2009. (Cited on page 117.)

[115] Jing-Rebecca Li, Hang Tuan Nguyen, Dang Van Nguyen, Houssem Haddar, Julien Coatléven, and Denis Le Bihan. Numerical study of a macroscopic finite pulse model of the diffusion MRI signal. Journal of Magnetic Resonance, 248:54 – 65, 2014. (Cited on pages 38 and 45.)

[116] Jing-Rebecca Li, Hang Tuan Nguyen, Dang Van Nguyen, Houssem Haddar, Julien Coatléven, and Denis Le Bihan. Numerical study of a macroscopic finite pulse model of the diffusion MRI signal. Journal of Magnetic Resonance, 248(0):54–65, 2014. (Cited on pages 53, 54, 63, and 65.)

[117] Per Linse and OLLE Soderman. The validity of the short-gradient-pulse approximation in NMR studies of restricted diffusion. Simulations of molecules diffusing between planes, in cylinders and spheres. Journal of Magnetic Resonance, Series A, 116(1):77–86, 1995. (Cited on page 35.)

[118] Michael L. Lipton. Totally accessible MRI: a user's guide to principles, technology, and applications. Springer Science & Business Media, 2010. (Cited on pages 9, 18, 19, 154, 155, 156, 157, 160, 161, and 162.)

[119] Chunlei Liu, Roland Bammer, Burak Acar, and Michael E. Moseley. Characterizing non-gaussian diffusion by using generalized diffusion tensors. Magnetic Resonance in Medicine, 51(5):924–937, 2004. (Cited on page 25.)

[120] Chunlei Liu, Roland Bammer, and Michael E Moseley. Generalized Diffusion Tensor Imaging (GDTI): A Method for Characterizing and Imaging Diffusion Anisotropy Caused by Non-Gaussian Diffusion. Israel Journal of Chemistry, 43(1-2):145–154, 2003. (Cited on page 36.)

[121] Hanzhang Lu, Jens H Jensen, Anita Ramani, and Joseph A Helpern. Three-dimensional characterization of non-gaussian water diffusion in humans using diffusion kurtosis imaging. NMR Biomed., 19(2):236–247, 2006. (Cited on page 25.)

[122] Richard Magin, Xu Feng, and Dumitru Baleanu. Solving the fractional order Bloch equation. Concepts in Magnetic Resonance Part A, 34A(1):16–23, 2009. (Cited on pages 47 and 71.)

[123] Richard L Magin, Osama Abdullah, Dumitru Baleanu, and Xiaohong Joe Zhou. Anomalous diffusion expressed through fractional order differential operators in the Bloch-Torrey equation. Journal of Magnetic Resonance, 190(2):255–270, 2008. (Cited on pages 42, 43, 47, and 71.)

[124] Stephan E Maier, Peter Bogner, Gabor Bajzik, Hatsuho Mamata, Yoshiaki Mamata, Imre Repa, Ferenc A Jolesz, and Robert V Mulkern. Normal Brain and Brain Tumor: Multicomponent Apparent Diffusion Coefficient Line Scan Imaging. Radiology, 219(3):842–849, 2001. (Cited on pages 42, 43, and 71.)

[125] Stephan E Maier, Yanping Sun, and Robert V Mulkern. Diffusion imaging of brain tumors. NMR Biomed., 23(7):849–864, 2010. (Cited on pages 23 and 153.)

[126] Christian Meier, Wolfgang Dreher, and Dieter Leibfritz. Diffusion in compartmental systems. I. A comparison of an analytical model with simulations. Magnetic Resonance in Medicine, 50(3):500–509, 2003. (Cited on pages 35 and 51.)

[127] Ralf Metzler and Joseph Klafter. The random walk's guide to anomalous diffusion: a fractional dynamics approach. Physics Reports, 339(1):1 – 77, 2000. (Cited on page 47.)

[128] Ludovico Minati and Władysław P. Węglarz. Physical foundations, models, and methods of diffusion magnetic resonance imaging of the brain: A review. Concepts in Magnetic Resonance Part A, 30A(5):278–307, 2007. (Cited on page 35.)

[129] Partha P. Mitra, Pabitra N. Sen, and Lawrence M. Schwartz. Short-time behavior of the diffusion coefficient as a geometrical probe of porous media. Phys. Rev. B, 47:8565–8574, Apr 1993. (Cited on pages 41 and 112.)

[130] Partha P Mitra, Pabitra N Sen, Lawrence M Schwartz, and Pierre Le Doussal. Diffusion propagator as a probe of the structure of porous media. Physical review letters, 68(24):3555–3558, 1992. (Cited on pages 5, 6, 7, 8, 15, 16, 17, 41, 72, 112, 120, 129, 132, 133, and 150.)

[131] M E Moseley, J Kucharczyk, J Mintorovitch, Y Cohen, J Kurhanewicz, N Derugin, H Asgari, and D Norman. Diffusion-weighted MR imaging of acute stroke: correlation with T2- weighted and magnetic susceptibility-enhanced MR imaging in cats. AJNR Am J Neuroradiol, 11(3):423–429, 1990. (Cited on pages 23, 24, and 153.)

[132] Robert V Mulkern, Hakon Gudbjartsson, Carl-Fredrik Westin, Hale Pinar Zengingonul, Werner Gartner, Charles R G Guttmann, Richard L Robertson, Walid Kyriakos, Richard

Schwartz, David Holtzman, Ferenc A Jolesz, and Stephan E Maier. Multi-component apparent diffusion coefficients in human brain†. NMR Biomed., 12(1):51–62, 1999. (Cited on pages 42, 43, and 71.)

[133] C H Neuman. Spin echo of spins diffusing in a bounded medium. The Journal of Chemical Physics, 60:4508, 1974. (Cited on pages 39, 41, 49, and 112.)

[134] Dang Van Nguyen, Jing-Rebecca Li, Denis Grebenkov, and Denis Le Bihan. A finite elements method to solve the Bloch-Torrey equation applied to diffusion magnetic resonance imaging. Journal of Computational Physics, 263(0):283–302, April 2014. (Cited on pages 35 and 84.)

[135] Hang Tuan Nguyen, Denis Grebenkov, Dang Van Nguyen, Cyril Poupon, Denis Le Bihan, and Jing-Rebecca Li. Parameter estimation using macroscopic diffusion MRI signal models. Physics in Medicine and Biology, 60(8):3389, 2015. (Cited on page 45.)

[136] Thoralf Niendorf, Rick M Dijkhuizen, David G Norris, Menno van Lookeren Campagne, and Klaas Nicolay. Biexponential diffusion attenuation in various states of brain tissue: Implications for diffusion-weighted imaging. Magn. Reson. Med., 36(6):847–857, 1996. (Cited on pages 42, 43, and 71.)

[137] Markus Nilsson, Jimmy Latt, Emil Nordh, Ronnie Wirestam, Freddy Stahlberg, and Sara Brockstedt. On the effects of a varied diffusion time in vivo: is the diffusion in white matter restricted? Magnetic Resonance Imaging, 27(2):176–187, 2009. (Cited on page 51.)

[138] Dmitry S Novikov, Els Fieremans, Jens H Jensen, and Joseph A Helpern. Random walks with barriers. Nat Phys, 7(6):508–514, 2011. (Cited on pages 41, 42, 48, 49, 72, 111, 112, and 125.)

[139] Dmitry S Novikov, Jens H Jensen, Joseph A Helpern, and Els Fieremans. Revealing mesoscopic structural universality with diffusion. Proceedings of the National Academy of Sciences, 2014. (Cited on pages 42, 48, 49, and 111.)

[140] Dmitry S Novikov and Valerij G Kiselev. Effective medium theory of a diffusion-weighted signal. NMR in Biomedicine, 23(7):682–697, 2010. (Cited on pages 42, 48, 71, and 111.)

[141] Dmitry S. Novikov and Valerij G. Kiselev. Surface-to-volume ratio with oscillating gradients. Journal of Magnetic Resonance, 210(1):141 – 145, 2011. (Cited on pages 30 and 31.)

[142] Evren Özarslan and Peter J. Basser. Microscopic anisotropy revealed by NMR double pulsed field gradient experiments with arbitrary timing parameters. The Journal of Chemical Physics, 128(15), 2008. (Cited on page 30.)

[143] Evren Özarslan, Peter J Basser, Timothy M Shepherd, Peter E Thelwall, Baba C Vemuri, and Stephen J Blackband. Observation of anomalous diffusion in excised tissue by characterizing the diffusion-time dependence of the mr signal. Journal of Magnetic Resonance, 183(2):315–323, 2006. (Cited on pages 47 and 48.)

[144] Evren Özarslan, Cheng Guan Koay, and Peter J Basser. Remarks on q-space MR propagator in partially restricted, axially-symmetric, and isotropic environments. Magnetic resonance imaging, 27(6):834–844, 2009. (Cited on page 36.)

[145] Evren Özarslan and Thomas H. Mareci. Generalized diffusion tensor imaging and analytical relationships between diffusion tensor imaging and high angular resolution diffusion imaging. Magnetic Resonance in Medicine, 50(5):955–965, 2003. (Cited on page 25.)

[146] Evren Özarslan, Timothy M Shepherd, Cheng Guan Koay, Stephen J Blackband, and Peter J Basser. Temporal scaling characteristics of diffusion as a new mri contrast: findings in rat hippocampus. Neuroimage, 60(2):1380–1393, 2012. (Cited on page 48.)

[147] Evren Özarslan, Timothy M. Shepherd, Baba C. Vemuri, Stephen J. Blackband, and Thomas H. Mareci. Resolution of complex tissue microarchitecture using the diffusion orientation transform (DOT). NeuroImage, 31(3):1086 – 1103, 2006. (Cited on page 25.)

[148] Evren Özarslan, Baba C. Vemuri, and Thomas H. Mareci. Generalized scalar measures for diffusion mri using trace, variance, and entropy. Magnetic Resonance in Medicine, 53(4):866–876, 2005. (Cited on page 25.)

[149] M. Palombo, A. Gabrielli, S. De Santis, C. Cametti, G. Ruocco, and S. Capuani. Spatio-temporal anomalous diffusion in heterogeneous media by nuclear magnetic resonance. The Journal of Chemical Physics, 135(3), 2011. (Cited on page 47.)

[150] Eleftheria Panagiotaki, Torben Schneider, Bernard Siow, Matt G. Hall, Mark F. Lythgoe, and Daniel C. Alexander. Compartment models of the diffusion MR signal in brain white matter: A taxonomy and comparison. NeuroImage, 59(3):2241 – 2254, 2012. (Cited on page 49.)

[151] Muriel Perrin, Yann Cointepas, Arnaud Cachia, Cyril Poupon, Bertrand Thirion, Denis Riviere, Pascal Cathier, Vincent El Kouby, André Constantinesco, Denis Le Bihan, et al. Connectivity-based parcellation of the cortical mantle using q-ball diffusion imaging. Journal of Biomedical Imaging, 2008:4, 2008. (Cited on page 25.)

[152] Mark Peyron, Gregory K. Pierens, Alun J. Lucas, Laurance D. Hall, and Robert C. Stewart. The modified stretched-exponential model for characterization of NMR relaxation in porous media. Journal of Magnetic Resonance, Series A, 118(2):214 – 220, 1996. (Cited on page 47.)

[153] Josef Pfeuffer, Ulrich Flogel, Wolfgang Dreher, and Dieter Leibfritz. Restricted diffusion and exchange of intracellular water: theoretical modelling and diffusion time dependence of 1H NMR measurements on perfused glial cells. NMR in Biomedicine, 11(1):19–31, 1998. (Cited on page 51.)

[154] Carlo Pierpaoli, Jeffry R Alger, Andrea Righini, James Mattiello, Russell Dickerson, Daryl Des Pres, Alan Barnett, and Giovanni Di Chiro. High Temporal Resolution Diffusion MRI of Global Cerebral Ischemia and Reperfusion. J Cereb Blood Flow Metab, 16(5):892–905, 1996. (Cited on page 24.)

[155] Olivier Pironneau, Frédéric Hecht, and Jacques Morice. freeFEM++, www.freefem.org/, 2015. (Cited on page 84.)

[156] Marco Pizzolato, Aurobrata Ghosh, Timothé Boutelier, and Rachid Deriche. Magnitude and Complex Based Diffusion Signal Reconstruction, pages 127–140. Springer International Publishing, Cham, 2014. (Cited on page 36.)

[157] Adilson Prando. Diffusion-weighted MRI of peripheral zone prostate cancer: comparison of tumor apparent diffusion coefficient with Gleason score and percentage of tumor on core biopsy. International braz j urol, 36:504 – 517, 08 2010. (Cited on page 25.)

[158] William S Price. Pulsed-field gradient nuclear magnetic resonance as a tool for studying translational diffusion: Part 1. Basic theory. Concepts Magn. Reson., 9(5):299–336, 1997. (Cited on pages 19, 20, and 49.)

[159] William S Price. NMR studies of translational motion: principles and applications. Cambridge University Press, 2009. (Cited on page 153.)

[160] Nadya Pyatigorskaya, Denis Le Bihan, Olivier Reynaud, and Luisa Ciobanu. Relationship between the diffusion time and the diffusion MRI signal observed at 17.2 tesla in the healthy rat brain cortex. Magnetic Resonance in Medicine, pages n/a—-n/a, 2013. (Cited on pages 73 and 111.)

[161] James D Quirk, G Larry Bretthorst, Timothy Q Duong, Avi Z Snyder, Charles S Springer, Joseph J H Ackerman, and Jeffrey J Neil. Equilibrium water exchange between the intra- and extracellular spaces of mammalian brain. Magn. Reson. Med., 50(3):493–499, 2003. (Cited on page 51.)

[162] Baldwin Robertson. Spin-echo decay of spins diffusing in a bounded region. Physical Review, 151(1):273, 1966. (Cited on pages 39, 41, and 112.)

[163] Damien Rohmer, Arkadiusz Sitek, and Grant T. Gullberg. Reconstruction and visualization of fiber and sheet structure with regularized tensor diffusion MRI in the human heart. Lawrence Berkeley National Laboratory Publication. LBNL-60277, 2006. (Cited on pages 25, 34, and 153.)

[164] Y Roth, A Ocherashvilli, D Daniels, J Ruizcabello, S Maier, A Orenstein, and Y Mardor. Quantification of water compartmentation in cell suspensions by diffusion-weighted and T2-weighted MRI. Magnetic Resonance Imaging, 26(1):88–102, 2008. (Cited on page 51.)

[165] S. Sarkar, M. C. Craig, M. Catani, F. Dell'Acqua, T. Fahy, Q. Deeley, and D. G. M. Murphy. Frontotemporal white-matter microstructural abnormalities in adolescents with conduct disorder: a diffusion tensor imaging study. Psychological Medicine, 43:401–411, 2 2013. (Cited on page 25.)

[166] Dirk Schnapauff, Martin Zeile, Manuel Ben Niederhagen, Barbara Fleige, Per-Ulf Tunn, Bernd Hamm, and Oliver Dudeck. Diffusion-weighted echo-planar magnetic resonance imaging for the assessment of tumor cellularity in patients with soft-tissue sarcomas. J. Magn. Reson. Imaging, 29(6):1355–1359, 2009. (Cited on page 23.)

[167] Pabitra N. Sen. Time-dependent diffusion coefficient as a probe of the permeability of the pore wall. The Journal of Chemical Physics, 119(18):9871–9876, 2003. (Cited on pages 41 and 42.)

[168] Pabitra N Sen and Peter J Basser. A Model for Diffusion in White Matter in the Brain. Biophys J, 89(5):2927–2938, 2005. (Cited on page 71.)

[169] ME Shenton, HM Hamoda, JS Schneiderman, S Bouix, O Pasternak, Y Rathi, M-A Vu, MP Purohit, K Helmer, I Koerte, et al. A review of magnetic resonance imaging and diffusion tensor imaging findings in mild traumatic brain injury. Brain imaging and behavior, 6(2):137–192, 2012. (Cited on pages 1, 11, and 19.)

[170] Greg J Stanisz. Diffusion MR in biological systems: tissue compartments and exchange. Israel journal of chemistry, 43(1-2):33–44, 2003. (Cited on page 43.)

[171] Greg J Stanisz, Graham A Wright, R Mark Henkelman, and Aaron Szafer. An analytical model of restricted diffusion in bovine optic nerve. Magn. Reson. Med., 37(1):103–111, 1997. (Cited on pages 49, 50, and 51.)

[172] E O Stejskal and J E Tanner. Spin Diffusion Measurements: Spin Echoes in the Presence of a Time-Dependent Field Gradient. The Journal of Chemical Physics, 42(1):288–292, 1965. (Cited on pages 5, 7, 14, 16, 22, 30, 33, 36, 51, and 75.)

[173] Janez Stepišnik. Time-dependent self-diffusion by NMR spin-echo. Physica B: Condensed Matter, 183(4):343 – 350, 1993. (Cited on page 49.)

[174] Takeshi Sugahara, Yukunori Korogi, Masato Kochi, Ichiro Ikushima, Yoshinori Shigematu, Toshinori Hirai, Tomoko Okuda, Luxia Liang, Yulin Ge, Yasuyuki Komohara, Yukitaka Ushio, and Mutsumasa Takahashi. Usefulness of diffusion-weighted MRI with echo-planar technique in the evaluation of cellularity in gliomas. J. Magn. Reson. Imaging, 9(1):53–60, 1999. (Cited on pages 23 and 153.)

[175] Aaron Szafer, Jianhui Zhong, and John C Gore. Theoretical Model for Water Diffusion in Tissues. Magn. Reson. Med., 33(5):697–712, 1995. (Cited on pages 47, 73, and 111.)

[176] J E Tanner and Edward O Stejskal. Restricted Self-Diffusion of Protons in Colloidal Systems by the Pulsed-Gradient, Spin-Echo Method. The Journal of Chemical Physics, 49:1768, 1968. (Cited on pages 30 and 36.)

[177] Ido Tavor, Shir Hofstetter, and Yaniv Assaf. Micro-structural assessment of short term plasticity dynamics. Neuroimage, 81:1–7, 2013. (Cited on page 131.)

[178] Andrej Nikolaevich Tikhonov and Vasiliy Yakovlevich Arsenin. Solutions of ill-posed problems. 1977. (Cited on pages 9, 17, and 150.)

[179] S Torquato and M D Rintoul. Effect of the Interface on the Properties of Composite Media. Phys. Rev. Lett., 75(22):4067—-, 1995. (Cited on pages 7, 16, 42, 47, 73, and 111.)

[180] H C Torrey. Bloch Equations with Diffusion Terms. Physical Review Online Archive (Prola), 104(3):563–565, 1956. (Cited on pages 1, 11, 28, 72, 75, and 95.)

[181] Yoshito Tsushima, Ayako Takahashi-Taketomi, and Keigo Endo. Magnetic resonance (MR) differential diagnosis of breast tumors using apparent diffusion coefficient (ADC) on 1.5-T. J. Magn. Reson. Imaging, 30(2):249–255, 2009. (Cited on pages 23 and 153.)

[182] David S Tuch, Timothy G Reese, Mette R Wiegell, and Van J Wedeen. Diffusion MRI of complex neural architecture. Neuron, 40(5):885–895, 2003. (Cited on pages 25, 39, and 153.)

[183] H. Uzawa. Iterative methods for concave programming. Studies in Linear and Nonlinear Programming, pages 154–165, 1958. (Cited on pages 9, 17, 132, 142, and 150.)

[184] P. Vangelderen, D. Despres, P.C.M. Vanzijl, and C.T.W. Moonen. Evaluation of Restricted Diffusion in Cylinders. phosphocreatine in Rabbit Leg Muscle. Journal of Magnetic Resonance, Series B, 103(3):255 – 260, 1994. (Cited on page 49.)

[185] Peter Vestergaard-Poulsen, Gregers Wegener, Brian Hansen, Carsten R Bjarkam, Stephen J Blackband, Niels C Nielsen, and Sune N Jespersen. Diffusion-weighted MRI and quantitative biophysical modeling of hippocampal neurite loss in chronic stress. PloS one, 6(7):e20653, 2011. (Cited on page 131.)

[186] A.Reginald Waldeck, Philip W Kuchel, Alison J Lennon, and Bogdan E Chapman. NMR diffusion measurements to characterise membrane transport and solute binding. Progress in Nuclear Magnetic Resonance Spectroscopy, 30(1–2):39–68, 1997. (Cited on page 51.)

[187] S Warach, D Chien, W Li, M Ronthal, and R R Edelman. Fast magnetic resonance diffusion-weighted imaging of acute human stroke. Neurology, 42(9):1717–, 1992. (Cited on pages 23 and 153.)

[188] Rachel A. Weber, Edward S. Hui, Jens H. Jensen, Xingju Nie, Maria F. Falangola, Joseph A. Helpern, and DeAnna L. Adkins. Diffusional kurtosis and diffusion tensor imaging reveal different time-sensitive stroke-induced microstructural changes. Stroke, 46(2):545–550, 2015. (Cited on page 24.)

[189] VJ Wedeen, TG Reese, DS Tuch, MR Weigel, JG Dou, RM Weiskoff, and D Chessler. Mapping fiber orientation spectra in cerebral white matter with fourier-transform diffusion MRI. In Proceedings of the 8th Annual Meeting of ISMRM, Denver, page 82, 2000. (Cited on page 25.)

[190] J Xu, M D Does, and J C Gore. Numerical study of water diffusion in biological tissues using an improved finite difference method. Physics in medicine and biology, 52(7), April 2007. (Cited on pages 35 and 85.)

[191] Junzhong Xu, Mark D Does, and John C Gore. Quantitative characterization of tissue microstructure with temporal diffusion spectroscopy. Journal of Magnetic Resonance, 200(2):189–197, 2009. (Cited on page 30.)

[192] Dmitriy Yablonskiy, Larry Bretthorst, and Joseph Ackerman. Statistical model for diffusion attenuated MR signal. Magnetic Resonance in Medicine, 50(4):664–669, 2003. (Cited on pages 27, 42, 43, and 71.)

[193] Hui Zhang, Tim B. Dyrby, and Daniel C. Alexander. Medical Image Computing and Computer-Assisted Intervention – MICCAI 2011: 14th International Conference, Toronto, Canada, September 18-22, 2011, Proceedings, Part II, chapter Axon Diameter Mapping in Crossing Fibers with Diffusion MRI, pages 82–89. Springer Berlin Heidelberg, Berlin, Heidelberg, 2011. (Cited on pages 50 and 131.)

[194] Hui Zhang, Penny L. Hubbard, Geoff J.M. Parker, and Daniel C. Alexander. Axon diameter mapping in the presence of orientation dispersion with diffusion MRI. NeuroImage, 56(3):1301 – 1315, 2011. (Cited on page 50.)

[195] Hui Zhang, Torben Schneider, Claudia A. Wheeler-Kingshott, and Daniel C. Alexander. NODDI: Practical in vivo neurite orientation dispersion and density imaging of the human brain. NeuroImage, 61(4):1000 – 1016, 2012. (Cited on pages 50 and 131.)

[196] Xiaohong Joe Zhou, Qing Gao, Osama Abdullah, and Richard L. Magin. Studies of anomalous diffusion in the human brain using fractional order calculus. Magnetic Resonance in Medicine, 63(3):562–569, 2010. (Cited on page 47.)

université PARIS-SACLAY | École doctorale de mathématiques Hadamard (EDMH)

Titre : Modélisation du signal de l'IRM de diffusion par des techniques analytiques et d'homogénéisation

Mots clefs : IRMD, CDA dependant du temps, modèle de Kärger, impulsions finies, modèles homogénéisés, problèmes inverses.

Résumé : L'imagerie par résonance magnétique de diffusion (IRMD) est une technique d'imagerie qui teste les propriétés diffusives d'un échantillon en le soumettant aux impulsions d'un gradient de champ magnétique. Une importante quantité mesurée par l'IRMD dans chaque voxel est le Coefficient de Diffusion Apparent (CDA). Il existe dans la littérature un nombre important de modèles macroscopiques décrivant le CDA allant du plus simple au plus complexe. Le but de cette thèse est de construire des modèles simples, disposant d'une bonne validité applicative, en se fondant sur une modélisation de la diffusion à l'échelle microscopique à l'aide d'EDP et de techniques d'homogénéisation.
Dans un article antérieur, le modèle homogénéisé FPK a été déduit de l'EDP de Bloch-Torrey sous l'hypothèse que la perméabilité de la membrane soit petite et le temps de diffusion long. Nous effectuons tout d'abord une analyse de ce modèle et établissons sa convergence vers le modèle classique de Kärger lorsque la durée des impulsions magnétiques tend vers 0. Notre analyse montre que le modèle FPK peut être vu comme une généralisation de celui de Kärger, permettant la prise en compte de durées d'impulsions magnétiques arbitraires. Le CDA du modèle FPK est indépendant du temps ce qui entre en contradiction avec nombreuses observations expérimentales. Par conséquent, notre objectif suivant est de corriger ce modèle pour de petites valeurs de ce que l'on appelle des b-valeurs afin que le CDA homogénéisé qui en résulte soit sensible à la fois à la durée des impulsions et à la fois au temps de diffusion. Pour atteindre cet objectif, nous utilisons une technique d'homogénéisation similaire à celle utilisée pour le FPK, tout en proposant un redimensionnement adapté de l'échelle de temps et de l'intensité du gradient pour la gamme de b-valeurs considérées. Nous établissons aussi des résultats analytiques d'approximation du modèle asymptotique qui fournissent des formules explicites de la dépendance temporelle du CDA.
Enfin nous étudions le problème inverse consistant en la détermination d'information qualitative se rapportant à la fraction volumique des cellules à partir de signaux IRMD mesurés.

Title : Homogenized and analytical models for the diffusion MRI signal

Keywords : DMRI, time dependent ADC, Kärger model, finite-pulses, homogenized models, inverse problems.

Abstract : Diffusion magnetic resonance imaging (dMRI) is an imaging modality that probes the diffusion characteristics of a sample via the application of magnetic field gradient pulses. An important quantity measured in dMRI in each voxel is the Apparent Diffusion Coefficient (ADC). There is a large variety of macroscopic models for ADC in the literature, ranging from simple to complicated. The goal of this thesis is to derive simple (but sufficiently sound for applications) models starting from fine PDE modelling of diffusion at microscopic scale using homogenization techniques.
In a previous work, the homogenized FPK model was derived starting from the Bloch-Torrey PDE equation under the assumption that membrane's permeability is small and diffusion time is large. We first analyse this model and establish a convergence result to the well known Kärger model as the magnetic pulse duration goes to 0. In that sense, our analysis shows that the FPK model is a generalisation of the Kärger one for the case of arbitrary duration of the magnetic pulses.
The ADC for the FPK model is time-independent which is not compatible with some experimental observations. Our goal next is to correct this model for small so called b-values so that the resulting homogenised ADC is sensitive to both the pulses duration and the diffusion time. To achieve this goal, we employed a similar homogenization technique as for FPK, but we include a suitable time and gradient intensity scalings for the range of considered b-values. We also obtain some analytical approximations (using short time expansion of surface potentials for the heat equation and eigenvalue decompositions) of the asymptotic model that yield explicit formulas of the time dependency of ADC.
Finally we explored the inverse problem of determining qualitative information on the cells volume fractions from measured dMRI signals. While finding sphere distributions seems feasible from measurement of the dMRI signal, we show that ADC alone would not be sufficient to obtain this information.

Université Paris-Saclay
Espace Technologique / Immeuble Discovery
Route de l'Orme aux Merisiers RD 128 / 91190 Saint-Aubin, France